Enhanced Nanoscale Characterization of van der Waals Materials
Combining Electron Energy Loss Spectroscopy

Brokkelkamp, A.R.

DOI
10.4233/uuid:d321f3f6-7b0e-4f45-938c-bbd2a22a89df

Publication date
2025

Document Version
Final published version

Citation (APA)
Brokkelkamp, A. R. (2025). *Enhanced Nanoscale Characterization of van der Waals Materials: Combining Electron Energy Loss Spectroscopy*. [Dissertation (TU Delft), Delft University of Technology]. https://doi.org/10.4233/uuid:d321f3f6-7b0e-4f45-938c-bbd2a22a89df

Enhanced Nanoscale Characterization of Van der Waals Materials

Combining Electron Energy Loss Spectroscopy with Machine Learning

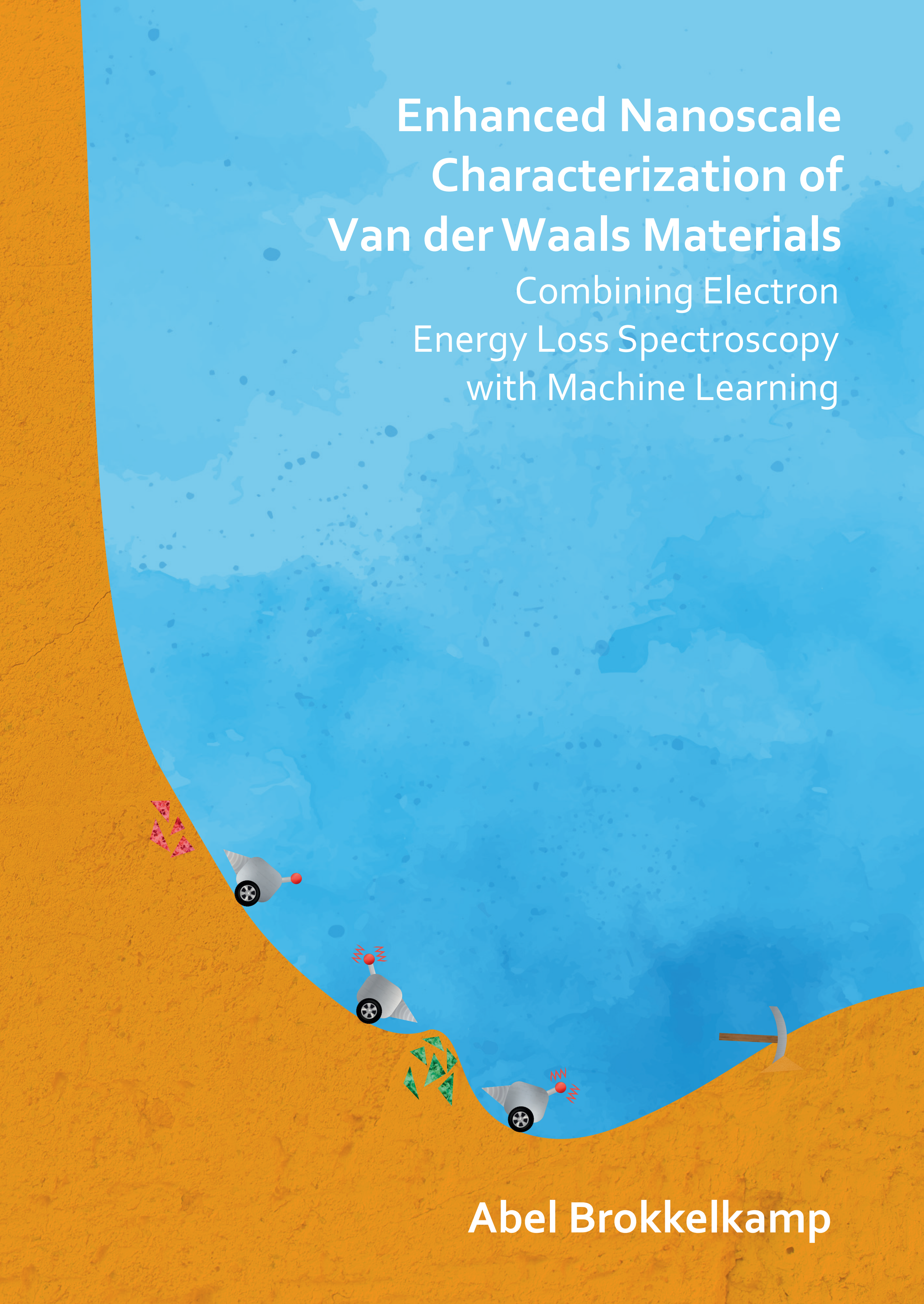

Abel Brokkelkamp

ENHANCED NANOSCALE CHARACTERIZATION OF TWO-DIMENSIONAL VAN DER WAALS MATERIALS

COMBINING ELECTRON ENERGY LOSS SPECTROSCOPY WITH MACHINE LEARNING

ENHANCED NANOSCALE CHARACTERIZATION OF TWO-DIMENSIONAL VAN DER WAALS MATERIALS

COMBINING ELECTRON ENERGY LOSS SPECTROSCOPY WITH MACHINE LEARNING

Proefschrift

ter verkrijging van de graad van doctor
aan de Technische Universiteit Delft,
op gezag van de Rector Magnificus prof. dr. ir. T.H.J.J. van der Hagen,
voorzitter van het College voor Promoties,
in het openbaar te verdedigen op Maandag 7 April 2025 om 10:00 uur

door

Abel Rutger BROKKELKAMP

Master of Science in Applied Physics,
Technische Universiteit Delft, Nederland,

geboren te Diemen, Nederland.

Dit proefschrift is goedgekeurd door de promotoren

Samenstelling promotiecommissie:

Rector Magnificus,	voorzitter
Dr. S. Conesa-Boj,	Technische Universiteit Delft, promotor
Prof. dr. L. Kuipers,	Technische Universiteit Delft, promotor
Onafhankelijke leden:	
Prof. dr. J. Verbeeck,	Universiteit Antwerpen
Dr. ir. M.A. van Huis,	Universiteit Utrecht
Prof. dr. J. Ferrer Rodriguez,	Universidad de Oviedo
Prof. dr. G.A. Steele,	Technische Universiteit Delft
Prof. dr. A.F. Otte,	Technische Universiteit Delft, reservelid

Keywords:	electron energy loss spectroscopy, transmission electron microscopy, transition metal dichalcogenides nanostructures, van der waals materials, machine learning
Printed by:	Gildeprint
Front & Back:	Artistic impression of the low electron energy loss region with little machines on the spectrum looking for hidden features.

ISBN (Printed Version) 978-94-6384-746-9
ISBN (Electronic Version) 978-94-6518-025-0

An electronic version of this dissertation is available at
`http://repository.tudelft.nl/`.

The depth of learning is in direct relation
to the intensity of the experience.

- Robert A. Monroe

CONTENTS

Summary **xi**

Samenvatting **xiii**

1 Introduction **1**

References 6

2 Deep Learning for the Zero Loss Peak **13**

2.1 Introduction 14
2.2 The spectral image 14
 2.2.1 Pooling of the spectral image 17
 2.2.2 Clustering the spectral image 18
2.3 A deep-learning model for the zero-loss peak 20
 2.3.1 Improving the deep learning model 22
2.4 Deconvolution of EEL spectra. 23
 2.4.1 The single-scattering distribution 24
 2.4.2 Fourier Log deconvolution. 25
 2.4.3 Discrete Fourier transforms. 26
References 26

3 Spatially resolved Band gap and Dielectric function **31**

3.1 Introduction 32
3.2 Thickness determination by Kramers-Krönig analysis 32
3.3 Band gap analysis of the EELS low-loss region 34
3.4 Complex dielectric function from EEL spectra using Kramers-Krönig analysis 37
 3.4.1 The role of surface scatterings. 39
 3.4.2 Complex dielectric function in InSe and WS_2 40
3.5 Conclusions and outlook 42
References 43

4 Peak Identification in Loss and Gain Regions of EELS **47**

4.1 Introduction 48
4.2 Case study: 1D-MoS_2 nanostructures 48
 4.2.1 Structural characterisation. 49
 4.2.2 Spatially-resolved STEM-EELS characterisation 52
 4.2.3 Automated EELS Peak Detection and Analysis 53
 4.2.4 Spatially-Resolved Band Gap Energy of 1D-MoS_2 Nanostructures . . 56
 4.2.5 Sensitivity of the Exciton Peak Location 58
 4.2.6 Conclusions 60

4.3 Case study: Topological Insulator Bi_2Te_3 61
  4.3.1 Structural composition 61
  4.3.2 Spatially resolved EEGS 62
  4.3.3 Peak identification procedure 63
  4.3.4 Uncertainty propagation in EEGS 67
  4.3.5 Conclusions 69
4.4 Summary and Outlook 70
References 70

5 Edge-Localised Plasmonic Resonances in WS_2 Nanostructures from Electron Energy-Loss Spectroscopy **77**
5.1 Introduction 78
5.2 Results and Discussion 78
  5.2.1 NMF Decomposition of Spectral Features 80
  5.2.2 Electrodynamical Simulations of EELS Edge Profiles 83
  5.2.3 Dispersion relation of edge-localised plasmonic modes 85
5.3 Summary and Outlook 88
References 89

6 Conclusions and Outlook **95**
References 98

A Supplementary information to Chapter 2 **99**
A.1 EELSFITTER code usage 99
  A.1.1 Pre-training preparations 99
  A.1.2 Training ZLP models 100
  A.1.3 Post processing 102
  A.1.4 Quantitative analysis 102
  A.1.5 Plotting in EELSFITTER 103

B Supplementary information to Chapter 3 **105**
B.1 Methods 105
B.2 Structural characterisation of the InSe specimen 105
B.3 Band gap analysis of 2H/3R WS_2 nanoflowers 108
B.4 Validation of Kramer-Krönig analysis against HyperSpy 110
References 111

C Supplementary information to Chapter 4 **113**
C.1 Case study: 1D-MoS_2 nanostructures 113
  C.1.1 Methods 113
  C.1.2 Characterization of 1D-MoS_2 Nanostructures 114
  C.1.3 Partial Sulfurization and Intermediate MoO_3 Formation 114
  C.1.4 EELS Analysis of an Interconnected 1D-MoS_2 Nanostructure 115
  C.1.5 Band Gap Energy Map of 1D-MoS_2 Nanostructures 115

C.2 Case study: Topological Insulator Bi_2Te_3 119
C.2.1 Methods 119
C.2.2 Atomic structure characterisation of Bi_2Te_3 119
C.2.3 Robustness of the models 119
C.2.4 Peak location in the energy-loss region. 121
C.2.5 Energy-gain peaks in different Bi_2Te_3 specimens. 122
C.2.6 HRTEM analysis of the Bi_2O_3 region 126
References 127

D Supplementary information to Chapter 5 129

D.1 Structural Characterization of WS_2 Nanostructures 130
D.1.1 WS_2 Nanostructure Thickness Mapping 130
D.1.2 Morphology and Thickness Mapping of Additional WS_2 Nanostructures 130
D.2 Spatially-Resolved EELS Data Processing 132
D.2.1 Decomposition of EELS data using NMF. 132
D.2.2 NMF decomposition of all nanotriangles 134
D.2.3 Validation of the NMF Abundance Maps from EELS Point Spectra . . 135
D.3 EELS-GDM Electrodynamical Simulations 142
D.3.1 Edge Dispersions of Nanotriangles. 142
D.3.2 EELS Probability Maps 142
D.3.3 Potential Limitations of the Simulation Model 145
D.4 Extracting Edge Modes in WS_2 nanotriangles from NMF 149
D.4.1 Advantages of NMF Over Conventional Intensity Mapping Methods. 150
References 151

Curriculum Vitæ **153**

List of Publications **155**

Acknowledgements **157**

SUMMARY

Two-dimensional (2D) layered materials are integral to modern condensed matter research due to their remarkable electronic and optical properties. A key feature of these materials is that their properties can be adjusted by making small changes to their structure at the nano- and atomic scale. Understanding and linking these electronic and optical properties to structural features at the nanoscale is crucial for unlocking the full potential of 2D layered materials and maximizing their use in advanced devices.

This thesis uses electron-based microscopy and spectroscopy to achieve the high spatial and energy resolution required for this goal. These techniques address the limitations of optical and X-ray spectroscopy, which, while offering excellent spectral resolution, lack the spatial precision needed to resolve nanoscale morphologies and atomic structures critical for understanding 2D materials.

To achieve this, we employ two advanced electron microscopy methodologies: probe-corrected Scanning Transmission Electron Microscopy (STEM) and monochromated Electron Energy-Loss Spectroscopy (EELS). Together, these techniques enable the acquisition of high-quality Spectral Images (SIs) with both exceptional spatial and spectral resolution, providing a powerful platform for the detailed characterization of 2D layered materials. To further enhance the potential of STEM-EELS, we integrate Machine Learning (ML)-based approaches. These approaches introduce innovative solutions such as the removal of the dominant Zero Loss Peak (ZLP) background in the low-loss energy region, peak identification and multivariate techniques to separate overlapping signals and so fully leverage the rich information contained in STEM-EELS SIs

Chapter 2 establishes the data processing methodology used in this work. It provides an overview of STEM-EELS SIs, detailing how they are acquired, interpreted, and the challenges involved in processing these high-dimensional datasets. A key focus is on our ML-based approach for image-wide subtraction of the ZLP in SIs. This step is crucial for isolating spatially localized information in the low-loss energy region, which would otherwise be obscured by the ZLP tail. The methodology incorporates ML techniques originally developed in high-energy physics for probing the interior structure of protons, demonstrating the adaptability of these methods to electron microscopy. This analysis framework, named EELSFitter, serves as the foundation for the remainder of the thesis, where it is applied to the characterization of 2D layered materials. Developed in Python, the framework is open-source and freely available for use by the research community.

In Chapter 3, the framework EELSFitter is applied to investigate Indium Selenide (InSe) nanosheets and Tungsten Disulfide (WS_2) flakes with mixed polytipism (2H/3R). The thickness and stacking order of layers are critical structural features that influence the optoelectronic properties of 2D materials, including their band gap. For InSe, the stacking order or crystalline phase determines whether the band gap is direct or indirect and affects its value. In the case of WS_2, a member of the Transition Metal Dichalcogenides (TMDs) family, thickness plays a direct role in tuning the band gap, making it an ideal benchmark for validating the ML-based approach. Using robust ZLP subtraction in the SIs of these materials, we achieve nanoscale precision in spatially resolving their band gap and dielectric function. Additionally, we correlate the electronic properties to structural features, with a particular focus on local specimen thickness, demonstrating the effectiveness of this methodology.

We extend the data processing techniques and analytical methods to tackle automated feature identification within the energy-loss and energy-gain region of EELS in Chapter 4. The first part of this chapter focuses on one-dimensional (1D) Molybdenum Disulfide (MoS_2) nanostructures. As a TMD material similar to WS_2, MoS_2 in a 1D morphology allows us to study the effects of curvature-induced strain on its optoelectronic properties. We characterise excitonic and plasmonic resonances, revealing how these features are influenced by the 1D geometry. Additionally, we investigate excitonic behaviour and the band gap value in relation to localized curvature-induced strain, comparing the properties at the tips of the 1D structures with those at the body.

The second part of the chapter examines the layered topological insulator Bismuth Telluride Bi_2Te_3. Here, we focus on the energy-gain region, applying ML-based techniques originally developed for modelling the loss region of the ZLP. Using this approach, we extract a well-defined collective excitation at -0.8 eV on the energy-loss axis. By relying on the energy-gain region, we avoid complications from multiple scattering, enabling the characterization of this excitation with enhanced spectral precision. This chapter highlights the versatility of our methods for analysing diverse materials and morphologies.

In Chapter 5, we focus on WS_2 nanotriangles, examining localised plasmonic resonances that form along their edges. By employing non-negative matrix factorization (NMF), we identify the spatial distribution of these resonances and successfully separate them from signals originating from overlapping WS_2 nanotriangles. The results of the NMF analysis are compared with electrodynamical simulations, which reveal strong agreement with the observed localized plasmonic resonances. Further, we quantify these resonances by analysing their dispersion relation through a 1D Fabry-Perot model. This analysis demonstrates a quadratic dispersion characteristic of surface plasmonic phenomena, offering deeper insights into the optical behaviour of WS_2 nanotriangles.

This thesis presents the development of novel strategies for processing and interpreting STEM-EELS SIs in both the low energy-loss and energy-gain regions. Through these advancements, we provide valuable insights into the relationship between structural and physical properties across various morphologies and material types of layered materials. Importantly, all computational frameworks developed during this work are open-source and freely available, ensuring that the methodologies and approaches can be easily adopted by other researchers. This accessibility promotes the wider application of electron microscopy and related techniques to the study of nanostructured materials, fostering further advancements in the field.

SAMENVATTING

Twee-dimensionale (2D) gelaagde materialen zijn integraal voor hedendaags gecondenseerde materie onderzoek vanwege hun opmerkelijke elektrische en optische eigenschappen. Een belangrijk kenmerk van deze materialen is dat hun eigenschappen aangepast kunnen worden door kleine aanpassingen in hun structuur op nano- en atomaire schaal. Het begrijpen en koppelen van deze elektrische en optische eigenschappen naar structurele eigenschappen op nanoschaal is cruciaal om de volledige potentie van 2D materialen te benutten en hun gebruik in geavanceerde apparaten te maximaliseren.

Dit proefschrift richt zich op het gebruik van elektronen-gebaseerde microscopie en spectroscopie, die bij uitstek geschikt zijn voor het bereiken van de hoge ruimtelijke resolutie en energie resolutie die nodig zijn voor dit doel. Deze technieken kaarten de tekortkomingen van optische en röntgenstraling spectroscopie aan, die, hoewel ze uitstekende spectrale resolutie bieden, ruimtelijke precisie missen die nodig is om nano- en atomaire vormen in beeld te brengen en kritisch is voor het begrijpen van 2D materialen.

Om dit te bereiken passen we twee geavanceerde elektronen microscopie methodologieën toe: bundel-gecorrigeerde Raster Transmissie Elektronen Microscopie (Engels: Scanning Transmission Electron Microscopy (STEM)) en monochromatische Elektronen Energy-Verlies Spectroscopie (Engels: Electron Energy-Loss Spectroscopy (EELS)). Deze technieken samen zijn in staat Spectrale Afbeeldingen (Engels: Spectral Image (SI)) van hoge kwaliteit op te nemen, met zowel een exceptionele ruimtelijke als spectrale resolutie, en dus een krachtig platform bieden voor gedetailleerde karakterisatie van 2D gelaagde materialen. Om de potentie van STEM-EELS verder te verhogen integreren we Machinaal Leren (Engels: Machine Learning (ML)) gebaseerde benaderingen. Met deze aanpak introduceren we innovatieve oplossingen zoals het verwijderen van de dominante Nul Verlies Piek (Engels: Zero Loss Peak (ZLP)) achtergrond in the lage energie verlies regio, piek identificatie en multivariate technieken om overlappende signalen te separeren om zo de informatie rijke STEM-EELS SIs te benutten.

In Hoofdstuk 2 wordt de gegevensverwerking methodologie van dit proefschrift vastgesteld. Er wordt een overzicht van STEM-EELS SIs gegeven, met details over hoe deze worden opgenomen, geïnterpreteerd en welke uitdagingen te pas komen bij het verwerken van deze hoge-dimensionale gegevensset. Een belangrijk aandachtspunt is op onze ML-gebaseerde benadering voor het afbeeldingsbrede verwijdering van de ZLPs in SIs. Deze stap is cruciaal voor het isoleren van ruimtelijk gelokaliseerde informatie in de lage energie verlies regio, die anders verborgen zou zijn door de ZLP staart. Deze methodologie bevat ML technieken oorspronkelijk ontwikkeld in hoge-energie fysica voor het bestuderen van het interieur van protonen en demonstreert hiermee het aanpassingsvermogen van deze methodes in elektronen microscopie. Dit kader, genaamd EELSFITTER, dient als basis voor de rest van het proefschrift, waar het wordt toegepast voor het karakteriseren van 2D gelaagde materialen. Geschreven in Python is dit kader open-source en gratis beschikbaar voor gebruik door het onderzoeksgemeenschap.

In Hoofdstuk 3 wordt EELSFITTER toegepast om Indiumselenide (InSe) nanobladen en Wolfraamdisulfide (WS_2) schilfers van gemixte polytipisme (2H/3R) te onderzoeken. De dikte en de stapelvolgorde van de lagen zijn belangrijke structurele eigenschappen die invloed hebben op de opto-elektronische eigenschappen van 2D materialen, onder andere hun verboden zone. Voor InSe bepaalt de stapelvolgorde of kristalfase, of de verboden zone een directe of indirecte transitie bevat en bepaalt het van de waarde van de verboden zone. In het geval van WS_2, een lid van de familie van Transitiemetaal Dichalcogenides (TMDs), speelt de dikte direct een rol in het afstemmen van de verboden zone, wat het een ideale maatstaf maakt voor het valideren van de ML-gebaseerde benadering. Gebruikmakend van een robuuste verwijdering van de ZLP in de SIs van deze materialen, bereiken we nanoschaal precisie in het ruimtelijke bepalen van hun verboden zone en diëlektrische functie. Daarbij komend correleren we de elektronische eigenschappen met de structurele eigenschappen, met een specifieke focus op de lokale dikte en demonstreren hiermee de effectiviteit van de methodologie.

We breiden de gegevensverwerkingstechnieken en analytische methodes uit met automatische kenmerk identificatie in de energieverlies en energiewinst regio van EELS in Hoofdstuk 4. In het eerste deel van dit hoofdstuk bestuderen we één-dimensionale (1D) Molybdeendisulfide (MoS_2) nanostructuren. MoS_2 is net als WS_2 een TMD, en met het bestuderen van MoS_2 in een 1D morfologie kunnen we de effecten bestuderen van kromming-geïnduceerde spanning op de opto-elektronische eigenschappen. We karakteriseren de excitonische en plasmonische resonanties en onthullen hoe deze eigenschappen worden beïnvloed door de 1D geometrie. Daarbij onderzoeken we het excitonische gedrag en de waarde van de verboden zone in relatie tot de gelokaliseerde kromming-geïnduceerde spanning door het vergelijken van de eigenschappen aan de puntjes van de 1D structuren ten opzichte van hun kern.

In het tweede deel van het hoofdstuk onderzoeken we de gelaagde topologische isolator Bismuttelluride (Bi_2Te_3). Hier zetten we de focus op de energiewinst regio en passen de ML-gebaseerde technieken toe oorspronkelijk ontwikkeld voor de energieverlies regio van de ZLP. Met deze benadering extraheren we een goed gedefinieerde collectieve excitatie op -0.8 eV op de energieverlies as. Door het gebruik van de energiewinst regio voorkomen we complicaties van meervoudige verstrooiing waardoor we deze excitatie kunnen karakteriseren met verbeterde spectrale precisie. Dit hoofdstuk benadrukt de veelzijdigheid van onze methodes voor het analyseren van diverse materialen en vormen.

In Hoofdstuk 5 leggen we de focus op WS_2 nanodriehoeken en onderzoeken we gelokaliseerde plasmonische resonanties die vormgeven aan hun randen. Met het toepassen van niet-negatieve matrix factorisatie (NMF) identificeren we de ruimtelijke verdeling van deze resonanties en scheiden we ze met succes van signalen die komen van overlappende WS_2 nanodriehoeken. Het resultaat van de NMF analyse wordt vergeleken met elektrodynamische simulaties, die in sterke overeenstemming zijn met de geobserveerde gelokaliseerde plasmonische resonanties. Verder kwantificeren we deze resonanties door het analyseren van hun dispersie middels een 1D Fabry-Perot model. Deze analyse demonstreert een kwadratische dispersie karakteristiek voor plasmonische oppervlak fenomenen en biedt een dieper inzicht in het optische gedrag van WS_2 nanodriehoeken.

Dit proefschrift presenteert de ontwikkelingen van nieuwe strategieën voor het verwerken en interpreteren van STEM-EELS SIs in zowel lage energieverlies en energiewinst regio's. Door deze vooruitgangen zorgen we voor waardevolle inzichten in the relatie tussen structurele en fysische eigenschappen over verscheidene vormen en materiaal types van gelaagde materialen. Belangrijk is dat alle computationele kaders ontwikkeld tijdens dit werk open-source en gratis beschikbaar zijn, zodat deze methodologieën en benaderingen makkelijk door andere onderzoekers gebruikt kunnen worden. Deze toegankelijkheid bevordert de bredere toepassing van elektronen microscopie en verwante technieken voor de studie van nano-gestructureerde materialen, en behartigt verdere vooruitgangen in het veld.

1

INTRODUCTION

Seeing the small is called clarity

- Tao Te Ching chapter 52

TWO-DIMENSIONAL LAYERED MATERIALS

Since the groundbreaking first isolation and identification of graphene, a single layer of graphite, in 2004 [1], two-dimensional (2D) layered materials, also known as van der Waals (vdW) materials, have grown to be present in nearly every field of condensed matter research [2], [3].

The characteristic feature of these materials is that, when one zooms into a bulk crystal, one finds layers neatly stacked on top of each other that can be easily separated among them. Indeed, while within a single layer the atoms are strongly held together by covalent bonds, between adjacent layers they are instead loosely bound together by the weak Van der Waals force. These defining structural properties of 2D layered materials have a profound impact on their electronic properties, which have been shown to depend on the underlying atomic arrangement down to the single monolayer level. Furthermore, in order to satisfy the requirements of smaller, faster, and more efficient performance for optoelectronic and nanophotonic applications, 2D materials are particularly attractive since they can be tuned to exhibit specific properties on demand [4], [5]. In this endeavour, the precise characterisation and correlation of their structural properties and optoelectronic plays an essential role.

Of direct relevance for this thesis are the 2D materials of the family of Transition Metal Dichalcogenides (TMDs). These compound materials are composed by a transition metal element sandwiched by chalcogen atoms [6]. Two particularly relevant instances of TMDs are Tungsten Disulfide (WS_2) and Molybdenum Disulfide (MoS_2). TMDs typically exhibit, as opposed to graphene, a semiconducting behaviour, and hence offer great potential to eventually replace silicon in a wide variety of applications such as flexible and transparent electronics [7], light-harvesting technologies [8]–[10], and quantum optics [5].

As extensive research has demonstrated, the remarkable properties of layered materials can be successfully tailored by varying structural parameters such as the number of layers, strain, or the relative angle (twist) between adjacent layers. Using WS_2 as an example, when going from bulk material to the monolayer level, its band gap transitions from a 1.3 eV indirect gap to a 2.0 eV direct gap with as a result an enhanced optical response [11]. Another powerful handle that can be deployed to harness their electronic properties is the stacking order among layers. This is highlighted by Indium Selenide (InSe), another of the materials studied in this thesis, where the choice of arrangement of its layers can either result in a direct band gap at 1.29 eV or an indirect band gap at 1.4 eV [12].

The overall morphology of 2D materials can also have a profound impact on the resulting properties, and in particular it can induce the localisation of excitonic and plasmonic resonances (among others), which is a highly desirable feature for a broad palette of optoelectronic applications. It has been reported that localised excitons in TMD-based nanostructures exhibit strikingly different behaviours compared to their bulk counterparts, directly impacting the resulting optoelectronic functionalities. To emphasize the potentialities of this important feature, one can mention that localised excitons in TMD materials exhibit longer lifetimes [13] and narrower photoluminescence line widths [14] which make them highly appealing for applications such as single-photon emitters [15], [16], to be deployed in future quantum technologies like quantum optics [17], [18] and quantum networking [19], [20].

With this motivation, a particularly attractive route to realise exciton localisation in TMDs is based on exploiting the effects of strain in these materials [21]–[23]. Indeed, strain has been shown to induce shifts in the exciton energy, and therefore by precisely controlling the level of strain present in the TMD nanomaterial, one can robustly adjust the excitonic properties [21]–[23]. Intrinsic strain can be conveniently induced in TMDs by departing from the traditional planar configuration of layered materials and moving to novel morphologies, such as the one-dimensional (1D) configuration. This route enables accurate control over the resulting intrinsic strain arising in the crystal structure and its localisation across the material [24], [25], by means of suitable adjusting the nanofabrication strategies adopted to grow TMDs in 1D morphologies.

The remarkable versatility of van der Waals materials is also reflected by their demonstrated potential to exhibiting localised plasmonic properties, which are conventionally considered mostly in noble metals but not in semiconductor materials. Indeed, spatially-localised plasmonic resonances in 2D materials have garnered increasing interest due to their ability to confine electromagnetic fields at the nanoscale, hence enabling enhanced light-matter interactions [26]–[29]. In the case of TMD materials, the morphology and edge configurations play a critical role in determining their plasmonic response. In particular, edge structures in TMDs are instrumental to harness this plasmonic response [30], [31], for instance by inducing metallic behaviour due to the exposed transition metal atoms [32], [33]. Additionally, 2D topological insulator materials such as Bi_2Te_3 also provide a possible path to tune plasmonic resonances thanks to their metallic surface states, which induce plasmonic localisation at the edges [34].

BOOSTING ELECTRON-BASED SPECTROSCOPY WITH AI

Given that, for TMD materials, their structural characteristics down to the atomic scale determine the resulting optoelectronic properties, in order to fully exploit the potential of TMDs and related 2D materials, charting both their crystal structure and their optoelectronic response with the highest possible resolution becomes of utmost importance.

For such a task, optical and X-ray spectroscopies benefit from excellent spectral (energy) resolution, but lack the spatial resolution necessary to fully resolve nanoscale morphologies and atomic lattices. For instance, in optical and X-ray spectroscopies, assessing the impact of structural defects is challenging since it relies on the assumption that these are present without the explicit confirmation from direct measurements of the crystal lattice. Similar considerations apply when assessing the effects of strain on the optoelectronic properties of TMD nanomaterials. Although externally-applied strain can be quantified using light-based spectroscopies at microscale level [35], gauging the consequences of intrinsic strain fields remains elusive for these techniques, in particular concerning nanoscale-size specimens and 1D morphologies. This limitation introduces a fundamental ambiguity when interpreting the interplay between electronic and structural properties, hindering the development of TMD-based devices.

To bypass these challenges of light-based microscopy and spectroscopy techniques, electron-based microscopy and spectroscopy techniques provide a way forward. In particular, in this thesis we adopt Scanning Transmission Electron Microscopy (STEM) in combination with Electron Energy-Loss Spectroscopy (EELS) to provide a comprehensive characterisation of the functionalities of different TMD materials for novel morphologies and configuration. Here we benefit from recent advances in TEM instrumentation, such as probe correctors and electron monochromators, which have turned STEM-EELS into a state-of-the-art method for the analysis of nanoscale materials and structures [36]–[38], providing access to key properties such as band gaps [39], [40], excitonic transitions [23], localised plasmonic resonances [41]–[45], and phonons [46], [47].

Crucially, most of these important features arise as signals in the low-loss region of the electron energy-loss spectra, defined as the contributions of those electrons that have lost an energy of $E_{\text{loss}} \lesssim 50$ eV after interacting with the specimen. The theoretical interpretation of this low-loss region is however complicated by the overwhelming Zero-Loss Peak (ZLP) background, associated to electrons which do not interact inelastically with the specimen together with the associated instrumental broadening, and which is specially dominant in the $E_{\text{loss}} \lesssim 5$ eV region. Several strategies have been proposed to solve the problem of ZLP subtraction, such as the power-law approach commonly applied for core-loss EELS ($E_{\text{loss}} \gtrsim 50$ eV), but these fail to model the steeply-falling ZLP background. Other approaches include taking measurements of the ZLP in the vacuum and using those as a baseline for its subtraction, but this approach neglects the influence of the specimen thickness on the overall ZLP shape. Mirroring the ZLP using data from the energy-gain region, $E_{\text{loss}} < 0$, has also been attempted, however this requires the dubious assumption that the ZLP is fully symmetric. More recently, novel approaches to this problem based on machine learning (ML) algorithms to model the ZLP have been put forward. ML and related Artificial Intelligence (AI) tools have become ubiquitous in about every aspect of science as exemplified with the recent 2024 Nobel Prize in Physics [48], and hence their increasing use in the field of EELS [49]–[51] is not an exception.

Another defining feature associated to STEM-EELS measurements is that these can be acquired as spectral images (SI), whereby each pixel corresponds to a highly localised region of the specimen. The capabilities of STEM-EELS for producing high quality SI make it possible to visualise the effects of morphology, strain, defects, and interface effects on their electronic and optical properties with nanoscale resolution in 2D materials. A trade off in the acquisition of SI is the dwell time per pixel, given that higher pixel counts and longer dwell times imply longer measurement times, putting the sample at risk for radiation damage or contamination, as well as the reliability of the measurement itself due to instrumental instabilities. While these issues exacerbate the problems of traditional approaches for removing the ZLP, in the context of ML-based techniques the abundance of spectra in the SI taken under the same microscope conditions provides instead previous information for accurately modelling the ZLP. Indeed, thanks to EELS-SI, several hundreds of ML models for the ZLP can be trained in parallel to infer a confidence level interval for the ZLP model. In turn, this enables a reliable uncertainty estimate for related quantities such as the band gap energy extracted from the onset of the ZLP-subtracted inelastic spectra.

Another benefit of ZLP-subtracted EELS-SI is that they are further amenable to advanced data processing techniques to robustly extract physical signatures from the data. Multivariate techniques that deal with multidimensional data are of particular interest for this thesis, in particular non-negative matrix factorization (NMF), which among many other uses has been shown to efficiently identify plasmonic resonances in noble metals [52]. In case of 2D materials such as TMDs, these plasmonic resonances may be less well defined due to their dielectric nature, thus the need for proper removal of the ZLP before performing NMF becomes more pressing. Furthermore, the combination of EELS-SI with NMF should enable a clean identification of the spatially-localised plasmonic resonances which may arise, for instance, at the edges of TMD nanomaterials.

SCOPE AND OUTLINE OF THE THESIS

The aim of this thesis is two-fold. First, to develop novel computational frameworks tailored to the processing and theoretical interpretation of spectral images acquired in STEM-EELS in an effective and robust manner. We achieve this goal by realizing novel data processing algorithms based on machine learning techniques developed in the field of high energy physics and applying them to STEM-EELS SI, in particular for the modelling and subtraction of the ZLP. Subsequently, we combine our approach with advanced processing techniques, such as non-negative matrix factorisation, in order to identify subtle signals in the low-loss EELS region, such as localised plasmonic resonances in TMD materials, which would otherwise remain hidden were one to use more traditional techniques.

The second, and closely connected, aim of the present thesis is to deploy these novel computational strategies to characterise the optoelectronic response of van der Waals materials, focusing in particular in non-conventional morphologies from nanosheets and 1D nanostructures to nanotriangles. The developed strategies successfully reveal novel insights into the fascinating structure-property relationships in low-dimensional nanostructured TMD materials, despite the challenging environment posed by these specimens with various confounding factors that potentially challenge the interpretation of the results, hence highlighting the robustness and flexibility of our approach. These findings provide valuable inputs to harness the tunability of the physical properties of TMD nanomaterials, also by studying them in morphologies which may be more suitable for their eventual deployment in TMD-based devices.

The outline of this thesis is as follows. First, we establish our data processing methodology and in particular how STEM-EELS SI measurements are acquired and interpreted. In Chapter 2 we therefore begin with an overview of the acquisition of spectral images and address the complexities that the processing of such high dimensional datasets involve. We also present the model-independent deep-learning approach that is used for the image-wide subtraction of the ZLP in SIs and required to extract spatially-localised information from the low-loss region. In addition, we provide the formalism underlying the extraction of single-scattering distributions, important in subsequent chapters in order to quantify optoelectronic features form the EELS-SI. This chapter hence lays the theoretical foundations for the processing and interpretation of EELS-SI deployed in the rest of the thesis.

Moving to Chapter 3, we present a first direct application of the deep learning approach described in Chapter 2. We first examine Sn-doped InSe nanosheets, where optoelectronic properties such as the band gap value and type depend sensitively on structural factors such as layer stacking (phase like β, γ, and ϵ) and doping levels. The same method is applied to a different TMD nanostructure, WS_2 flakes, showcasing mixed polytypism (2H/3R) and that is chosen as a benchmark to validate the ML-based approach. This application, accompanied by the release of an updated version of the EELSfitter open-source code, validates our new ML approach for bias-free ZLP removal, makes possible the spatially resolved determination of the band gap energy and the dielectric function across a specimen, and highlights the capabilities of our approach for efficiently handling higher-dimensional STEM-EELS datasets.

Subsequently, we extend the data processing techniques and analytical methods that were introduced in Chapter 2 and Chapter 3 to tackle automated feature identification within the energy-loss and energy-gain regions of the EEL spectrum in Chapter 4. We consider two case studies to emphasize the impact of advanced EELS-based feature techniques to resolve and identify optoelectronic properties in nanostructured materials. In the first part, we study 1D Molybdenum Disulfide (MoS_2) nanostructures, characterising excitonic and plasmonic resonances and their interplay with the curvature-induced strain associated to the specimen morphology. We reveal spatially-dependent variations in both the excitonic behaviour and the band gap energy value, and correlate these effects to the localised strain arising in the 1D material.

In the second study, we investigate Bi_2Te_3, a topological insulator, focusing on collective excitations arising in the energy-gain region with $E_{\text{loss}} < 0$. Using a Gaussian model for the ZLP in combination with the Monte Carlo replica method for uncertainty estimation, our analysis determines that energy-gain EELS can reveal low-energy collective excitations with enhanced spectral precision, circumventing issues associated with multiple scattering, and stablish their correlation with structural features in the specimen such as rapid thickness variations.

In Chapter 5 we investigate WS_2 in a nanotriangle configuration, and characterise localised plasmonic resonances situated along the edges of the nanotriangles. We uncover the spatial localisation of these resonances with the use of non-negative matrix factorization (NMF), which makes it possible to disentangle resonances from overlapping WS_2 nanotriangles in a stacked configuration with otherwise remain undetected. The obtained results of the NMF components are scrutinised against electrodynamical theoretical simulations, showing good agreement between all localised plasmonic resonances observed and the various specimen morphologies. We further quantify the dispersion relation of the edge-localised plasmonic resonances using a 1D Fabry-Perot model, finding agreement with the expected quadratic dispersion relation associated to surface plasmonic phenomena.

We conclude this thesis (Chapter 6) summarising the key results from the presented studies and provide an outlook for further research prospects.

References

[1] K. S. Novoselov, A. K. Geim, S. V. Morozov, *et al.*, "Electric field effect in atomically thin carbon films", *Phys. Rev. Lett*, vol. 306, pp. 666–669, Oct. 2004. [Online]. Available: `www.arXiv.org/quant-ph/`.

[2] P. Ajayan, P. Kim, and K. Banerjee, "Two-dimensional van der waals materials", *Physics Today*, vol. 69, pp. 38–44, 9 2016, ISSN: 00319228. DOI: `10.1063/PT.3.3297`.

[3] K. S. Novoselov, A. Mishchenko, A. Carvalho, and A. H. C. Neto, “2d materials and van der waals heterostructures”, *Science*, vol. 353, 6298 2016, ISSN: 10959203. DOI: `10.1126/science.aac9439`.

[4] H. Hashtroudi, I. D. MacKinnon, and M. Shafiei, “Emerging 2d hybrid nanomaterials: Towards enhanced sensitive and selective conductometric gas sensors at room temperature”, *Journal of Materials Chemistry C*, vol. 8, pp. 13 108–13 126, 38 2020, ISSN: 20507526. DOI: `10.1039/d0tc01968b`.

[5] S. B. Anantharaman, K. Jo, and D. Jariwala, “Exciton-photonics: From fundamental science to applications”, *ACS Nano*, vol. 15, pp. 12 628–12 654, 8 Aug. 2021, ISSN: 1936086X. DOI: `10.1021/acsnano.1c02204`.

[6] W. Choi, N. Choudhary, G. H. Han, J. Park, D. Akinwande, and Y. H. Lee, “Recent development of two-dimensional transition metal dichalcogenides and their applications”, *Materials Today*, vol. 20, pp. 116–130, 3 Apr. 2017, ISSN: 18734103. DOI: `10.1016/j.mattod.2016.10.002`.

[7] S. J. Kim, K. Choi, B. Lee, Y. Kim, and B. H. Hong, “Materials for flexible, stretchable electronics: Graphene and 2d materials”, *Annual Review of Materials Research*, vol. 45, pp. 63–84, Jul. 2015, ISSN: 15317331. DOI: `10.1146/annurev-matsci-070214-020901`.

[8] S. Roy and P. Bermel, “Electronic and optical properties of ultra-thin 2d tungsten disulfide for photovoltaic applications”, *Solar Energy Materials and Solar Cells*, vol. 174, pp. 370–379, Jan. 2018, ISSN: 09270248. DOI: `10.1016/j.solmat.2017.09.011`.

[9] P. Tao, S. Yao, F. Liu, B. Wang, F. Huang, and M. Wang, “Recent advances in exfoliation techniques of layered and non-layered materials for energy conversion and storage”, *Journal of Materials Chemistry A*, vol. 7, pp. 23 512–23 536, 41 2019, RV2-PT, ISSN: 20507496. DOI: `10.1039/c9ta06461c`.

[10] M. Shanmugam, C. A. Durcan, R. Jacobs-Gedrim, and B. Yu, “Layered semiconductor tungsten disulfide: Photoactive material in bulk heterojunction solar cells”, *Nano Energy*, vol. 2, pp. 419–424, 3 May 2013, ISSN: 22112855. DOI: `10.1016/j.nanoen.2012.11.011`.

[11] A. Kumar and P. K. Ahluwalia, “Tunable dielectric response of transition metals dichalcogenides mx 2 (m=mo, w; x=s, se, te): Effect of quantum confinement”, *Physica B: Condensed Matter*, vol. 407, pp. 4627–4634, 24 Dec. 2012, ISSN: 09214526. DOI: `10.1016/j.physb.2012.08.034`.

[12] D. W. Boukhvalov, B. Gürbulak, S. Duman, *et al.*, “The advent of indium selenide: Synthesis, electronic properties, ambient stability and applications”, *Nanomaterials*, vol. 7, pp. 1–16, 11 2017, ISSN: 20794991. DOI: `10.3390/nano7110372`.

[13] G. Moody, K. Tran, X. Lu, *et al.*, “Microsecond Valley Lifetime of Defect-Bound Excitons in Monolayer WSe2”, *Phys. Rev. Lett.*, vol. 121, no. 5, p. 057 403, 2018. DOI: `10.1103/PhysRevLett.121.057403`.

[14] I. Niehues, R. Schmidt, M. Drüppel, *et al.*, “Strain Control of Exciton–Phonon Coupling in Atomically Thin Semiconductors”, *Nano Lett.*, vol. 18, no. 3, pp. 1751–1757, 2018, ISSN: 1530-6984. DOI: 10.1021/acs.nanolett.7b04868.

[15] S. Kumar, A. Kaczmarczyk, and B. D. Gerardot, “Strain-Induced Spatial and Spectral Isolation of Quantum Emitters in Mono- and Bilayer WSe2”, *ACS Publications*, 2015. DOI: 10.1021/acs.nanolett.5b03312.

[16] Q. Wang, J. Maisch, F. Tang, *et al.*, “Highly Polarized Single Photons from Strain-Induced Quasi-1D Localized Excitons in WSe2”, *Nano Lett.*, vol. 21, no. 17, pp. 7175–7182, 2021, ISSN: 1530-6984. DOI: 10.1021/acs.nanolett.1c01927.

[17] I. Aharonovich, D. Englund, and M. Toth, “Solid-state single-photon emitters”, *Nat. Photonics*, vol. 10, no. 10, pp. 631–641, 2016, ISSN: 1749-4893. DOI: 10.1038/nphoton.2016.186.

[18] *Quantum Dots for Quantum Information Technologies*. Cham, Switzerland: Springer International Publishing, 2017, ISBN: 978-3-319-56378-7. [Online]. Available: https://link.springer.com/book/10.1007/978-3-319-56378-7.

[19] H. J. Kimble, “The quantum internet”, *Nature*, vol. 453, no. 7198, pp. 1023–1030, 2008, ISSN: 1476-4687. DOI: 10.1038/nature07127.

[20] Y.-M. He, G. Clark, J. R. Schaibley, *et al.*, “Single quantum emitters in monolayer semiconductors”, *Nature nanotechnology*, vol. 10, no. 6, pp. 497–502, 2015.

[21] H. J. Conley, B. Wang, J. I. Ziegler, R. F. Haglund, S. T. Pantelides, and K. I. Bolotin, “Bandgap engineering of strained monolayer and bilayer mos2”, *Nano Letters*, vol. 13, pp. 3626–3630, 8 Aug. 2013, ISSN: 15306984. DOI: 10.1021/nl4014748.

[22] T. P. Darlington, C. Carmesin, M. Florian, *et al.*, “Imaging strain-localized excitons in nanoscale bubbles of monolayer WSe2 at room temperature”, *Nat. Nanotechnol.*, vol. 15, no. 10, pp. 854–860, 2020, ISSN: 1748-3395. DOI: 10.1038/s41565-020-0730-5.

[23] P. H. López, S. Heeg, C. Schattauer, *et al.*, “Strain control of hybridization between dark and localized excitons in a 2d semiconductor”, *Nature Communications*, vol. 13, 1 Dec. 2022, ISSN: 20411723. DOI: 10.1038/s41467-022-35352-9.

[24] F. Lee, M. Tripathi, R. S. Salas, *et al.*, “Localised strain and doping of 2d materials”, *Nanoscale*, vol. 15, pp. 7227–7248, 16 Mar. 2023, ISSN: 20403372. DOI: 10.1039/d2nr07252a.

[25] G. Wang, H. Hou, Y. Yan, *et al.*, “Recent advances in the mechanics of 2d materials”, *International Journal of Extreme Manufacturing*, vol. 5, 3 Sep. 2023, ISSN: 26317990. DOI: 10.1088/2631-7990/accda2.

[26] M. Wang, A. Krasnok, T. Zhang, *et al.*, “Tunable fano resonance and plasmon–exciton coupling in single au nanotriangles on monolayer ws2 at room temperature”, *Advanced Materials*, vol. 30, 22 May 2018, ISSN: 15214095. DOI: 10.1002/adma.201705779.

[27] Y. Liu, W. Huang, W. Chen, *et al.*, “Plasmon resonance enhanced ws 2 photodetector with ultra-high sensitivity and stability”, *Applied Surface Science*, vol. 481, pp. 1127–1132, Jul. 2019, ISSN: 01694332. DOI: 10.1016/j.apsusc.2019.03.179.

[28] C. Han, Y. Wang, W. Zhou, M. Liang, and J. Ye, "Strong anisotropic enhancement of photoluminescence in ws2 integrated with plasmonic nanowire array", *Scientific Reports*, vol. 11, 1 Dec. 2021, ISSN: 20452322. DOI: `10.1038/s41598-021-89136-0`.

[29] J. Zhang, X. Zhang, J. Li, *et al.*, "Simultaneous visible and ultraviolet photoresponse improvement of mos2/zno heterostructure photodetector via direct resonant coupling of au nanoparticles localized surface plasmon resonance", *Optical Materials*, vol. 124, p. 111 997, 2022, ISSN: 0925-3467. DOI: `https://doi.org/10.1016/j.optmat.2022.111997`.

[30] S. Zhang, C.-G. Wang, M.-Y. Li, *et al.*, "Defect Structure of Localized Excitons in a WSe2 Monolayer", *Phys. Rev. Lett.*, vol. 119, no. 4, p. 046 101, 2017. DOI: `10.1103/PhysRevLett.119.046101`.

[31] Y. J. Zheng, Y. Chen, Y. L. Huang, *et al.*, "Point Defects and Localized Excitons in 2D WSe2", *ACS Nano*, 2019. DOI: `10.1021/acsnano.9b02316`.

[32] S. L. Xiao, W. Z. Yu, and S. P. Gao, "Edge preference and band gap characters of mos2 and ws2 nanoribbons", *Surface Science*, vol. 653, pp. 107–112, Nov. 2016, ISSN: 00396028. DOI: `10.1016/j.susc.2016.06.011`.

[33] M. Tinoco, L. Maduro, M. Masaki, E. Okunishi, and S. Conesa-Boj, "Strain-dependent edge structures in mos2 layers", *Nano Letters*, vol. 17, pp. 7021–7026, 11 Nov. 2017, ISSN: 15306992. DOI: `10.1021/acs.nanolett.7b03627`.

[34] M. Zhao, M. Bosman, M. Danesh, *et al.*, "Visible surface plasmon modes in single bi2te3 nanoplate", *Nano Letters*, vol. 15, pp. 8331–8335, 12 Dec. 2015, ISSN: 15306992. DOI: `10.1021/acs.nanolett.5b03966`.

[35] X. He, H. Li, Z. Zhu, *et al.*, "Strain engineering in monolayer ws2, mos2, and the ws2/mos2 heterostructure", *Applied Physics Letters*, vol. 109, 17 Oct. 2016, ISSN: 00036951. DOI: `10.1063/1.4966218`.

[36] M. Terauchi, M. Tanaka, K. Tsuno, and M. Ishida, "Development of a high energy resolution electron energy-loss spectroscopy microscope", *Journal of Microscopy*, vol. 194, pp. 203–209, 1 1999, ISSN: 00222720. DOI: `10.1046/j.1365-2818.1999.00450.x`.

[37] B. Freitag, S. Kujawa, P. M. Mul, J. Ringnalda, and P. C. Tiemeijer, "Breaking the spherical and chromatic aberration barrier in transmission electron microscopy", *Ultramicroscopy*, vol. 102, pp. 209–214, 3 Feb. 2005, ISSN: 03043991. DOI: `10.1016/j.ultramic.2004.09.013`.

[38] R. Erni, N. D. Browning, Z. R. Dai, and J. P. Bradley, "Analysis of extraterrestrial particles using monochromated electron energy-loss spectroscopy", *Micron*, vol. 36, pp. 369–379, 4 2005, ISSN: 09684328. DOI: `10.1016/j.micron.2004.12.011`.

[39] B. Rafferty and L. Brown, "Direct and indirect transitions in the region of the band gap using electron-energy-loss spectroscopy", *Physical Review B - Condensed Matter and Materials Physics*, vol. 58, pp. 10 326–10 337, 16 1998, ISSN: 1550235X. DOI: `10.1103/PhysRevB.58.10326`.

[40] B. Rafferty, S. J. Pennycook, and L. M. Brown, “Zero loss peak deconvolution for bandgap eel spectra”, *Journal of Electron Microscopy*, vol. 49, pp. 517–524, 4 2000, ISSN: 00220744. DOI: 10.1093/oxfordjournals.jmicro.a023838.

[41] B. Schaffer, K. Riegler, G. Kothleitner, W. Grogger, and F. Hofer, “Monochromated, spatially resolved electron energy-loss spectroscopic measurements of gold nanoparticles in the plasmon range”, *Micron*, vol. 40, pp. 269–273, 2 Feb. 2009, ISSN: 09684328. DOI: 10.1016/j.micron.2008.07.004.

[42] F. J. García de Abajo, “Optical excitations in electron microscopy”, *Rev. Mod. Phys.*, vol. 82, pp. 209–275, 1 Feb. 2010. DOI: 10.1103/RevModPhys.82.209.

[43] Y. Wu, G. Li, and J. P. Camden, “Probing nanoparticle plasmons with electron energy loss spectroscopy”, *Chemical Reviews*, vol. 118, pp. 2994–3031, 6 Mar. 2018, ISSN: 15206890. DOI: 10.1021/acs.chemrev.7b00354.

[44] A. Polman, M. Kociak, and F. J. G. de Abajo, “Electron-beam spectroscopy for nanophotonics”, *Nature Materials*, vol. 18, pp. 1158–1171, 11 Nov. 2019, ISSN: 14764660. DOI: 10.1038/s41563-019-0409-1.

[45] F. J. G. D. Abajo and V. D. Giulio, “Optical excitations with electron beams: Challenges and opportunities”, *ACS Photonics*, vol. 8, pp. 945–974, 4 Apr. 2021, ISSN: 23304022. DOI: 10.1021/acsphotonics.0c01950.

[46] R. Egoavil, N. Gauquelin, G. T. Martinez, S. V. Aert, G. V. Tendeloo, and J. Verbeeck, “Atomic resolution mapping of phonon excitations in stem-eels experiments”, *Ultramicroscopy*, vol. 147, pp. 1–7, 2014, ISSN: 18792723. DOI: 10.1016/j.ultramic.2014.04.011.

[47] M. J. Lagos, I. C. Bicket, S. S. M. M., and G. A. Botton, “Advances in ultrahigh-energy resolution eels: Phonons, infrared plasmons and strongly coupled modes”, *Microscopy*, vol. 71, pp. I174–I199, Mar. 2022, ISSN: 20505701. DOI: 10.1093/jmicro/dfab050.

[48] *The nobel prize in physics 2024*, https://www.nobelprize.org/prizes/physics/2024/summary/, Accessed: 2024-11-13.

[49] S. S. M. M, A. Pofelski, H. Teimoori, and G. A. Botton, “Alignment-invariant signal reality reconstruction in hyperspectral imaging using a deep convolutional neural network architecture”, *Scientific Reports*, vol. 12, 1 Dec. 2022, ISSN: 20452322. DOI: 10.1038/s41598-022-22264-3.

[50] D. del-Pozo-Bueno, D. Kepaptsoglou, F. Peiró, and S. Estradé, “Comparative of machine learning classification strategies for electron energy loss spectroscopy: Support vector machines and artificial neural networks”, *Ultramicroscopy*, vol. 253, Nov. 2023, ISSN: 18792723. DOI: 10.1016/j.ultramic.2023.113828.

[51] A. Annys, D. Jannis, and J. Verbeeck, “Deep learning for automated materials characterisation in core-loss electron energy loss spectroscopy”, *Scientific Reports*, vol. 13, 1 Dec. 2023, ISSN: 20452322. DOI: 10.1038/s41598-023-40943-7.

[52] O. Nicoletti, F. D. L. Peña, R. K. Leary, D. J. Holland, C. Ducati, and P. A. Midgley, "Three-dimensional imaging of localized surface plasmon resonances of metal nanoparticles", *Nature*, vol. 502, pp. 80–84, 7469 2013, ISSN: 00280836. DOI: `10.1038/nature12469`.

2

DEEP LEARNING FOR THE ZERO LOSS PEAK

Electron Energy Loss Spectroscopy (EELS) in combination with Scanning Transmission Electron Microscopy (STEM) provides a plethora of access to structural, chemical and local electronic information. A key aspect in EELS is the zero-loss peak (ZLP), a narrow and high intensity peak centred around 0 eV. A result of the requirement that TEM specimens have to be electron transparent and most incident electrons not interacting with the specimen at all. The ZLP acts as both a feature (proxy for the specimen thickness) and background masking low-loss features of the EEL spectrum. Due to the irregular shape of the ZLP that can depend on several factors, current methods for modelling the ZLP fall short for effectively processing spectral images. Here, we built upon previous work in our group for modelling the ZLP using machine learning. We extend capabilities of the framework to process spectral images and make use of the large number of individual spectra present to change the underlying Monte Carlo replica method from a parametric to empirical. A key aspect to achieve this is the use of K-means to cluster the spectral image based on the known integrated intensity of the ZLP. The addition of a penalty term in the cost function of the network and a new automated process for determining the hyperparameters further increase the robustness of our approach. The models for the ZLP can then be used for deconvolution of EEL spectra to obtain the single scattering distribution (SSD) and quantify the aforementioned properties found in the EELS data.

2.1. INTRODUCTION

Accelerating ongoing investigations of two-dimensional (2D) materials, whose electronic properties depend on the underlying atomic arrangement down to the single monolayer level, demands novel approaches able to map this sensitive interplay with the highest possible resolution. In this context, Electron Energy Loss Spectroscopy (EELS) analyses in Scanning Transmission Electron Microscopy (STEM) provide access to a plethora of structural, chemical, and local electronic information [1]–[5], from thickness and composition to the band gap and complex dielectric function. Crucially, EELS-STEM measurements can be acquired as spectral images (SI), whereby each pixel corresponds to a highly localised region of the specimen. The combination of the excellent spatial and energy resolution provided by state-of-the-art STEM-EELS analyses [6]–[8] makes possible deploying EELS-SI as a powerful and versatile tool to realise the spatially-resolved simultaneous characterisation of structural and electric properties in nanomaterials. Such approach is complementary to related techniques such as cathodoluminescence in STEM (STEM-CL), which however is restricted to radiative processes while STEM-EELS probes both radiative and non-radiative processes [9]–[11].

Fully exploiting this potential requires tackling two main challenges. First, each SI is composed by up to tens of thousands of individual spectra, which need to be jointly processed in a coherent manner. Second, each spectra is affected by a different Zero-Loss Peak (ZLP) background [12], which depends in particular with the local thickness [5], [13]. A robust subtraction of this ZLP is instrumental to interpret the low-loss region, $E \lesssim$ few eV, in terms of phenomena [9] such as phonons, excitons, intra- and inter-band transitions, and to determine the local band gap. Furthermore, one should avoid the pitfalls of traditional ZLP subtraction methods [14]–[22] such as the need to specify an *ad hoc* parametric functional dependence.

In this work we bypass these challenges by presenting a novel strategy for the spatially-resolved determination of the band gap and complex dielectric function in nanostructured materials from EELS-SI. Our approach is based on machine learning (ML) techniques originally developed in particle physics [23]–[25] and achieves a spatial resolution down to a few nanometers. Individual EEL spectra are first classified as a function of the thickness with K-means clustering and subsequently used to train a deep-learning model of the dominant ZLP background [26]. The resultant ZLP models are amenable to theoretical processing, in particular in terms of Fourier transform deconvolution of the complete spectral image and Kramers-Krönig analyses, leading to a precise determination of relevant structural and electronic properties at the nanoscale.

2.2. THE SPECTRAL IMAGE

Spectral images in EELS-STEM are constituted by a large number, up to $\mathcal{O}(10^5)$, of individual spectra acquired across the analysed specimen. They combine the excellent spatial resolution, $\mathcal{O}(40\text{ pm})$, achievable with STEM with the competitive energy resolution, $\mathcal{O}(20\text{ meV})$, offered by monochromated EELS. From these EELS-SI it is possible to evaluate key quantities such as the local thickness, the band gap energy and type, and the complex dielectric function, provided one first subtracts the ZLP background which dominates the low-loss region of the EEL spectra. The information provided by an EELS-

SI can hence be represented by a three-dimensional data cube, Fig. 2.1a,

$$I^{(i,j)}_{\rm EELS}(E_\ell) = I^{(i,j)}_{\rm ZLP}(E_\ell) + I^{(i,j)}_{\rm inel}(E_\ell)\,, \quad i=1,\ldots,n_x\,, \quad j=1,\ldots,n_y\,, \quad \ell=1,\ldots,n_E\,, \tag{2.1}$$

where $I^{(i,j)}_{\rm EELS}$ indicates the total recorded intensity for an electron energy loss E_ℓ corresponding to the position (i,j) in the specimen. This intensity receives contributions from the inelastic scatterings off the electrons in the specimen, $I_{\rm inel}$, and from the ZLP arising from elastic scatterings and instrumental broadening, $I_{\rm ZLP}$. In order to reduce statistical fluctuations, it is convenient to combine the information from neighbouring spectra using the pooling procedure described in Section 2.2.1.

Since the ZLP intensity depends strongly on the local thickness of the specimen, first of all we group individual spectra as a function of their thickness by means of unsupervised machine learning, specifically by means of the K-means clustering algorithm presented in Section 2.2.1. The cluster assignments are determined from the minimisation of a cost function, $C_{\rm Kmeans}$, defined in thickness space,

$$C_{\rm Kmeans} = \sum_{r=1}^{n_x\times n_y}\sum_{k=1}^{K} d_{rk}\left|\ln\left(\frac{\widetilde{N}^{(k)}}{N^{(r)}_{\rm tot}}\right)\right|^p\,, \qquad r = i + (n_y-1)\,j\,, \tag{2.2}$$

with d_{rk} being a binary assignment variable, equal to 1 if r belongs to cluster k ($d_{rk}=1$ for $r\in T_k$) and zero otherwise, and with the exponent satisfying $p>0$. Here $N^{(r)}_{\rm tot}$ represents the integral of $I^{(i,j)}_{\rm EELS}$ over the measured range of energy losses, which provides a suitable proxy for the local thickness, and $\widetilde{N}^{(k)}$ is the k-th cluster mean. The number of clusters K is a user-defined parameter.

Subsequently to this clustering, we train a deep-learning model parametrising the specimen ZLP by extending the approach that we developed in [26]. The adopted neural network architecture is displayed in Figure 2.1b, where the inputs are the energy loss E and the integrated intensity $N_{\rm tot}$. The model parameters $\boldsymbol{\theta}$ are determined from the minimisation of the cost function,

$$C_{\rm ZLP}(\boldsymbol{\theta}) \propto \sum_{k=1}^{K}\sum_{\ell_k=1}^{n_E^{(k)}} \frac{\left[I^{(i_k,j_k)}(E_{\ell_k}) - I^{(\rm NN)}_{\rm ZLP}\left(E_{\ell_k}, \ln\left(N^{(i_k,j_k)}_{\rm tot}\right);\boldsymbol{\theta}\right)\right]^2}{\sigma_k^2\left(E_{\ell_k}\right)}\,, \qquad E_{\ell_k} \le E_{{\rm I},k}\,, \tag{2.3}$$

where within the k-th thickness cluster a representative spectrum (i_k, j_k) is randomly selected, and with $\sigma_k\left(E_{\ell_k}\right)$ being the variance within this cluster. The hyperparameters $E_{{\rm I},k}$ in Equation (2.3) define the model training region for each cluster ($E_{\ell_k}\le E_{{\rm I},k}$) where the ZLP dominates the total recorded intensity. They are automatically determined from the features of the first derivative $dI_{\rm EELS}/dE$, e.g. by demanding that only f% of the replicas have crossed $dI_{\rm EELS}/dE=0$, with $f\approx 10\%$. Typical values of $E_{{\rm I},k}$ are displayed in Figure 2.1c, where vacuum measurements are also included as reference. To avoid over-learning, the input data is separated into disjoint training and validation subsets, with the latter used to determine the optimal training length using look-back stopping [24]. Figure 2.1d displays the distribution of the training and validation cost functions, Equation (2.3), evaluated over 5000 models. Both Figure 2.1c and d correspond to the WS_2 nanoflower specimen first presented in [26] and revisited here. Further details on the deep-learning model training are reported in Section 2.3.

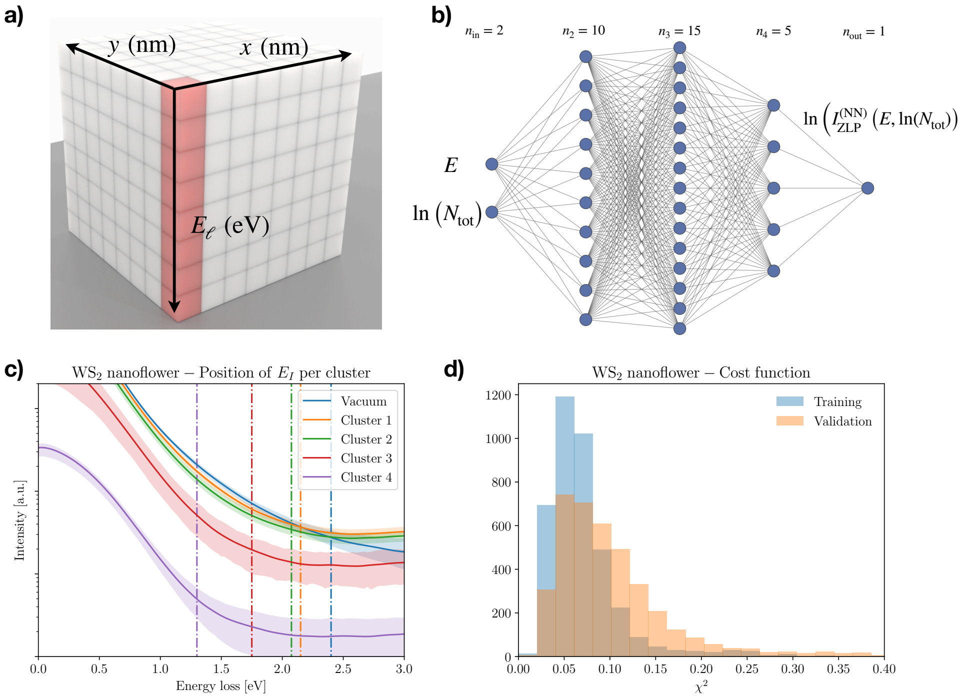

Figure 2.1: **(a)** Schematic data-cube representing EELS-SI measurements, with two directions labelling the location across the specimen and the third one the energy loss, and whose entries are the total intensity $I^{(i,j)}_{\text{EELS}}(E_\ell)$ in Eq. (2.1). **(b)** The network architecture parametrising the ZLP. The input neurons are the energy loss E and the integrated intensity N_{tot}, while the output neuron is the model prediction for the ZLP intensity. **(c)** The E_{I} hyperparameter defines the model training region, and is determined from the first derivative dI_{EELS}/dE in each thickness cluster. **(d)** The training and validation cost function C_{ZLP}, Eq. (2.3), evaluated over 5000 models. Both (b) and (c) correspond to the WS$_2$ nanoflower specimen.

This procedure is repeated for a large number of models N_{rep}, each based on a different random selection of cluster representatives, known in this context as "replicas". One ends up with a Monte Carlo representation of the posterior probability density in the space of ZLP models, providing a faithful estimate of the associated uncertainties,

$$\boldsymbol{I}_{\text{ZLP}}^{(\text{NN})} \equiv \left\{ I_{\text{ZLP}}^{(\text{NN})(n)}\left(E, \ln\left(N_{\text{tot}}\right)\right), \quad n = 1, \ldots, N_{\text{rep}} \right\}, \tag{2.4}$$

which makes possible a model-independent subtraction of the ZLP and hence disentangling the contribution from inelastic scatterings I_{inel}. Following a deconvolution procedure based in discrete Fourier transforms and reviewed in Section 2.4.3, these subtracted spectra allow us to extract the single-scattering distribution across the specimen and in turn the complex dielectric function from a Kramers-Krönig analysis. In contrast to existing methods, our approach provides an detailed estimate of the uncertainties associated to the ZLP subtraction, and hence quantifies the statistical significance of the determined properties by evaluating confidence level (CL) intervals from the posterior distributions in the space of models.

2.2.1. POOLING OF THE SPECTRAL IMAGE

Let us consider a two-dimensional region of the analysed specimen with dimensions $L_x \times L_y$ where EEL spectra are recorded for $n_p = n_x \times n_y$ pixels. Then the information contained within an EELS-SI may be expressed as

$$I^{(i,j)}_{\rm EELS}(E_\ell)\,, \quad i=1,\ldots,n_x\,, \quad j=1,\ldots,n_y\,, \quad \ell=1,\ldots,n_E\,, \tag{2.5}$$

where $I^{(i,j)}_{\rm EELS}(E_\ell)$ indicates the recorded total electron energy loss intensity for an energy loss E_ℓ for a location in the specimen (pixel) labelled by (i,j), and n_E is the number of bins that compose each spectrum. The spatial resolution of the EELS-SI in the x and y directions is usually taken to be the same, implying that

$$\Delta x = \Delta y \approx \frac{L_x}{n_x} = \frac{L_y}{n_y}\,. \tag{2.6}$$

For the specimens analysed in this work we have $n_p = \mathcal{O}(10^4)$ spectra corresponding to a spatial resolution of $\Delta x \approx 10$ nm. On the one hand, a higher spatial resolution is important to allow the identification and characterisation of localised features within a nanomaterial, such as structural defects, phase boundaries, surfaces or edges. On the other hand, if the resolution Δx becomes too small the individual spectra become noisy due to limited statistics. Hence, the optimal spatial resolution can be determined from a compromise between these two considerations.

In general it is not known what the optimal spatial resolution should be prior to the STEM-EELS inspection and analysis of a specimen. Therefore, it is convenient to record the spectral image with a high spatial resolution and then, if required, combine subsequently the information on neighbouring pixels by means of a procedure known as pooling or sliding-window averaging. The idea underlying pooling is that one carries out the following replacement for the entries of the EELS spectral image listed in Equation (2.5):

$$I^{(i,j)}_{\rm EELS}(E_\ell) \quad \to I^{(i,j)}_{\rm EELS}(E_\ell)\Big|_{\rm pooled} = \frac{1}{N^{(i,j)}_{\rm pool}} \sum_{|i'-i|\le d} \sum_{|j'-j|\le d} \left(\omega_{|i'-i|,|j'-j|} \times I^{(i',j')}_{\rm EELS}(E_\ell)\right)\,, \tag{2.7}$$

where d indicates the pooling range, $\omega_{|i'-i|,|j'-j|}$ is a weight factor, and the pooling normalisation is determined by the sum of the relevant weights,

$$N^{(i,j)}_{\rm pool} = \sum_{|i'-i|\le d} \sum_{|j'-j|\le d} \omega_{|i'-i|,|j'-j|}\,. \tag{2.8}$$

By increasing the pooling range d, one combines the local information from a higher number of spectra and thus reduces statistical fluctuations, at the price of some loss on the spatial resolution of the measurement. For instance, $d = 3/2$ averages the information contained on a 3×3 square centred on the pixel (i,j). Given that there is no unique choice for the pooling parameters, one has to verify that the interpretation of the information contained on the spectral images does not depend sensitively on their value. In this work, we consider uniform weights, $\omega_{|i'-i|,|j'-j|} = 1$, but other options such as Gaussian weights

$$\omega_{|i'-i|,|j'-j|} = \exp\left(-\frac{(i-i')^2}{2d^2} - \frac{(j-j')^2}{2d^2}\right)\,, \tag{2.9}$$

with $\sigma^2 = d^2$ as variance are straightforward to implement in EELSFITTER. The outcome of this procedure is a modified spectral map with the same structure as Equation (2.5) but now with pooled entries. In this work we typically use $d = 3$ to tame statistical fluctuations on the recorded spectra.

2.2.2. CLUSTERING THE SPECTRAL IMAGE

As indicated by Equation (2.5), the total EELS intensity recorded for each pixel of the SI receives contributions from both inelastic scatterings and from the ZLP, where the latter must be subtracted before one can carry out the theoretical interpretation of the low-loss region measurements. Given that the ZLP arises from elastic scatterings with the atoms of the specimen, and that the likelihood of these scatterings increases with the thickness, its contribution will depend sensitively with the local thickness of the specimen. Hence, before one trains the deep-learning model of the ZLP it is necessary to first group individual spectra as a function of their thickness. In this work this is achieved by means of unsupervised machine learning, specifically with the K-means clustering algorithm. Since the actual calculation of the thickness has as prerequisite the ZLP determination (see Equation (3.1) in Chapter 3), it is suitable to use instead the total integrated intensity as a proxy for the local thickness for the clustering procedure. That is, we cluster spectra as a function of

$$N^{(i,j)}_{\rm tot} \equiv \int_{-\infty}^{\infty} dE\, I^{(i,j)}_{\rm EELS}(E) = \int_{-\infty}^{\infty} dE \left(I^{(i,j)}_{\rm ZLP}(E) + I^{(i,j)}_{\rm inel}(E)\right) = N^{(i,j)}_0 + N^{(i,j)}_{\rm inel} \,, \qquad (2.10)$$

which coincides with the sum of the ZLP and inelastic scattering normalisation factors. Equation (2.10) is inversely proportional to the local thickness t and therefore represents a suitable replacement in the clustering algorithm. In practice, the integration in Equation (2.10) is restricted to the measured region in energy loss.

The starting point of K-means clustering is a dataset composed by $n_p = n_x \times n_y$ points,

$$\ln\left(N^{(r)}_{\rm tot}\right), \quad r = 1,\ldots,n_p\,, \qquad r = i + (n_y - 1)\,j\,, \qquad (2.11)$$

which we want to group into K separate clusters T_k, whose means are given by

$$\ln\left(\widetilde{N}^{(k)}\right), \quad k = 1,\ldots,K\,. \qquad (2.12)$$

The cluster means represent the main features of the k-th cluster to which the data points will be assigned in the procedure. Clustering on the logarithm of $N^{(r)}_{\rm tot}$ rather than on its absolute value is found to be more efficient, given that depending on the specimen location the integrated intensity will vary by orders of magnitude.

In K-means clustering, the determination of the cluster means and data point assignments follows from the minimisation of a cost function. This is defined in terms of a distance in specimen thickness space, given by

$$C_{\rm Kmeans}\left(\boldsymbol{N}_{\rm tot}, \boldsymbol{T}\right) = \sum_{r=1}^{n_p} \sum_{k=1}^{K} d_{rk} \left| \ln \left(\frac{\widetilde{N}^{(k)}}{N^{(r)}_{\rm tot}} \right) \right|^p \,, \qquad (2.13)$$

with d_{rk} being a binary assignment variable, equal to 1 if r belongs to cluster k ($d_{rk} = 1$ for $r \in T_k$) and zero otherwise, and with the exponent satisfying $p > 0$. Here we adopt

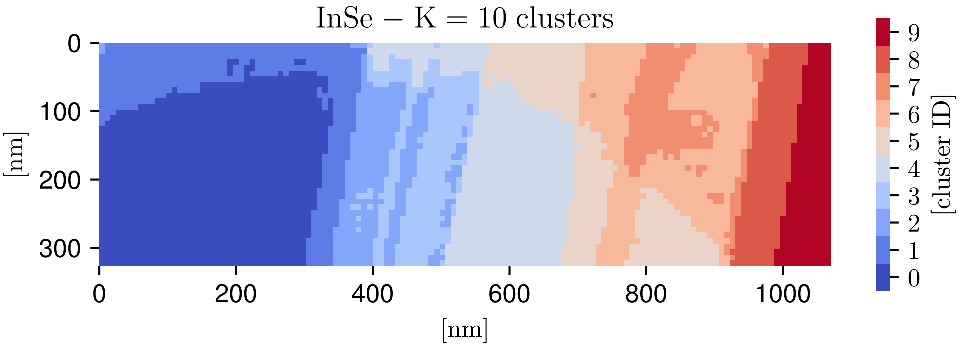

Figure 2.2: The outcome of the K-means clustering procedure applied to the InSe specimen, where each colour represents one of the K=10 thickness clusters. This clustering map can be compared with the thickness map of Figure 3.1d, highlighting how the total integrated intensity N_{tot} provides a good proxy for the thickness.

$p = 1/2$, which reduces the weight of eventual outliers in the calculation of the cluster means, and we verify that results are stable if $p = 1$ is used instead. Furthermore, since clustering is exclusive, one needs to impose the following sum rule

$$\sum_{k=1}^{K} d_{rk} = 1\,, \quad \forall\, r\,. \tag{2.14}$$

The minimisation of Equation (2.13) results in a cluster assignment such that the internal variance is minimised and is carried out by means of a semi-analytical algorithm. This algorithm is iterated until a convergence criterion is achieved, e.g. when the change in the cost function between two iterations is below some threshold. Note that, as opposed to supervised learning, here is it not possible to overfit and eventually one is guaranteed to find the solution that leads to the absolute minimum of the cost function. The end result of the clustering process is that now we can label the information contained in the (pooled) spectral image (for $r = i + (n_y - 1)\,j$) as follows

$$I^{(i,j)}_{\mathrm{EELS},k}(E_\ell) = \begin{cases} I^{(r)}_{\mathrm{EELS}}(E_\ell) & \text{if} \quad r \in T_k \\ 0 \quad \text{otherwise} \end{cases} \,, \quad k = 1, \ldots, K\,. \tag{2.15}$$

This cluster assignment makes possible training the ZLP deep-learning model across the complete specimen recorded in the SI accounting for the (potentially large) variations in the local thickness.

The number of clusters K is a free parameter that needs to be fixed taking into consideration how rapidly the local thickness varies within a given specimen. We note that K cannot be too high, else it will not be possible to sample a sufficiently large number of representative spectra from each cluster to construct the prior probability distributions, as required for the Monte Carlo method used in this work. We find that $K = 10$ for the InSe and $K = 5$ for the WS$_2$ specimens are suitable choices. Figure 2.2 displays the outcome of the K-means clustering procedure applied to the InSe specimen, where each colour represents one of the K=10 thickness clusters. It can be compared with the corresponding thickness map in Fig. 2(d); the qualitative agreement further confirms that the total integrated intensity in each pixel $N_{\rm tot}^{(i,j)}$ represents a suitable proxy for the local specimen thickness.

2.3. A DEEP-LEARNING MODEL FOR THE ZERO-LOSS PEAK

Given that the zero-loss peak background cannot be evaluated from first principles, in this work we deploy supervised machine learning combined with Monte Carlo methods to construct a neural network parametrisation of the ZLP. Within this approach, one can faithfully model the ZLP dependence on both the electron energy loss and on the local specimen thickness. Our approach, first presented in [26], is here extended to model the thickness dependence and to the simultaneous interpretation of the $\mathcal{O}(10^4)$ spectra that constitute a typical EELS-SI. One key advantage is the robust estimate of the uncertainties associated to the ZLP modelling and subtraction procedures using the Monte Carlo replica method [27].

The neural network architecture adopted in this work is displayed in Fig. 2(b). It contains two input variables, namely the energy loss E and the logarithm of the integrated intensity $\ln(N_{\rm tot})$, the latter providing a proxy for the thickness t. Both E and $\ln(N_{\rm tot})$ are preprocessed and rescaled to lie between 0.1 and 0.9 before given as input to the network. Three hidden layers contain 10, 15, and 5 neurons respectively. The activation state of the output neuron in the last layer, $\xi_1^{(n_L)}$, is then related to the intensity of the ZLP as

$$I_{\rm ZLP}^{\rm (NN)}(E,\ln(N_{\rm tot})) = \exp\left(\xi_1^{(n_L)}(E,\ln(N_{\rm tot}))\right), \qquad (2.16)$$

where an exponential function is chosen to facilitate the learning, given that the EELS intensities in the training dataset can vary by orders of magnitude. Sigmoid activation functions are adopted for all layers except for a ReLU in the final layer, to guarantee a positive-definite output of the network and hence of the predicted intensity.

The training of this neural network model for the ZLP is carried out as follows. Assume that the input SI has been classified into K clusters following the procedure of Section 2.2.1. The members of each cluster exhibit a similar value of the local thickness. Then one selects at random a representative spectrum from each cluster,

$$\left\{I_{\rm EELS}^{(i_1,j_1)}(E), I_{\rm EELS}^{(i_2,j_2)}(E), \ldots, I_{\rm EELS}^{(i_K,j_K)}(E)\right\}, \qquad (2.17)$$

each one characterised by a different total integrated intensity evaluated from Equation (2.10),

$$\left\{N_{\rm tot}^{(i_1,j_1)}, N_{\rm tot}^{(i_2,j_2)}, \ldots, N_{\rm tot}^{(i_K,j_K)}\right\}, \qquad (2.18)$$

such that (i_k, j_k) belongs to the k-th cluster. To ensure that the neural network model accounts only for the energy loss E dependence in the region where the ZLP dominates the recorded spectra, we remove from the training dataset those bins with $E \geq \Delta E_{{\rm I},k}$ with $\Delta E_{{\rm I},k}$ being a model hyperparameter [26] which varies in each thickness cluster. The cost function $C_{\rm ZLP}$ used to train the NN model is then

$$C_{\rm ZLP} = \frac{1}{n_E}\sum_{k=1}^{K}\sum_{\ell_k=1}^{n_E^{(k)}} \frac{\left[I_{\rm EELS}^{(i_k,j_k)}(E_{\ell_k}) - I_{\rm ZLP}^{\rm (NN)}\left(E_{\ell_k},\ln\left(N_{\rm tot}^{(i_k,j_k)}\right)\right)\right]^2}{\sigma_k^2\left(E_{\ell_k}\right)}, \qquad E_{\ell_k} \leq E_{{\rm I},k}, \qquad (2.19)$$

where the total number of energy loss bins that enter the calculation is the sum of bins in each individual spectrum, $n_E = \sum_{k=1}^{K} n_E^{(k)}$. The denominator of Equation (2.19) is given by $\sigma_k\left(E_{\ell_k}\right)$, which represents the variance within the k-th cluster for a given value of the energy loss E_{ℓ_k}. This variance is evaluated as the size of the 68% confidence level (CL) interval of the intensities associated to the k-th cluster for a given value of E_{ℓ_k}.

For such a random choice of representative cluster spectra, Equation (2.17), the parameters (weights and thresholds) of the neural network model are obtained from the minimisation of Equation (2.19) until a suitable convergence criterion is achieved. Here this training is carried out using stochastic gradient descent (SGD) as implemented in the `PyTorch` library [28], specifically by means of the ADAM minimiser. The optimal training length is determined by means of the look-back cross-validation stopping. In this method, the training data is divided 80%/20% into training and validation subsets, with the best training point given by the absolute minimum of the validation cost function $C_{\rm ZLP}^{(\rm val)}$ evaluated over a sufficiently large number of iterations.

In order to estimate and propagate uncertainties associated to the ZLP parametrisation and subtraction procedure, here we adopt a variant of the Monte Carlo replica method [26] benefiting from the high statistics (large number of pixels) provided by an EELS-SI. The starting point is selecting $N_{\rm rep} \simeq \mathcal{O}(5000)$ subsets of spectra such as the one in Equation (2.17) containing one representative of each of the K clusters considered. One denotes this subset of spectra as a Monte Carlo (MC) replica, and we denote the collection of replicas by

$$\boldsymbol{I}^{(m)} = \left\{ I_{\rm EELS}^{(i_{m,1},j_{m,1})}(E),\, I_{\rm EELS}^{(i_{m,2},j_{m,2})}(E),\ldots,\, I_{\rm EELS}^{(i_{m,K},j_{m,K})}(E)\right\}, \qquad m=1,\ldots,N_{\rm rep}\,. \tag{2.20}$$

where now the superindices $(i_{m,k}, j_{m,k})$ indicate a specific spectrum from the k-th cluster that has been assigned to the m-th replica. Given that these replicas are selected at random, they provide a representation of the underlying probability density in the space of EELS spectra, e.g. those spectra closer to the cluster mean will be represented more frequently in the replica distribution.

By training now a separate model to each of the $N_{\rm rep}$ replicas, one ends up with another Monte Carlo representation, now of the probability density in the space of ZLP parametrisations. This is done by replacing the cost function Equation (2.19) by

$$C_{\rm ZLP}^{(m)} = \frac{1}{n_E}\sum_{k=1}^{K}\sum_{\ell_k=1}^{n_E^{(k)}} \frac{\left[I_{\rm EELS}^{(i_{m,k},j_{m,k})}(E_{\ell_k}) - I_{\rm ZLP}^{(\rm NN)(m)}\left(E_{\ell_k}, \ln\left(N_{\rm tot}^{(i_{m,k},j_{m,k})}\right)\right)\right]^2}{\sigma_k^2\left(E_{\ell_k}\right)}\,, \qquad E_{\ell_k} \le \Delta E_{{\rm I},k}\,, \tag{2.21}$$

and then performing the model training separately for each individual replica. Note that the denominator of the cost function Equation (2.21) is independent of the replica. The resulting Monte Carlo distribution of ZLP models, indicated by

$$\boldsymbol{I}_{\rm ZLP}^{(\rm NN)} = \left\{ I_{\rm ZLP}^{(\rm NN)(1)}\left(E, \ln\left(N_{\rm tot}\right)\right),\ldots, I_{\rm ZLP}^{(\rm NN)(N_{\rm rep})}\left(E, \ln\left(N_{\rm tot}\right)\right)\right\} \tag{2.22}$$

makes possible subtracting the ZLP from the measured EELS spectra following the matching procedure described in [26] and hence isolating the inelastic contribution in each pixel,

$$I_{\rm inel}^{(i,j)(m)}(E) \simeq \left[I_{\rm EELS}^{(i,j)}(E) - I_{\rm ZLP}^{(\rm NN)(m)}\left(E, \ln\left(N_{\rm tot}^{(i,j)}\right)\right)\right], \qquad m=1,\ldots,N_{\rm rep}\,. \tag{2.23}$$

The variance of $I^{(i,j)}_{\text{inel}}(E)$ over the MC replica sample estimates the uncertainties associated to the ZLP subtraction procedure. By means of these MC samplings of the probability distributions associated to the ZLP and inelastic components of the recorded spectra, one can evaluate the relevant derived quantities with a faithful error estimate. Note that in our approach error propagation is realised without the need to resort to any approximation, e.g. linear error analysis.

One important benefit of Equation (2.21) is that the machine learning model training can be carried out fully in parallel, rather than sequentially, for each replica. Hence our approach is most efficiently implemented when running on a computer cluster with a large number of CPU (or GPU) nodes, since this configuration maximally exploits the parallelisation flexibility of the Monte Carlo replica method.

As mentioned above, the cluster-dependent hyperparameters $E_{\text{I},k}$ ensure that the model is trained only in the energy loss data region where ZLP dominates total intensity. This is illustrated by the scheme of Figure 3.3 in [26], which displays a toy simulation of the ZLP and inelastic scattering contributions adding up to the total recorded EELS intensity. The neural network model for the ZLP is then trained on the data corresponding to region I, while region II is obtained entirely from model predictions. To determine the values of $E_{\text{I},k}$, we evaluate the first derivative of the total recording intensity, $dI_{\text{EELS}}(E)/dE$, for each of the members of the k-th cluster. When this derivative crosses zero, the contribution from I_{inel} will already be dominant. There are then two options. First, one sets $E_{\text{I},k} = f \times E_{\text{min},k}$, where $f < 1$ and $E_{\text{min},k}$ is the energy where the median of dI_{EELS}/dE crosses zero (first local minimum) for cluster k. Second, one sets $E_{\text{I},k}$ to be the value where at most f% of the models have crossed $dI_{\text{EELS}}/dE = 0$, with $f \simeq 10\%$. This choice implies that 90% of the models still exhibit a negative derivative. We have verified that compatible results are obtained with the two choices, indicating that results are reasonably stable with respect to the value of the hyperparameter $E_{\text{I},k}$.

The second model hyperparameter, denoted by $E_{\text{II},k}$ in Fig. 3.3 in [26], indicates the region for which the ZLP can be considered as fully negligible. Hence in this region III we impose that $I_{\text{ZLP}}(E) \to 0$ by means of the Lagrange multiplier method. This condition fixes the model behaviour in the large energy loss limit, which otherwise would remain unconstrained. Since the ZLP is known to be a steeply-falling function, $E_{\text{II},k}$ should not chosen not too far from $E_{\text{I},k}$ to avoid an excessive interpolation region. In Chapter 3 we use $E_{\text{II},k} = 3 \times E_{\text{I},k}$, though this choice can be adjusted by the user.

2.3.1. IMPROVING THE DEEP LEARNING MODEL

The deep learning model has been improved throughout the years of development on EELSFITTER. The previously described methods are applied in Chapter 3, however the updated methods describe in this section are applied in Chapter 4 Starting with the hyperparameters, as mentioned before, the spectra in the spectral image are separated into three regions. In region I the recorded intensity is dominated by the contribution from the ZLP. In region II, the inelastic scattering contribution is significant in comparison to the contribution from the ZLP. Finally, in region III, the contribution to the intensity from the ZLP is approximately zero. The updated approach to determine $E_{\text{I},k}$ and $E_{\text{II},k}$ is by using the kneedle algorithm to determine the kneedle location and the first local minimum [29]. The kneedle refers to the point of highest curvature in a concave or convex curve. By taking the region between the Full Width at Half Maximum (FWHM) and the first local minimum of the spectra we obtain such a curve. In the cases of spectra where the signal of the sample might not overcome the signal of the ZLP tail + noise floor (which could occur in aloof areas of a spectral image) the first local minimum could be located far beyond the initial onset of the signal. $E_{\mathrm{I},k}$ is then determined by multiplying the kneedle location by some factor, this way we ensure $E_{\mathrm{I},k}$ is much more reliably located near the ZLP. $E_{\mathrm{II},k}$ is determined by fitting a log10 function through the kneedle location and the local minimum and finding where it intersects with a single count (minimal possible contribution from the ZLP). We find that this approach puts $E_{\mathrm{II},k}$ in a similar location compared to the SNR method presented in the first version of EELSFITTER, without the need for a separate vacuum measurement of the ZLP with the same microscope conditions [26].

The second notable improvement is regarding the cost function. A key requirement of the ZLP is that it monotonically decreases in region II. As mentioned before, the distance between $E_{\mathrm{I},k}$ and $E_{\mathrm{II},k}$ should not be too far for avoiding excessive interpolation in this region, as region II is simply unseen during the training of the deep learning network. Nonetheless, we observed that a handful of models would always shoot upwards regardless of the distance, as the generalisation of the network in such cases is poor, resulting in incorrect predictions for the ZLP intensity. To solve this issue, the cost function was updated to include a regularisation term that incurs a penalty if the derivative turns positive in region II. The updated cost function to minimise during training on replica m then becomes

$$\begin{aligned} C^{(m)}_{\mathrm{ZLP}} = {} & \frac{1}{n_{E_{\mathrm{I}}}} \sum_{k=1}^{K} \sum_{\ell_k=1}^{n^{(k)}_{E_{\mathrm{I}}}} \frac{\left[I^{(i_{m,k},j_{m,k})}_{\mathrm{EELS}}\left(E_{\ell_k}\right) - I^{(\mathrm{NN})(m)}_{\mathrm{ZLP}}\left(E_{\ell_k}, \ln\left(N^{(i_{m,k},j_{m,k})}_{\mathrm{peak}}\right)\right)\right]^2}{\sigma^2_k\left(E_{\ell_k}\right)} \\ & + \lambda \sum_{k=1}^{K} \sum_{r_k=1}^{n^{(k)}_{E_{\mathrm{II}}}} \mathrm{ReLU}\left(\frac{\mathrm{d} I^{(\mathrm{NN})(m)}_{\mathrm{ZLP}}\left(E_{r_k}, \ln\left(N^{(i_{m,k},j_{m,k})}_{\mathrm{peak}}\right)\right)}{\mathrm{d}E} \right), \\ & E_{\ell_k} \leq E_{\mathrm{I},k}, \quad E_{\mathrm{I},k} \leq E_{r_k} \leq E_{\mathrm{II},k}, \end{aligned} \tag{2.24}$$

where $I^{(\mathrm{NN})(m)}_{\mathrm{ZLP}}$ is the ZLP intensity predicted by the neural network for replica m, $n^{(k)}_{E_{\mathrm{i}}}$ is the number of energy bins in region i of the spectrum originating from cluster k, $n_{E_{\mathrm{I}}}$ is the sum of $n^{(k)}_{E_{\mathrm{I}}}$ over all clusters, $\sigma_k\left(E_{\ell_k}\right)$ is the variance within cluster k at the energy loss E_{ℓ_k}, and λ weighs the two terms in the cost function against each other.

Comparing models before and after the regularisation term, models no longer shot upwards. Thus, by adding a regularisation term the generalisation capability of the neural network is improved.

2.4. DECONVOLUTION OF EEL SPECTRA

Here we provide an overview of the theoretical formalism, based on [19], adopted to evaluate the single-scattering distribution, local thickness, band gap energy and type and complex dielectric function from the measured EELS spectra. As indicated by Equation (2.1) these spectra receive three contributions: the one from inelastic single scatterings off the electrons in the specimen, the one associated to multiple inelastic scatterings, and then the ZLP arising from elastic scatterings and instrumental broadening. Hence a generic EEL spectrum $I_{\rm EELS}(E)$ can be decomposed as

$$I_{\rm EELS}(E) = I_{\rm ZLP}(E) + I_{\rm inel}(E) = I_{\rm ZLP}(E) + \sum_{n=1}^{\infty} I^{(n)}_{\rm inel}(E)\,, \tag{2.25}$$

where E is the energy loss experienced by the electrons upon traversing the specimen, $I_{\rm ZLP}$ is the ZLP intensity, and $I^{(n)}_{\rm inel}$ indicates the contribution associated to n inelastic scatterings. The ZLP intensity can be further expressed as

$$I_{\rm ZLP}(E) = N_0 R(E)\,, \qquad \int_{-\infty}^{\infty} dE\, R(E) = 1\,, \tag{2.26}$$

where $R(E)$ is known as the resolution or instrumental response function whose full width at half-maximum (FWHM) indicates the resolution of the instrument. The normalisation factor N_0 thus corresponds to the integrated intensity under the zero-loss peak. In the following, we assume that the ZLP contribution to Equation (2.25) has already been disentangled from that associated to inelastic scatterings by means of the subtraction procedure described in Section 2.3.

2.4.1. THE SINGLE-SCATTERING DISTRIBUTION

If one denotes by t the local thickness of the specimen and by λ the mean free path of the electrons, then assuming that inelastic scatterings are uncorrelated and that $t \lesssim \lambda$, one has that the integral over the n-scatterings distribution $I^{(n)}_{\rm inel}$ is a Poisson distribution

$$N_n \equiv \int_{-\infty}^{\infty} dE\, I^{(n)}_{\rm inel}(E) = B \frac{(t/\lambda)^n}{n!} e^{-t/\lambda}\,, \qquad n = 1,2,\ldots,\infty\,, \tag{2.27}$$

with B a normalisation constant. From the combination of Equations. (2.25) and (2.27) it follows that

$$N_{\rm inel} \equiv \int_{-\infty}^{\infty} dE\, I_{\rm inel}(E) = \sum_{n=1}^{\infty} N_n = B \sum_{n=1}^{\infty} \frac{(t/\lambda)^n}{n!} e^{-t/\lambda} = B\left(1 - e^{-t/\lambda}\right)\,, \tag{2.28}$$

and hence one finds that the integral over the n-scatterings distribution is such that

$$N_n = \frac{N_{\rm inel}}{\left(1 - e^{-t/\lambda}\right)} \frac{(t/\lambda)^n}{n!} e^{-t/\lambda}\,, \tag{2.29}$$

in terms of the normalisation $N_{\rm inel}$ of the full inelastic scattering distribution, the sample thickness t and the mean free path λ. Note also that the ZLP normalisation factor N_0 is then given in terms of the inelastic one as

$$N_0 = \frac{N_{\rm inel}}{e^{t/\lambda} - 1}\,, \tag{2.30}$$

and hence one has the following relations between integrated inelastic scattering intensities

$$\frac{N_1^n}{N_n} = n! N_0^{n-1}\,, \qquad \forall\ n \geq 1\,. \tag{2.31}$$

In order to evaluate the local thickness of the specimen and the corresponding dielectric function, it is necessary to deconvolute the measured spectra and extract from them the single-scattering distribution (SSD), $I_{\rm SSD}(E)$. The SSD is related to the experimentally measured $n=1$ distribution, $I^{(1)}_{\rm inel}(E)$ by the finite resolution of our measurement apparatus:

$$I^{(1)}_{\rm inel}(E) = R(E)\otimes I_{\rm SSD}(E) \equiv \int_{-\infty}^{\infty} dE'\, R(E-E')\, I_{\rm SSD}(E')\,, \tag{2.32}$$

where in the following $\otimes$ denotes the convolution operation. It can be shown, again treating individual scatterings as uncorrelated, that the experimentally measured $n=2$ and $n=3$ multiple scattering distributions can be expressed in terms of the SSD as

$$\begin{aligned} I^{(2)}_{\rm inel}(E) &= R(E)\otimes I_{\rm SSD}(E)\otimes I_{\rm SSD}(E)/\left(2!N_0\right)\,, && (2.33)\\ I^{(3)}_{\rm inel}(E) &= R(E)\otimes I_{\rm SSD}(E)\otimes I_{\rm SSD}(E)\otimes I_{\rm SSD}(E)/\left(3!N_0^2\right)\,, && (2.34)\end{aligned}$$

and likewise for $n\geq 4$. Combining this information, one observes that the spectrum Equation (2.25) can be expressed in terms of the resolution function R, the ZLP normalisation N_0, and the single-scattering distribution $I_{\rm SSD}$ as follows

$$\begin{aligned} I_{\rm EELS}(E) &= N_0 R(E) + R(E)\otimes I_{\rm SSD}(E) + R(E)\otimes I_{\rm SSD}(E)\otimes I_{\rm SSD}(E)/\left(2!N_0\right) + \dots\\ &= R(E)\otimes\left(N_0\delta(E) + I_{\rm SSD}(E) + I_{\rm SSD}(E)\otimes I_{\rm SSD}(E)/\left(2!N_0\right)+\dots\right)\\ &= N_0 R(E)\otimes\left(\delta(E) + \sum_{n=1}^{\infty}\left[I_{\rm SSD}(E)\otimes\right]^n \delta(E)/\left(n!N_0^n\right)\right)\,, \end{aligned} \tag{2.35}$$

where $\delta(E)$ is the Dirac delta function. If the ZLP normalisation factor N_0 and resolution function $R(E)$ are known, then one can use Equation (2.35) to extract the SSD from the measured spectra by means of a deconvolution procedure.

2.4.2. FOURIER LOG DECONVOLUTION

The structure of Equation (2.35) indicates that transforming to Fourier space will lead to an algebraic equation which can then be solved for the SSD. Here we define the Fourier transform $\widetilde{f}(\nu)$ of a function $f(E)$ as follows

$$\mathscr{F}\left[f(E)\right](\nu) \equiv \widetilde{f}(\nu) \equiv \int_{-\infty}^{\infty} dE\, f(E) e^{-2\pi i E\nu}\,, \tag{2.36}$$

whose inverse is given by

$$\mathscr{F}^{-1}\left[\widetilde{f}(\nu)\right](E) = f(E) \equiv \int_{-\infty}^{\infty} d\nu\, \widetilde{f}(\nu) e^{2\pi i E\nu}\,, \tag{2.37}$$

which has the useful property that convolutions such as Equation (2.32) are transformed into products,

$$\text{if } f(E) = g(E)\otimes h(E) \quad \text{then} \quad \mathscr{F}\left[f(E)\right] = \widetilde{f}(\nu) = \widetilde{g}(\nu)\widetilde{h}(\nu)\,. \tag{2.38}$$

The Fourier transform of Equation (2.35) leads to the Taylor expansion of the exponential and hence

$$\widetilde{I}_{\rm EELS}(\nu) = N_0 \widetilde{R}(\nu) \exp\left(\frac{\widetilde{I}_{\rm SSD}(\nu)}{N_0}\right)\,, \tag{2.39}$$

which can be solved for the Fourier transform of the single scattering distribution

$$\widetilde{I}_{\mathrm{SSD}}(\nu) = N_0 \ln \frac{\widetilde{I}_{\mathrm{EELS}}(\nu)}{N_0 \widetilde{R}(\nu)} = N_0 \ln \frac{\mathscr{F}\left[I_{\mathrm{EELS}}(E)\right](\nu)}{N_0 \mathscr{F}\left[R(E)\right](\nu)} \,. \tag{2.40}$$

By taking the inverse Fourier transform, one obtains the sought-for expression for the single scattering distribution as a function of the electron energy loss

$$I_{\mathrm{SSD}}(E) = N_0 \mathscr{F}^{-1}\left[\ln \frac{\mathscr{F}\left[I_{\mathrm{EELS}}\right]}{N_0 \mathscr{F}\left[R\right]}\right] , \tag{2.41}$$

where the only required inputs are the experimentally measured EELS spectra, Equation (2.25), with the corresponding ZLP.

2.4.3. DISCRETE FOURIER TRANSFORMS.

Equation (2.41) can be evaluated numerically by approximating the continuous transform Equation (2.36) by its discrete Fourier transform equivalent. The discrete Fourier transform of a discretised function $f(E)$ defined at $E_n \in \{E_0, \ldots, E_{N-1}\}$ is given by:

$$\mathscr{F}_D\left[f(E)\right](\nu_k) = \widetilde{f}(\nu_k) = \sum_{n=0}^{N-1} \mathrm{e}^{-i2\pi kn/N} f(E_n), \qquad \forall\, k \in \{0, \ldots, N-1\} , \tag{2.42}$$

with the corresponding inverse transformation being

$$\mathscr{F}_D^{-1}\left[\widetilde{f}(\nu)\right](E_n) = f(E_n) = \frac{1}{N} \sum_{k=0}^{N-1} \mathrm{e}^{i2\pi kn/N} \widetilde{f}(\nu_k) \qquad \forall\, n \in \{0, \ldots, N-1\} . \tag{2.43}$$

If one approximates the continuous function $f(E)$ by its discretised version $f(E_0 + n\Delta E)$ and likewise $\widetilde{f}(\nu)$ by $\widetilde{f}(k\Delta\nu)$ where $\Delta x \Delta\nu = N^{-1}$ one finds that

$$\widetilde{f}(\nu) \approx \Delta x e^{-i2\pi k\Delta\nu E_0} \mathscr{F}_D\left[f(E)\right] , \tag{2.44}$$

and likewise for the inverse transform

$$f(E) \approx \frac{1}{\Delta x} \mathscr{F}_D^{-1}\left[\widetilde{g}(k\Delta\nu)\right] , \qquad \widetilde{g}(k\Delta\nu) \equiv e^{i2\pi k\Delta\nu E_0} \widetilde{f}(k\Delta\nu) . \tag{2.45}$$

In practice, the EELS spectra considered are characterised by a fine spacing in E and the discrete approximation for the Fourier transform produces results very close to the exact one.

REFERENCES

[1] J. Geiger, "Inelastic electron scattering in thin films at oblique incidence", *physica status solidi (b)*, vol. 24, pp. 457–460, 2 1967, ISSN: 15213951. DOI: 10.1002/pssb.19670240207.

[2] B. Rafferty and L. Brown, "Direct and indirect transitions in the region of the band gap using electron-energy-loss spectroscopy", *Physical Review B - Condensed Matter and Materials Physics*, vol. 58, pp. 10 326–10 337, 16 1998, ISSN: 1550235X. DOI: 10.1103/PhysRevB.58.10326.

[3] R. Erni, N. D. Browning, Z. R. Dai, and J. P. Bradley, "Analysis of extraterrestrial particles using monochromated electron energy-loss spectroscopy", *Micron*, vol. 36, pp. 369–379, 4 2005, ISSN: 09684328. DOI: 10.1016/j.micron.2004.12.011.

[4] B. Schaffer, K. Riegler, G. Kothleitner, W. Grogger, and F. Hofer, "Monochromated, spatially resolved electron energy-loss spectroscopic measurements of gold nanoparticles in the plasmon range", *Micron*, vol. 40, pp. 269–273, 2 Feb. 2009, ISSN: 09684328. DOI: 10.1016/j.micron.2008.07.004.

[5] M. Stöger-Pollach, "Optical properties and bandgaps from low loss eels: Pitfalls and solutions", *Micron*, vol. 39, pp. 1092–1110, 8 2008, ISSN: 09684328. DOI: 10.1016/j.micron.2008.01.023.

[6] C. Ellegaard, A. E. Hansen, A. Haaning, *et al.*, "Electron microscopy image enhanced", *Phys. Rev. Lett*, vol. 90, pp. 768–769, Apr. 1998.

[7] M. Terauchi, M. Tanaka, K. Tsuno, and M. Ishida, "Development of a high energy resolution electron energy-loss spectroscopy microscope", *Journal of Microscopy*, vol. 194, pp. 203–209, 1 1999, ISSN: 00222720. DOI: 10.1046/j.1365-2818.1999.00450.x.

[8] B. Freitag, S. Kujawa, P. M. Mul, J. Ringnalda, and P. C. Tiemeijer, "Breaking the spherical and chromatic aberration barrier in transmission electron microscopy", *Ultramicroscopy*, vol. 102, pp. 209–214, 3 Feb. 2005, ISSN: 03043991. DOI: 10.1016/j.ultramic.2004.09.013.

[9] F. J. García de Abajo, "Optical excitations in electron microscopy", *Rev. Mod. Phys.*, vol. 82, pp. 209–275, 1 Feb. 2010. DOI: 10.1103/RevModPhys.82.209.

[10] A. Polman, M. Kociak, and F. J. G. de Abajo, "Electron-beam spectroscopy for nanophotonics", *Nature Materials*, vol. 18, pp. 1158–1171, 11 Nov. 2019, ISSN: 14764660. DOI: 10.1038/s41563-019-0409-1.

[11] F. J. G. D. Abajo and V. D. Giulio, "Optical excitations with electron beams: Challenges and opportunities", *ACS Photonics*, vol. 8, pp. 945–974, 4 Apr. 2021, ISSN: 23304022. DOI: 10.1021/acsphotonics.0c01950.

[12] R. F. Egerton, "Electron energy-loss spectroscopy in the tem", *Reports on Progress in Physics*, vol. 72, 1 2009, ISSN: 00344885. DOI: 10.1088/0034-4885/72/1/016502.

[13] J. Park, S. Heo, J. G. Chung, *et al.*, "Bandgap measurement of thin dielectric films using monochromated stem-eels", *Ultramicroscopy*, vol. 109, pp. 1183–1188, 9 2009, ISSN: 03043991. DOI: 10.1016/j.ultramic.2009.04.005.

[14] A. D. Dorneich, R. H. French, H. Müllejans, S. Loughin, and M. Rühle, "Quantitative analysis of valence electron energy-loss spectra of aluminium nitride", *Journal of Microscopy*, vol. 191, pp. 286–296, 3 1998, ISSN: 00222720. DOI: 10.1046/j.1365-2818.1998.00370.x.

[15] B. Rafferty, S. J. Pennycook, and L. M. Brown, "Zero loss peak deconvolution for bandgap eel spectra", *Journal of Electron Microscopy*, vol. 49, pp. 517–524, 4 2000, ISSN: 00220744. DOI: 10.1093/oxfordjournals.jmicro.a023838.

[16] K. V. Benthem, C. Elsässer, and R. H. French, "Bulk electronic structure of srtio3: Experiment and theory", *Journal of Applied Physics*, vol. 90, pp. 6156–6164, 12 Dec. 2001, ISSN: 00218979. DOI: 10.1063/1.1415766.

[17] R. F. Egerton and M. Malac, "Improved background-fitting algorithms for ionization edges in electron energy-loss spectra", *Ultramicroscopy*, vol. 92, pp. 47–56, 2002.

[18] S. Lazar, G. A. Botton, M. Y. Wu, F. D. Tichelaar, and H. W. Zandbergen, "Materials science applications of hreels in near edge structure analysis and low-energy loss spectroscopy", in *Ultramicroscopy*, vol. 96, Elsevier, 2003, pp. 535–546. DOI: 10.1016/S0304-3991(03)00114-1.

[19] R. F. Egerton, *Electron Energy-Loss Spectroscopy in the Electron Microscope*. Springer US, 2011, ISBN: 978-1-4419-9583-4. [Online]. Available: https://link.springer.com/book/10.1007/978-1-4419-9583-4.

[20] C. S. Granerød, W. Zhan, and Ø. Prytz, "Automated approaches for band gap mapping in stem-eels", *Ultramicroscopy*, vol. 184, pp. 39–45, 2018, ISSN: 18792723. DOI: 10.1016/j.ultramic.2017.08.006.

[21] J. T. Held, H. Yun, and K. A. Mkhoyan, "Simultaneous multi-region background subtraction for core-level eel spectra", *Ultramicroscopy*, vol. 210, Mar. 2020, ISSN: 18792723. DOI: 10.1016/j.ultramic.2019.112919.

[22] K. L. Fung, M. W. Fay, S. M. Collins, *et al.*, "Accurate eels background subtraction – an adaptable method in matlab", *Ultramicroscopy*, vol. 217, Oct. 2020, ISSN: 18792723. DOI: 10.1016/j.ultramic.2020.113052.

[23] R. D. Ball, L. D. Debbio, S. Forte, *et al.*, "A determination of parton distributions with faithful uncertainty estimation", *Nuclear Physics B*, vol. 809, pp. 1–63, 1-2 Mar. 2009, ISSN: 05503213. DOI: 10.1016/j.nuclphysb.2008.09.037.

[24] R. D. Ball, V. Bertone, S. Carrazza, *et al.*, "Parton distributions for the lhc run ii", *Journal of High Energy Physics*, vol. 2015, pp. 1–148, 4 Apr. 2015, ISSN: 10298479. DOI: 10.1007/JHEP04(2015)040.

[25] R. D. Ball, V. Bertone, S. Carrazza, *et al.*, "Parton distributions from high-precision collider data: Nnpdf collaboration", *European Physical Journal C*, vol. 77, 10 Oct. 2017, ISSN: 14346052. DOI: 10.1140/epjc/s10052-017-5199-5.

[26] L. I. Roest, S. E. van Heijst, L. Maduro, J. Rojo, and S. Conesa-Boj, "Charting the low-loss region in electron energy loss spectroscopy with machine learning", *Ultramicroscopy*, vol. 222, p. 113 202, 2021, ISSN: 0304-3991. DOI: https://doi.org/10.1016/j.ultramic.2021.113202.

[27] L. D. Debbio, S. Forte, J. I. Latorre, A. Piccione, and J. Rojo, *Neural network determination of parton distributions: The nonsinglet case*, 2007. [Online]. Available: http://jhep.sissa.it/archive/papers/jhep032007039/jhep032007039.pdf.

[28] A. Paszke, S. Gross, F. Massa, *et al.*, *Pytorch: An imperative style, high-performance deep learning library*, 2019.

[29] V. Satopää, J. Albrecht, D. Irwin, and B. Raghavan, “Finding a "kneedle" in a haystack: Detecting knee points in system behavior”, in *Proceedings - International Conference on Distributed Computing Systems*, 2011, pp. 166–171, ISBN: 9780769543864. DOI: `10.1109/ICDCSW.2011.20`.

3

SPATIALLY RESOLVED BAND GAP AND DIELECTRIC FUNCTION

The electronic properties of two-dimensional (2D) materials depend sensitively on the underlying atomic arrangement down to the monolayer level. With Electron Energy Loss Spectroscopy (EELS) we can correlate these electronic properties with the structural morphology at nanoscale precision. In this Chapter we apply EELS in junction with our novel strategy for processing EEL spectral images, as discussed in Chapter 2 of this thesis, and spatially resolve the local thickness, band gap and complex dielectric function in indium selenide (InSe) flakes and polytopic tungsten disulfide(WS_2) nanoflowers. The first material, InSe, is a direct band gap semiconductor and the specimen presented in this study in particular has a staircase structure. This gives the opportunity to study this material at different levels of thickness in a single dataset. The second material is the polytopic WS_2 is an indirect band gap semiconductor and the specimen has the shape of a flower petal, with varying thickness from the centre to the edges of the petal. This specimen was used in the first iteration of our machine learning approach and acts as a benchmark to show the improvements added to the framework. With our approach, we are able to process and quantify structural and electronic properties with relative ease.

Parts of this chapter have been published in The Journal of Physical Chemistry A: **A. Brokkelkamp**, J. ter Hoeve, I. Postmes, S. E. van Heijst, L. Maduro, A. V. Davydov, S. Krylyuk, J. Rojo, S. Conesa-Boj, J. Phys. Chem. A **126**, 1255-1262 (2022).

3.1. INTRODUCTION

Electron Energy Loss Spectroscopy (EELS) in combination with Scanning Transmission Electron Microscopy (STEM) offers unprecedented access to spatial and spectral resolution in nanoscale research. The ability to study electronic properties at nanoscale resolution, such as the band gap [1]–[3] and dielectric function [4], [5] and correlate them with morphology and structural properties holds great potential in the development of novel technologies. The group of van der Waals materials specifically benefit from EELS-STEM as research methodology. The structural and electronic properties are intrinsically linked, such as layer dependence the band gap or strain causing exciton shifts [6]–[9]. These unique characteristics has made this class of materials of great interest in a wide range of fields, from nanoelectronics to nanophotonics.

Accessing properties such as the band gap, excitons, phonons and interband transitions in EELS is not straightforward, the dominance of the zero-loss peak (ZLP) tends to overshadow these features. In Chapter 2 of this thesis we outline our novel strategy for dealing with the ZLP and the processing of EEL spectral images, using a machine learning (ML) based approach using techniques from high-energy physics [10]–[12].

In this chapter, as a proof-of-concept we employ our strategy to the determination of the band gap and the complex dielectric function in two representative van der Waals materials. First, to InSe nanosheets prepared by exfoliation of a Sn-doped InSe crystal and deposited onto a holey carbon TEM grid. The electronic properties of InSe, such as the band gap value and type, are sensitive to both the layer stacking (β, γ, or ε-phase) as well as to the magnitude and type of doping [13]–[16]. Second, to horizontally-standing WS_2 flakes belonging to flower-like nanostructures (nanoflowers) characterised by a mixed 2H/3R polytypism. This nanomaterial, member of the transition metal dichalcogenide (TMD) family, was already considered in the original study [17], [18] and hence provides a suitable benchmark to validate our new strategy. One important property of WS_2 is that the indirect band gap of its bulk form switches to direct at the monolayer level [19]–[21]. Our approach is amenable to generalisation to other families of nanostructured materials, is suitable for application to higher-dimensional datasets such as momentum-resolved EELS, and is made available as a new release of the EELSFITTER open-source framework [18].

3.2. THICKNESS DETERMINATION BY KRAMERS-KRÖNIG ANALYSIS

The first step in quantitive analysis of EEL spectra is obtaining the Single Scattering Distribution (SSD) (as explained in Section 2.4.1). Once the SSD has been determined by means of the deconvolution procedure summarised by Equation (2.41), it can be used as input in order to evaluate the local sample thickness t from the experimentally measured spectra [22]. Kramers-Krönig analysis provides the following relation between the thickness t, the ZLP normalisation N_0, and the single-scattering distribution,

$$t = \frac{4a_0FE_0}{N_0\left(1-\mathrm{Re}\left[1/\epsilon(0)\right]\right)}\int_0^\infty dE\frac{I_{\mathrm{SSD}}(E)}{E\ln\left(1+\beta^2/\theta_E^2\right)}, \tag{3.1}$$

where we have assumed that the effects of surface scatterings can be neglected. Here, $a_0 = 0.0529$ nm is Bohr's radius, F is a relativistic correction factor written as,

$$F = \frac{1 + E_0/(1022\ \text{keV})}{[1 + E_0/(511\ \text{keV})]^2}\,, \tag{3.2}$$

with E_0 being the incident electron energy, $\epsilon(E)$ is the complex dielectric function, and θ_E is the characteristic angle defined by

$$\theta_E = \frac{E}{\gamma m_0 v^2} = \frac{E}{\left(E_0 + m_0 c^2\right)(v/c)^2} \tag{3.3}$$

with γ being the usual relativistic dilation factor, $\gamma = \left(1 - v^2/c^2\right)^{-1/2}$, and β the collection semi-angle of the microscope. [1] For either an insulator or a semiconductor material with refractive index n, one has that

$$\text{Re}\,[1/\epsilon(0)] = n^{-2}\,, \tag{3.4}$$

while $\text{Re}\,[1/\epsilon(0)] = 0$ for a metal or semi-metal. Hence, the determination of the dielectric function is not a pre-requisite to evaluate the specimen thickness, and for given microscope operation conditions we can express Equation (3.1) as

$$t = \frac{A}{N_0}\int_0^\infty dE \frac{I_{\text{SSD}}(E)}{E \ln\left(1 + \beta^2/\theta_E^2\right)}\,, \tag{3.5}$$

with A constant across the specimen. If the thickness of the specimen is already known at some location, then Equation (3.5) can be used to calibrate A and evaluate this thickness elsewhere. Furthermore, if the thickness of the material has already been determined by means of an independent experimental technique, then Equation (3.1) can be inverted to determine the refractive index n of an insulator or semi-conducting material using

$$n = \left[1 - \frac{4 a_0 F E_0}{N_0 t}\left(\int_0^\infty dE \frac{I_{\text{SSD}}(E)}{E \ln\left(1 + \beta^2/\theta_E^2\right)}\right)\right]^{-1/2}. \tag{3.6}$$

Figure 3.1a shows a representative EEL spectrum from the InSe specimen, where the original data is compared with the deep-learning ZLP parametrisation and the subtracted inelastic contribution. The red dashed region indicates the onset of inelastic scatterings, from which the band gap energy E_{bg} and type can be extracted from the procedure described in Section 3.3. We zoom in Figure 3.1b in the low-loss region of the same spectrum, where the ZLP and inelastic components become of comparable size. The error bands denote the 68% CL intervals evaluated over $N_{\text{rep}} = 5000$ Monte Carlo replicas.

By training the ZLP model on the whole InSe EELS-SI displayed in Figure 3.1c (see Figures B.1a,b in the Supplementary Information for the corresponding STEM measurements) we end up with a faithful parametrisation of $I^{(\text{NN})}_{\text{ZLP}}(E, N_{\text{tot}})$ which can be used to disentangle the inelastic contributions across the whole specimen and carry out a

---

[1] Which should not be confused with the normalised velocity often used in relativity, $\beta = v/c$.

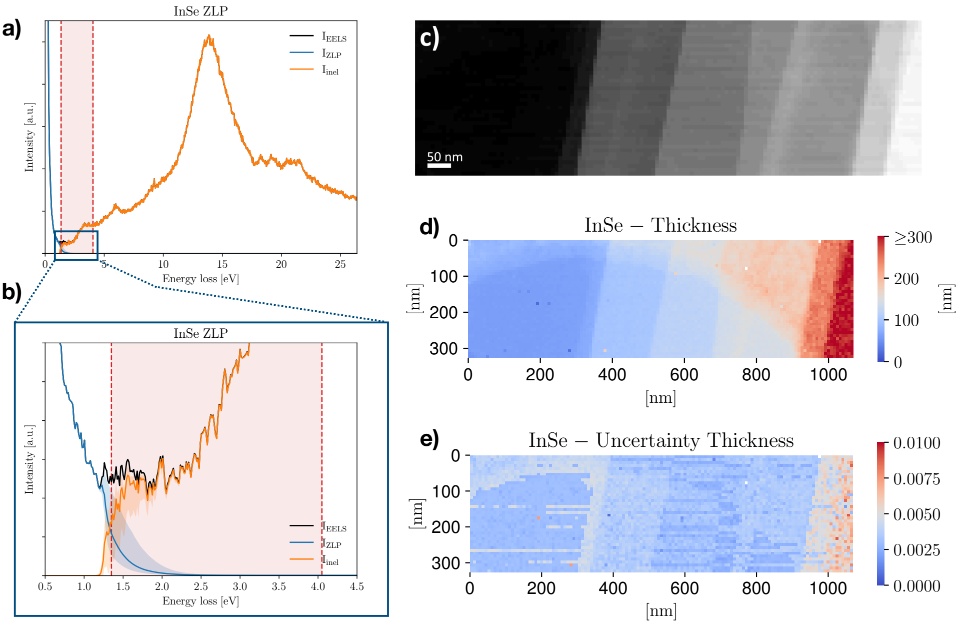

Figure 3.1: **(a)** Representative EEL spectrum from the InSe specimen, where we display the data, the ZLP parametrization, and the subtracted inelastic spectrum. The red dashed region indicates the onset of inelastic scatterings where the bandgap is extracted. **(b)** Same spectrum, now zooming in the low-loss region marked with a blue square in (a). **(c)** EELS-SI acquired on the InSe specimen displayed on Fig. E.1(a,b) in the Supplementary Information, where each pixel corresponds to an individual spectrum. **(d,e)** The thickness map corresponding to the InSe SI of (c) and the associated relative uncertainties respectively.

spatially-resolved determination of relevant physical quantities. To illustrate these capabilities, Fig. 3.1d,e displays the maps associated to the median thickness and its corresponding uncertainties respectively for the same InSe specimen, where a resolution of 8 nm is achieved. One can distinguish the various terraces that compose the specimen, as well as the presence of the hole in the carbon film substrate as a thinner semi-circular region, (see Section B.2 of the Supporting Information). The specimen thickness is found to increase from around 20 nm to up to 300 nm as we move from left to right of the map, while that of the carbon substrate is measured to be around 30 nm consistent with the manufacturer specifications. Uncertainties on the thickness are below the 1% level, as expected since its calculation depends on the bulk (rather than the tails) of the ZLP.

3.3. BAND GAP ANALYSIS OF THE EELS LOW-LOSS REGION

In the same manner as for the thickness, the ZLP-subtracted SI contains the required information to carry out a specially-resolved determination of the band gap. The reason is that the onset of the inelastic scattering intensity provides information on the value of the band gap energy E_{bg}, while its shape for $E \gtrsim E_{\mathrm{bg}}$ is determined by the underlying band structure. Different approaches have been put forward to evaluate E_{bg} from subtracted EEL spectra, such as by means of the inflection point of the rising intensity or a linear fit to the maximum positive slope [1], [23]. Following [18], here we adopt the method of [24], [25], where the behaviour of $I_{\text{inel}}(E)$ in the region close to the onset of the inelastic scatterings is described by

$$I_{\text{inel}}(E) \simeq A\left(E - E_{\text{bg}}\right)^{b}\,, \quad E \gtrsim E_{\text{bg}}\,, \tag{3.7}$$

and vanishes for $E < E_{\text{bg}}$. Here A is a normalisation constant, while the exponent b provides information on the type of band gap: it is expected to be $b \simeq 0.5$ (1.5) for a semiconductor material characterised by a direct (indirect) band gap. While Equation (3.7) requires as input the complete inelastic distribution, in practice the onset region is dominated by the single-scattering distribution, since multiple scatterings contribute only at higher energy losses.

The band gap energy E_{bg}, the overall normalisation factor A, and the band gap exponent b can be determined from a least-squares fit to the experimental data on the ZLP-subtracted spectra. This polynomial fit is carried out in the energy loss region around the band gap energy, $\left[E^{(\text{fit})}_{\text{min}}, E^{(\text{fit})}_{\text{max}}\right]$. A judicious choice of this interval is necessary to achieve stable results: a too wide energy range will bias the fit by probing regions where Equation (3.7) is not necessarily valid, while a too narrow fit range might not contain sufficient information to stabilise the results and be dominated by statistical fluctuation.

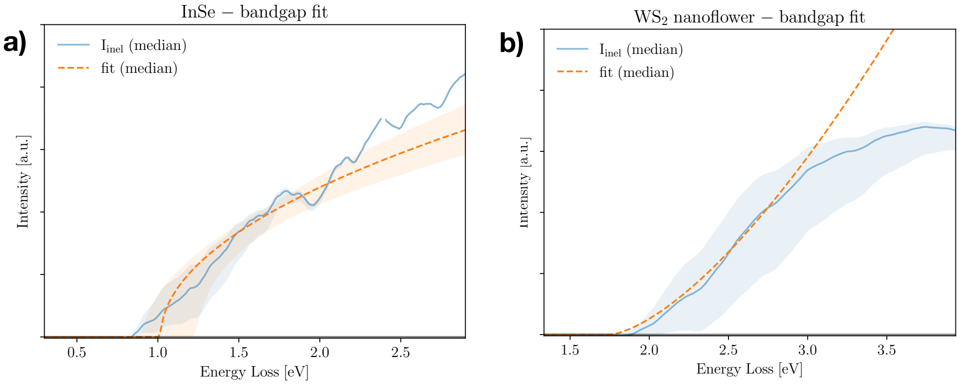

Figure 3.2: Representative examples of band gap fits to the onset of inelastic spectra in the InSe **(a)** and WS_2 **(b)** specimens. The red shaded areas indicate the polynomial fitting range, the blue curve and band corresponds to the median and 68% CL intervals of the ZLP-subtracted intensity $I_{\text{inel}}(E)$, and the outcome of the band gap fits based on Eq. (3.7) is indicated by the orange dashed curve (median) and band (68% CL intervals).

Figure 3.2a,b displays representative examples of band gap fits to the onset of the inelastic spectra in the InSe and WS_2 specimens respectively. The red shaded areas indicate the fitting range, bracketed by $E^{(\text{fit})}_{\text{min}}$ and $E^{(\text{fit})}_{\text{max}}$. The blue curve and band corresponds to the median and 68% CL intervals of the ZLP-subtracted intensity $I_{\text{inel}}(E)$, and the outcome of the band gap fits based on Equation (3.7) is indicated by the green dashed curve (median) and band (68% CL intervals). Here the onset exponents b have been kept fixed to $b = 0.5$ (1.5) for the InSe (WS_2) specimen given the direct (indirect) nature of the underlying band-gaps. One observes how the fitted model describes well the behaviour of $I_{\text{inel}}(E)$ in the onset region for both specimens, further confirming the reliability of our strategy to determine the band gap energy E_{bg}. As mentioned in [25], it is important to avoid taking a too large interval for $[E^{(\mathrm{fit})}_{\mathrm{min}}, E^{(\mathrm{fit})}_{\mathrm{max}}]$, else the polynomial approximation ceases to be valid, as one can also see directly from these plots.

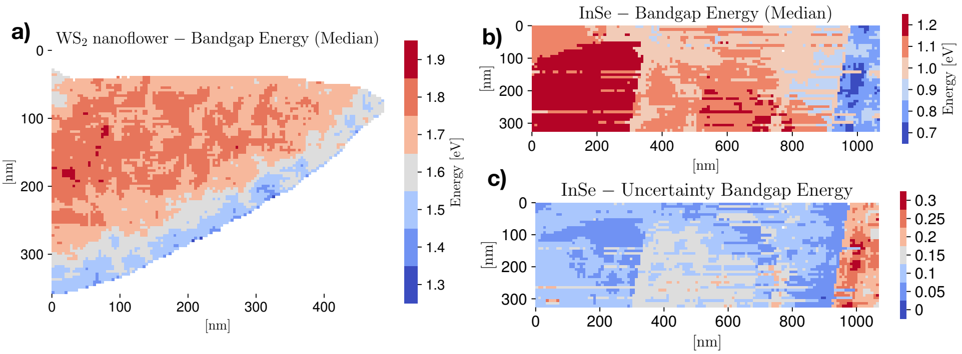

Figure 3.3: **(a)** Spatially-resolved map of the bandgap for the WS$_2$ nanoflower specimen, where a mask has been applied to remove the vacuum and pure substrate pixels. **(b,c)** The median value of the bandgap energy E_{bg} and its corresponding 68% CL relative uncertainties across the InSe specimen, respectively.

Figure 3.3a displays the band gap map for the WS$_2$ nanoflower specimen, where a mask has been applied to remove the vacuum and pure-substrate pixels. A value $b = 1.5$ for the onset exponent is adopted, corresponding to the reported indirect band gap. The uncertainties on E_{bg} are found to range between 15% and 25%. The map of Figure 3.3a is consistent with the findings of Reference [18], which obtained a value of the band gap of 2H/3R polytypic WS$_2$ of $E_{\mathrm{bg}} = (1.6 \pm 0.3)$ eV with a exponent of $b = 1.3^{+0.3}_{-0.7}$ from a single spectrum. These results also agree within uncertainties with first-principles calculations based on Density Functional Theory for the band structure of 2H/3R polytypic WS$_2$ [26]. Furthermore, the correlation between the thickness and band gap maps points to a possible dependence of the value of E_{bg} on the specimen thickness, though this trend is not statistically significant.

Moving to the InSe specimen, Figures 3.3b and c display the corresponding maps for the median value of the band gap energy and for its uncertainties, respectively. Photoluminescence (PL) measurements carried out on the same specimen, and described in the Supporting Information Section B.1, indicate a direct band gap with energy value around $E_{\mathrm{bg}} \approx 1.27$ eV, hence we adopt $b = 0.5$ for the onset exponent. The median values of E_{bg} are found to lie in the range between 0.9 eV and 1.3 eV, with uncertainties of 10% to 20% except for the thickest region where they are as large as 30%. This spatially-resolved determination of the band gap of InSe is consistent with the spatially-averaged PL measurements as well as with previous reports in the literature [27]. Interestingly, there appears to be a dependence of E_{bg} with the thickness, with thicker (thinner) regions in the right (left) parts of the specimen favouring lower (higher) values. This correlation, which remains robust once we account for the model uncertainties, is suggestive of the reported dependence of E_{bg} in InSe with the number of monolayers [28].

Within our approach it is also possible to determine simultaneously the exponent b together with the band gap energy E_{bg}. As already observed in Reference [18], this exponent is typically affected by large uncertainties. Nevertheless, it is found that in the case of the InSe specimen all pixels in the SI are consistent with $b = 0.5$ and that the alternative scenario with $b = 1.5$ is strongly disfavoured. By retaining only those pixels where the determination of b is achieved with a precision of better than 50%, one finds an average value of $b = 0.50 \pm 0.26$, confirming that indeed this material is a direct semiconductor and in agreement with the spatially-integrated PL results. In addition, the extracted values of $E_{\rm bg}$ are found to be stable irrespective of whether the exponent b is kept fixed or instead is also fitted.

3.4. COMPLEX DIELECTRIC FUNCTION FROM EEL SPECTRA USING KRAMERS-KRÖNIG ANALYSIS

The dielectric function of a material, also known as permittivity, is a measure of how easy or difficult it is to polarise a dielectric material such an insulator upon the application of an external electric field. In the case of oscillating electric fields such as those that constitute electromagnetic radiation, the dielectric response will have both a real and a complex part and will depend on the oscillation frequency ω,

$$\epsilon(\omega) = \mathrm{Re}\left[\epsilon(\omega)\right] + i\mathrm{Im}\left[\epsilon(\omega)\right] \,, \tag{3.8}$$

which can also be expressed in terms of the energy $E = \hbar\omega$ of the photons that constitute this electromagnetic radiation,

$$\epsilon(E) = \mathrm{Re}\left[\epsilon(E)\right] + i\mathrm{Im}\left[\epsilon(E)\right] \,. \tag{3.9}$$

In the vacuum, the real and imaginary parts of the dielectric function reduce to $\mathrm{Re}\left[\epsilon(E)\right] = 1$ and $\mathrm{Im}\left[\epsilon(E)\right] = 0$. Furthermore, the dielectric function is related to the susceptibility χ by

$$\epsilon(E) = 1 - v\chi(E) \,, \tag{3.10}$$

where v is the so-called Coulomb matrix.

The single scattering distribution $I_{\rm SSD}(E)$ is related to the imaginary part of the complex dielectric function $\epsilon(E)$ by means the following relation

$$I_{\rm SSD}(E) = \frac{N_0 t}{\pi a_0 m_0 v^2} \mathrm{Im}\left[\frac{-1}{\epsilon(E)}\right] \ln\left[1 + \left(\frac{\beta}{\theta_E}\right)^2\right] \,, \tag{3.11}$$

in terms of the sample thickness t, the ZLP normalisation N_0, and the microscope operation parameters defined in Section 3.2. We can invert this relation to obtain

$$\mathrm{Im}\left[\frac{-1}{\epsilon(E)}\right] = \frac{\pi a_0 m_0 v^2}{N_0 t} \frac{I_{\rm SSD}(E)}{\ln\left[1 + \left(\frac{\beta}{\theta_E}\right)^2\right]} \,. \tag{3.12}$$

Since the prefactor in Equation (3.12) does not depend on the energy loss E, we see that $\mathrm{Im}[-1/\epsilon(E)]$ will be proportional to the single scattering distribution $I_{\rm SSD}(E)$ with a denominator that decreases with the energy (since $\theta_E \propto E$) and hence weights more higher energy losses.

Given that the dielectric response function is causal, the real part of the dielectric function can be obtained from the imaginary one by using a Kramers-Krönig relation of the form

$$\mathrm{Re}\left[\frac{1}{\epsilon(E)}\right] = 1 - \frac{2}{\pi}\mathscr{P}\int_0^{\infty} dE'\,\mathrm{Im}\left[\frac{-1}{\epsilon(E')}\right]\frac{E'}{E'^2 - E^2}\,, \tag{3.13}$$

where $\mathscr{P}$ stands for Cauchy's prescription to evaluate the principal part of the integral. A particularly important application of this relation is the $E = 0$ case,

$$\mathrm{Re}\left[\frac{1}{\epsilon(0)}\right] = 1 - \frac{2}{\pi}\mathscr{P}\int_0^{\infty} dE\,\mathrm{Im}\left[\frac{-1}{\epsilon(E)}\right]\frac{1}{E}\,, \tag{3.14}$$

which is known as the Kramers-Krönig sum rule. Equation (3.14) can be used to determine the overall normalisation of $\mathrm{Im}\,[-1/\epsilon(E)]$, since $\mathrm{Re}\,[1/\epsilon(0)]$ is known for most materials. For instance, as mentioned in Equation (3.4), for an insulator or semiconductor material it is given in terms of its refractive index n.

Once the imaginary part of the dielectric function has been determined from the single-scattering distribution, Equation (3.12), then one can obtain the corresponding real part by means of the Kramers-Krönig relation, Equation (3.13). Afterwards, the full complex dielectric function can be reconstructed by combining the calculation of the real and imaginary parts, since

$$\epsilon(E) = \mathrm{Re}\,[\epsilon(E)] + i\mathrm{Im}\,[\epsilon(E)] \equiv \epsilon_1(E) + i\epsilon_2(E)\,, \tag{3.15}$$

implies that

$$\mathrm{Re}\left[\frac{1}{\epsilon(E)}\right] = \frac{\epsilon_1(E)}{\epsilon_1^2(E)+\epsilon_2^2(E)}\,, \qquad \mathrm{Im}\left[\frac{-1}{\epsilon(E)}\right] = \frac{\epsilon_2(E)}{\epsilon_1^2(E)+\epsilon_2^2(E)}\,, \tag{3.16}$$

and hence one can express the dielectric function in terms of experimentally accessible quantities,

$$\epsilon(E) = \frac{\mathrm{Re}\left[\frac{1}{\epsilon(E)}\right] + i\mathrm{Im}\left[\frac{-1}{\epsilon(E)}\right]}{\left(\mathrm{Re}\left[\frac{1}{\epsilon(E)}\right]\right)^2 + \left(\mathrm{Im}\left[\frac{-1}{\epsilon(E)}\right]\right)^2}\,. \tag{3.17}$$

Once the complex dielectric function of a material has been determined, it is possible to evaluate related quantities that also provide information about the opto-electronic properties of a material. One example of this would be the optical absorption coefficient, given by

$$\mu(E) = \frac{E}{\hbar c}\left[2\left(\epsilon_1^2(E)+\epsilon_2^2(E)\right)^{1/2} - 2\epsilon_1(E)\right]^{1/2}\,, \tag{3.18}$$

which represents a measure of how far light of a given wavelength $\lambda = hc/E$ can penetrate into a material before it is fully extinguished via absorption processes. Furthermore, combining Equations (3.4) and (3.16) one has that for a semiconductor material, such as those considered in this work, the refractive index is given by the relation

$$n = \left(\frac{\epsilon_1(0)}{\epsilon_1^2(0)+\epsilon_2^2(0)}\right)^{-1/2}\,, \tag{3.19}$$

which implies a positive, non-zero value of the real part of the complex dielectric function at $E = 0$.

The complex dielectric function $\epsilon(E)$ provides direct information on the opto-electronic properties of a material, for example those associated to plasmonic resonances. Specifically, a collective plasmonic excitation should be indicated by the condition that the real part of the dielectric function crosses the x axis, $\epsilon_1(E) = 0$, with a positive slope. These plasmonic excitations typically are also translated by a well-defined peak in the energy loss spectra. Hence, verifying that a plasmonic transition indicated by $\epsilon_1(E) = 0$ corresponds to specific energy-loss features provides a valuable handle to pinpoint the nature of local electronic excitations present in the analysed specimen.

3.4.1. THE ROLE OF SURFACE SCATTERINGS.

The previous derivations assume that the specimen is thick enough such that the bulk of the measured energy loss distributions arises from volume inelastic scatterings, while edge- and surface-specific contributions can be neglected. However, for relatively thin samples with thickness t below a few tens of nm, this approximation is not necessarily suitable. Assuming a locally flat specimen with two surfaces, in this case Equation (2.25) must be generalised to

$$I_{\rm EELS}(E) = I_{\rm ZLP}(E) + I_{\rm inel}(E) + I_S(E) \tag{3.20}$$

with $I_S(E)$ representing the contribution from surface-specific inelastic scattering. This surface contribution can be evaluated in terms of the real ϵ_1 and imaginary ϵ_2 components of the complex dielectric function [29],

$$I_S(E) = \frac{N_0}{\pi a_0 k_0 T}\left[\frac{\tan^{-1}(\beta/\theta_E)}{\theta_E} - \frac{\beta}{\beta^2+\theta_E^2}\right]\left(\frac{4\epsilon_2}{(\epsilon_1+1)^2+\epsilon_2^2} - {\rm Im}\left[\frac{-1}{\epsilon(E)}\right]\right), \tag{3.21}$$

where the electron kinetic energy is $T = m_e v^2/2$.

The main challenge to evaluate the surface component from Equation (3.21) is that it depends on the complex dielectric function $\epsilon(E)$, which in turn is a function of the single scattering distribution obtained from the deconvolution of $I_{\rm inel}(E)$ obtained assuming that $I_S(E)$ vanishes. For not too thin specimens, the best approach is then an iterative procedure, whereby one starts by assuming that $I_S(E) \simeq 0$, evaluates $\epsilon(E)$, and uses it to evaluate a first approximation to $I_S(E)$ using Equation (3.21). This approximation is then subtracted from Equation (3.20) and hence provides a better estimate of the bulk contribution $I_{\rm inel}(E)$. One can then iterate the procedure until some convergence criterion is met. Whether or not this procedure converges will depend on the specimen under consideration, and specifically on the features of the EELS spectra at low energy losses, $E \lesssim 10$ eV. For the specimens considered in this work, it is found that this iterative procedure to determine the surface contributions converges best provided that the local sample thickness satisfies $t \gtrsim 20$ nm. We evaluate now the properties of the complex dielectric function $\epsilon(E)$ using the aforementioned Kramers-Krönig analysis. The local dielectric function provides key information on the nature and location of relevant electronic properties of the specimen.

3.4.2. COMPLEX DIELECTRIC FUNCTION IN INSE AND WS$_2$

To illustrate the adopted procedure, Figure 3.4a displays another representative InSe spectrum from the same EELS-SI of Figure 3.1c. Noticeable features include a marked peak at $E \approx 14$ eV, corresponding to the bulk plasmon of InSe, as well as a series of smaller peaks in the low-loss region. The real and imaginary parts of the complex dielectric function associated to the same location in the InSe specimen are shown in Figure 3.4b. The values of the energy loss for which the real component exhibits a crossing, $\epsilon_1(E_c) = 0$, with a positive slope can be traced back to collective excitations such as a plasmonic resonances. Indeed, one observes how the real component $\epsilon_1(E)$ exhibits a crossing in the vicinity of $E \approx 13$ eV, consistent with the location of the bulk plasmon peak.

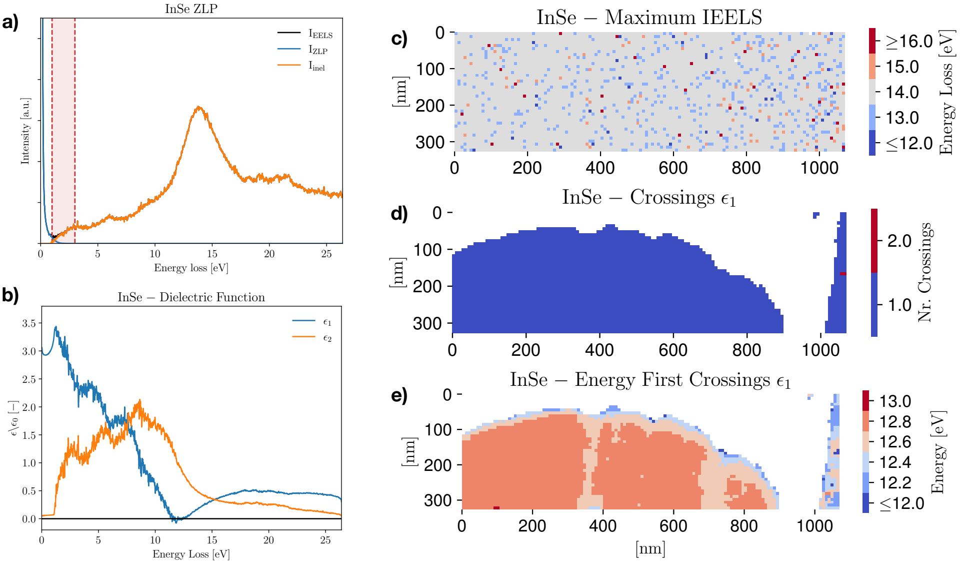

Figure 3.4: **(a)** A representative EEL spectrum from the InSe specimen. **(b)** The real, $\epsilon_1(E)$, and imaginary, $\epsilon_2(E)$, components of the complex dielectric function associated to the same location. **(c)** The energy value associated to the global maximum of the inelastic scattering intensity $I_{\rm inel}(E)$ across the InSe specimen. **(d,e)** The numbers of crossings of $\epsilon_1(E)$ and the associated value of the E respectively across the same specimen, where the SI has been masked to remove pixels with carbon substrate underneath.

Furthermore, the local maxima of the imaginary component $\epsilon_2(E)$ can be associated to interband transitions. From Figure 3.4b, one finds that $\epsilon_2(E)$ exhibits local maxima in the low-loss region, immediately after the onset of inelastic scatterings, at energy losses around 3 eV, 6 eV, and 9 eV. The location of these maxima do match with the observed peaks in the low-loss region of Figure 3.4a, strengthening their interpretation of interband transitions between the valence and conduction bands, and consistent also with previous reports in the literature [30]. The dielectric function in Figure 3.4b provides also access to $\epsilon_1(0)$, the static dielectric constant and hence the refractive index n of bulk InSe. Our results are in agreement with previous reports [31] once the thickness of our specimen is taken into account.

As for the thickness and the band gap, one can also map the variation of relevant features in the dielectric function $\epsilon(E)$ across the specimen. Extending the analysis of Figures 3.4a,b, Figure 3.4c shows the value of the energy loss associated to the maximum of the inelastic scattering intensity $I_{\rm inel}(E)$, while Figures 3.4d,e display the numbers of crossings of $\epsilon_1(E)$ and the corresponding value of the energy loss respectively. In Figures 3.4d,e, the SI has been masked to remove pixels with carbon substrate underneath, the reason being that its contribution contaminates the recorded spectra and hence prevents from robustly extracting $\epsilon(E)$ associated to InSe. It is found that the specimen exhibits a single crossing whose energy E_c ranges between 12.5 eV and 13 eV, close to the maximum of $I_{\rm inel}$ and hence consistent with the location of the InSe bulk plasmonic resonance. Uncertainties on E_c are below the 1% level, since the calculation of $\epsilon(E)$ depends mildly on the onset region where model errors are the largest. Dielectric function maps such as Figure 3.4e represent a sensitive method to chart the local electronic properties of a nanostructured material, complementing approaches such as fitting multi-Gaussian models to EELS spectra to identify resonances and transitions. In particular, maps for the local maxima of $\epsilon_1(E)$ and $\epsilon_2(E)$ could be also be constructed to gauge their variation across the specimen.

Interestingly, as was also the case for the band gap energy in Figure 3.3c, by comparing Figure 3.4e with Figure 3.1d there appears to be a moderate correlation between the crossing energy and the specimen thickness, whereby E_c decreases as the specimen becomes thicker. While dedicated theoretical and modelling work would be required to ascertain the origin of this sensitivity on the thickness, our results illustrate how our framework makes possible a precise characterisation of the local electronic properties of materials at the nanoscale and their correlation with structural features.

Next, we characterise the complex dielectric function of the 2H/3R WS_2 nanoflower specimen from [17], [18] across the whole EELS-SI and present the corresponding results for the spatially-resolved determination of the real, $\epsilon_1(E)$, and imaginary, $\epsilon_2(E)$, parts. Figure 3.5 displays $\epsilon_1(E)$ and $\epsilon_2(E)$ corresponding to two representative spectra of this WS_2 nanoflower specimen. In this analysis we account for the effects of the surface contributions and the error bands quantify the uncertainties associated to the ZLP subtraction procedure.

Of particular interest are the values of the energy loss for which the real component of the dielectric function exhibits a crossing, $\epsilon_1(E) = 0$ with a positive slope. These crossings can be interpreted as indicating a phase transition involving a collective electronic excitation, such as a plasmonic resonance. Here we define that a crossing takes place wherever $\epsilon_1(E) = 0$ at the 90% CL as estimated from the Monte Carlo representation. For the selected spectra displayed in Figures 3.5a,b, this condition is satisfied for $E \simeq 22$ eV and $E \simeq 18$ eV respectively. These values are consistent with the bulk and surface plasmonic resonances in 2H/3R polytypic WS_2 identified in [17].

Figure 3.5c displays the number of such crossings exhibited by the real part of the dielectric function across the whole WS_2 nanoflower specimen. The vacuum and substrate regions have been masked such that only the spectra corresponding to the specimen are retained. One finds that the majority of the spectra are characterised by either one or zero crossings, while a minority showing two or even three crossings. By comparing with Figure B.4b, one observes how it is in the thicker region of the specimen for which the condition $\epsilon_1(E) = 0$ is typically not satisfied, with the exception of the very bottom

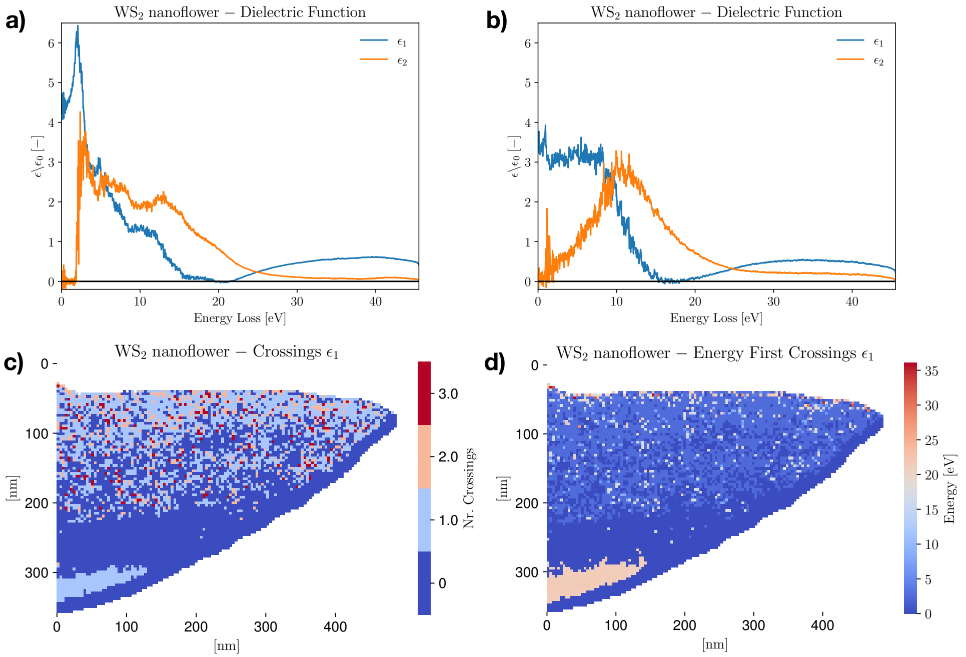

Figure 3.5: **(a,b)** The real $\epsilon_1(E)$ and imaginary $\epsilon_2(E)$ components of the complex dielectric function corresponding to two representative spectra of the WS$_2$ nanoflower specimen. The energy values for which the real component exhibits a crossing, $\epsilon_1(E) = 0$ with positive slope, can be attributed to collective electronic transitions. **(c)** The number of crossings exhibited by the real part of the dielectric function for the same specimen. **(d)** The energy value of the left-most crossing in (c) for the pixels with ≥ 1 crossings. Both in (c) and (d) only the pixels corresponding to the specimen are retained.

region which consistently displays one crossing.

Finally, Figure 3.5d displays the energy E associated to the left-most crossing in Figure 3.5c for those pixels with ≥ 1 crossings. For the upper region of the specimen (characterised by smaller thicknesses), the first crossing is found to be in the low-loss region, while in the bottom (thicker) region, one has a first crossing at $E_c \simeq 21$ eV consistent with the WS$_2$ bulk plasmon peak. We note that one could also show the values of E_c for the subsequent crossings, for those pixels exhibiting more than one crossing.

3.5. CONCLUSIONS AND OUTLOOK

In this work we have presented a novel framework for the automated processing and interpretation of spectral images in electron energy loss spectroscopy. By deploying machine learning algorithms originally developed in particle physics, we achieve the robust subtraction of the ZLP background and hence a mapping of the low-loss region in EEL spectra with precise spatial resolution. In turn, this makes possible realising a spatially-resolved ($\approx$ 10 nm) determination of the bandgap energy and complex dielectric function in layered materials, here represented by 2H/3R polytypic WS$_2$ nanoflowers and by InSe flakes. We have also assessed how these electronic properties correlate with structural features, in particular with the local specimen thickness. Our results have been implemented in a new release of the PYTHON open-source EELS analysis framework EELSFITTER, available from GitHub[2], together with a detailed online documentation[3].

While here we have focused on the interpretation of EELS-SI for layered materials, our approach is fully general and can be extended both to higher-dimensional datasets, such as momentum-resolved EELS [32] acquired in the energy-filtered TEM mode, as well as to different classes of nanostructured materials, from topological insulators to complex oxides. One could also foresee extending the method to the interpretation of nanostructured materials stacked in heterostructures, and in particular to the removal of the substrate contributions, e.g. for specimens fabricated on top of a solid substrate. In addition, in this work we have restricted ourselves to a subset of the important features contained in EEL spectra, while our approach could be extended to the automated identification and characterisation across the entire specimen (e.g. in terms of peak position and width) of the full range of plasmonic, excitonic, or intra-band transitions to streamline their physical interpretation. Finally, another exciting application of our approach would be to assess the capabilities of novel nanomaterials as prospective light (e.g. sub-GeV) Dark Matter detectors [33] by means of their electron energy loss function [34], [35], which could potentially extend the sensitivity of ongoing Dark Matter searches by orders of magnitude.

REFERENCES

[1] S. Schamm and G. Zanchi, “Study of the dielectric properties near the band gap by veels: Gap measurement in bulk materials”, in *Ultramicroscopy*, vol. 96, Elsevier, 2003, pp. 559–564. DOI: `10.1016/S0304-3991(03)00116-5`.

[2] L. Gu, V. Srot, W. Sigle, *et al.*, “Band-gap measurements of direct and indirect semiconductors using monochromated electrons”, *Physical Review B - Condensed Matter and Materials Physics*, vol. 75, 19 May 2007, ISSN: 10980121. DOI: `10.1103/PhysRevB.75.195214`.

[3] W. Zhan, V. Venkatachalapathy, T. Aarholt, A. Y. Kuznetsov, and Ø. Prytz, “Band gap maps beyond the delocalization limit: Correlation between optical band gaps and plasmon energies at the nanoscale”, *Scientific Reports*, vol. 8, 1 Dec. 2018, ISSN: 20452322. DOI: `10.1038/s41598-017-18949-9`.

[4] L. Zhang, R. Erni, J. Verbeeck, and G. V. Tendeloo, “Retrieving the dielectric function of diamond from valence electron energy-loss spectroscopy”, *Physical Review B - Condensed Matter and Materials Physics*, vol. 77, 19 May 2008, ISSN: 10980121. DOI: `10.1103/PhysRevB.77.195119`.

[5] Q. Meng, L. Wu, H. L. Xin, and Y. Zhu, “Retrieving the energy-loss function from valence electron energy-loss spectrum: Separation of bulk-, surface-losses and cherenkov radiation”, *Ultramicroscopy*, vol. 194, pp. 175–181, Nov. 2018, ISSN: 18792723. DOI: `10.1016/j.ultramic.2018.08.014`.

---

[2] Available from `https://github.com/LHCfitNikhef/EELSfitter`

[3] Available from `https://lhcfitnikhef.github.io/EELSfitter/index.html.`

[6] H. J. Conley, B. Wang, J. I. Ziegler, R. F. Haglund, S. T. Pantelides, and K. I. Bolotin, “Bandgap engineering of strained monolayer and bilayer mos2”, *Nano Letters*, vol. 13, pp. 3626–3630, 8 Aug. 2013, ISSN: 15306984. DOI: `10.1021/nl4014748`.

[7] S. L. Xiao, W. Z. Yu, and S. P. Gao, “Edge preference and band gap characters of mos2 and ws2 nanoribbons”, *Surface Science*, vol. 653, pp. 107–112, Nov. 2016, ISSN: 00396028. DOI: `10.1016/j.susc.2016.06.011`.

[8] M. Tinoco, L. Maduro, M. Masaki, E. Okunishi, and S. Conesa-Boj, “Strain-dependent edge structures in mos2 layers”, *Nano Letters*, vol. 17, pp. 7021–7026, 11 Nov. 2017, ISSN: 15306992. DOI: `10.1021/acs.nanolett.7b03627`.

[9] P. H. López, S. Heeg, C. Schattauer, *et al.*, “Strain control of hybridization between dark and localized excitons in a 2d semiconductor”, *Nature Communications*, vol. 13, 1 Dec. 2022, ISSN: 20411723. DOI: `10.1038/s41467-022-35352-9`.

[10] R. D. Ball, L. D. Debbio, S. Forte, *et al.*, “A determination of parton distributions with faithful uncertainty estimation”, *Nuclear Physics B*, vol. 809, pp. 1–63, 1-2 Mar. 2009, ISSN: 05503213. DOI: `10.1016/j.nuclphysb.2008.09.037`.

[11] R. D. Ball, V. Bertone, S. Carrazza, *et al.*, “Parton distributions for the lhc run ii”, *Journal of High Energy Physics*, vol. 2015, pp. 1–148, 4 Apr. 2015, ISSN: 10298479. DOI: `10.1007/JHEP04(2015)040`.

[12] R. D. Ball, V. Bertone, S. Carrazza, *et al.*, “Parton distributions from high-precision collider data: Nnpdf collaboration”, *European Physical Journal C*, vol. 77, 10 Oct. 2017, ISSN: 14346052. DOI: `10.1140/epjc/s10052-017-5199-5`.

[13] B. Gürbulak, M. Şata, S. Dogan, S. Duman, A. Ashkhasi, and E. F. Keskenler, “Structural characterizations and optical properties of inse and inse:ag semiconductors grown by bridgman/stockbarger technique”, *Physica E: Low-Dimensional Systems and Nanostructures*, vol. 64, pp. 106–111, 2014, ISSN: 13869477. DOI: `10.1016/j.physe.2014.07.002`.

[14] C. M. Julien and M. Balkanski, “Lithium reactivity with iii-vi layered compounds”, *Materials Science and Engineering: B*, vol. 100, pp. 263–270, 3 Jul. 2003, ISSN: 09215107. DOI: `10.1016/S0921-5107(03)00113-2`.

[15] J. Rigoult, A. Rimsky, and A. Kuhn, “Refinement of the 3r γ-indium monoselenide structure type”, *Acta Crystallographica Section B Structural Crystallography and Crystal Chemistry*, vol. 36, pp. 916–918, 4 1980, ISSN: 05677408. DOI: `10.1107/s0567740880004840`.

[16] S. Lei, L. Ge, S. Najmaei, *et al.*, “Evolution of the electronic band structure and efficient photo-detection in atomic layers of inse”, *ACS Nano*, vol. 8, pp. 1263–1272, 2 Feb. 2014, ISSN: 19360851. DOI: `10.1021/nn405036u`.

[17] S. E. van Heijst, M. Mukai, E. Okunishi, *et al.*, “Illuminating the electronic properties of ws2 polytypism with electron microscopy”, *Annalen der Physik*, vol. 533, 3 Mar. 2021, ISSN: 15213889. DOI: `10.1002/andp.202000499`.

[18] L. I. Roest, S. E. van Heijst, L. Maduro, J. Rojo, and S. Conesa-Boj, “Charting the low-loss region in electron energy loss spectroscopy with machine learning”, *Ultramicroscopy*, vol. 222, p. 113 202, 2021, ISSN: 0304-3991. DOI: `https://doi.org/10.1016/j.ultramic.2021.113202`.

[19] A. Kumara and P. K. Ahluwalia, “Electronic structure of transition metal dichalcogenides monolayers 1h-mx2 (m = mo, w; x = s, se, te) from ab-initio theory: New direct band gap semiconductors”, *European Physical Journal B*, vol. 85, 6 Jun. 2012, ISSN: 14346028. DOI: `10.1140/epjb/e2012-30070-x`.

[20] Z. Peng, X. Chen, Y. Fan, D. J. Srolovitz, and D. Lei, “Strain engineering of 2D semiconductors and graphene: from strain fields to band-structure tuning and photonic applications”, *Light Sci. Appl.*, vol. 9, no. 190, pp. 1–25, 2020, ISSN: 20477538. DOI: `10.1038/s41377-020-00421-5`.

[21] I. Shlyakhov, K. Iakoubovskii, S. Banerjee, *et al.*, “Measurement of direct and indirect bandgaps in synthetic ultrathin mos2and ws2films from photoconductivity spectra”, *Journal of Applied Physics*, vol. 129, 15 Apr. 2021, ISSN: 10897550. DOI: `10.1063/5.0046305`.

[22] R. Egerton and S. Cheng, “Measurement of local thickness by electron energy-loss spectroscopy”, *Ultramicroscopy*, vol. 21, no. 3, pp. 231–244, 1987, ISSN: 03043991. DOI: `https://doi.org/10.1016/0304-3991(87)90148-3`.

[23] M. Dimitrievska, F. S. Hage, S. E. Steinvall, *et al.*, “The advantage of nanowire configuration in band structure determination”, *Advanced Functional Materials*, vol. 31, 41 Oct. 2021, ISSN: 16163028. DOI: `10.1002/adfm.202105426`.

[24] B. Rafferty and L. Brown, “Direct and indirect transitions in the region of the band gap using electron-energy-loss spectroscopy”, *Physical Review B - Condensed Matter and Materials Physics*, vol. 58, pp. 10 326–10 337, 16 1998, ISSN: 1550235X. DOI: `10.1103/PhysRevB.58.10326`.

[25] B. Rafferty, S. J. Pennycook, and L. M. Brown, “Zero loss peak deconvolution for bandgap eel spectra”, *Journal of Electron Microscopy*, vol. 49, pp. 517–524, 4 2000, ISSN: 00220744. DOI: `10.1093/oxfordjournals.jmicro.a023838`.

[26] L. Maduro, S. E. van Heijst, and S. Conesa-Boj, “First-principles calculation of optoelectronic properties in 2d materials: The polytypic ws2 case”, *ACS Physical Chemistry Au*, vol. 2, pp. 191–198, 3 May 2022, ISSN: 26942445. DOI: `10.1021/acsphyschemau.1c00038`.

[27] H. Henck, D. Pierucci, J. Zribi, *et al.*, “Evidence of direct electronic band gap in two-dimensional van der waals indium selenide crystals”, *Physical Review Materials*, vol. 3, 3 Mar. 2019, ISSN: 24759953. DOI: `10.1103/PhysRevMaterials.3.034004`.

[28] M. J. Hamer, J. Zultak, A. V. Tyurnina, *et al.*, “Indirect to direct gap crossover in two-dimensional inse revealed by angle-resolved photoemission spectroscopy”, *ACS Nano*, vol. 13, pp. 2136–2142, 2 Feb. 2019, ISSN: 1936086X. DOI: `10.1021/acsnano.8b08726`.

[29] R. F. Egerton, *Electron Energy-Loss Spectroscopy in the Electron Microscope*. Springer US, 2011, ISBN: 978-1-4419-9583-4. [Online]. Available: `https://link.springer.com/book/10.1007/978-1-4419-9583-4`.

[30] A. Politano, D. Campi, M. Cattelan, *et al.*, "Indium selenide: An insight into electronic band structure and surface excitations", *Scientific Reports*, vol. 7, p. 3445, 1 Dec. 2017, ISSN: 2045-2322. DOI: `10.1038/s41598-017-03186-x`.

[31] K. R. Allakhverdiev, S. S. Babaev, E. Y. Salaev, and M. M. Tagyev, "Angular behaviour of the polar optical phonons in aiiibvi layered semiconductors", *physica status solidi (b)*, vol. 96, pp. 177–182, 1 1979, ISSN: 15213951. DOI: `10.1002/pssb.2220960116`.

[32] R. Senga, K. Suenaga, P. Barone, S. Morishita, F. Mauri, and T. Pichler, "Position and momentum mapping of vibrations in graphene nanostructures", *Nature*, vol. 573, pp. 247–250, 7773 Sep. 2019, ISSN: 14764687. DOI: `10.1038/s41586-019-1477-8`.

[33] S. Knapen, T. Lin, and K. M. Zurek, "Light dark matter: Models and constraints", *Physical Review D*, vol. 96, 11 Dec. 2017, ISSN: 24700029. DOI: `10.1103/PhysRevD.96.115021`.

[34] S. Knapen, J. Kozaczuk, and T. Lin, "Dark matter-electron scattering in dielectrics", *Physical Review D*, vol. 104, 1 Jul. 2021, ISSN: 24700029. DOI: `10.1103/PhysRevD.104.015031`.

[35] S. Knapen, J. Kozaczuk, and T. Lin, "Python package for dark matter scattering in dielectric targets", *Physical Review D*, vol. 105, 1 Jan. 2022, ISSN: 24700029. DOI: `10.1103/PhysRevD.105.015014`.

4

PEAK IDENTIFICATION IN LOSS AND GAIN REGIONS OF EELS

In this chapter, we discuss peak identification in the loss and gain regions of the electron energy-loss spectroscopy (EELS) spectrum through two case studies. The first study examines electronic properties and band gap variations in one-dimensional (1D) molybdenum disulfide (MoS_2) nanostructures, revealing excitonic peaks around 2 *eV and* 3 *eV at the ends or sides and a plasmonic resonance at* 8.3 *eV in the inner region, with a band gap of approximately* 1.2 *eV affected by curvature-induced strain. We used SciPy's* $find\_peaks()$ *function, pooling and smoothing spectra to construct histograms of detected peaks, enabling analysis of spatial distribution and strain effects. The second study investigates the energy-gain peak around* -0.8 *eV after subtracting the zero-loss peak (ZLP) using a Gaussian model. Robustness was ensured by comparing various ZLP models and using the Monte Carlo replica method to estimate uncertainties, demonstrating the capability of energy-gain EELS in mapping collective excitations in van der Waals materials.*

Parts of this chapter have been published in Advanced Functional Materials: S. van der Lippe, **A. Brokkelkamp**, J. Rojo, S. Conesa-Boj, Adv. Func. Mat. **33**, 2307610 (2023) and Ultramicroscopy: H. La, **A. Brokkelkamp**, S. van der Lippe, J. ter Hoeve, J. Rojo, S. Conesa-Boj, Ultramicroscopy **254**, 113841 (2023).

4.1. INTRODUCTION

Developing techniques for automatic feature identification is more relevant than ever to keep up with technological advances. In this chapter, we present two case studies that address feature identification using different approaches, focusing on both the loss and gain regions of the EELS spectrum.

Peak identification is particularly crucial for the group of layered materials. For instance, central to the optical functionalities of the transition metal dichalcogenide (TMD) MoS_2 are excitons, electron-hole bound states whose behaviour can be modified by localisation arising from potential minima [1] induced by defects [2], [3], strain [4], [5], or local potential variations [6]. Additionally, topological insulator (TI) materials, such as Bi_2Te_3 can support plasmonic excitations, leading to enhanced light-matter interactions such as strong scattering, absorption, and emission. Notably, low-energy plasmons have been reported in Bi_2Te_3 below 3 eV and correlated plasmons at around 1 eV in Bi_2Te_3 [7], [8].

Electron-based spectroscopic techniques, such as electron energy-loss spectroscopy (EELS), have demonstrated their suitability to investigate the electronic and optical properties of a wide range of materials, including the study of their plasmonic resonances [9]–[15]. Moreover, recent advancements in instrumentation, such as the improvement in the stability of electron sources, have greatly enhanced the precision of electron energy-loss spectroscopy. [16], [17] These development have helped uncovered features that where previously either not visible, have shifted based on a multitude of factors, or even uncovered new yet unidentified phenomenon. In this chapter, we present two case studies that address feature identification using different approaches, focusing on both the loss and energy-gain regions of the EELS spectrum.

For MoS_2, we take a look at the TMD in a one dimensional configuration and explore the low-loss energy region to study the exciton behaviour. In contrast, for Bi_2Te_3, we investigate the energy-gain region. The latter offers the advantage of avoiding obscuration by multiple scattering continua and other electronic transitions in the energy-loss ($\Delta E > 0$) region, allowing for the clean identification of narrow collective excitations with enhanced spectral resolution. In both case studies, accurate and automated peak identification can reveal significant variations in electronic properties, exciton behaviour, and band gap modulation. By understanding the spatially dependent electronic properties of these nanostructures, we can design and optimise nanoscale devices more effectively, resulting in enhanced performance and advancements in nanophotonics and optoelectronic applications.

4.2. CASE STUDY: 1D-MoS_2 NANOSTRUCTURES

Two-dimensional (2D) van der Waals (vdW) materials, both in the traditional planar configuration as well as in their one-dimensional (1D) counterpart, have captivated substantial interest due to their remarkable electrical and optical properties. In this context, the study of 1D-MoS_2 nanostructures holds tremendous potential for unlocking novel possibilities in customisation and design complementing those provided by the planar configuration. Understanding these properties is crucial for the design and optimization of nanoscale devices in applications to nanoelectronics and optoelectronics.

The unique platform provided by 1D-MoS$_2$ nanostructures is expected to allow the hosting of localised excitons through curvature-induced quantum confinement. However, a comprehensive understanding of the properties of these localised excitons in 1D-MoS$_2$ remains so far elusive. A challenge of this configuration is the possible presence of several confounding effects, including strain fields and structural defects, which may alter the optoelectronic properties such as the band gap and the location and intensity of localised excitonic transitions.

In this study, we undertake a thorough investigation of localised excitons in 1D-MoS$_2$ nanostructures, complemented by the assessment of their band gap energy modulation. This is achieved by leveraging and extending our previously developed approach [18], [19] for the automated processing and interpretation of electron energy-loss spectroscopy (EELS) spectral images (SI) with nanometer spatial resolution implemented within the open-source EELSFITTER framework.

4.2.1. STRUCTURAL CHARACTERISATION

The 1D-MoS$_2$ nanostructures investigated in this work were synthesised by means of chemical vapour deposition (CVD) techniques [20]. They were directly grown on a 5 nm thick Si$_3$N$_4$ membrane spanning the Transmission Electron Microscopy (TEM) grid. More details on the growth methodology can be found in the Methods section.

The synthesised nanostructures exhibit a characteristic core-shell structure as illustrated in the bright-field TEM image of Fig. 4.1a. Confirmation of the presence of MoS$_2$ in both the core and the shell regions was achieved by acquiring EELS at two distinct positions within the nanostructure, Figure 4.1b, displaying the plasmon peak located at 22.5 eV consistent with previous studies [21]–[25]. Further evidence is provided in Figure 4.1d with line profiles extracted from the high-resolution HAADF-STEM image of the tip of the same 1D-MoS$_2$ nanostructure (Figure 4.1c. The distances between the peaks in the line profile provides information on the interlayer spacing, which is found to be approximately 6 Å and consistent with the interlayer distance of MoS$_2$ reported in the literature [26]. We also observe that as we move closer to the outer layer of the nanostructure, this interlayer distance increases. Upon closer examination of the nanostructure's edge, we observe bright spots (indicated with a blue rectangle in Figure 4.1c indicating atomic contrast arising from Mo atoms. To determine the Mo-Mo distance, we also conducted a line profile analysis finding the expected separation of approximately 0.262 nm. The 1D-MoS$_2$ nanostructures considered in this work are showcased in Figure C.1 in the Supporting Information and exhibit an average length and diameter of 960 nm and 60 nm respectively. Their close examination reveals several interesting features. In particular, the rolling up of the MoS$_2$ sheets along the MoS$_2$ core leads to the formation of tubular structures, which display distinctive faceted caps at their tips (see Figure 4.1a, with dashed lines highlighting these features) which should induce the formation of localised tensile strain. To quantify the strain distribution within the 1D-MoS$_2$ nanostructures, we employ the Geometrical Phase Analysis (GPA) method [27], [28]. Figure 4.2 presents the GPA strain analysis of two representative regions of the 1D-MoS$_2$ nanostructure, one located near the maximum bending point in the tip and providing insight into the strain distribution in a highly curved region, while the other is positioned along the length of the nanostructure and allowing us to examine strain variations in a relatively straight

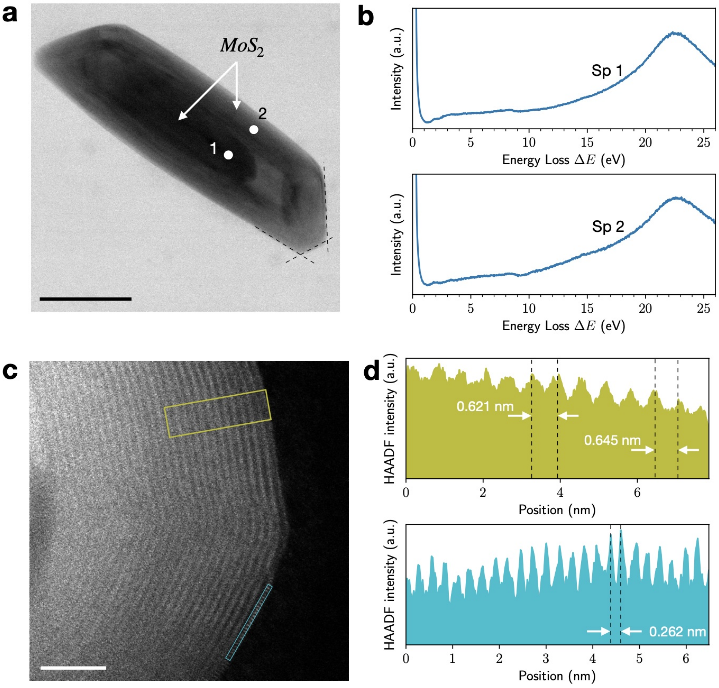

Figure 4.1: **Morphology of the 1D-MoS$_2$ nanostructures.** **(a)** Bright-field image of a representative 1D-MoS$_2$ nanostructure. The size of the scale bar is 50 nm. **(b)** High-resolution EEL spectra corresponding to the regions indicated in (a) and displaying the MoS$_2$ bulk plasmon peak at 22.5 eV. **(c)** High-resolution HAADF-STEM image of the tip of the same 1D-MoS$_2$ nanostructure. The size of the scale bar is now 5 nm. **(d)** Line scans acquired in the regions marked in (c) with green and blue rectangles. The top line scan identifies the separation between atomic planes to be approximately 0.63 nm, while the inter-atomic distance is determined to be around 0.262 nm from the bottom line scan. The line scan origin corresponds to the left-most end of the marked regions.

section. In the vicinity of the maximum bending point, the MoS$_2$ layers are found to exhibit tensile strain, with values reaching up to 0.45 % (Figures 4.2b,c) with respect to the reference region for the diagonal components ϵ_{xx} and ϵ_{yy}. Interestingly, strain is comparatively lower at the precise maximum bending region, marked by a dashed white rectangle in Figure 4.2a, and which also reveals the presence of structural defects in the form of discontinuous layers in this region. The observed decrease in strain at the maximum bending point, accompanied by the presence of structural defects, can be attributed to the inherent requirements for the MoS$_2$ layers to satisfy stacking order and orientation relationship with respect to the previous layer. The strain involved in the formation of these 1D-MoS$_2$ nanostructures, especially at their pronounced tips, is therefore relaxed through the formation of structural defects. The type of defects identified in Figure 4.2a correspond to basal plane dislocations, which in turn can lead to twin defects. [29] The formation of the latter in 2D materials minimises the total energy by balancing the strain energy caused by lattice distortion with the van der Waals energy between neighbouring planes.

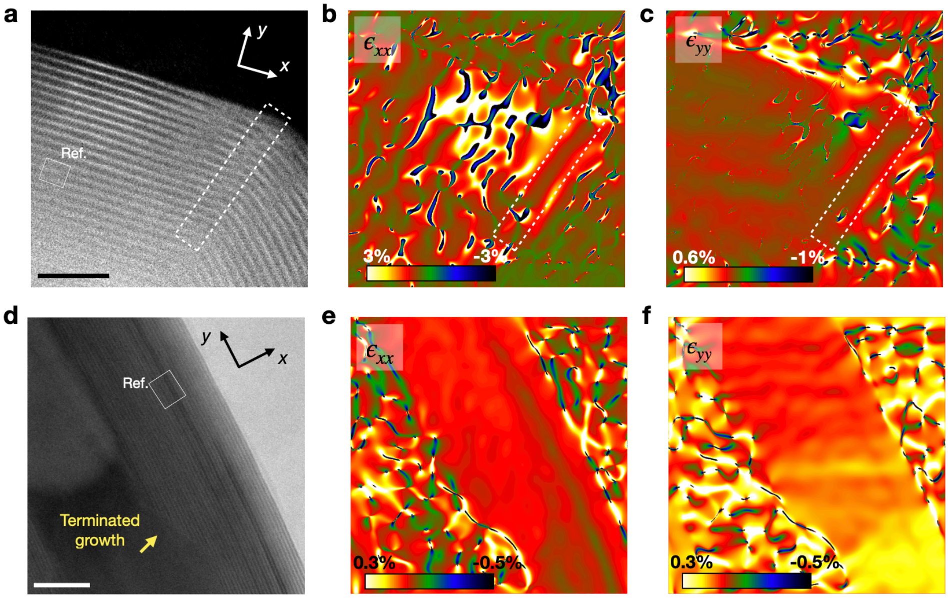

Figure 4.2: **Strain analysis of 1D-MoS$_2$ nanostructures.** **(a)** HAADF-STEM image of a region located around the bend region of the tip of a 1D-MoS$_2$ nanostructure. The size of the scale bar is 5 nm. **(b,c)** The strain components ϵ_{xx} and ϵ_{yy} extracted by means of GPA from (a), revealing the presence of tensile strain peaking at 0.45 % near the bend with a decrease at the point of maximum bending. This tensile strain is associated with the presence of structural defects. **(d)** High-resolution TEM image of a region along the length of the nanostructure close to the tip, displaying terminated growth of the inner layers of the 1D-MoS$_2$ nanostructures leading to variations in wall thickness and diameter along this length. The size of the scale bar is 10 nm. **(e,f)** Strain components ϵ_{xx} and ϵ_{yy} extracted by means of GPA from (d). Tensile strain is observed along the length, which gradually increases as the shell thickness varies. The reference regions for strain calculation are indicated with a white solid rectangle in (a) and (d).

Furthermore, one observes that the inner layers of the 1D-MoS$_2$ nanostructure considered exhibit terminated growth (marked by an arrow in Figure 4.2d). This results in variations in the wall thickness on the two sides of the 1D-MoS$_2$ nanostructures and leads to a varying diameter of the shell along the length of the nanostructure (see Figure C.1 in the Supporting Information). This type of terminated growth has been previously reported in metallic-filled carbon nanotubes [30] and in WS$_2$ nanotubes [31]. Strain is also observed along the length of the 1D-MoS$_2$ nanostructures, as quantified by the ϵ_{xx} and ϵ_{yy} maps in Figures 4.2e and 4.2f. In particular, we find tensile strain which gradually increases as the shell thickness varies.

As shown in Figure C.2, our growth strategy also results in alternative morphologies for the 1D-MoS$_2$ nanostructures, and in particular a fraction of them are connected by their end regions. In the subsequent analysis, we consider both a individual 1D-MoS$_2$ nanostructure as well as joint pair of nanostructure. The presence of bent layers, varying diameters, and interconnected arrangements in these nanostructures has associated the potential to modulate their local electronic properties, demonstrated in the next section.

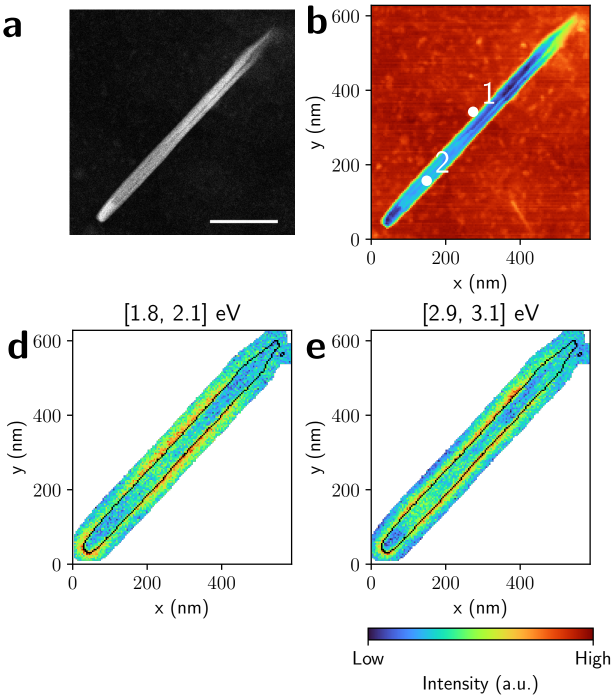

Figure 4.3: **Spatially-resolved EELS analysis of a 1D-MoS$_2$ nanostructure.** **(a)** HAADF-STEM image of a MoS$_2$ nanostructure with a length of 760 nm and a diameter of 40 nm. The size of the scale bar is 200 nm. **(b)** The corresponding EELS-SI, where the colour map corresponds to the total integrated intensity per pixel. **(c)** Representative spectra associated to the pixels indicated in **(b)**. These spectra exhibit intensity enhancements at specific energies and are offset in the vertical direction for clarity. **(d)**-**(f)** Same as **(b)**, now with the intensity of the EEL spectra integrated over the indicated energy windows, also highlighted as vertical grey bands in **(b)**, where intensity enhancements are observed. A black curve indicates the boundary of the nanostructure, and we filter out the substrate. Each panel uses a different intensity range.

4.2.2. SPATIALLY-RESOLVED STEM-EELS CHARACTERISATION

The morphological and structural features of 1D-MoS$_2$ nanostructures reported in Figures 4.1 and 4.2 motivate the in-depth analysis of their local optoelectronic properties. To this end, we conduct electron energy-loss spectroscopy (EELS) measurements on individual nanostructures to identify and study collective electronic excitations, such as excitons and plasmons, and to determine their band gap energy. Our focus is primarily the low-loss region, with energy losses $\Delta E \leq 50$ eV, providing direct insights into the sought-for excitonic and plasmonic behaviour. This analysis builds upon the open-source EELSFITTER framework [18], [19] for the processing of spatially-resolved EELS data (as explained in Chapter 2), here extended with automated peak-tracking algorithms.

Figure 4.3a displays a HAADF-STEM image of a representative 1D-MoS$_2$ nanostructure. Figure 4.3b displays the EELS spectral image acquired on this specimen, where the colour map corresponds to the total integrated intensity per pixel. In Figure 4.3c, individual EEL spectra acquired at two distinct positions on the nanostructure (indicated in

Figure 4.3b) are shown. In order to reduce statistical noise, spectra are pooled using a 3×3 mask. They are also normalised to a common factor and offset in the vertical direction to facilitate visualisation. The highlighted spectra exhibit significant variations between the two positions in the specimen, one close to the surface (spectrum 1, sp1 for short) and another towards the center (sp2). Specifically, sp1 (surface) displays prominent peak-like features at energies of around 1.9 eV and 3.0 eV, while sp2 (central region) exhibits instead localised intensity enhancements around 3.0 eV and 8.3 eV.

4.2.3. AUTOMATED EELS PEAK DETECTION AND ANALYSIS

Analysing individual spectra within an EELS spectral image to identify intensity enhancements by manual inspection is both inefficient and challenging, especially when dealing with multiple spectral images. To automate the peak detection and analysis in EELS-SI, here we employed the `find_peaks()` function from SCIPY. To optimise the results, we pooled spectra within a 3×3 area and applied a smoothing process to prevent the algorithm from erroneously identifying peaks caused by measurement noise. By repeating this approach for all pixels within the EELS spectral image and constructing a histogram based on the positions of the detected peaks, we are able to automatically determined energy-loss regions displaying intensity enhancements for their subsequent inspection.

As an illustration, we applied the described procedure to the 1D-MoS$_2$ specimen analysed in Figure 4.9 In Figure 4.4a, we present a histogram displaying the identified peaks within the $[0, 10]$ eV range across the whole specimen. The histogram indicates that intensity enhancements are clustered at energy losses of approximately 1.7 eV, 2.0 eV, 2.7 eV, 3.0 eV and 8.3 eV. Manual inspection of the spectral image in the vicinity of these energy values confirms the presence of peaks within the data, as shown in Figure 4.9b. By applying this procedure to all the EELS-SI images considered, we are able to identify in an unbiased manner the most relevant energy-loss windows for further analysis, in particular concerning their spatial distribution across the specimen.

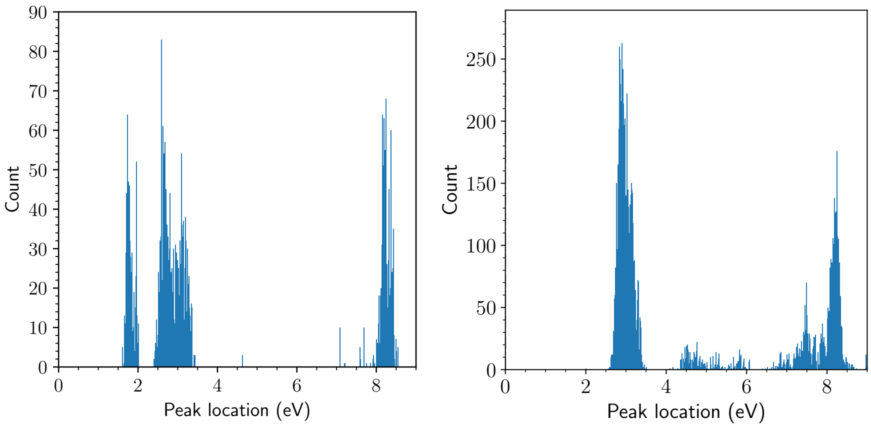

Figure 4.4: **(a)** Histogram of identified peak locations associated to the EELS-SI of Fig. 4**a**. **(b)** Same for the EELS-SI of Fig. 3**b**.

The same procedure applied to the EELS-SI of Figure C.4b is shown in Figure 4.4b. For this specimen, the algorithm does not find a cluster of peaks around 2.0 eV. Manual inspection of EEL spectra reveals nevertheless the clear presence of the peak at $\Delta E \sim 2.0$ eV also for this specimen. The reason it is not identified by our algorithm is that the resonant feature at $\Delta E \sim 2.8$ eV is quite broad and partially overlaps with the one at 2 eV. This result highlights the importance of complementing the outcome of the automated peak finding algorithm with manual inspection of the acquired spectra.

The spatially-resolved EELS analysis of Figure 4.3d-f illustrates how the peak-like features reported in the individual spectra of Figure 4.3c vary across the 1D-MoS_2 nanostructure. In the energy-loss range of $[1.8, 2.1]$ eV, the strongest signal intensity is observed at one of the tips of the nanostructure as well as along the sides, specially in the central region. For the energy-loss range of $[2.9, 3.1]$ eV, the signal is most marked along the sides of the nanostructure, with a moderate enhancement observed at one of the tips as well. In the $[8.2, 8.4]$ eV energy-loss range, the intensity is mostly enhanced along half of the length of the nanostructure, excluding the tip regions. It has been reported [13] that for MoS_2 the peaks at 8.3 eV appear only for non-zero momentum q. Overall, one finds that the energy value and intensity of several peak-like features in the EELS spectra vary sensitively with respect to the spatial location within the nanostructure.

Figure 4.5 then presents a similar analysis as that of Figure 4.3 now for a different morphology: two 1D-MoS_2 nanostructures connected by their endpoints, as demonstrated by the HAADF-STEM analysis presented in Figure C.2 in the Supporting Information and in particular by the HAADF-STEM image of Figure C.2a. With the aim of identifying the implications of this interconnected configuration, Figure 4.5b displays three representative spectra taken at different locations in the specimen, again exhibiting distinctive features depending on the location. Marked peak-like intensity enhancements at around 1.7 eV (sp1), 2.0 eV (sp2) and at both 2.7 eV and 8.3 eV (sp3) respectively are observed. The integrated intensity maps shown in Figures 4.5c-f indicate that these intensity enhancements are localised in the range $[1.6, 1.8]$ eV at the tips of the bottom nanostructure, along the edge in the middle region of the top nanostructure for $[1.9, 2.1]$ eV, at the middle parts of the nanostructures as well as at the region where the nanostructures are connected for $[2.6, 2.8]$ eV, and at the inner part of the nanostructures for the $[8.2, 8.4]$ eV energy-loss range. The reproducibility of this analysis is confirmed by the results in section C.1.4 in the Supporting Information, corresponding to another connected specimen with a similar morphology. The intensity enhancement around 1.7 eV, absent for the nanostructure in Figure 4.3, can be ascribed to strain effects shifting the exciton peak at 2 eV to smaller energies.

The energies of some of the observed peak-like intensity enhancements in the analysed 1D-MoS_2 nanostructures align closely with values reported in the literature for two-dimensional MoS_2 specimens based on theoretical calculations [32], EELS studies [13], [33], [34] and photoluminescence studies [35]. Specifically, the peaks located around 2 and 3 eV can be explained as arising from excitonic transitions, while the peak at 8.3 eV can be attributed to a plasmonic resonance [13]. For the latter case, an enhancement around 8.3 eV is observed in the inner region of the 1D-MoS_2 nanostructures across all the analysed structures, in alignment with previous reports on plasmonic resonances in 2D-MoS_2 nanosheets [13].

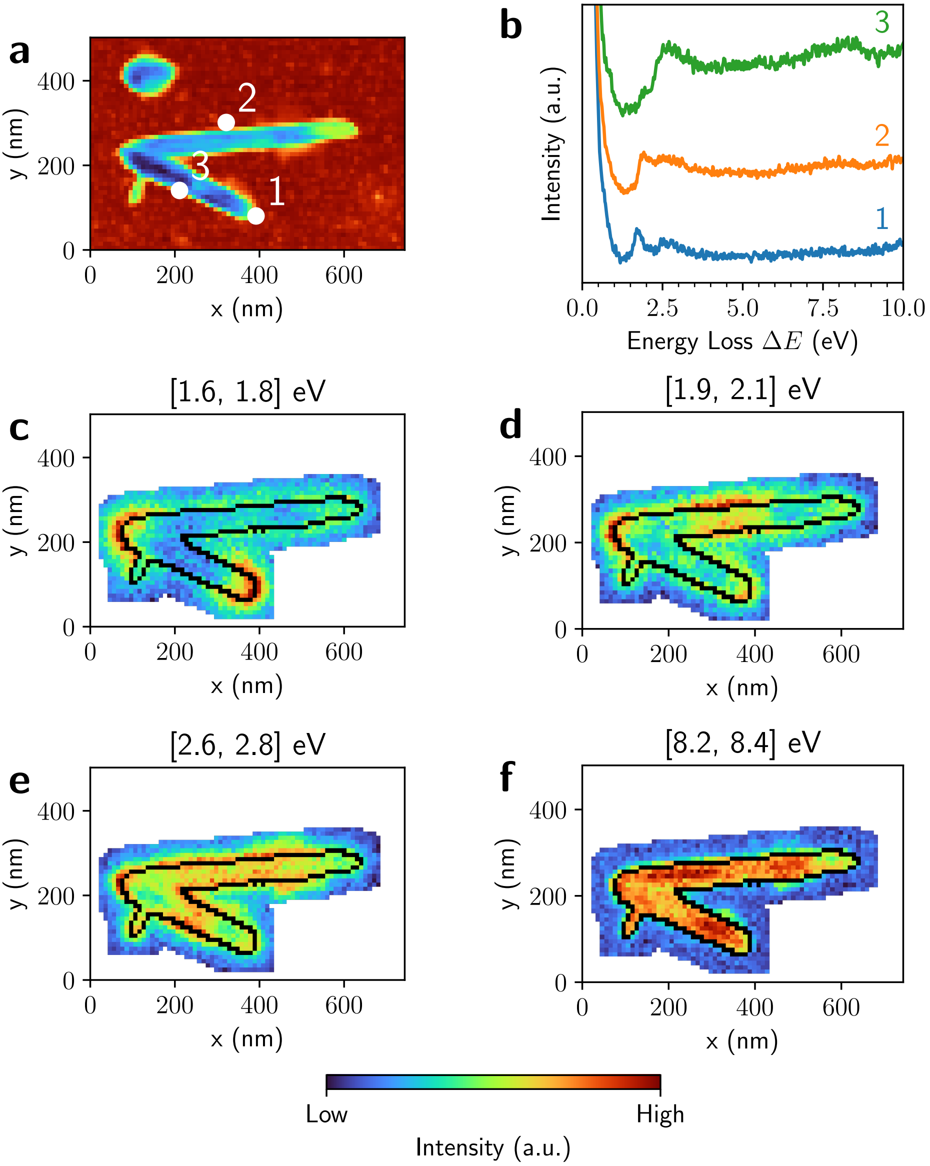

Figure 4.5: **Spatially-resolved EELS analysis of connected 1D-MoS$_2$ nanostructures.** Same as Fig. 4.3 now for two 1D-MoS$_2$ nanostructures, with a length of 540 nm and a diameter of 57 nm (top), and a length of 336 nm and a diameter of 62 nm (bottom) respectively, connected by their ends. The corresponding HAADF-STEM image is provided in Figure C.2**a**.

The main differences between our findings on 1D-MoS_2 nanostructures and previous investigations on the 2D configuration are summarised by the spatially-resolved analyses of Figures 4.3 and 4.5, as well as in Figure C.4, which establish their correlation with specific locations in the specimen. In contrast with results on 2D-MoS_2 nanosheets, where intensity enhancements are typically observed at the edge regions [13], we find that the enhancements around 2 and 3 eV are localised at either end of the 1D-MoS_2 nanostructures (Figures 4.5c and C.4c) or along their lateral sides (Figures 4.3d, 4.5d, and C.4d). The fact that these peaks are associated to excitonic transitions [13] and that our analysis indicates that these are restricted to specific regions in the 1D-MoS_2 nanostructures appears to indicate that the observed signals can be associated to spatially-confined MoS_2 excitons.

The origin of the peaks observed around 2.7 and 3.0 eV in Figures. 4.5b and C.4b and (see also Figures. 4.5e and C.4d,e) therefore admits a common origin. Indeed, as previously reported [13], the enhancement observed at around 3 eV can experience an energy downshift and exhibit a tail extending up to 3.5 eV, consistent with our observations. Furthermore, the intensity distribution across the specimen in the energy intervals around 2.7 and 3.0 eV demonstrates a similar pattern, as displayed in Figures C.4d,e.

4.2.4. SPATIALLY-RESOLVED BAND GAP ENERGY OF 1D-MoS_2 NANOSTRUCTURES

Complementary insights on the local electronic properties of the 1D-MoS_2 nanostructures are provided by the spatial distribution of their band gap energy E_{bg}. Here spatially-revolved maps of E_{bg} are determined by analysing individual EEL spectra after subtracting the ZLP background, following the procedure in [18], [19]. Figure 4.6 displays the E_{bg} maps associated to the 1D-MoS_2 nanostructures studied in Figures 4.3 (individual) and 4.5 (connected). The first and third columns display the lower (upper) bound of the 90% CL interval for E_{bg} while the second displays the median. The corresponding band gap analysis for the specimen analysed in the Supporting Information are collected in Section C.1.5. For all specimens considered we obtain an indirect band gap.

The spatially resolved maps of Figure 4.6 enable identifying correlations between the E_{bg} sensitivity and specific structural features. On the one hand, in the central region of the nanostructures the median E_{bg} is approximately 1.2 eV, consistent with previous findings for bulk MoS_2 [36], [37]. On the other hand, one observes how the values of E_{bg} tend to decrease, as compared to the central region, in the endpoint regions and in the connection region for the joint nanostructure. To quantify this trend, we evaluate in Table 4.1 the weighted average band gap energy in distinct regions within each nanostructure. Specifically, we define the endpoint regions as 20% of the total length of the 1D-MoS_2 nanostructures with the central region given by the remaining 60%. This analysis confirms that E_{bg} is reduced in the endpoint regions as compared to the central ones. The statistical significance of this band gap energy variation is found to be between the 1σ and 2σ level, depending on the nanostructure.

A possible explanation of this trend is provided by the presence of curvature-induced local strain identified in Figures 4.2b,c and e,f in the endpoint and in the lateral regions respectively, which has been reported to modify the band gap energy. The relative decrease of E_{bg} observed in regions with tensile strain at the level quantified in Figure 4.2

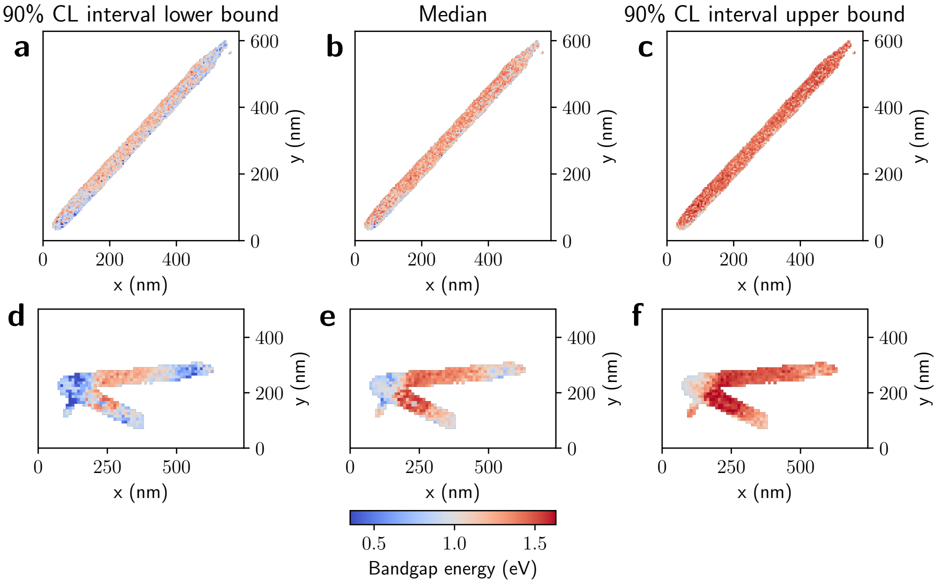

Figure 4.6: **Spatially-resolved band gap energy in 1D-MoS$_2$ nanostructures**. The median value (second column) and 90% CL lower and upper bounds (first and third column, respectively) for the band gap energy E_{bg} determined across the 1D-MoS$_2$ nanostructures considered in Figs. 4.3 (top) and 4.5 (bottom).

Table 4.1: The weighted average for E_{bg} (in eV) for the 1D-MoS$_2$ nanostructures analysed in Fig. 4.6, separated into three regions: the left-most endpoint (20% of the total length of the nanostructure), the central region (60%), and right-most endpoint (20%). We also indicate the uncertainty obtained from the 90% CL interval for the weighted average band gap energy.

Specimen	**Left-most endpoint**	**Central region**	**Right-most endpoint**
Fig. 4.3	1.2 ± 0.2	1.3 ± 0.1	1.2 ± 0.2
Fig. 4.5 (bottom)	0.8 ± 0.1	1.1 ± 0.3	1.0 ± 0.2
Fig. 4.5 (top)	0.8 ± 0.2	1.2 ± 0.2	1.0 ± 0.3

is consistent, within uncertainties, with previous reports on 2D-MoS_2 [38], [39].

Local strain is also known to induce a downshift in the excitonic transition energies [28], [40]. We verify in Section 4.2.5 which analyses the modulation of the 1.9 eV exciton peak location across the specimen, that indeed a downshift between 3% and 4% is obtained in our 1D-MoS_2 specimens. The decrease in the band gap energy E_{bg} in the endpoint regions of the 1D-MoS_2 nanostructures as compared to the central region may hence be attributed to curvature-induced local strain fields, which in turn is consistent with the observed exciton localisation pattern.

4.2.5. SENSITIVITY OF THE EXCITON PEAK LOCATION

It has been reported that strain fields can induce a shift in the energy of MoS_2 exciton peak located near 1.9 eV peak [28], [40]. To study whether this is also true in our specimens, we analyse here the exciton peak position at various locations within the samples studied in the main manuscript. Figure 4.7a presents the spectral image from Figure 4.3, with a selection of pixels marked across the sample. These marked pixels correspond to specific regions of interest for analysis. To improve the signal-to-noise ratio, the spectra associated with these pixels underwent principal component analysis. Afterwards, a least-square fit was performed on the resulting spectra, involving the subtraction of the zero loss peak (ZLP) background and the fitting of a sum of two Gaussian distributions within the $[1.3, 3.5]$ eV range. The purpose of this fitting process was to extract the precise location of the excitonic peak near 1.9 eV, as shown in Figure 4.7b. The fitting results for spectra 1 through 4 are displayed in Figure 4.8a through d, respectively.

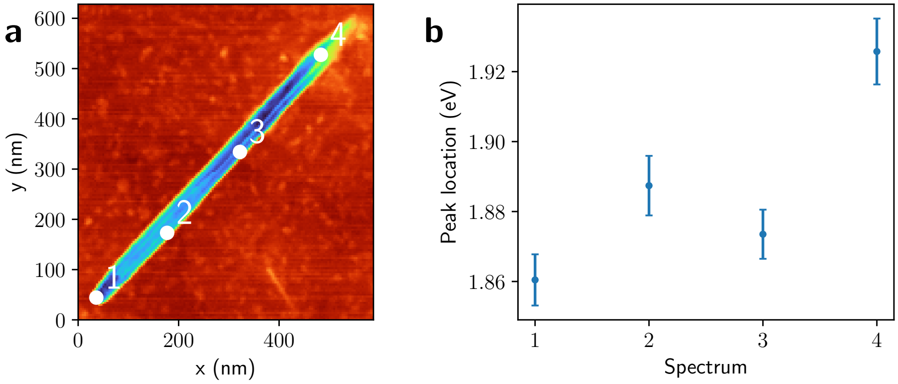

Figure 4.7: **Strain-induced exciton energy shift.** **(a)** Same as Figure 4.3a indicating pixels distributed across the specimen. **(b)** The location of the excitonic peak in the spectra corresponding to the pixels marked in (a).

A similar analysis was conducted for the sample corresponding to Figure 4.5, as shown in Figs. 4.9and 4.10. We indeed observe a decrease in the energy of the exciton peak near 1.9 eV in regions affected by strain. This phenomenon is evident in spectrum 1 of Fig. 4.7 and spectrum 1 and 2 in Fig. 4.9), aligning with previous studies [28], [40]. Conversely, spectrum 4 in both figures corresponds to region where the layers do not wrap around the nanostructure, resulting in open-ended tips which are unaffected by strain. Conse-

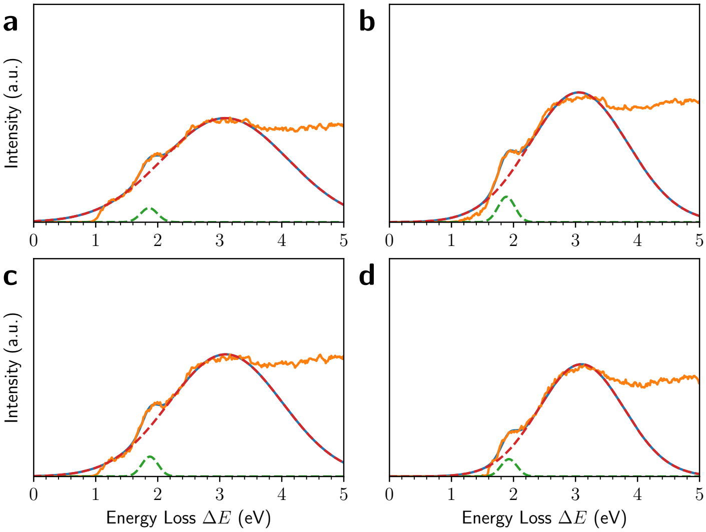

Figure 4.8: **Least-square sum of Gaussians fit to individual spectra**. **(a)-(d)** correspond to spectra $1-4$ in Figure 4.7a. The spectra are treated with principal component analysis to improve signal-to-noise ratio.

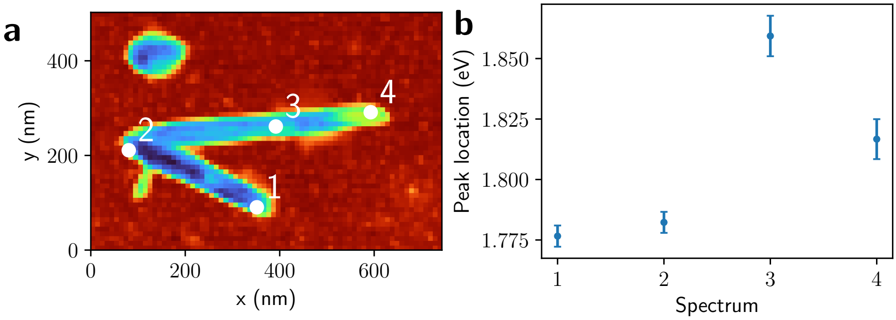

Figure 4.9: Same as Figure 4.7 for the sample analysed in Figure 4.5

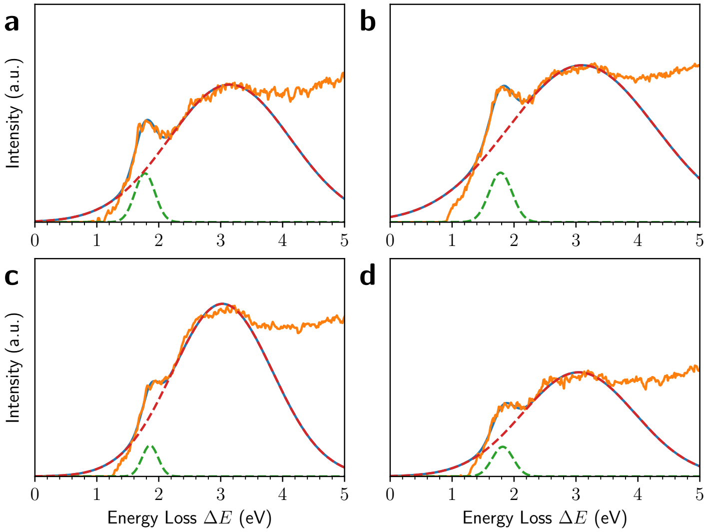

Figure 4.10: Same as Figure 4.8 for the sample analysed in Figure 4.5.

quently, no energy downshift is observed in these spectra.

4.2.6. CONCLUSIONS

Our investigation of the electronic and structural characteristics of 1D-MoS_2 nanostructures has resulted into several key insights. Firstly, we observed excitonic transitions localised at either the endpoints or the lateral sides of the nanostructures, particularly around energy losses of 2 eV and 3 eV, at odds with the case of 2D-MoS_2 materials where the analogous intensity enhancements are typically observed across the structure. Secondly, our studies identifies the presence of plasmonic resonances localised at 8.3 eV in the inner region of the 1D-MoS_2 nanostructures, aligning with previous observations in 2D-MoS_2. Thirdly, we have quantified the spatial modulation of the band gap energy across the 1D-MoS_2 nanostructures, finding that the endpoint regions display a decreased band gap as compared to the bulk MoS_2 value due to the presence of curvature-induced local strain effects. The same curvature-driven strain fields are likely to be responsible for the localisation of the confined excitonic transitions observed.

Our results underscore the rich diversity of electronic behaviours in 1D-MoS_2 nanostructures and highlight the potential for tailoring these properties for specific applications by engineering the nanostructure's morphology and spatial configuration. In particular, they showcase the potential of curvature-induced strain as a useful handle to tune optoelectronic properties. This strain-dependent modulation of the band gap energy in 1D-MoS_2 nanostructures could be leveraged in strain-engineered optoelectronic devices, while being able to reproducibly generate strain-confined excitons opens new avenues for single-photon emitters to be used in quantum optics and quantum networks.

4.3. CASE STUDY: TOPOLOGICAL INSULATOR $\mathrm{BI_2TE_3}$

Topological insulator (TI) materials, such as Bi_2Te_3 [41]–[43] and Bi_2Se_3, possess unique properties that make them well suited for the design of nanoplasmonic devices operating in the THz and mid-infrared frequency ranges. [44]–[48] Topological insulators can also support plasmonic excitations, collective oscillations of electrons that interact strongly with light or other electrons and lead to enhanced light-matter interactions such as strong scattering, absorption, and emission. In particular, low-energy plasmons [7] have been reported in Bi_2Te_3 below 3 eV while correlated plasmons at energies ~ 1 eV have been identified for Bi_2Se_3 [8]. In this context, advancing our understanding of how to optimally deploy TIs for the development of tunable plasmonic devices that operate efficiently in optical frequencies has the potential to benefit a wide range of applications, including quantum computing [49], [50], terahertz detectors [51], and spintronic devices [52].

Here we investigate low-energy collective excitations in the TI material Bi_2Te_3 by means of EELS spectral images focusing on the energy-gain ($\Delta E < 0$) region [14], [53]–[55]. As compared to traditional EELS, this strategy offers the key advantage that gain peaks are not obscured by the multiple scatterings continuum and other electronic transitions taking place in the energy-loss region ($\Delta E > 0$), enabling the clean identification of narrow collective excitations with enhanced spectral resolution. The resulting characterisation of Bi_2Te_3 specimens makes it possible to search for collective resonances in the low-gain region, and correlate their spatial distribution with distinct structural features such as surfaces, edges, and regions with sharp thickness variations.

4.3.1. STRUCTURAL COMPOSITION

Figure 4.11a displays a high-angle annular dark-field (HAADF) Scanning Transmission Electron Microscopy (STEM) image of a representative Bi_2Te_3 specimen. For closer examination, Figure 4.11b shows the magnified top right corner of the same specimen. Further characterisation of the atomic structure of this specimen is provided in Section C.2.2 of the Supplementary Information. By means of electron energy-loss spectroscopy (EELS), we acquire a spectral image (Figure 4.11c) of the specimen in the same region, indicated with a white square in Figure 4.11a. The colour map corresponds to the integrated intensity in the energy range $[-9.05, 92.3]$ eV in each pixel, covering the total energy range in which signal was acquired. The black line indicates the edge of the Bi_2Te_3 specimen, which is automatically determined from the spatially-resolved thickness map associated to the spectral image [19], specifically from its local rate of change.

Figure 4.11d displays EELS spectra taken at three different locations within the spectral image, labelled as spectra sp1, sp2, and sp3 in the following. Spectra sp1, sp2, and sp3 are acquired in the region between the vacuum and the edge of the specimen, in the vicinity of the specimen edge towards the inner region, and in the innermost part of the specimen, respectively. The three spectra reveal the presence of distinct spectral features located at approximately energy losses of 8.6 eV and 16.6 eV, where the latter corresponds to the bulk plasmon peak in accordance with previous studies. [56] Furthermore, the peaks at 25.6 eV and 27.9 eV observed in sp3 can be identified with the Bi $O_{4,5}$ edges excited from Bi 5d electrons, also reported in the literature. [57] Figure 4.11e compares three other EEL spectra (labelled as sp4, sp5, and sp6) acquired in the immedi-

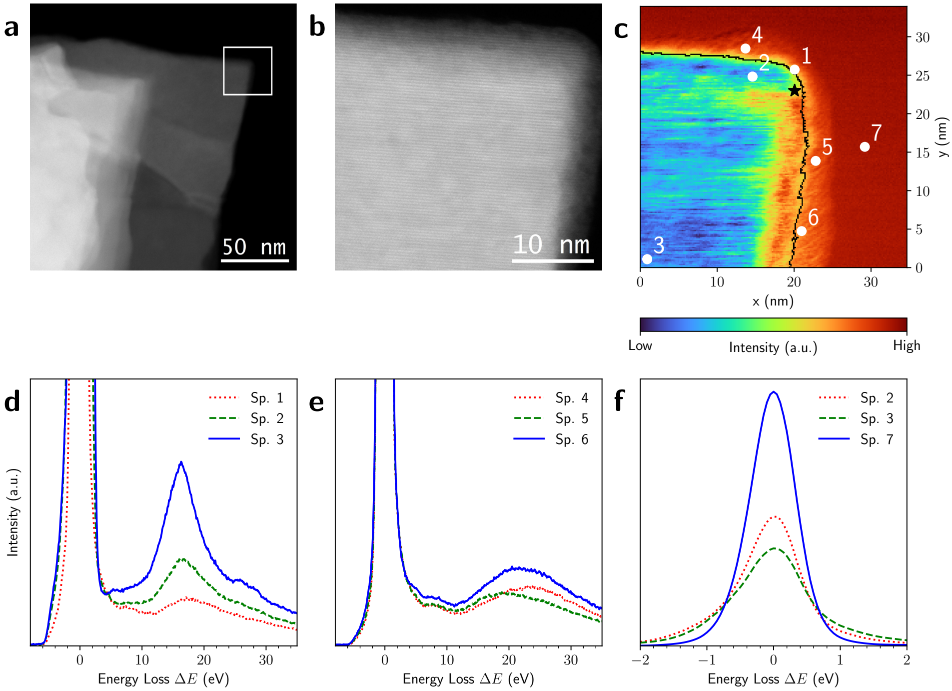

Figure 4.11: **Spatially-resolved EELS analysis of Bi_2Te_3.** **(a)** HAADF-STEM image of a representative Bi_2Te_3 flake. **(b)** Magnified region of the top right corner of the specimen around the white square in **(a)**. **(c)** EELS spectral image corresponding to the white square region in **(a)**. The colour map corresponds to the total integrated intensity in each pixel. The black line indicates the edge of the Bi_2Te_3 specimen, determined from the thickness map as described in the text. **(d)** EELS spectra corresponding to the different regions of the specimen indicated in **(c)**: between the vacuum and the edge (sp. 1); the vicinity of the edge towards the inner region (sp. 2); and the innermost, thicker part (sp. 3). Spectra sp. 1, sp. 2 and sp. 3 display the bulk plasmon peak of Bi_2Te_3 at around 16 eV. Additionally, sp. 3 also shows the Bi $O_{4,5}$ edges excited from Bi 5d electrons at 25.6 eV and 27.9 eV. **(e)** Same as **(d)** for EELS spectra in the immediate vicinity of the Bi_2Te_3 edge, displaying characteristic features of Bi_2O_3. **(f)** A comparison of sp. 2, sp. 3, and sp. 7 in the low loss and gain regions ($|\Delta E| \leq 2$ eV).

ate vicinity of the specimen edge. The three spectra exhibit a broad peak located around 21 eV, which can be identified with the bulk plasmon of Bi_2O_3. [58], [59] It is worth nothing that the presence of Bi_2O_3 in the surfaces of the specimen is not visible from the HAADF images. The reason is that HAADF intensity scales with Z^n, with Z being the atomic number, which is much smaller in O as compared to Te. This presence of Bi_2O_3 in the edge region of the Bi_2Te_3 specimen is further supported by a High-Resolution TEM (HRTEM) analysis reported in Section C.2.6 of the Supplementary Information.

4.3.2. SPATIALLY RESOLVED EEGS

Figure 4.11f compares the EELS intensities in the region of energy losses ΔE restricted to the window $[-2\text{ eV}, 2\text{ eV}]$ for spectra sp2, sp3, and sp7. This comparison illustrates the dependence of the dominant Zero-Loss Peak (ZLP) background with respect to the location in the specimen: bulk (sp3), close to edge (sp2), and vacuum (sp7). On the one hand, as one moves from the vacuum towards the bulk region, the ZLP intensity gradually decreases. This effect can be ascribed to the greater number of inelastic scattering events that occur in the bulk (thicker) regions, compared to the vacuum where the beam electrons do not experience inelastic scatterings. On the other hand, we also observe an enhanced intensity in the specimen regions as compared to the vacuum for $|\Delta E| \geq 0.6$ eV, highlighting material-sensitive contributions to the spectra which contain direct information on its local electronic properties.

Removing this ZLP background is instrumental in order to identify the presence of localised collective excitations such as phonons [60] and plasmon peaks [15] in the low energy-loss region. The same considerations apply to the cleaner energy-gain region [55], where the continuum of inelastic scattering contributions is absent. Here we model the ZLP in terms of a Gaussian distribution following the procedure described in Section 4.3.3, with the fitting region restricted to $[-0.4, 0.4]$ eV to remove the overlap with ΔE values at which plasmonic modes of Bi_2Te_3 have been reported. [7] Subsequently, the ZLP is removed pixel by pixel in the EELS spectral image and the resulting spectra are inspected to identify peaks and other well-defined features in an automated manner. We note that the small band gap [43], [52] of Bi_2Te_3, $E_{bg} \sim 0.15$ eV, prevents reliably training deep learning models for the ZLP parametrisation and subtraction as done in previous studies from our group. [18], [19], [61] Furthermore, although here we focus on a Bi_2Te_3 specimen, the procedure is fully general and applicable to other materials which can be inspected with EELS.

4.3.3. PEAK IDENTIFICATION PROCEDURE

Here we describe the procedure used to identify and characterise energy-gain peaks in Bi_2Te_3. We demonstrate how our approach is robust with respect to the model adopted for the ZLP. While here we focus on a Bi_2Te_3 specimen, our energy-gain peak identification algorithm is general and could be applied to other materials.

The results presented are based on a Gaussian model for the ZLP,

$$I_{\rm ZLP}(\Delta E) = I^{\rm (max)}_{\rm ZLP} \exp\left(-\frac{(\Delta E - \Delta E_0)^2}{2\sigma^2}\right), \tag{4.1}$$

with ΔE being the energy loss (and hence $\Delta E < 0$ implies energy gains), ΔE_0 and σ^2 being the mean and variance of the distribution, and $I^{\rm (max)}_{\rm ZLP}$ is the maximal intensity of the ZLP. This Gaussian model for the ZLP, Equation (4.1), is fitted independently to each individual spectra composing the spectral image. The fit region is restricted to $[-0.4, 0.4]$ eV in order to remove the possible overlap with those values of ΔE at which plasmonic modes of Bi_2Te_3 have been previously reported. Subsequently, the ZLP Gaussian model Equation (4.1) is removed from the measured spectral image and the resulting subtracted spectra are inspected to identify peaks or other relevant features in a fully automated manner.

In this work we identify energy-gain peaks by fitting the subtracted spectra in the energy region $[-3.5, -0.4]$ eV with a Lorentzian function given by

$$I_{\rm peak}(\Delta E) = I_{\rm max} \frac{\Gamma^2}{\Gamma^2 + (\Delta E - E_g)^2} \tag{4.2}$$

where $I_{\max}$ is the height of the peak, Γ its width, and E_g its median, the latter corresponding to the most likely location of the peak being identified. Once one has determined the parameters of the Lorentzian model Equation (4.2) for each of the pixels composing the spectral image, we can determine relevant estimators such as the FWHM and the area underneath it. This way, it is possible to determine the statistical significance of the observed features. Although in this work we consider only single-peak identification, in the presence of multiple features in the energy-gain region Equation (4.2) could be extended to a sum of a series of independent Lorentzian resonances.

In order to further characterise the energy-gain peak identified in Figure 4.12c and to correlate its properties with local structural features of the specimen, Figures 4.13a and b display the intensity of the ZLP-subtracted EEL spectra integrated in the energy windows $[-1.1, -0.6]$ eV and $[0.6, 1.1]$ eV for the gain and loss regions respectively. These ΔE intervals are chosen to contain the range of E_g values displayed in Figure 4.12c and then mirrored to the energy-loss region. In the latter case, the EEL spectra receive additional contributions to the inelastic scattering distribution beyond those considered here. The most notable feature of Figure 4.13a is an enhancement of the integrated intensity in the edge region of the specimen characterised by a sharp variation of the local thickness (Figure 4.12d).

To quantify the statistical significance of the identified energy-gain peak, it is convenient to evaluate the ratio

$$s_g \equiv \left(A_g / A_{\text{zlp}}\right)_{\text{g-fwhm}} , \tag{4.3}$$

where A_g and A_{zlp} are defined as the areas under the full width at half-maximum (FWMH) of the Lorentzian fit signal, filled region in Figure 4.12b, and under the ZLP in the same ΔE region, respectively. In other words, s_g measures the significance of the energy-gain peak in units of the ZLP background. Figure 4.13c displays a spatially-resolved map of s_g across the specimen. The region of enhanced intensity reported in Figure 4.13a and associated to the specimen edge corresponds to the highest values of s_g in Figure 4.13c, reaching up to a factor two. This high significance confirms that the observe intensity enhancement in the gain region is a genuine feature of the data rather than an artefact of the ZLP removal procedure.

It is also interesting to compare the features of the approximately symmetric peaks appearing in the energy-gain and energy-loss regions, whose values E_g and E_ℓ respectively are mapped across the specimen in Figure C.8 of the Supporting Information. One observes in general a stronger intensity of the energy-gain peak as compared to its energy-loss counterpart. To quantify this observation and to compare their relative intensities, we display in Figure 4.13d the ratio A_g / A_ℓ of the areas under the FWHM of the energy-gain Lorentzian fit to that of the energy-loss peak. The vacuum region is masked out to facilitate readability. As can be seen, in the bulk of the sample the ratio A_g / A_ℓ is of the order unity, whereas in the edge region of the specimen the ratio reaches a factor of around 4. The latter result indicates that surface and edge effects enhance the relative intensity of the energy-gain peak. The combination Figures 4.12 and 4.13 demonstrates the presence of a well-defined, significant energy-gain peak in Bi_2Te_3 located around $E_g \simeq -0.9$ eV whose intensity is enhanced in the edge regions of the specimen close to the boundary.

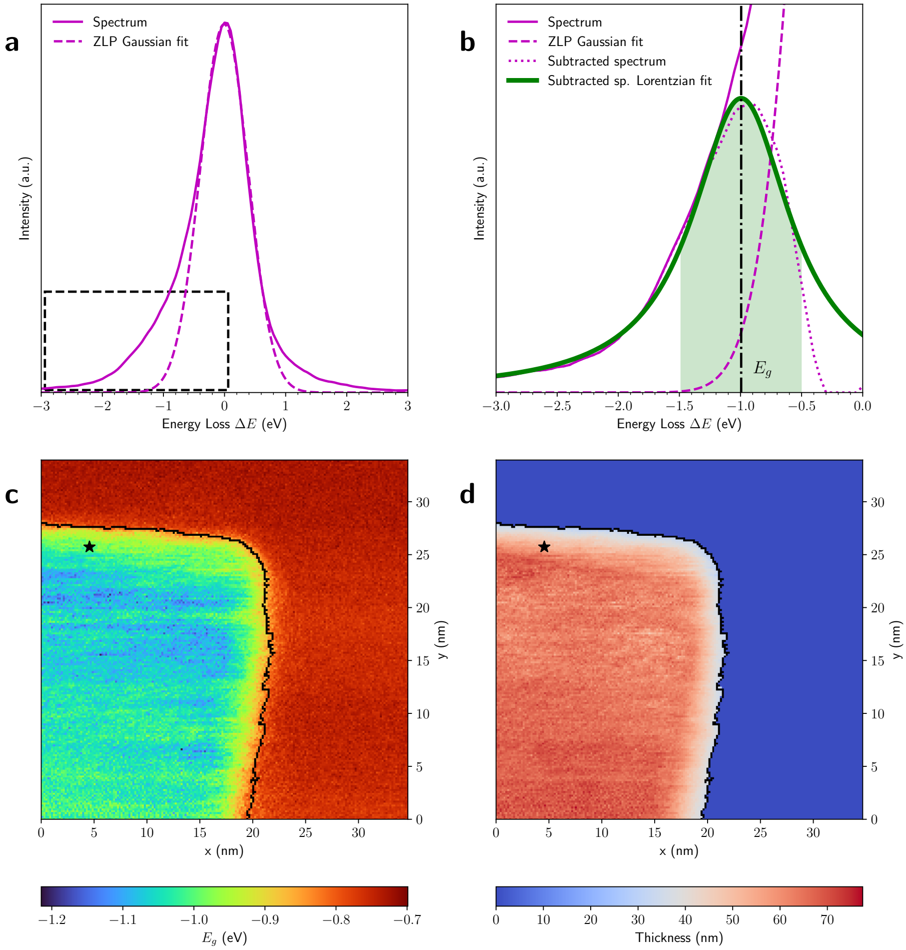

Figure 4.12: **Energy-gain peak identification in Bi_2Te_3.** **(a)** The EEL spectrum (solid) in the pixel indicated with a star in Figure 4.11c together with the corresponding fit to the ZLP (dashed curve). **(b)** Close-up of the dashed rectangle in (a), now adding the Lorentzian fit (thick solid line) to the subtracted spectrum (dotted line). The vertical line indicates the mean of the Lorentzian energy-gain peak E_g, while the filled region indicates the corresponding FWHM. **(c)** Spatially-resolved map displaying the location of the energy-gain peak E_g, determined following the procedure of (b) across the whole spectral image of Figure 4.11c. **(d)** Same as (c) now for the local specimen thickness. The dark blue region beyond the specimen edge corresponds to the vacuum region of the spectral image.

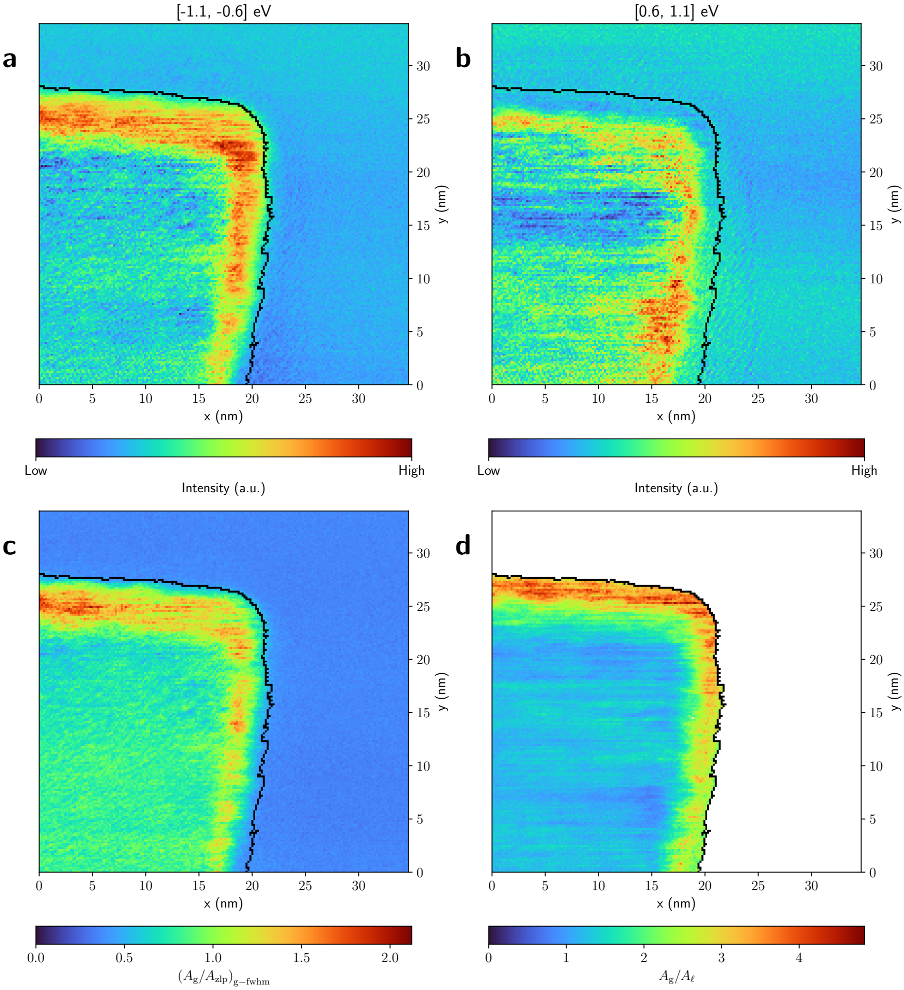

Figure 4.13: **Spatially-resolved characterisation of energy-gain peaks.** **(a)** Same as Figure 4.11c, now with the intensity of the EEL spectra (after ZLP subtraction) integrated in the window $[-1.1, -0.6]$ eV where the gain peak identified in Figure 4.12c is located. **(b)** Same as **(a)** for the mirrored energy-loss window, $[0.6, 1.1]$ eV. **(c)** Spatially-resolved map of the ratio s_g, Equation (4.3), defined as the area under the FWHM of the Lorentzian fit to the energy-gain peak, filled region in Figure 4.12b, to the area under the ZLP in the same ΔE window. **(d)** Ratio of the area A_g under the FWHM of the Lorentzian fit to the energy-gain peak to its counterpart A_ℓ in the loss region, where the vacuum region is masked out for clarity.

4.3.4. UNCERTAINTY PROPAGATION IN EEGS

A potential limitation of this analysis concerns the lack of a systematic estimate of the functional uncertainties associated to the ZLP modelling and its subsequent subtraction from the EELS spectral image. To this purpose, we deploy the Monte Carlo replica method for error propagation, originally developed for proton structure studies in high-energy physics [62]–[66] and then extended to deep learning models of the ZLP within the EELSFITTER framework. [18], [19] First, one applies K-means clustering to the EELS spectral image with the similarity measure being the area under the three bins of the EELS intensity around $\Delta E = 0$, which operates as a proxy for the local thickness map of Figure 4.12d. This procedure results in the 20 clusters shown in Figure 4.14a, each of them composed by pixels with similar thickness. Within each cluster, the EELS intensities are assumed to be sampled from the same underlying distribution, and N_{rep} spectra ("replicas") are randomly selected from each cluster. By fitting a separate ZLP model to each replica, one ends up with a sampling of N_{rep} models of the ZLP which can be used to estimate uncertainties and propagate them to the subtracted spectra and the subsequent Lorentzian fits.

Figure 4.14b displays the same ZLP-subtracted spectrum as in Figure 4.12b now with the Monte Carlo replica method used to estimate ZLP model uncertainties. For the ZLP fit, the subtracted spectrum, and the Lorentzian fit to the latter the bands indicate the 68% confidence level (CL) intervals evaluated over the N_{rep} replicas. By repeating this approach in all clusters, we calculate the area ratio s_g defined in Equation (4.3) for all pixels in the spectral image using the replicas to propagate uncertainties. This results in lower and upper bounds of the 68% confidence interval of the area ratio shown in Figure 4.14c and d respectively. The corresponding map of the median of s_g is consistent with that reported in Figure 4.13c and shown in Figure 4.15 in the Supplementary Material. Given that a good significance (above unity) of the energy-gain peak is still observed in the map of the lower limit of the 68% CL interval for the relevant edge region, one can conclude that the results of this work are not distorted by unaccounted-for methodological or procedural uncertainties.

To confirm the reproducibility of our findings, we have performed additional measurements on a different Bi_2Te_3 specimen characterised by the same crystal structure and with comparable features as the one discussed here. The resulting analysis is summarised in Section C.2.5 of the Supplementary Material and reveals the same qualitative features in the energy-gain region, namely a well-defined, narrow peak at energy gains around −0.7 eV whose intensity is enhanced in edge and surface regions and whose significance reaches values of $s_g \sim 4$. The lower and upper 68% confidence level intervals computed on the ratio between the area within the FWHM of the gain peak and that of the ZLP in the same ΔE region, estimated from the spread of the Monte Carlo replicas, were already showed in the bottom panels of Figure 4.14. In Figure 4.15, for completeness, we also report on the corresponding spatially-resolved map for the median of this 68% CL interval. The qualitative agreement between panels a-c of Figure 4.15 indicate that uncertainties associated to the ZLP modelling and substraction procedure are moderate and do not distort the main results obtained in this work.

This independent analysis further confirms the robustness of our results, in particular the strong correlation between the enhanced intensity of the energy-gain peak lo-

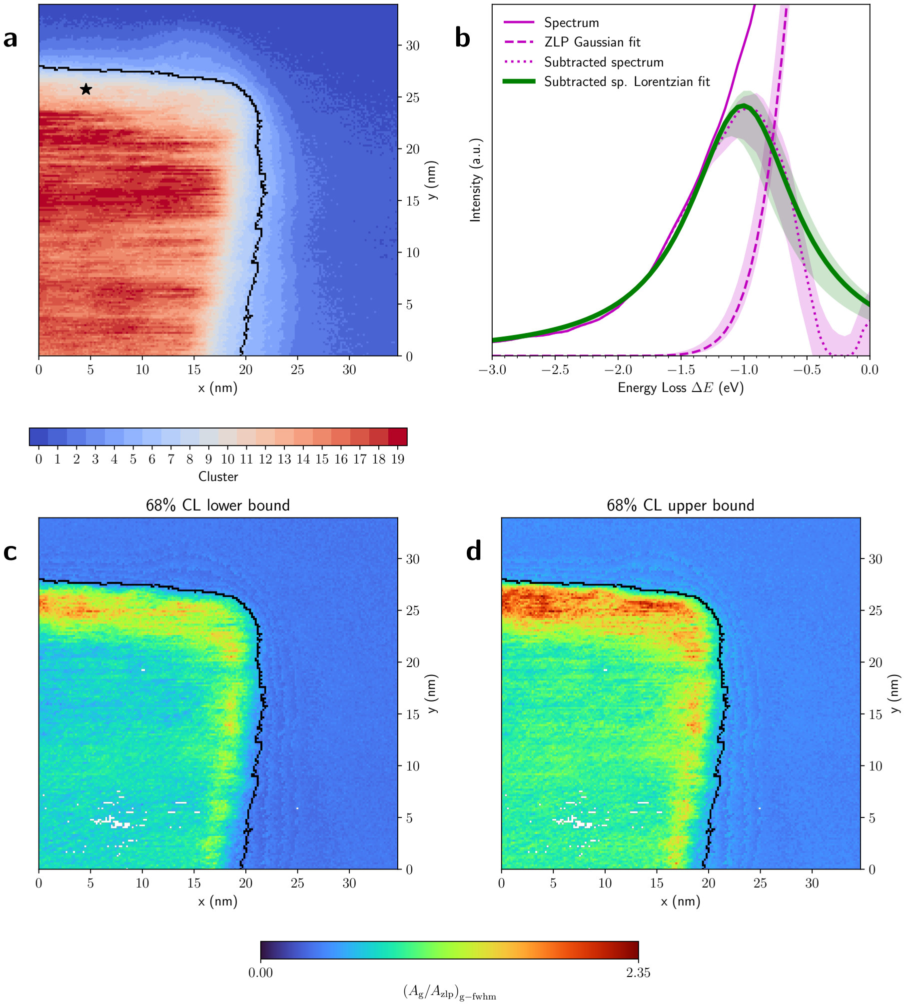

Figure 4.14: **Energy-gain peak characterisation with the Monte Carlo replica method.** **(a)** The EELS spectral image of Fig. 4.11**c** classified into 20 clusters, each of them composed by pixels with similar thickness. **(b)** Same as Fig. 4.12**b** now using the Monte Carlo replica method to estimate and propagate the ZLP fitting model uncertainties. For the ZLP Gaussian fit, the subtracted spectrum, and the Lorentzian fit to the latter we display both the median over replicas and the 68% CL intervals. **(c,d)** Same as Fig. 4.13**c** now the lower and upper ranges respectively, of the 68% CL interval for the area ratio evaluated over the Monte Carlo replicas. See Fig. 4.15 in the Supplementary Material for the corresponding median map.

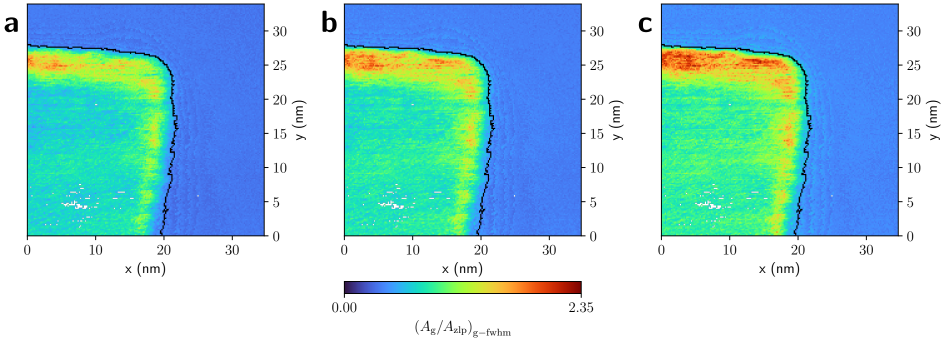

Figure 4.15: Spatially-resolved map of the lower 68% CL bound (**a**), median (**b**), and upper 68% CL bound (**c**) of the ratio between the area within the FWHM of the gain peak and that of the ZLP in the same ΔE region, estimated from the spread of the Monte Carlo replicas. The lower and upper bounds were already showed in the bottom panels of Fig. 4.14 and are repeated here for completeness.

cated around $[-0.9,-0.7]$ eV and specimen regions displayed sharp thickness variations including edges and surfaces.

It is beyond our scope to identify the underlying physical phenomena leading to the observed edge- and surface-induced energy-gain peaks in Bi_2Te_3. Several mechanisms have been explored leading to resonance signatures in the ΔE region relevant for our results, such as wedge Dyakonov waves [67] and edge- and surface-located Dirac-plasmons in the closely related TI material Bi_2Se_3. One can in any case exclude thermal effects associated to a Bose-Einstein distribution, given that states with ~ 1 eV have a very low occupation probability at room temperatures. Disentangling the specific mechanisms explaining our observations requires dedicated theoretical simulations mapping the EELS response of Bi_2Te_3 with different structural and geometric configurations and is left for future work.

4.3.5. CONCLUSIONS

In this work we have presented a systematic, spatially-resolved investigation of the energy-gain region of EELS spectral images acquired on Bi_2Te_3 specimens. The main motivation was to avoid the inelastic continuum that pollutes the energy-loss region, which may prevent identifying exotic phenomena appearing at ΔE values below a few eV. An automated peak-identification procedure identifies a narrow feature located around $\Delta E \sim -0.8$ eV whose intensity and significance are strongly enhanced in regions characterised by sharp thickness variations, such as surfaces and edges. We assess the role of methodological uncertainties associated to e.g. the ZLP subtraction procedure and find that our results are robust against them. The observed resonance could be the signature of edge- and surface-plasmons such as those reported in Bi_2Se_3, thought dedicated simulations would be required to unambiguously ascertain its origin.

4.4. SUMMARY AND OUTLOOK

The goal of the two case studies presented in this chapter was to detect, quantify and spatially resolve the peaks present in EELS data and do this in an automated manner. As energy resolution improves, peaks become more defined and the necessity of peak tracking will increase in importance. While here we focus on 1D-MoS_2 and Bi_2Te_3 as a proof-of-concepts for these approaches, our approach for ZLP subtraction and peak tracking is fully general and can be deployed to any specimen for which EELS-SI measurements are acquired.

Our approach is made available in the new release of the EELSFITTER framework and hence can be straightforwardly used by other researchers aiming to explore the information contained in the energy-gain region of EELS-SI to identify, model, and correlate localised collective excitations in nanostructured materials. Possible future improvements include the extension to multiple gain-peaks deconvolution and the improved modelling of the loss region describing the inelastic continuum background. All in all, our findings illustrate the powerful reach of energy-loss & gain EELS to accurately map and characterise the signatures of collective excitations and other exotic resonances arising in quantum materials.

REFERENCES

[1] P. H. López, S. Heeg, C. Schattauer, *et al.*, "Strain control of hybridization between dark and localized excitons in a 2d semiconductor", *Nature Communications*, vol. 13, 1 Dec. 2022, ISSN: 20411723. DOI: 10.1038/s41467-022-35352-9.

[2] S. Zhang, C.-G. Wang, M.-Y. Li, *et al.*, "Defect Structure of Localized Excitons in a WSe2 Monolayer", *Phys. Rev. Lett.*, vol. 119, no. 4, p. 046 101, 2017. DOI: 10.1103/PhysRevLett.119.046101.

[3] Y. J. Zheng, Y. Chen, Y. L. Huang, *et al.*, "Point Defects and Localized Excitons in 2D WSe2", *ACS Nano*, 2019. DOI: 10.1021/acsnano.9b02316.

[4] H. Li, A. W. Contryman, X. Qian, *et al.*, "Optoelectronic crystal of artificial atoms in strain-textured molybdenum disulphide", *Nat. Commun.*, vol. 6, no. 1, pp. 1–7, 2015, ISSN: 2041-1723. DOI: 10.1038/ncomms8381.

[5] T. P. Darlington, C. Carmesin, M. Florian, *et al.*, "Imaging strain-localized excitons in nanoscale bubbles of monolayer WSe2 at room temperature", *Nat. Nanotechnol.*, vol. 15, no. 10, pp. 854–860, 2020, ISSN: 1748-3395. DOI: 10.1038/s41565-020-0730-5.

[6] C. Chakraborty, L. Kinnischtzke, K. M. Goodfellow, R. Beams, and A. N. Vamivakas, "Voltage-controlled quantum light from an atomically thin semiconductor", *Nat. Nanotechnol.*, vol. 10, no. 6, pp. 507–511, 2015, ISSN: 1748-3395. DOI: 10.1038/nnano.2015.79.

[7] M. Zhao, M. Bosman, M. Danesh, *et al.*, "Visible surface plasmon modes in single bi2te3 nanoplate", *Nano Letters*, vol. 15, pp. 8331–8335, 12 Dec. 2015, ISSN: 15306992. DOI: 10.1021/acs.nanolett.5b03966.

[8] T. J. Whitcher, M. G. Silly, M. Yang, *et al.*, "Correlated plasmons in the topological insulator bi2se3 induced by long-range electron correlations", *NPG Asia Materials*, vol. 12, 1 Dec. 2020, ISSN: 18844057. DOI: 10.1038/s41427-020-0218-7.

[9] M. W. Chu, V. Myroshnychenko, C. H. Chen, J. P. Deng, C. Y. Niou, and F. J. G. D. Abajo, "Probing bright and dark surface-plasmon modes in Individual and coupled noble metal nanoparticles using an electron beam", *Nano Letters*, vol. 9, pp. 399–404, 1 Jan. 2009, ISSN: 15306984. DOI: 10.1021/nl803270x.

[10] F. J. García de Abajo, "Optical excitations in electron microscopy", *Rev. Mod. Phys.*, vol. 82, pp. 209–275, 1 Feb. 2010. DOI: 10.1103/RevModPhys.82.209.

[11] V. Myroshnychenko, J. Nelayah, G. Adamo, *et al.*, "Plasmon spectroscopy and imaging of individual gold nanodecahedra: A combined optical microscopy, cathodoluminescence, and electron energy-loss spectroscopy study", *Nano Letters*, vol. 12, pp. 4172–4180, 8 Aug. 2012, ISSN: 15306984. DOI: 10.1021/nl301742h.

[12] T. Coenen, D. T. Schoen, S. A. Mann, *et al.*, "Nanoscale spatial coherent control over the modal excitation of a coupled plasmonic resonator system", *Nano Letters*, vol. 15, pp. 7666–7670, 11 Nov. 2015, ISSN: 15306992. DOI: 10.1021/acs.nanolett.5b03614.

[13] H. C. Nerl, K. T. Winther, F. S. Hage, *et al.*, "Probing the local nature of excitons and plasmons in few-layer mos2", *npj 2D Materials and Applications*, vol. 1, 1 Dec. 2017, ISSN: 23977132. DOI: 10.1038/s41699-017-0003-9.

[14] M. J. Lagos, A. Trügler, U. Hohenester, and P. E. Batson, "Mapping vibrational surface and bulk modes in a single nanocube", *Nature*, vol. 543, pp. 529–532, 7646 Mar. 2017, ISSN: 14764687. DOI: 10.1038/nature21699.

[15] A. B. Yankovich, B. Munkhbat, D. G. Baranov, *et al.*, "Visualizing spatial variations of plasmon-exciton polaritons at the nanoscale using electron microscopy", *Nano Letters*, vol. 19, pp. 8171–8181, 11 Nov. 2019, ISSN: 15306992. DOI: 10.1021/acs.nanolett.9b03534.

[16] P. E. Batson, N. Dellby, and O. L. Krivanek, "Sub-aångstrom resolution using aberration corrected electron optics", *Nature*, vol. 418, pp. 617–620, 6898 Aug. 2002, ISSN: 00280836. DOI: 10.1038/nature00972.

[17] M. Mukai, S. Morishita, H. Sawada, and K. Suenaga, "Performances of aberration-corrected monochromatic low-voltage analytical electron microscope", in *European Microscopy Congress 2016: Proceedings*. John Wiley & Sons, Ltd, 2016, pp. 338–339, ISBN: 9783527808465. DOI: https://doi.org/10.1002/9783527808465.EMC2016.6063.

[18] L. I. Roest, S. E. van Heijst, L. Maduro, J. Rojo, and S. Conesa-Boj, "Charting the low-loss region in electron energy loss spectroscopy with machine learning", *Ultramicroscopy*, vol. 222, p. 113 202, 2021, ISSN: 0304-3991. DOI: https://doi.org/10.1016/j.ultramic.2021.113202.

[19] A. Brokkelkamp, J. T. Hoeve, I. Postmes, *et al.*, "Spatially resolved band gap and dielectric function in two-dimensional materials from electron energy loss spectroscopy", *Journal of Physical Chemistry A*, vol. 126, pp. 1255–1262, 7 Feb. 2022, ISSN: 15205215. DOI: 10.1021/acs.jpca.1c09566.

[20] M. Bolhuis, J. Hernandez-Rueda, S. E. V. Heijst, M. T. Rivas, L. Kuipers, and S. Conesa-Boj, "Vertically-oriented mos2 nanosheets for nonlinear optical devices", *Nanoscale*, vol. 12, pp. 10 491–10 497, 19 May 2020, ISSN: 20403372. DOI: 10.1039/d0nr00755b.

[21] M. Tinoco, L. Maduro, and S. Conesa-Boj, "Metallic edge states in zig-zag vertically-oriented mos2 nanowalls", *Scientific Reports*, vol. 9, 1 Dec. 2019, ISSN: 20452322. DOI: 10.1038/s41598-019-52119-3.

[22] B. Yue, F. Hong, K.-D. Tsuei, *et al.*, "High-energy electronic excitations in a bulk MoS_2 single crystal", *Phys. Rev. B*, vol. 96, no. 12, p. 125 118, 2017, ISSN: 2469-9969. DOI: 10.1103/PhysRevB.96.125118.

[23] L. Martin, R. Mamy, A. Couget, and C. Raisin, "Optical Properties and Collective Excitations in MoS2 and NbSe2 in the 1.7 to 30 eV Range", *Phys. Status Solidi B*, vol. 58, no. 2, pp. 623–627, 1973, ISSN: 0370-1972. DOI: 10.1002/pssb.2220580223.

[24] K. Zeppenfeld, "Electron energy losses and optical anisotropy of MoS2 single crystals", *Opt. Commun.*, vol. 1, no. 8, pp. 377–378, 1970, ISSN: 0030-4018. DOI: 10.1016/0030-4018(70)90074-X.

[25] W. Y. Liang and S. L. Cundy, "Electron energy loss studies of the transition metal dichalcogenides", *Philosophical Magazine: A Journal of Theoretical Experimental and Applied Physics*, vol. 19, no. 161, pp. 1031–1043, 1969, ISSN: 0031-8086. DOI: 10.1080/14786436908225867.

[26] A. Splendiani, L. Sun, Y. Zhang, *et al.*, "Emerging photoluminescence in monolayer mos2", *Nano Letters*, vol. 10, pp. 1271–1275, 4 Apr. 2010, ISSN: 15306984. DOI: 10.1021/nl903868w.

[27] J. Rouvière and E. Sarigiannidou, "Theoretical discussions on the geometrical phase analysis", *Ultramicroscopy*, vol. 106, no. 1, pp. 1–17, 2005, ISSN: 0304-3991. DOI: https://doi.org/10.1016/j.ultramic.2005.06.001.

[28] M. Tinoco, L. Maduro, M. Masaki, E. Okunishi, and S. Conesa-Boj, "Strain-dependent edge structures in mos2 layers", *Nano Letters*, vol. 17, pp. 7021–7026, 11 Nov. 2017, ISSN: 15306992. DOI: 10.1021/acs.nanolett.7b03627.

[29] A. P. Rooney, Z. Li, W. Zhao, *et al.*, "Anomalous twin boundaries in two dimensional materials", *Nature Communications*, vol. 9, 1 Dec. 2018, ISSN: 20411723. DOI: 10.1038/s41467-018-06074-8.

[30] N. Grobert, M. Mayne, M. Terrones, *et al.*, "Metal and alloy nanowires: Iron and invar inside carbon nanotubes", *AIP Conference Proceedings*, vol. 591, no. 1, pp. 287–290, Nov. 2001, ISSN: 0094-243X. DOI: 10.1063/1.1426872.

[31] J. Sloan, J. L. Hutchison, R. Tenne, Y. Feldman, T. Tsirlina, and M. Homyonfer, "Defect and ordered tungsten oxides encapsulated inside 2h–wx2(x=s and se) fullerene-related structures", *Journal of Solid State Chemistry*, vol. 144, no. 1, pp. 100–117, 1999, ISSN: 0022-4596. DOI: https://doi.org/10.1006/jssc.1998.8125.

[32] A. Molina-Sánchez, D. Sangalli, K. Hummer, A. Marini, and L. Wirtz, "Effect of spin-orbit interaction on the optical spectra of single-layer, double-layer, and bulk MoS_2", *Phys. Rev. B*, vol. 88, no. 4, p. 045 412, 2013, ISSN: 2469-9969. DOI: 10.1103/PhysRevB.88.045412.

[33] L. H. G. Tizei, Y.-C. Lin, M. Mukai, *et al.*, "Exciton Mapping at Subwavelength Scales in Two-Dimensional Materials", *Phys. Rev. Lett.*, vol. 114, no. 10, p. 107 601, 2015, ISSN: 1079-7114. DOI: 10.1103/PhysRevLett.114.107601.

[34] X. Sui, H. Wang, C. Liang, *et al.*, "Ultrafast Internal Exciton Dissociation through Edge States in MoS2 Nanosheets with Diffusion Blocking", *Nano Lett.*, vol. 22, no. 14, pp. 5651–5658, 2022, ISSN: 1530-6984. DOI: 10.1021/acs.nanolett.1c04987.

[35] X. Hong, J. Kim, S.-F. Shi, *et al.*, "Ultrafast charge transfer in atomically thin MoS2/WS2 heterostructures", *Nat. Nanotechnol.*, vol. 9, no. 9, pp. 682–686, 2014, ISSN: 1748-3395. DOI: 10.1038/nnano.2014.167.

[36] K. K. Kam and B. A. Parkinson, "Detailed photocurrent spectroscopy of the semiconducting group VIB transition metal dichalcogenides", *J. Phys. Chem.*, vol. 86, no. 4, pp. 463–467, 1982, ISSN: 0022-3654. DOI: 10.1021/j100393a010.

[37] J. Gusakova, X. Wang, L. L. Shiau, *et al.*, "Electronic Properties of Bulk and Monolayer TMDs: Theoretical Study Within DFT Framework (GVJ-2e Method)", *Phys. Status Solidi A*, vol. 214, no. 12, p. 1 700 218, 2017, ISSN: 1862-6300. DOI: 10.1002/pssa.201700218.

[38] Z. Peng, X. Chen, Y. Fan, D. J. Srolovitz, and D. Lei, "Strain engineering of 2D semiconductors and graphene: from strain fields to band-structure tuning and photonic applications", *Light Sci. Appl.*, vol. 9, no. 190, pp. 1–25, 2020, ISSN: 20477538. DOI: 10.1038/s41377-020-00421-5.

[39] H. J. Conley, B. Wang, J. I. Ziegler, R. F. Haglund, S. T. Pantelides, and K. I. Bolotin, "Bandgap engineering of strained monolayer and bilayer mos2", *Nano Letters*, vol. 13, pp. 3626–3630, 8 Aug. 2013, ISSN: 15306984. DOI: 10.1021/nl4014748.

[40] S. Pak, J. Lee, Y.-W. Lee, *et al.*, "Strain-Mediated Interlayer Coupling Effects on the Excitonic Behaviors in an Epitaxially Grown MoS_2/WS_2 van der Waals Heterobilayer", *Nano Lett.*, vol. 17, no. 9, pp. 5634–5640, 2017, ISSN: 1530-6984. DOI: 10.1021/acs.nanolett.7b02513.

[41] H. Zhang, C.-X. Liu, X.-L. Qi, X. Dai, Z. Fang, and S.-C. Zhang, "Topological insulators in Bi2Se3, Bi2Te3 and Sb2Te3 with a single Dirac cone on the surface", *Nat. Phys.*, vol. 5, no. 6, pp. 438–442, 2009, ISSN: 1745-2481. DOI: 10.1038/nphys1270.

[42] Y. Xia, D. Qian, D. Hsieh, *et al.*, "Observation of a large-gap topological-insulator class with a single Dirac cone on the surface", *Nat. Phys.*, vol. 5, no. 6, pp. 398–402, 2009, ISSN: 1745-2481. DOI: 10.1038/nphys1274.

[43] D. Hsieh, Y. Xia, D. Qian, *et al.*, "Observation of Time-Reversal-Protected Single-Dirac-Cone Topological-Insulator States in Bi_2Te_3 and Sb_2Te_3", *Phys. Rev. Lett.*, vol. 103, no. 14, p. 146 401, 2009, ISSN: 1079-7114. DOI: 10.1103/PhysRevLett.103.146401.

[44] A. N. Grigorenko, M. Polini, and K. S. Novoselov, "Graphene plasmonics", *Nature Photonics*, vol. 6, pp. 749–758, 11 Nov. 2012, ISSN: 17494885. DOI: 10.1038/nphoton.2012.262.

[45] P. D. Pietro, M. Ortolani, O. Limaj, *et al.*, "Observation of dirac plasmons in a topological insulator", *Nature Nanotechnology*, vol. 8, pp. 556–560, 8 2013, ISSN: 17483395. DOI: 10.1038/nnano.2013.134.

[46] M. Autore, F. D'Apuzzo, A. Di Gaspare, *et al.*, "Plasmon–phonon interactions in topological insulator microrings", *Advanced Optical Materials*, vol. 3, no. 9, pp. 1257–1263, 2015. DOI: https://doi.org/10.1002/adom.201400513.

[47] J. Yin, H. N. Krishnamoorthy, G. Adamo, *et al.*, "Plasmonics of topological insulators at optical frequencies", *NPG Asia Materials*, vol. 9, 8 2017, ISSN: 18844057. DOI: 10.1038/AM.2017.149.

[48] F. Giorgianni, E. Chiadroni, A. Rovere, *et al.*, "Strong nonlinear terahertz response induced by dirac surface states in bi2se3 topological insulator", *Nature communications*, vol. 7, no. 1, p. 11 421, 2016. DOI: https://doi.org/10.1038/ncomms11421.

[49] A. Kitaev and J. Preskill, "Topological Entanglement Entropy", *Phys. Rev. Lett.*, vol. 96, p. 110 404, 11 Mar. 2006. DOI: 10.1103/PhysRevLett.96.110404. [Online]. Available: https://link.aps.org/doi/10.1103/PhysRevLett.96.110404.

[50] L. Fu and C. L. Kane, "Superconducting Proximity Effect and Majorana Fermions at the Surface of a Topological Insulator", *Phys. Rev. Lett.*, vol. 100, no. 9, p. 096 407, 2008, ISSN: 1079-7114. DOI: 10.1103/PhysRevLett.100.096407.

[51] X. Zhang, J. Wang, and S.-C. Zhang, "Topological insulators for high-performance terahertz to infrared applications", *Phys. Rev. B*, vol. 82, p. 245 107, 24 Dec. 2010. DOI: https://doi.org/10.1103/PhysRevB.82.245107.

[52] Y. L. Chen, J. G. Analytis, J.-H. Chu, *et al.*, "Experimental Realization of a Three-Dimensional Topological Insulator, Bi2Te3", *Science*, vol. 325, no. 5937, pp. 178–181, 2009. DOI: 10.1126/science.1173034.

[53] H. Boersch, J. Geiger, and W. Stickel, "Interaction of 25-kev electrons with lattice vibrations in lif. experimental evidence for surface modes of lattice vibration", *Phys. Rev. Lett.*, vol. 17, pp. 379–381, 7 Aug. 1966. DOI: 10.1103/PhysRevLett.17.379.

[54] A. Asenjo-Garcia and F. J. G. de Abajo, "Plasmon electron energy-gain spectroscopy", *New Journal of Physics*, vol. 15, no. 10, p. 103 021, Oct. 2013. DOI: 10.1088/1367-2630/15/10/103021.

[55] J. C. Idrobo, A. R. Lupini, T. Feng, *et al.*, "Temperature measurement by a nanoscale electron probe using energy gain and loss spectroscopy", *Phys. Rev. Lett.*, vol. 120, p. 095 901, 9 Mar. 2018. DOI: 10.1103/PhysRevLett.120.095901.

[56] N. Peranio, Z. Aabdin, W. Töllner, *et al.*, "Low loss eels and eftem study of bi2te3 based bulk and nanomaterials", *MRS Online Proceedings Library (OPL)*, vol. 1329, mrss11–1329-i10–21, 2011. DOI: 10.1557/opl.2011.1238.

[57] V. Nascimento, V. de Carvalho, R. Paniago, E. Soares, L. Ladeira, and H. Pfannes, "Xps and eels study of the bismuth selenide", *Journal of Electron Spectroscopy and Related Phenomena*, vol. 104, no. 1, pp. 99–107, 1999, ISSN: 0368-2048. DOI: https://doi.org/10.1016/S0368-2048(99)00012-2.

[58] P. Torruella, C. Coll, G. Martín, *et al.*, "Assessing oxygen vacancies in bismuth oxide through eels measurements and dft simulations", *Journal of Physical Chemistry C*, vol. 121, 39 2017, ISSN: 19327455. DOI: 10.1021/acs.jpcc.7b06310.

[59] Y. Li, M. Wen, Y. Wang, G. Tian, C. Wang, and J. Zhao, "Plasmonic hot electrons from oxygen vacancies for infrared light-driven catalytic co2 reduction on bi2o3-x", *Angewandte Chemie International Edition*, vol. 60, no. 2, pp. 910–916, 2021. DOI: https://doi.org/10.1002/anie.202010156.

[60] A. A. Govyadinov, A. Konečná, A. Chuvilin, *et al.*, "Probing low-energy hyperbolic polaritons in van der waals crystals with an electron microscope", *Nature Communications*, vol. 8, 1 Dec. 2017, ISSN: 20411723. DOI: 10.1038/s41467-017-00056-y.

[61] S. E. van Heijst, M. Mukai, E. Okunishi, *et al.*, "Illuminating the electronic properties of ws2 polytypism with electron microscopy", *Annalen der Physik*, vol. 533, 3 Mar. 2021, ISSN: 15213889. DOI: 10.1002/andp.202000499.

[62] G. Watt and R. S. Thorne, "Study of Monte Carlo approach to experimental uncertainty propagation with MSTW 2008 PDFs", *J. High Energy Phys.*, vol. 2012, no. 8, pp. 52–38, 2012, ISSN: 1029-8479. DOI: 10.1007/JHEP08(2012)052.

[63] The NNPDF Collaboration, L. D. Debbio, S. Forte, J. I. Latorre, A. Piccione, and J. Rojo, "Neural network determination of parton distributions: The nonsinglet case", *Journal of High Energy Physics*, vol. 2007, no. 03, p. 039, 2007. DOI: 10.1088/1126-6708/2007/03/039.

[64] R. D. Ball *et al.*, "Parton distributions for the LHC Run II", *JHEP*, vol. 04, p. 040, 2015. DOI: 10.1007/JHEP04(2015)040.

[65] N. P. Hartland, F. Maltoni, E. R. Nocera, *et al.*, "A Monte Carlo global analysis of the Standard Model Effective Field Theory: the top quark sector", *JHEP*, vol. 04, p. 100, 2019. DOI: 10.1007/JHEP04(2019)100. arXiv: 1901.05965 [hep-ph].

[66] A. Candido, A. Garcia, G. Magni, T. Rabemananjara, J. Rojo, and R. Stegeman, "Neutrino Structure Functions from GeV to EeV Energies", *JHEP*, vol. 05, p. 149, 2023. DOI: 10.1007/JHEP05(2023)149. arXiv: 2302.08527 [hep-ph].

[67] N. Talebi, C. Ozsoy-Keskinbora, H. M. Benia, K. Kern, C. T. Koch, and P. A. V. Aken, "Wedge dyakonov waves and dyakonov plasmons in topological insulator bi2se3 probed by electron beams", *ACS Nano*, vol. 10, pp. 6988–6994, 7 Jul. 2016, ISSN: 1936086X. DOI: 10.1021/acsnano.6b02968.

5

EDGE-LOCALISED PLASMONIC RESONANCES IN WS_2 NANOSTRUCTURES FROM ELECTRON ENERGY-LOSS SPECTROSCOPY

Localised plasmon resonances in two-dimensional (2D) transition metal dichalcogenides (TMDs) offer a powerful means to enhance light-matter interactions at the nanoscale, making them ideal candidates for advanced optoelectronic applications. However, disentangling the complex plasmonic interactions in these materials, especially in the low energy regime, presents significant challenges. In this work, we investigate localised plasmon resonances in chemical vapour deposition (CVD)-grown tungsten disulfide (WS_2) nanotriangles, using a combination of advanced spectral analysis and simulation techniques. By combining Non-Negative Matrix Factorization (NMF) with Electron Energy Loss Spectroscopy (EELS), we identify and characterise distinct plasmonic modes to provide a comprehensive analysis of the plasmonic landscape of individual and stacked WS_2 nanotriangles. Furthermore, we quantify the dispersion relation of these localised plasmon resonances and demonstrate their evolution across different WS_2 triangular geometries. We validate our experimental characterisation of plasmonic resonances in WS_2 through dedicated numerical simulations based on the PYGDM *package.. Our findings highlight the critical role of localised plasmon resonances in modulating the electronic and optical properties of WS_2, offering new insights into the design and optimisation of TMD-based devices for optoelectronic and nanophotonic applications.*

Parts of this chapter have been published in Small Science : **A. Brokkelkamp**, S. E. van Heijst, S. Conesa-Boj, Small Science, 2400558 (2025)

5.1. INTRODUCTION

Two-dimensional (2D) transition metal dichalcogenides (TMDs) have emerged as a versatile family of materials with extraordinary optoelectronic properties [1]–[5], positioning them at the forefront of nanoscale device research. Among TMDs, tungsten disulfide (WS_2) stands out due to its direct bandgap and strong excitonic effects [5]–[9], making it highly attractive for applications in light harvesting [10]–[12], sensing [13]–[15], and quantum optics [16]–[18]. However, while excitonic behaviour of WS_2 has been extensively studied, its plasmonic properties, particularly in the low-energy regime, remain less explored.

Specifically, spatially-localised plasmon resonances in 2D materials have garnered increasing interest due to their ability to confine electromagnetic fields at the nanoscale, hence enabling enhanced light-matter interactions [19]–[22]. In WS_2 nanostructures, the geometric arrangement, thickness, and edge configurations play critical roles in determining the plasmonic response, which can be tuned to optimize device performance. The ability to precisely characterise these localised plasmonic modes at the nanoscale is key to harnessing them for applications in optoelectronics and nanophotonics [23], [24].

To this aim, electron energy-loss spectroscopy (EELS) provides a powerful technique for probing localised plasmonic excitations [25]–[27], uniquely combining high spatial precision with competitive energy resolution [28]. In particular, EELS enables a detailed characterisation of the low-loss region ($\Delta E \leq 50$ eV) where multiple plasmonic and excitonic resonances are expected. The main challenge here lies in the interpretation of the complex spectral data, where overlapping signals make it difficult to cleanly disentangle localised plasmon resonances in dielectrics [29] and fully resolving the individual modes. Tackling these challenges requires advancements in data analysis techniques, such as non-negative matrix factorization (NMF), which have shown considerable promise in separating overlapping spectral features [30]–[32] and unveiling hidden plasmonic resonances.

Here, we report the identification of localised plasmonic modes in WS_2 nanostructures using a combination of advanced EELS and NMF analyses. By applying NMF to low-loss EELS data, we disentangle the distinct localised plasmonic components arising across various WS_2 triangular geometries. To further validate our findings, we demonstrate the agreement of the experimental results with dedicated electrodynamical simulations. These numerical simulations confirm the features of the extracted localised plasmonic modes, and provide complementary insights on their spatial and spectral evolution.

Our results pave the way for the enhanced design of WS_2-based devices, where the precise control over the performance of localised plasmonic resonances leads to improved functionalities in next-generation optoelectronic and nanophotonic technologies.

5.2. RESULTS AND DISCUSSION

The WS_2 nanostructures investigated in this work were synthesized using chemical vapour deposition (CVD) and directly grown on a 5 nm thick Si_3N_4 membrane. This process yielded well-defined triangular WS_2 morphologies, with side lengths ranging from 330 nm

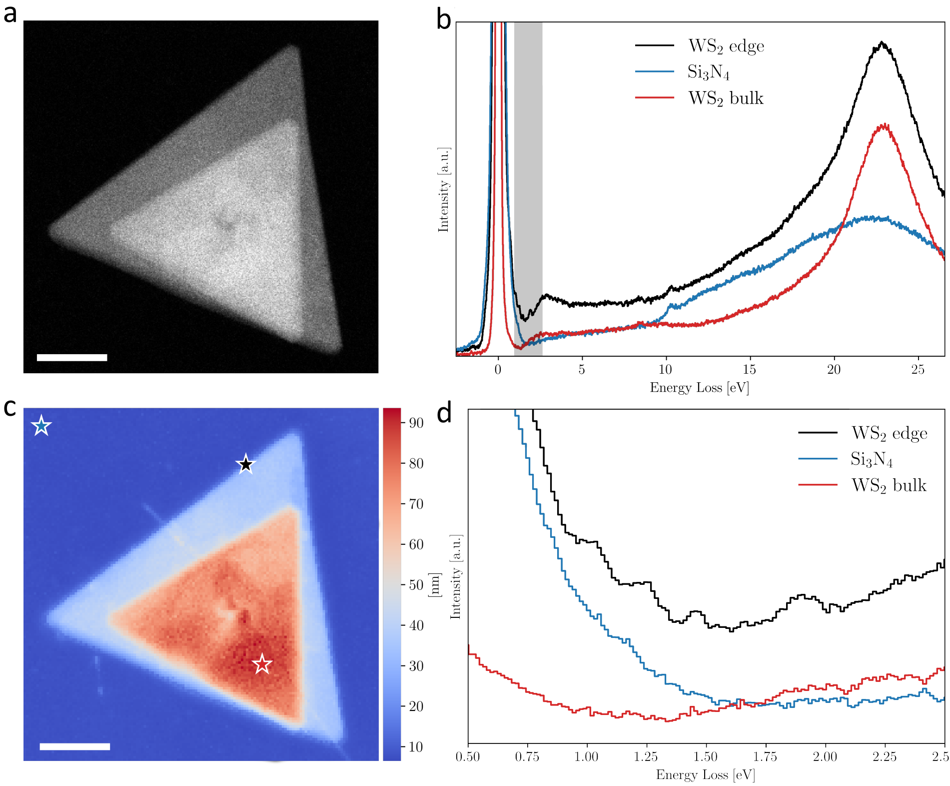

Figure 5.1: **Characterization of the stacked WS$_2$ nanotriangles.** **(a)** High-angle annular dark field (HAADF) scanning transmission electron microscopy (STEM) image of the stacked WS$_2$ nanotriangles, revealing their morphology and relative arrangement. **(c)** The associated thickness map obtained from the EELS spectral image. Scale bars indicate 200 nm. **(b)** Averaged EEL spectra taken from the three regions highlighted in (c): WS$_2$ edge, WS$_2$ bulk, and Si$_3$N$_4$ substrate. The shaded area indicates the energy range between 0.5 eV and 2.5 eV. **(d)** Close up of the energy range highlighted in (b) and displaying, as will be shown in Fig. 5.2, periodic oscillations corresponding to distinct plasmonic modes.

to 980 nm (see Supplementary Sect. D.1). In addition to single WS_2 nanotriangles, more complex configurations such as the stacked WS_2 nanotriangles shown in Fig. 5.1(a) are also present. In this nanostructure, two misaligned triangles are stacked on top of each other, with the smaller triangle (side lengths 680 nm) rotated by 6° relative to the larger one at the base (side lengths 980 nm).

Both single and stacked WS_2 nanostructures exhibit uniform thicknesses, as verified through scanning transmission electron microscopy (STEM) and electron energy loss spectroscopy (EELS) measurements (see Supplementary Sect. D.1). These nanostructures represent a flexible platform to investigate spatially-localised WS_2 plasmons, with the single triangles providing the baseline and the stacked structures a complementary avenue for exploring novel plasmonic phenomena in WS_2. Detailed information regarding the growth methodology is provided in the Methods section.

Our investigations of the WS_2 specimens focus on the low-loss EELS region, targeting energy losses $\Delta E \leq 50$ eV to uncover plasmonic or excitonic signatures [29], [33]. Representative EEL spectra obtained from the stacked nanotriangles of Fig. 5.1(a) are displayed in Fig. 5.1(b), corresponding to the regions marked by the star-shaped symbols (10 × 10 pixel area average) in the thickness map of Fig. 5.1(c). The chosen regions highlight the bulk WS_2 region, the transition zone at the WS_2 edges, and the surrounding Si_3N_4 membrane.

The spectra for both the bulk WS_2 region and the Si_3N_4 membrane show distinct features characteristic of each material. The Si_3N_4 membrane spectrum displays, as expected, the bulk plasmon peak at 22.3 eV. This Si_3N_4 contribution appears superimposed with the spectrum of WO_3 used for the CVD growth process, which is indicated by the small peak at 10.2 eV and characteristic for oxides [34]. The bulk WS_2 region exhibits a pronounced peak at 23 eV corresponding to the bulk plasmon and a peak at 8 eV associated to the surface plasmon [35], [36].

Interestingly, in the transition region at the WS_2 edges, one finds sizeable new contributions to the spectrum for energy losses between the Zero Loss Peak (ZLP) and the onset of the inelastic scattering continuum. These contributions are highlighted in gray in Fig. 5.1(b) and further amplified in Fig. 5.1(d). This energy window reveals periodic oscillations spanning from 0.5 eV to 2.5 eV, which are absent from the spectra of either bulk WS_2 or Si_3N_4, suggesting the presence of low-energy excitations localised at the WS_2 edges. Given that TMDs such as WS_2 are known to exhibit metallic-like edge states, especially for sharp geometries [12], [37]–[39], these edge regions may provide favourable conditions for the formation of localised plasmon resonances. While surface plasmon resonances are primarily influenced by geometry and refractive index, the presence of metallic edge states in TMDs can enhance plasmonic behaviour by supporting free or quasi-free charge carriers along the edges.

5.2.1. NMF Decomposition of Spectral Features

The recorded WS_2 EELS spectra are composed by a complex mixture of overlapping features. To investigate the physical mechanisms underlying the periodic signals identified in the edge regions of the WS_2 nanotriangles between 0.5 eV to 2.5 eV in Fig. 5.1, we employ two complementary EELS data processing techniques. First, a machine learning approach was deployed [40]–[43] for the model-independent subtraction of the ZLP background contaminating the inelastic scattering onset region, enhancing feature significance for energy losses critical for our analysis (see Supplementary Fig. D.4). Next, non-negative matrix factorization from SCIKIT-LEARN was applied to the ZLP-subtracted EELS spectral image to disentangle and resolve specific features arising for specific energy-loss windows, enabling the interpretability of the individual components to the total low-loss spectra.

NMF is a blind-source separation technique that can efficiently disentangle individual features present in the measured EELS spectra, enabling a refined understanding of the different plasmonic and excitonic resonances in a material. As such, it has found widespread use in EELS analyses of *e.g.* metallic nanostructures [44]–[48]. Similarly to the popular Principal Component Analysis (PCA) method, NMF also ranks the identified components by their statistical significance, starting from the most dominant feature. To reduce statistical noise while preserving spatial resolution, we applied pooling with a 2D Gaussian profile before performing the NMF decomposition to the complete EELS spectral image. Further details about the NMF decomposition of the WS_2 nanostructures are provided in the Supplementary Sect. D.2.1.

Fig. 5.2 displays the result of applying NMF to the EELS spectral image associated to the WS_2 stacked nanotriangles specimen of Fig. 5.1 when restricted to the energy window of interest, namely $[0.5, 2.5]$ eV. The outcome of a NMF decomposition is given by two elements for each components: the endmember, which corresponds to the identified unique spectral feature, and an abundance map, indicating the spatial distribution of the corresponding endmember across the EELS spectral image. In Fig. 5.2 we limit ourselves to the first four components, which represent a cumulative variance of around 98.5% as shown in the Supplementary Fig. D.4(c). Although endmembers are defined as pure signals, in some cases a given component may still reflect a superposition of multiple signals exhibit overlapping features or abundances. In the particular case of dielectric materials, it has been shown that their resonance modes are less defined as compared to their counterparts in metals [29], which can lead to features having a residual contribution to other NMF components beyond the main associated one.

Inspection of the NMF components reported in Fig. 5.2, together with analogous studies for individual WS_2 nanotriangles, reveal localised plasmon resonances arising in both the single and stacked triangular configurations. In the latter case, resonance modes in the two overlapping triangles may overlap in both energy loss and spatial localisation, which together with the worse definition of spectral features in dielectric materials demands a careful interpretation of the identified components.

The NMF component 1 in Fig. 5.2 corresponds to the bulk WS_2 spectrum. The characteristic A and B exciton peaks at the expected values around 1.9 eV and 2.3 eV are observed. Additional features at approximately 1.2 eV and 1.4 eV can also be seen. Though their origin remains unclear, their presence in component 1 suggest they are features related to the crystal structure, in particular to the surface of the smaller nanotriangle which may exhibit structural defects and strain [49].

NMF components 2 to 4 in Fig. 5.2 provide direct insights into the nature of the localised plasmonic behaviour of the inspected WS_2 nanostructure, with each component revealing different features which would otherwise remain hidden in the EELS spectral image due to overlapping signals. The abundance map associated to component

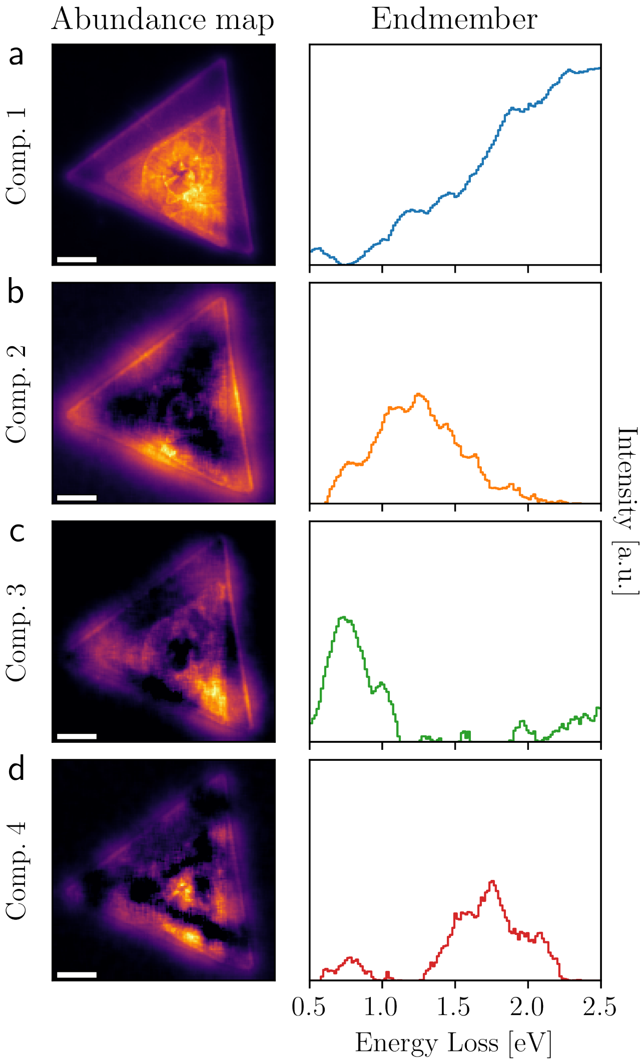

Figure 5.2: **NMF decomposition of EELS spectra in stacked WS$_2$ nanotriangles. (a-d)** The abundance maps (left) and endmembers (right panels) of the first 4 components of the NMF decomposition of the stacked WS$_2$ nanotriangles. Component 1 represents the bulk WS$_2$ spectrum, with the A- and B-exciton peaks at 1.9 and 2.3 eV. Component 2 corresponds to the 2nd-order resonance mode centred around 1.25 eV, with the abundance map displaying its characteristic node structure. Components 3 and 4 are dominated by the 1st-order and 3rd-order resonance modes of the large triangle, peaking at 0.75 eV and 1.75 eV respectively. In the right panels, vertical axes are uniformly scaled. Scale bars represent 200 nm.

2 clearly reveals its association with the second-order plasmonic resonance localised at the edges of the larger triangle, with three maxima and two minima across each edge. The corresponding endmember reveals a broad peak around 1.25 eV together with additional weaker signals. Component 3 displays two distinct peaks at 0.75 and 1 eV, which, based on the abundance map, are associated to the first-order resonances of both the large and small triangle, as confirmed by the dedicated theoretical EELS simulations to be discussed in Fig. 5.4 and Supporting Fig. D.15. The overlap in their spatial localisation at the corners of the triangles likely causes the two features to appear associated to the same component. Finally, component 4 features a broad peak centred around 1.75 eV, whose periodicity indicates the association with the third-order resonance in large triangle. We compare the components to point spectra selected from regions of high and low abundance in the abundance maps (see Supplementary Fig. D.10) and confirm the presence/absence of these features depending on the high/low abundance.

The NMF decomposition of Fig. 5.2 is restricted to the $[0.5, 2.5]$ eV and finds first-, second-, and third-order resonance modes. By extending the analysis to a broader energy window to $[2.0, 4.0]$ eV, it is possible to identify higher-order modes, as demonstrated in the Supplementary Fig. D.6. Specifically, we detect fourth- and fifth-order resonance modes for the large triangle, as well as indications for third- and fourth-order resonance modes in the small triangle.

The same NMF analysis has also been applied to stand-alone WS_2 nanotriangles with side lengths of 330, 880, and 920 nm single nanotriangles. For the 880 and 920 nm nanotriangles, we uncover the first-, second- and third-order resonance modes in the $[0.5, 2.5]$ eV energy window (Supplementary Fig. D.9 and Fig. D.7, respectively). For the 330 nm nanotriangle, an energy window of $[0.5, 4.0]$ eV reveals the first- and second-order resonance modes (Supplementary Fig. D.8). All in all, the emerging picture of localised low-energy plasmonic resonances in WS_2 is fully consistent between single and stacked nanotriangles.

5.2.2. ELECTRODYNAMICAL SIMULATIONS OF EELS EDGE PROFILES

To validate the plasmonic interpretation of the localised NMF components identified in the WS_2 nanostructures in Fig. 5.2, we have carried out dedicated electrodynamical simulations. Specifically, we numerically simulate the expected energy loss of the STEM-EELS electrons interacting with the edges of the large WS_2 nanotriangle using the PYGDM Python package [50], [51], denoted as edge profiles in the following. This package can be used to solve Maxwell's equations for arbitrary geometries and is based on a discretisation technique, the Green dyadic method (GDM), together with a generalised propagator for fast simulations. Here we simulate the EELS edge profiles of our WS_2 geometries using the fast electron module of PYGDM, with the incident electrons impinging at 200 keV perpendicular to WS_2 specimen. The simulations accounts for the experimental conditions with the WS_2 nanotriangles on top of a Si_3N_4 substrate surrounded by vacuum. Optical constants for WS_2 were taken from refractiveindex.info [52].

Fig. 5.3 displays the comparison between the experimental and simulated EELS profiles for the edge of the large WS_2 nanotriangle indicated in the inset. The theoretical prediction, Fig. 5.3(b), shows that plasmonic resonances tend to disperse towards a lower energy losses as they propagate from the centre toward the tip of the triangle, as

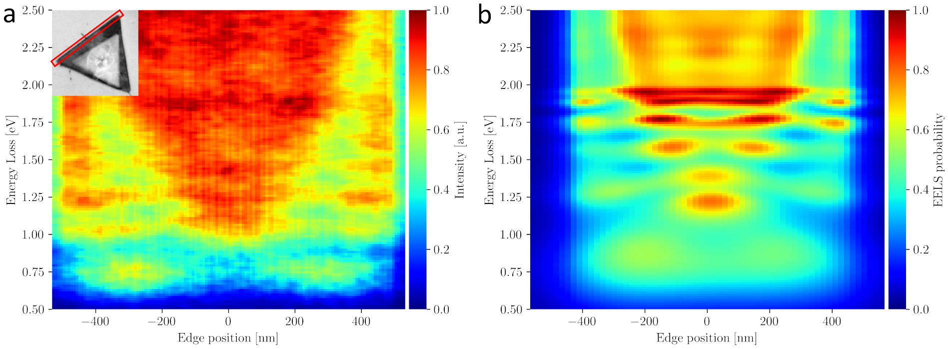

Figure 5.3: **Experimental and predicted EELS edge profiles in WS_2 nanotriangles.** **(a)** Experimental EELS edge profile (indicated in the inset, length of 980 nm) of the stacked WS_2 nanotriangles of Fig. 5.1. **(b)** The predictions of the corresponding electrodynamical simulation based on the PYGDM package. Both maps are normalized to their maximum value. Qualitative agreement in the energy-loss region of interest [0.5, 2.5] eV is observed, in particular concerning the oscillatory resonance structure characteristic of the identified plasmonic edge modes. The marked enhancement of the EELS edge profiles at 1.9 eV observed in both the data and the prediction is likely related to the resonance at 1.75 eV, as indicated by component 4 in Fig. 5.2(d).

also observed in the experimental EELS measurements. This behaviour, combined with the worse definition of plasmonic modes in dielectrics, leads to slight overlaps between higher-order plasmon modes at the tips and lower-order modes at the centre of the WS_2 specimen and a broadening of the associated energy peaks, as indicated by the NMF components 2 and 4 of Fig. 5.2(b,d). Inspection of Fig. 5.3 highlights the good agreement between the main qualitative features of the electrodynamical simulations of the EELS edge profiles and the associated experimental measurement is found, confirming their underlying plasmonic nature.

In Fig. 5.3(a) one observes the third-order plasmonic resonance mode between 1.7 eV and 2.0 eV, captured by the NMF component 4, Fig. 5.2(d), at approximately 1.75 eV and matching with the theoretical prediction in Fig. 5.3(b). For higher energy losses, both the data and the simulation display increases in the EELS intensity, which can be explained by the fourth- and fifth-order resonance modes as shown in the Supplementary Fig. D.6. In the Supplementary Sect. D.3.1 the edge dispersion of all triangular WS_2 nanostructures are compared to their simulated counterparts, see Supplementary Fig. D.12, finding also in this case agreement between data and predictions.

Despite this overall agreement between data and simulations, one should also note that some of the experimental features are not fully reproduced. For instance, the 1.0 eV peak in the experimental data, not captured by the prediction, can be attributed to the 1st-order resonance mode of the small WS_2 triangle leaking to the edge of the large triangle. The same phenomenon is reported for all three edges of the stacked WS_2 nanotriangles (Supplementary Fig. D.11).

Next, we compare the abundance maps obtained from the NMF decomposition (*e.g.* left panels of Fig. 5.2) with the simulated EELS maps for the associated plasmonic resonances. First, in Fig. 5.4(a-f) we compare the abundance maps of the 1st, 2nd, and 3rd resonance modes of the stand-alone triangle with side length of 920 nm, which has a similar morphology to the stacked nanotriangles and hence provides a suitable baseline for the latter. The simulated abundance maps are constructed by filtering the predicted EELS intensity in the energy-loss window associated to the corresponding endmember of the NMF component. The centre and width of this window are determined from a Gaussian fit to the endmembers (*e.g.* right panels of Fig. 5.2). Good agreement is obtained between the experimental and simulated abundance maps, further validating our interpretation of the EELS data in terms of the localised plasmonic resonances of WS_2. For the first-order mode, the bottom left corner of the triangle has a higher abundance compared to the other corners, most likely due to the thickness being slightly higher, see Supplementary Fig. D.1(b). A similar effect can be seen in the abundance maps of the second- and third-order modes.

Then Figs. 5.4(g-l) display the corresponding abundance maps for the stacked WS_2 nanotriangles, finding also qualitative agreement between data and electrodynamical simulations. Recall from Fig. 5.2 that the NMF components 2, 3, and 4 are found in this specimen to be associated to the 2nd, 1st, and 3rd order plasmonic resonances. The influence of the thickness on the resonance modes is evident in both experimental and simulation results. In Fig. 5.4(i), the abundance map also indicates an increased EELS emission in the centre of the structure, a feature absent the simulated maps. Revisiting the thickness map in Fig. 5.1(c), this is likely due to the non-uniform thickness of the smaller triangle. Indeed, the slight decrease in the thickness there indicates a hole at the centre of the small triangle may contribute to a shift in the EELS response between 1.7 and 2.0 eV, which as a consequence is grouped together with the 1.75 eV resonance in component 4 (Fig. 5.2(d)).

For completeness, experimental and abundance maps obtained from single WS_2 nanotriangles with different sizes are reported in the Supplementary Information. The Supplementary Fig. D.13 displays the maps of the first- and second-order plasmon resonances of the 330 nm nanotriangle and in Fig. D.14 the first-, second- and third-order of the 880 nm nanotriangle. Then, in the Supplementary Fig. D.15, we focus on simulating the small triangle with a side length of 680 nm, which is positioned on top of the large triangle. This simulation demonstrates that the localised plasmon resonances mode captured by NMF component 3, Figs. 5.2(c), corresponds with those hosted by the small triangle. In Supplementary Fig. D.16, we extend this analysis to confirm that the higher-order plasmon modes observed in the stacked WS_2 nanotriangles are indeed a superposition of the fourth- and fifth-order plasmon resonances of the large triangle, and the third- and fourth-order plasmon resonances of the small triangle, respectively. These observations align well with the findings from Supplementary Fig. D.6.

Overall, the numerical simulations of the EELS response in WS_2 nanotriangles with different morphologies are found to be fully consistent with the experimental data, in particular displaying the presence of higher-order localised plasmonic resonances, therefore providing additional validation for our interpretation of the EELS measurements.

5.2.3. DISPERSION RELATION OF EDGE-LOCALISED PLASMONIC MODES

Further scrutinising the nature of the observed edge-localised plasmonic WS_2 modes is possible through the determination of their dispersion relation, namely the value of the energy E_n associated to each the n-th mode as a function of the corresponding

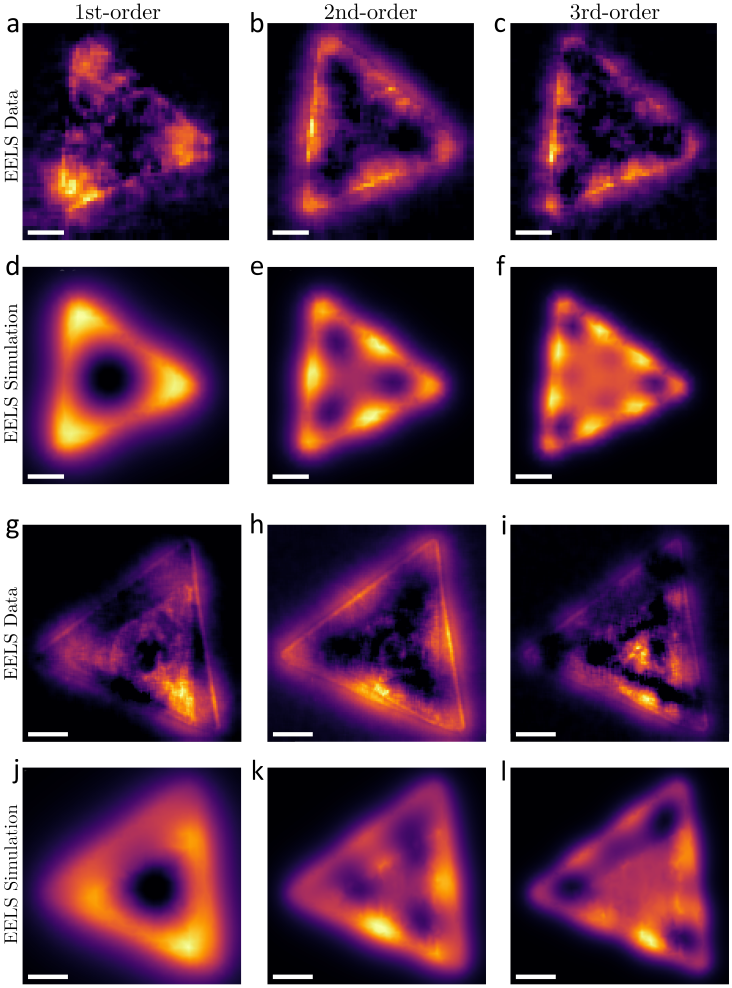

Figure 5.4: **Simulated abundance maps in WS_2 nanotriangles.** Comparison between the experimental and simulated abundance maps in individual **(a-f)** and stacked **(g-l)** WS_2 nanotriangles. The experimental maps are obtained from the NMF decomposition, while the simulated ones are constructed by filtering the predicted EELS intensity in the energy-loss window associated to the corresponding endmember of the NMF component. **(a-f)** For the experimental abundance maps of the 920 nm nanotriangle, we display the 1st, 2nd, and 3rd order plasmonic resonances whose associated endmembers peak at $\Delta E = 0.91$ eV, 1.28 eV, and 1.89 eV respectively, with the corresponding simulated maps filtered to the $[0.7, 0.9]$ eV, $[1.1, 1.3]$ eV, $[1.65, 1.85]$ eV energy windows. **(g-l)** Same for the stacked nanotriangle, for which the NMF endmembers associated to the 1st, 2nd, and 3rd order resonances peak at 0.75 eV, 1.22 eV, and 1.74 eV, with the corresponding simulated maps filtered to the $[0.7, 0.9]$ eV, $[1.1, 1.3]$ eV and $[1.65, 1.85]$ eV intervals. Scale bars correspond to 200 nm.

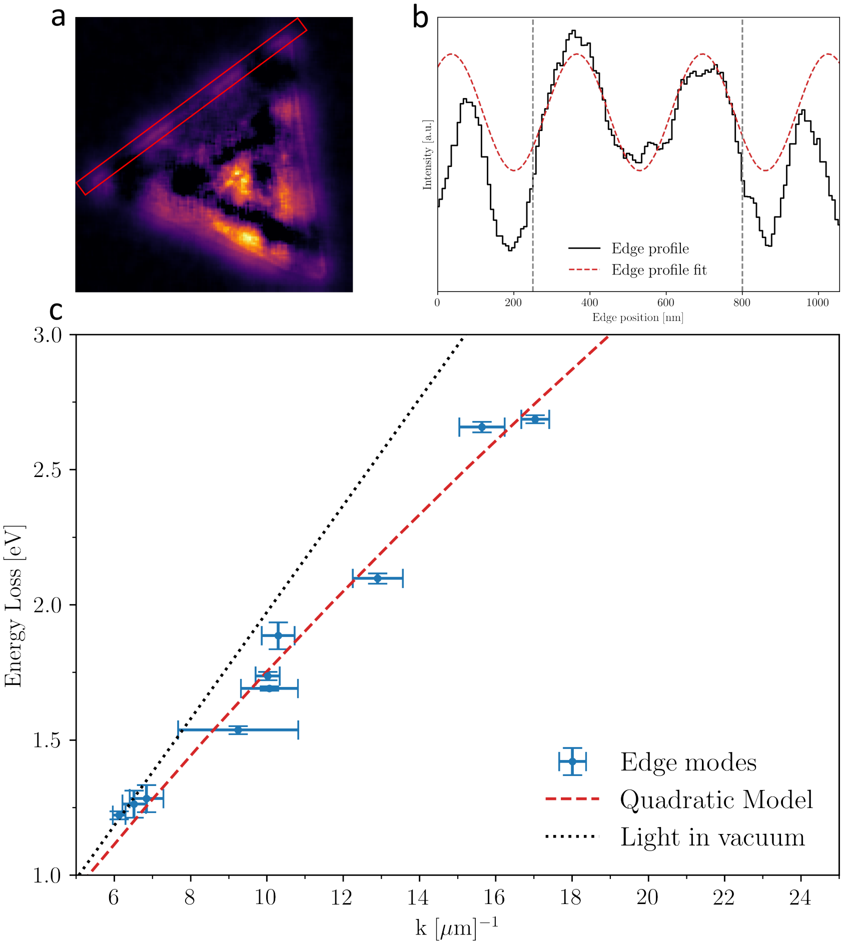

Figure 5.5: **Dispersion relation for the plasmonic edge modes in triangular WS_2 nanostructures. (a,b)** Summary of the fitting procedure adopted to extract the phase shift φ of the edge profile from the abundance map and entering Eq. (5.1), illustrated in the case of the 3rd-order resonance mode of the large nanotriangle. The dashed grey lines indicate the fitting ranges. **(c)** The measured values of dispersion relation of the edge-localised plasmon resonances, with the corresponding uncertainties, are well described quadratic polynomial fit, consistently with the expectation for the surface plasmon characteristics. For reference, we also display the dispersion relation of light in vacuum.

wavenumber k_n. The indexing for these edge-localised plasmonic modes is based on a one-dimensional Fabry-Perot model [53]–[56] which has been applied to describe edge modes in metallic triangular nanostructures [57].

In this model, the EELS intensity maps –specifically, the abundance maps of the localised plasmon resonances– arise due to the constructive interference within a one-dimensional Fabry-Perot cavity. This interference occurs when half of the plasmon resonance wavelength λ fits within the side length of the triangular nanostructure, and can be described by the relation

$$k_n L = n\pi - \varphi \,, \tag{5.1}$$

where k_n is the wavenumber, n is the order of the plasmon resonance, L the length of the cavity (nanotriangle side), and φ is the phase shift that occurs upon reflection at the boundaries of the nanostructure. This phase shift φ can be obtained by fitting the edge profile of the triangle using Supplementary Eq. (D.6), as illustrated in Fig. 5.5(a,b).

To illustrate the benefits of adopting NMF decomposition for this application, the Supplementary Fig. D.18 compares the fourth-order resonance of the edge profile large triangle edge profile obtained from the NMF abundance map to its counterpart obtained by taking the integrated EELS intensity of the energy window of the resonance. The edge profile obtained from NMF decomposition is much better defined, which is crucial to pin down the underlying nature of the observed resonances.

Fig. 5.5(c) displays the experimentally measured values of E_n, the peak energy of the n-th plasmonic resonance obtained from the NMF endmembers, as a function of the associated wavenumbers k_n computed from Eq. (5.1), together with the associated uncertainties. The measured values for the dispersion relation $E_n = f(k_n)$ are fitted to a quadratic model of the form $E_n = Ak_n^2 + Bk_n + C$, which is the expected behaviour given the surface plasmon characteristics [55], [58]–[60], finding good agreement. This polynomial fit is compared to a linear fit in Supplementary Fig. D.17, showing that the latter is insufficient to describe the experimental values. For reference, Fig. 5.5(c) also displays the dispersion relation associated to light propagating in vacuum.

The confirmation presented in Fig. 5.5(c) that the dispersion relations of the observed edge-localised periodic modes in our WS_2 nanostructures is well described by a quadratic model provides yet another piece of evidence demonstrating the plasmonic nature of the observed resonances from the EELS data.

5.3. SUMMARY AND OUTLOOK

In this study we have fingerprinted edge-localised plasmonic resonances arising in single and stacked WS_2 nanotriangles from a synergetic combination of spatially-resolved EELS and non-negative matrix factorization techniques. Our approach successfully resolves edge-localised plasmonic modes up to the fourth-order resonance in single nanotriangles and up to the fifth-order resonance in the stacked nanotriangles. In particular, we are able to disentangle the main features of the localised plasmonic resonances appearing in the smaller triangle for the stacked configuration, which would have been otherwise obscured by the bulk signal of the larger bottom triangle if one had relied on more traditional methods.

To validate the interpretation of our EELS-based analysis, we have compared the experimental results with dedicated electrodynamical simulations of the EELS edge profiles based on the PYGDM package, finding good agreement both in terms of the abundance maps of the localised plasmonic resonances and on the values of the associated energies for each resonance mode. Furthermore, the experimental determination of the dispersion relation of the edge-localised plasmonic modes obtained from the endmembers of the NMF decomposition is found to be well described by a quadratic model (but not by a linear one), consistently with the expected behaviour for surface plasmon characteristics.

All in all, our findings highlight the potential of boosting spatially-resolved EELS with sophisticated data processing algorithms, in this case non-negative matrix factorization supplemented with machine learning for the model-independent subtraction of the ZLP. This potential is most effective for analyses of nano-specimens with non-trivial morphologies, such as the overlapping WS_2 nanotriangles considered in this work, where conventional methods do not suffice to identify all the relevant features present in the data. More towards the future, the methodology presented in this work opens new avenues in exploiting the capabilities of localising plasmonic resonances with well-defined spectral characteristics to harness light-matter interactions in TMD materials, improving prospects for their applications to optoelectronic and nanophotonic devices, such as photodetectors with high spatial resolution. Exploiting the edge-localized plasmonic resonances for enhanced light absorption and local electric fields is another promising avenue avenue [21], as well as their use as nanoscale light sources [61], and their application to frequency conversion and ultrafast laser technologies in plasmon-enhanced nonlinear optics [62].

REFERENCES

[1] X. Hong, J. Kim, S.-F. Shi, *et al.*, "Ultrafast charge transfer in atomically thin MoS2/WS2 heterostructures", *Nat. Nanotechnol.*, vol. 9, no. 9, pp. 682–686, 2014, ISSN: 1748-3395. DOI: `10.1038/nnano.2014.167`.

[2] P. Ajayan, P. Kim, and K. Banerjee, "Two-dimensional van der waals materials", *Physics Today*, vol. 69, pp. 38–44, 9 2016, ISSN: 00319228. DOI: `10.1063/PT.3.3297`.

[3] K. F. Mak and J. Shan, "Photonics and optoelectronics of 2d semiconductor transition metal dichalcogenides", *Nature Photonics*, vol. 10, pp. 216–226, 4 2016, ISSN: 17494893. DOI: `10.1038/nphoton.2015.282`.

[4] Z. Peng, X. Chen, Y. Fan, D. J. Srolovitz, and D. Lei, "Strain engineering of 2D semiconductors and graphene: from strain fields to band-structure tuning and photonic applications", *Light Sci. Appl.*, vol. 9, no. 190, pp. 1–25, 2020, ISSN: 20477538. DOI: `10.1038/s41377-020-00421-5`.

[5] M. Tripathi, F. Lee, A. Michail, *et al.*, "Structural defects modulate electronic and nanomechanical properties of 2d materials", *ACS Nano*, vol. 15, pp. 2520–2531, 2 2021, ISSN: 1936086X. DOI: `10.1021/acsnano.0c06701`.

[6] R. Levi, O. Bitton, G. Leitus, R. Tenne, and E. Joselevich, "Field-effect transistors based on ws2 nanotubes with high current-carrying capacity", *Nano Letters*, vol. 13, pp. 3736–3741, 8 Aug. 2013, ISSN: 15306984. DOI: 10.1021/nl401675k.

[7] F. H. Koppens, T. Mueller, P. Avouris, A. C. Ferrari, M. S. Vitiello, and M. Polini, "Photodetectors based on graphene, other two-dimensional materials and hybrid systems", *Nature Nanotechnology*, vol. 9, pp. 780–793, 10 Jan. 2014, ISSN: 17483395. DOI: 10.1038/nnano.2014.215.

[8] C. Biswas, Y. H. Lee, R. Sebait, B. Song, and C. Seo, "Identifying defect-induced trion in monolayer ws2 via carrier screening engineering", *ACS Nano*, vol. 15, pp. 2849–2857, 2 Feb. 2021, ISSN: 1936086X. DOI: 10.1021/acsnano.0c08828.

[9] I. Shlyakhov, K. Iakoubovskii, S. Banerjee, *et al.*, "Measurement of direct and indirect bandgaps in synthetic ultrathin mos2and ws2films from photoconductivity spectra", *Journal of Applied Physics*, vol. 129, 15 Apr. 2021, ISSN: 10897550. DOI: 10.1063/5.0046305.

[10] M. Shanmugam, C. A. Durcan, R. Jacobs-Gedrim, and B. Yu, "Layered semiconductor tungsten disulfide: Photoactive material in bulk heterojunction solar cells", *Nano Energy*, vol. 2, pp. 419–424, 3 May 2013, ISSN: 22112855. DOI: 10.1016/j.nanoen.2012.11.011.

[11] S. Roy and P. Bermel, "Electronic and optical properties of ultra-thin 2d tungsten disulfide for photovoltaic applications", *Solar Energy Materials and Solar Cells*, vol. 174, pp. 370–379, Jan. 2018, ISSN: 09270248. DOI: 10.1016/j.solmat.2017.09.011.

[12] W. Lei, J. L. Xiao, H. P. Liu, Q. L. Jia, and H. J. Zhang, "Tungsten disulfide: Synthesis and applications in electrochemical energy storage and conversion", *Tungsten*, vol. 2, pp. 217–239, 3 Sep. 2020, ISSN: 26618036. DOI: 10.1007/s42864-020-00054-6.

[13] H. Hashtroudi, I. D. MacKinnon, and M. Shafiei, "Emerging 2d hybrid nanomaterials: Towards enhanced sensitive and selective conductometric gas sensors at room temperature", *Journal of Materials Chemistry C*, vol. 8, pp. 13 108–13 126, 38 2020, ISSN: 20507526. DOI: 10.1039/d0tc01968b.

[14] J. Ding, A. Feng, X. Li, S. Ding, L. Liu, and W. Ren, "Properties, preparation, and application of tungsten disulfide: A review", *Journal of Physics D: Applied Physics*, vol. 54, 17 Apr. 2021, ISSN: 13616463. DOI: 10.1088/1361-6463/abd9e8.

[15] G. Sanyal, A. Vaidyanathan, C. S. Rout, and B. Chakraborty, "Recent developments in two-dimensional layered tungsten dichalcogenides based materials for gas sensing applications", *Materials Today Communications*, vol. 28, Sep. 2021, ISSN: 23524928. DOI: 10.1016/j.mtcomm.2021.102717.

[16] S. B. Anantharaman, K. Jo, and D. Jariwala, "Exciton-photonics: From fundamental science to applications", *ACS Nano*, vol. 15, pp. 12 628–12 654, 8 Aug. 2021, ISSN: 1936086X. DOI: 10.1021/acsnano.1c02204.

[17] S. S. Sinha, L. Yadgarov, S. B. Aliev, *et al.*, “Mos2and ws2nanotubes: Synthesis, structural elucidation, and optical characterization”, *Journal of Physical Chemistry C*, vol. 125, pp. 6324–6340, 11 Mar. 2021, ISSN: 19327455. DOI: `10.1021/acs.jpcc.0c10784`.

[18] C. Li, D. Sang, S. Ge, L. Zou, and Q. Wang, “Recent excellent optoelectronic applications based on two-dimensional ws2 nanomaterials: A review”, *Molecules*, vol. 29, 14 Jul. 2024, ISSN: 14203049. DOI: `10.3390/molecules29143341`.

[19] M. Wang, A. Krasnok, T. Zhang, *et al.*, “Tunable fano resonance and plasmon–exciton coupling in single au nanotriangles on monolayer ws2 at room temperature”, *Advanced Materials*, vol. 30, 22 May 2018, ISSN: 15214095. DOI: `10.1002/adma.201705779`.

[20] Y. Liu, W. Huang, W. Chen, *et al.*, “Plasmon resonance enhanced ws 2 photodetector with ultra-high sensitivity and stability”, *Applied Surface Science*, vol. 481, pp. 1127–1132, Jul. 2019, ISSN: 01694332. DOI: `10.1016/j.apsusc.2019.03.179`.

[21] C. Han, Y. Wang, W. Zhou, M. Liang, and J. Ye, “Strong anisotropic enhancement of photoluminescence in ws2 integrated with plasmonic nanowire array”, *Scientific Reports*, vol. 11, 1 Dec. 2021, ISSN: 20452322. DOI: `10.1038/s41598-021-89136-0`.

[22] J. Zhang, X. Zhang, J. Li, *et al.*, “Simultaneous visible and ultraviolet photoresponse improvement of mos2/zno heterostructure photodetector via direct resonant coupling of au nanoparticles localized surface plasmon resonance”, *Optical Materials*, vol. 124, p. 111 997, 2022, ISSN: 0925-3467. DOI: `https://doi.org/10.1016/j.optmat.2022.111997`.

[23] M. Alamri, M. Gong, B. Cook, R. Goul, and J. Z. Wu, “Plasmonic ws2 nanodiscs/graphene van der waals heterostructure photodetectors”, *ACS Applied Materials and Interfaces*, vol. 11, pp. 33 390–33 398, 36 Sep. 2019, ISSN: 19448252. DOI: `10.1021/acsami.9b09262`.

[24] H. Ahmed and V. E. Babicheva, “Nanostructured tungsten disulfide ws 2 as mie scatterers and nanoantennas”, *MRS Advances*, vol. 5, pp. 1819–1826, 35-36 2020, ISSN: 20598521. DOI: `10.1557/adv.2020.173`.

[25] C. K. Xu, W. J. Liu, P. K. Zhang, *et al.*, “Nonlinear inelastic electron scattering revealed by plasmon-enhanced electron energy-loss spectroscopy”, *Nature Physics*, vol. 10, pp. 753–757, 10 Jan. 2014, ISSN: 17452481. DOI: `10.1038/nphys3051`.

[26] Y. Wu, G. Li, and J. P. Camden, “Probing nanoparticle plasmons with electron energy loss spectroscopy”, *Chemical Reviews*, vol. 118, pp. 2994–3031, 6 Mar. 2018, ISSN: 15206890. DOI: `10.1021/acs.chemrev.7b00354`.

[27] D. Kordahl, D. T. Alexander, and C. Dwyer, “Waveguide modes spatially resolved by low-loss stem-eels”, *Physical Review B*, vol. 103, 13 Apr. 2021, ISSN: 24699969. DOI: `10.1103/PhysRevB.103.134109`.

[28] K. I. Saitow, “1d, 2d, and 3d mapping of plasmon and mie resonances: A review of field enhancement imaging based on electron or photon spectromicroscopy”, *Journal of Physical Chemistry C*, vol. 128, pp. 5367–5393, 13 Apr. 2024, ISSN: 19327455. DOI: `10.1021/acs.jpcc.3c07393`.

[29] D. T. Alexander, V. Flauraud, and F. Demming-Janssen, “Stem-eels mapping of eigenmodes and coupling effects of photonic silicon nanocavities”, *Microscopy and Microanalysis*, vol. 28, pp. 2024–2025, S1 Aug. 2022, ISSN: 1431-9276. DOI: `10.1017/s1431927622007851`.

[30] M. Shiga, K. Tatsumi, S. Muto, *et al.*, “Sparse modeling of eels and edx spectral imaging data by nonnegative matrix factorization”, *Ultramicroscopy*, vol. 170, pp. 43–59, Nov. 2016, ISSN: 18792723. DOI: `10.1016/j.ultramic.2016.08.006`.

[31] S. Roesgaard, Q. Ramasse, J. Chevallier, M. Fyhn, and B. Julsgaard, “Electron energy-loss spectroscopy of single nanocrystals: Mapping of tin allotropes”, *Nanotechnology*, vol. 29, 21 Mar. 2018, ISSN: 13616528. DOI: `10.1088/1361-6528/aab563`.

[32] R. F. Cai, M. T. Chang, S. C. Lo, and C. C. Chen, “Novel spectral unmixing approach for electron energy-loss spectroscopy”, *New Journal of Physics*, vol. 22, 3 Mar. 2020, ISSN: 13672630. DOI: `10.1088/1367-2630/ab7a89`.

[33] S. E. van Heijst, M. Bolhuis, A. Brokkelkamp, J. J. Sangers, and S. Conesa-Boj, “Heterostrain-driven bandgap increase in twisted ws2: A nanoscale study”, *Advanced Functional Materials*, 2023, ISSN: 16163028. DOI: `10.1002/adfm.202307893`.

[34] J. Park, S. Heo, J. G. Chung, *et al.*, “Bandgap measurement of thin dielectric films using monochromated stem-eels”, *Ultramicroscopy*, vol. 109, pp. 1183–1188, 9 2009, ISSN: 03043991. DOI: `10.1016/j.ultramic.2009.04.005`.

[35] M. Kociak, O. Stéphan, L. Henrard, *et al.*, “Experimental evidence of surface-plasmon coupling in anisotropic hollow nanoparticles”, *Physical Review Letters*, vol. 87, pp. 75501-1-75501–4, 7 Aug. 2001, ISSN: 10797114. DOI: `10.1103/PhysRevLett.87.075501`.

[36] L. Maduro, S. E. van Heijst, and S. Conesa-Boj, “First-principles calculation of optoelectronic properties in 2d materials: The polytypic ws2 case”, *ACS Physical Chemistry Au*, vol. 2, pp. 191–198, 3 May 2022, ISSN: 26942445. DOI: `10.1021/acsphyschemau.1c00038`.

[37] F. López-Urías, A. L. Elías, N. Perea-López, H. R. Gutiérrez, M. Terrones, and H. Terrones, “Electronic, magnetic, optical, and edge-reactivity properties of semiconducting and metallic ws2 nanoribbons”, *2D Materials*, vol. 2, 1 Dec. 2015, ISSN: 20531583. DOI: `10.1088/2053-1583/2/1/015002`.

[38] E. Skúlason, G. S. Karlberg, J. Rossmeisl, *et al.*, “Density functional theory calculations for the hydrogen evolution reaction in an electrochemical double layer on the pt(111) electrode”, *Physical Chemistry Chemical Physics*, vol. 9, pp. 3241–3250, 25 2007, ISSN: 14639076. DOI: `10.1039/b700099e`.

[39] M. Tinoco, L. Maduro, and S. Conesa-Boj, “Metallic edge states in zig-zag vertically-oriented mos2 nanowalls”, *Scientific Reports*, vol. 9, 1 Dec. 2019, ISSN: 20452322. DOI: `10.1038/s41598-019-52119-3`.

[40] L. I. Roest, S. E. van Heijst, L. Maduro, J. Rojo, and S. Conesa-Boj, "Charting the low-loss region in electron energy loss spectroscopy with machine learning", *Ultramicroscopy*, vol. 222, p. 113 202, 2021, ISSN: 0304-3991. DOI: `https://doi.org/10.1016/j.ultramic.2021.113202`.

[41] A. Brokkelkamp, J. T. Hoeve, I. Postmes, *et al.*, "Spatially resolved band gap and dielectric function in two-dimensional materials from electron energy loss spectroscopy", *Journal of Physical Chemistry A*, vol. 126, pp. 1255–1262, 7 Feb. 2022, ISSN: 15205215. DOI: `10.1021/acs.jpca.1c09566`.

[42] S. van der Lippe, A. Brokkelkamp, J. Rojo, and S. Conesa-Boj, "Localized exciton anatomy and bandgap energy modulation in 1d mos2 nanostructures", *Advanced Functional Materials*, vol. 33, 52 Dec. 2023, ISSN: 16163028. DOI: `10.1002/adfm.202307610`.

[43] H. La, A. Brokkelkamp, S. van der Lippe, J. ter Hoeve, J. Rojo, and S. Conesa-Boj, "Edge-induced excitations in Bi2Te3 from spatially-resolved electron energy-gain spectroscopy", *Ultramicroscopy*, vol. 254, p. 113 841, 2023. DOI: `10.1016/j.ultramic.2023.113841`. arXiv: `2305.03752 [cond-mat.mes-hall]`.

[44] O. Nicoletti, F. D. L. Peña, R. K. Leary, D. J. Holland, C. Ducati, and P. A. Midgley, "Three-dimensional imaging of localized surface plasmon resonances of metal nanoparticles", *Nature*, vol. 502, pp. 80–84, 7469 2013, ISSN: 00280836. DOI: `10.1038/nature12469`.

[45] A. Eljarrat, L. López-Conesa, J. López-Vidrier, *et al.*, "Retrieving the electronic properties of silicon nanocrystals embedded in a dielectric matrix by low-loss eels", *Nanoscale*, vol. 6, pp. 14 971–14 983, 24 Dec. 2014, ISSN: 20403372. DOI: `10.1039/c4nr03691c`.

[46] S. Muto and M. Shiga, "Application of machine learning techniques to electron microscopic/spectroscopic image data analysis", *Microscopy*, vol. 69, pp. 110–122, 2 Apr. 2020, ISSN: 20505701. DOI: `10.1093/jmicro/dfz036`.

[47] N. Borodinov, P. Banerjee, S. H. Cho, *et al.*, "Enhancing hyperspectral eels analysis of complex plasmonic nanostructures with pan-sharpening", *Journal of Chemical Physics*, vol. 154, 1 Jan. 2021, ISSN: 10897690. DOI: `10.1063/5.0031324`.

[48] M. Pelaez-Fernandez, B. Majérus, D. Funes-Hernando, *et al.*, "Toward laser-induced tuning of plasmonic response in high aspect ratio gold nanostructures", *Nanophotonics*, vol. 11, pp. 3719–3728, 16 Sep. 2022, ISSN: 21928614. DOI: `10.1515/nanoph-2022-0193`.

[49] S. Neupane, H. Tang, and A. Ruzsinszky, "Defect-induced states, defect-induced phase transition, and excitonic states in bent tungsten disulfide (ws2) nanoribbons: Density functional vs. many body theory", *Physical Review Materials*, vol. 7, 12 Dec. 2023, ISSN: 24759953. DOI: `10.1103/PhysRevMaterials.7.124001`.

[50] P. R. Wiecha, "Pygdm—a python toolkit for full-field electro-dynamical simulations and evolutionary optimization of nanostructures", *Computer Physics Communications*, vol. 233, pp. 167–192, Jun. 2018, ISSN: 00104655. DOI: `https://doi.org/10.1016/j.cpc.2018.06.017`.

[51] P. R. Wiecha, C. Majorel, A. Arbouet, *et al.*, "“pygdm” - new functionalities and major improvements to the python toolkit for nano-optics full-field simulations", *Computer Physics Communications*, vol. 270, Jan. 2022, ISSN: 00104655. DOI: `10.1016/j.cpc.2021.108142`.

[52] B. Munkhbat, P. Wróbel, T. J. Antosiewicz, and T. O. Shegai, *Optical constants of ws2 (tungsten disulfide)*, Publicely available from `https://refractiveindex.info/?shelf=main&book=WS2&page=Munkhbat-o`, Online; accessed 4-oct-2024, 2024.

[53] E. S. Barnard, J. S. White, A. Chandran, *et al.*, "Spectral properties of plasmonic resonator antennas", *Optical Properties of Metal Clusters*, vol. 1, pp. 17 930–17 935, 8 Oct. 2008. DOI: `10.1364/OE.16.016529`.

[54] D. Rossouw, M. Couillard, J. Vickery, E. Kumacheva, and G. A. Botton, "Multipolar plasmonic resonances in silver nanowire antennas imaged with a subnanometer electron probe", *Nano Letters*, vol. 11, pp. 1499–1504, 4 Apr. 2011, ISSN: 15306984. DOI: `10.1021/nl200634w`.

[55] O. Nicoletti, M. Wubs, N. A. Mortensen, W. Sigle, P. A. van Aken, and P. A. Midgley, "Surface plasmon modes of a single silver nanorod: An electron energy loss study", *Inst. Phys. Conf. Ser*, vol. 3, pp. 191–194, 6950 Aug. 2011. DOI: `10.1364/OA_License_v1#VOR`.

[56] J. Martin, M. Kociak, Z. Mahfoud, J. Proust, D. Gérard, and J. Plain, "High-resolution imaging and spectroscopy of multipolar plasmonic resonances in aluminum nanoantennas", *Nano Letters*, vol. 14, pp. 5517–5523, 10 Oct. 2014, ISSN: 15306992. DOI: `10.1021/nl501850m`.

[57] A. Campos, A. Arbouet, J. Martin, *et al.*, "Plasmonic breathing and edge modes in aluminum nanotriangles", *ACS Photonics*, vol. 4, pp. 1257–1263, 5 May 2017, ISSN: 23304022. DOI: `10.1021/acsphotonics.7b00204`.

[58] P. Berini, "Plasmon-polariton waves guided by thin lossy metal films of finite width: Bound modes of asymmetric structures", *Physical Review B - Condensed Matter and Materials Physics*, vol. 63, 12 Mar. 2001, ISSN: 1550235X. DOI: `10.1103/PhysRevB.63.125417`.

[59] F. P. Schmidt, H. Ditlbacher, U. Hohenester, A. Hohenau, F. Hofer, and J. R. Krenn, "Universal dispersion of surface plasmons in flat nanostructures", *Nature Communications*, vol. 5, Apr. 2014, ISSN: 20411723. DOI: `10.1038/ncomms4604`.

[60] H. Saito and H. Kurata, "Direct measurement of dispersion relation for surface plasmon-polaritons on silver nanoantennas", *Microscopy*, vol. 63, pp. 155–159, 2 Apr. 2014, ISSN: 20505701. DOI: `10.1093/jmicro/dft048`.

[61] Z. He, Z. Han, J. Yuan, *et al.*, "Quantum plasmonic control of trions in a picocavity with monolayer ws2", *Science Advances*, vol. 5, 10 Oct. 2019. DOI: `10.1126/sciadv.aau8763`. [Online]. Available: `https://www.science.org`.

[62] J. Hernandez-Rueda, M. L. Noordam, I. Komen, and L. Kuipers, "Nonlinear optical response of a ws2monolayer at room temperature upon multicolor laser excitation", *ACS Photonics*, vol. 8, pp. 550–556, 2 Feb. 2021, ISSN: 23304022. DOI: `10.1021/acsphotonics.0c01567`.

6

CONCLUSIONS AND OUTLOOK

You and I are just swinging doors.
This kind of understanding is necessary.

- Shunryu Suzuki

This work has significantly advanced our understanding of nanoscale phenomena through the innovative integration of advanced Electron Energy-Loss Spectroscopy (EELS) and Scanning Transmission Electron Microscopy (STEM). By developing and applying cutting-edge machine learning (ML) methodologies, we have addressed the escalating challenges of interpreting complex and extensive datasets in van der Waals (vdW) nanomaterials research.

The key findings and contributions of this work include the development of a novel framework for the automated processing and interpretation of spectral images in EELS. This framework achieves robust subtraction of the Zero Loss Peak (ZLP) background, allowing for precise spatial mapping in the low-loss region of EEL spectra. Furthermore, it enables spatially-resolved determination of the bandgap energy and complex dielectric function in vdW layered materials. This approach has also allowed us to correlate electronic properties with structural features, such as local specimen thickness, providing a deeper understanding of these vdW materials.

These advancements provide a robust and adaptable framework for processing EELS data, allowing for reliable and interpretable outputs that go beyond conventional data-processing methods. Current techniques in transmission electron microscopy data analysis often rely on manual interpretation or simpler statistical methods, which may not fully capture the complex relationships within high-dimensional datasets typical of nanoscale materials studies. Our ML-based approaches offer an alternative by extracting nuanced information with precision, allowing for a deeper understanding of complex vdW materials properties.

Building on this capability, Chapters 2 and 3 present a novel framework for the automated processing and interpretation of spectral images in EELS. Through ML algorithms initially developed in particle physics [1]–[3], we achieved robust subtraction of the Zero Loss Peak (ZLP) background, enabling precise spatial mapping in the low-loss region of EEL spectra. This approach allowed for spatially-resolved determinations of the bandgap energy and complex dielectric function in layered materials, such as InSe and WS_2, revealing correlations between electronic properties and structural features, such as local specimen thickness. Implemented within the open-source PYTHON framework, EELSFITTER, this methodology is accessible and adaptable, with thorough documentation available online.

While initially focused on the interpretation of STEM-EELS spectral imaging (SI) for layered materials, this generalizable approach requires no assumptions about the shape of the ZLP, making it applicable to higher-dimensional datasets, including momentum-resolved EELS and various nanostructured materials like topological insulators, complex oxides, and heterostructures. Future extensions of this framework could include its application to core-loss spectra background modelling, providing a robust alternative to conventional methods, such as the linear combination of power laws [4]. This adaptability positions our framework as a versatile tool for in-depth analysis across a diverse range of material systems.

In Chapter 4, we extend this framework further, focusing on automated peak identification and characterization across entire specimens. Initially, we examine 1D-MoS_2 nanostructures, where the automated procedure revealed unique excitonic transitions localized at endpoints or lateral sides, differing from the uniform distribution observed in 2D-MoS_2. We found a modulated bandgap energy along 1D-MoS_2,particularly reduced at the endpoints, which correlated with intrinsic strain. This tunability of electronic behaviour via strain suggests potential applications of 1D-MoS_2 in quantum optics, particularly as single-photon emitters, although the challenge remains in achieving reliable fabrication methods for these structures.

The latter part of Chapter 4 applies automated peak identification to the energy-gain region of Bi_2Te_3, a topological insulator, where we identified a previously unobserved narrow feature on the ZLP tail. This feature, particularly pronounced at regions of sharp thickness variation, could potentially be related to edge- or surface-plasmons, though dedicated simulations would be needed for confirmation. Our analysis verified the robustness of these findings against methodological uncertainties in ZLP subtraction, underscoring the reliability of our approach.

In Chapter 5, we applied non-negative matrix factorization (NMF) to characterize edge-localized plasmonic resonances in WS_2 nanotriangles, resolving up to fifth-order edge-localized plasmonic modes. In stacked WS_2 nanotriangles, NMF allowed us to separate resonances from smaller triangles atop larger ones—achievements unattainable through traditional methods. Comparison with electrodynamical simulations confirmed the accuracy of the NMF-derived components. This analysis exemplifies the power of sophisticated data-processing techniques like NMF in specimens with non-trivial morphologies, highlighting the potential of spatially resolved EELS supplemented with advanced statistical methods. Looking forward, multivariate statistical techniques, such as NMF, will likely play a crucial role in EELS-SI analysis as datasets grow in complexity. Integration of methods like pan-sharpening [5] and predictive modelling can enhance both spectral and spatial resolution while preserving sample integrity, establishing a foundation for automated, high-precision data analysis that advances the study of layered and nanostructured materials.

In summary, with this dissertation we set out to develop novel tools for the analysis of EELS in the low loss region of layered materials Throughout this work we have highlighted how advanced data-processing methods can deepen our understanding of complex materials at very small scales. By combining precise imaging techniques with new ways of analysing data, we created tools that make it easier to study layered and nanostructured materials. Key in the development of these tools was to automate and streamline the data processing, reducing labour intensive work, while providing a robust output. Additionally, the methodology used is not limited to the type of data itself and could be applied in different manners as well. Looking ahead, there are still plenty of ways for further improvements to these tools. For instance, there is still room for more automation of the peak tracking approaches and the approach for background modelling could be extended core-loss region of EELS. Improvements in these areas will allow scientists to explore a wide range of materials with less intensive manual effort. For instance, more in depth research on the application and improvement of NMF in low loss EELS could be a potential fruitful endeavour, as most research on NMF in EELS and other approaches mostly focus on the core loss [6]–[8]. This work sets a strong foundation for future research, helping scientists better understand and develop new technologies in fields like quantum materials and energy.

REFERENCES

[1] R. D. Ball, L. D. Debbio, S. Forte, *et al.*, “A determination of parton distributions with faithful uncertainty estimation”, *Nuclear Physics B*, vol. 809, pp. 1–63, 1-2 Mar. 2009, ISSN: 05503213. DOI: 10.1016/j.nuclphysb.2008.09.037.

[2] R. D. Ball, V. Bertone, S. Carrazza, *et al.*, “Parton distributions for the lhc run ii”, *Journal of High Energy Physics*, vol. 2015, pp. 1–148, 4 Apr. 2015, ISSN: 10298479. DOI: 10.1007/JHEP04(2015)040.

[3] R. D. Ball, V. Bertone, S. Carrazza, *et al.*, “Parton distributions from high-precision collider data: Nnpdf collaboration”, *European Physical Journal C*, vol. 77, 10 Oct. 2017, ISSN: 14346052. DOI: 10.1140/epjc/s10052-017-5199-5.

[4] P. Cueva, R. Hovden, J. A. Mundy, H. L. Xin, and D. A. Muller, “Data processing for atomic resolution electron energy loss spectroscopy”, in *Microscopy and Microanalysis*, vol. 18, Aug. 2012, pp. 667–675. DOI: 10.1017/S1431927612000244.

[5] N. Borodinov, P. Banerjee, S. H. Cho, *et al.*, “Enhancing hyperspectral eels analysis of complex plasmonic nanostructures with pan-sharpening”, *Journal of Chemical Physics*, vol. 154, 1 Jan. 2021, ISSN: 10897690. DOI: 10.1063/5.0031324.

[6] M. Shiga, K. Tatsumi, S. Muto, *et al.*, “Sparse modeling of eels and edx spectral imaging data by nonnegative matrix factorization”, *Ultramicroscopy*, vol. 170, pp. 43–59, Nov. 2016, ISSN: 18792723. DOI: 10.1016/j.ultramic.2016.08.006.

[7] R. F. Cai, M. T. Chang, S. C. Lo, and C. C. Chen, “Novel spectral unmixing approach for electron energy-loss spectroscopy”, *New Journal of Physics*, vol. 22, 3 Mar. 2020, ISSN: 13672630. DOI: 10.1088/1367-2630/ab7a89.

[8] S. V. Kalinin, A. R. Lupini, R. K. Vasudevan, and M. Ziatdinov, “Gaussian process analysis of electron energy loss spectroscopy data: Multivariate reconstruction and kernel control”, *npj Computational Materials*, vol. 7, 1 Dec. 2021, ISSN: 20573960. DOI: 10.1038/s41524-021-00611-8.

A

SUPPLEMENTARY INFORMATION TO CHAPTER 2

A.1. EELSFITTER CODE USAGE

EELSFITTER is implemented into a python module, which is open source and available to download. In this section, a guide is provided for performing the basic steps of using EELSFITTER and performing effective data analysis. The package can first be installed into the python environment by `pip install eelsfitter`. Second, the package is imported as

```
import EELSFitter as ef
```

A.1.1. PRE-TRAINING PREPARATIONS

Loading a spectral image EELSFITTER is currently only capable of automatically processing images produced in Gatan's DigitalMicrograph: `.dm3`, `.dm4` and `.dm5`. To be able to process these files, EELSFITTER uses the ncempy.io.dm module. To load the spectral image, run:

```
image = ef.SpectralImage.load_dmfile(path_to_dm_file)
```

Alternatively, if the spectral image was in a different data format, simply load in the data manually as:

```
image = ef.SpectralImage(data)
```

Here data refers to the manually loaded data.

Clustering a spectral image The cluster method is based on K-means clustering, EELSFITTER uses the SCIKIT-LEARN implementation. One can choose the amount of clusters, and the value on which to cluster. For the latter, there are several options: `'sum'` (N_{tot}), `'log_sum'` ($\ln(N_{tot})$), `'log_peak'` ($\ln(N_{peak})$), `'log_zlp'` ($\ln(N_{zlp})$) and `'log_bulk'` ($\ln(N_{bulk})$) To cluster using the module, run:

```
image.cluster(n_clusters = K,
              based_on = value_mode)
```

Additionally, to help better choose the amount of clusters, one can plot the spectral image with the chosen value mode as a histogram by:

```
fig = image.find_optimal_amount_of_clusters(n_clusters = K,
                                            bins = n_bins,
                                            based_on = value_mode)
fig.show()
```

Here, bins refers to the amount of bins the data is plotted in. As this function produces a figure, it is necessary to plot the figure afterwards. In this function a Gaussian mixture model (GMM) is used to fit the data. The key here is to make the GMM fit the data as close as possible with as little clusters as possible. If the GMM does not fit the data well because of too little clusters, there will be too large of a spread in the ZLP models, reducing accuracy. On the opposite, too many clusters will lead to overfitting of the data as the spectra pool per clusters reduces.

Noise reduction The spectra in a spectral image can be noisy due to a variety of limitations, pooling the data can help reduce the noise while keeping the locality of features as much as possible. To pool the data, run the code:

```
image.data_pool = image.pool_image(image.data,
                                   area = n,
                                   gaussian = True)
```

This will create a new variable `image.data_pool` that can be called in the SpectralImage class. `area` indicates the area size around the pixel to be used for pooling. `gaussian = True` sets Gaussian weights to the surrounding pixels

A.1.2. Training ZLP models

Training the general models To train ZLP models for the spectral image, run the following code:

```
image.train_zlp_models(n_clusters = K,
                       based_on = value_mode,
                       n_replica = n_replica,
                       n_epochs = n_epochs,
                       shift_de1 = shift_dE1,
                       shift_de2 = shift_dE2,
                       path_to_models = path_to_models,
                       signal_type = 'EELS')
```

Here, in case there is no parallel training taking place, `n_replica` is directly related to the amount of models to be trained. `n_epochs` is the amount of epochs a replica is required to go through `shift_de1` and `shift_de2` are used to shift the hyperparameters dE_I and dE_{II}. Ideally, dE_I is placed near or on the onset of the scattering distribution and dE_{II}

is placed near or on the part where the contribution of the ZLP is negligible. How the hyperparameters are determined is described in detail in the main script. If the data is pooled, put `'pooled'` in `signal_type`, then the models are trained on pooled data.

If there is the option to train models in parallel (not by multi-threading, but by submitting individual jobs in parallel as done on HPC's), running the previous code is slightly altered:

```
image.train_zlp_models(n_clusters = K,
                       based_on = value_mode,
                       n_batch_of_replica = n_batch_of_replica,
                       n_batches = n_batches,
                       n_replica = n_replica,
                       n_epochs = n_epochs,
                       shift_de1 = shift_dE1,
                       shift_de2 = shift_dE2,
                       path_to_models = path_to_models,
                       signal_type = 'EELS')
```

There are two additional parameters here: `n_batches` refers to the amount of batches of replicas that need to be trained and `n_batch_of_replica` refers to the batch number of the replica batch that is currently trained, this is necessary for tracking of all the output files and ensure nothing is overwritten. Here `n_replica` × `n_batches` = *total number of models*

Generating general ZLP predictions from trained neural network To generate the ZLP models from the trained NN, the run the code:

```
zlps = image.get_zlp_models(integrated_intensity)
```

the `integrated_intensity` should match the `based_on` values that the models where trained on.

Matching general ZLP predictions to a specific spectrum To match the models to a specific spectrum, run the code:

```
zlps_matched = image.get_pixel_matched_zlp_models(i, j,
                                                  signal_type = 'EELS')
```

`i, j` are the y, x position of the pixels in the spectral image. Change `signal_type` to `'pooled'` to match on pooled data.

Loading in previously trained models After training models are automatically saved, these can be loaded back in by running:

```
image.load_zlp_models(path_to_models)
```

`path_to_models` points towards the folder with all the necessary files.

A.1.3. POST PROCESSING

Subtract ZLPs from spectrum Using a known ZLP, simply subtract this zlp from a spectrum by running the code:

```
signal_subtract = image.subtract_zlp(signal, zlp)
```

Deconvolute a spectrum Using a known ZLP, deconvolute a spectrum by Fourier Log deconvolution to remove plural scattering by running the code:

```
signal_ssd = image.deconvolution(signal, zlp, correction=True)
```

`correction` is used to remove a decreasing linear slope that sometimes occurs after deconvolution on the place of the ZLP. Set to `False` to disable.

Richardson-Lucy deconvolution Using a known ZLP, deconvolute a spectrum by Richardson-Lucy deconvolution to enhance features by running the code:

```
signal_rl = image.rl_deconvolution(signal, zlp, iterations = n)
```

Note that you cannot perform move Fourier Log and Richardson-Lucy deconvolution at the same time.

A.1.4. QUANTITATIVE ANALYSIS

To perform quantitative analysis on the spectral image, it is important to ensure the following acquisition parameters are set:

```
image.beam_energy
image.collection_angle
image.convergence_angle
```

Additionally, the refractive index and the mass density also need to be set. This can be done either as a global value or per cluster in case of multiple materials in the spectral image. One can run the following code for this:

```
image.set_refractive_index(n, n_background)
image.set_mass_density(rho, rho_background)
```

Remove the background variables in case they are not needed.

Thickness calculation With the previously set variables, it is now possible to calculate the thickness of a spectrum. Run the following code:

```
n_zlp = sum(zlp)

# Using refractive index
t = image.calc_thickness(signal_ssd, n, n_zlp)

# Using mass density
t = image.calc_thickness(signal, rho, n_zlp)
```

Complex dielectric function from KKA To calculate the complex dielectric function, run the code:

```
n_zlp = sum(zlp)

# Using refractive index
eps, t, signal_surface = image.kramers_kronig_analysis(signal_ssd,
                                                       n, n_zlp,
                                                       iterations = 5)

# Using thickness
eps, t, signal_surface = image.kramers_kronig_analysis(signal_ssd,
                                                       t, n_zlp,
                                                       iterations = 5)
```

The functions always has three outputs: the complex dielectric function `eps`, the thickness and the surface scattering. In case of using the refractive index and setting `iterations = 1`, the output for the thickness will be exactly the same as `calc_thickness` using the refractive index, since both methods are then exactly the same. with 2 or more iterations the output are updated every iteration. In case of using the thickness as input, it will not be updated on each iteration as it is a fixed quantity in this case, thus `t input` is the same as `t output`.

A.1.5. PLOTTING IN EELSFITTER

For consistency between EELSFITTER figures, a few plotting functions have been built in to easily plot a figure that encompasses the necessary information.

Plotting hyperparameters After training models, plot the location of the hyperparameters ΔE_I and ΔE_{II} by running the following code:

```
fig = im.train_zlps.plot_hp_cluster(title="Position of dE1 & dE2 per cluster",
                                    xlabel="Energy loss [eV]",
                                    ylabel="Intensity [a.u.]",
                                    xlim=[xmin, xmax],
                                    ylim=[ymin, ymax],
                                    yscale='log')
fig.show()
```

Here the figure is already given a title, axis labels, axis limits and a different *yscale*.

Plotting models To check the ZLP models per pixel, run the code:

```
fig = plot_zlp_per_pixel(im,
                         pixx=i, pixy=j,
                         signal_type='EELS',
                         zlp_gen=True, zlp_match=True,
                         subtract=False, deconv=True,
```

```
                                     hyper_par=True, random_zlp=None,
                                     xlabel="Energy loss [eV]",
                                     ylabel="Intensity [a.u.]",
                                     xlim=[xmin, xmax],
                                     ylim=[ymin, ymax])
fig.show()
```

Depending on which aspect to plot, set either `True` or `False`. For `random_zlp` fill in a random number and it will plot randomly selected zlp models. Here the plot is already given axis labels and axis limits.

It is also possible to plot the zlp models per cluster, run the code:

```
fig = plot_zlp_per_cluster(im,
                              cluster=n,
                              signal_type='EELS',
                              zlp_gen=True, hyper_par=False,
                              xlabel="Energy loss [eV]",
                              ylabel="Intensity [a.u.]",
                              xlim=[xmin, xmax],
                              ylim=[ymin, ymax])
fig.show()
```

Here it is only available to plot the general predictions and the hyperparameters on top of the cluster spread.

Plotting heatmaps To easily plot a consistent looking heatmap, regardless of the shape of the spectral image, there is a built in function for this purpose, run the code:

```
hmap = plot_heatmap(im,
                    data=im.cluster_labels,
                    cbarlabel='Cluster ID',
                    discrete_colormap=True,
                    cmap='coolwarm')
hmap.show()
```

This example plots the cluster labels after clustering the spectral image. If the heatmap has discretized values, enable the `discrete_colormap` variable, otherwise set to `False` or remove. For a different colourmap, simply fill in another value in `cmap`, check the MATPLOTLIB documentation for options.

B

SUPPLEMENTARY INFORMATION TO CHAPTER 3

B.1. METHODS

STEM-EELS measurements. The settings for the STEM-EELS measurements corresponding to the WS_2 specimen were acquired with a JEOL 2100F microscope with a cold field-emission gun equipped with aberration corrector operated at 60 kV. A Gatan GIF Quantum was used for the EELS analyses. The convergence and collection semi-angles were 30.0 mrad and 66.7 mrad respectively. The EELS data corresponding to the InSe specimen were collected in a ARM200F Mono-JEOL microscope equipped with a GIF continuum spectrometer and operated at 200 kV. For these measurements, a slit in the monochromator of 1.3 μm was used. A Gatan GIF Quantum was used for the EELS analyses with convergence and collection semi-angles of 23.0 mrad and 21.3 mrad respectively. The aperture of the spectrometer was set to 5 mm. For the STEM imaging and EELS analyses, a probe size of 8C and a camera length of 12 cm were used.

Photoluminescence measurements. The optical spectra are acquired using a home-built spectroscopy set-up. The sample is illuminated through an 0.85 NA Zeiss 100x objective. The excitation source is a continuous wave laser with a wavelength of 595 nm and a power of 1.6 mW/mm^2 (Coherent OBIS LS 594-60). The excitation light is filtered out using colour filters (Semrock NF03-594E-25 and FF01-593/LP-25). The sample emission is collected in reflection through the same objective as in excitation, and projected onto a CCD camera (Princeton Instruments ProEM 1024BX3) and spectrometer (Princeton Instruments SP2358) via a 4f lens system.

B.2. STRUCTURAL CHARACTERISATION OF THE INSE SPECIMEN

Here we provide details on the structural characterisation of the n-doped InSe specimens. Each specimen is composed by a InSe nanosheet exhibiting a range of thicknesses. The electronic properties of InSe, such as the band gap value and type, are sensitive to both the layer stacking (β, γ, or ε-phase) as well as to the magnitude and type of doping [1]–[4]. In particular, n-doped ε-phase InSe has been reported to exhibit a direct bandgap with value $E_{\text{bg}} = 1.25$ eV [5].

These InSe specimens have been grown by means of the Bridgman-Stockbarger method. Doping with Sn impurities is used to obtain n-type InSe. InSe flakes are obtained from bulk material by the sonication procedure [6], whereby single InSe crystals are pulverized and added to IPA with a ratio of 2:1 (mg:ml). This combination is then sonicated in a sonic bath for 6 hours while keeping the temperature in the range between 25 °C and 35 °C. The ultra high frequencies lead to gas formation between the layers of the material, building up pressure until adjacent layers split apart. The flakes in the resulting suspension are then collected and dispersed on top of a TEM grid by pipetting.

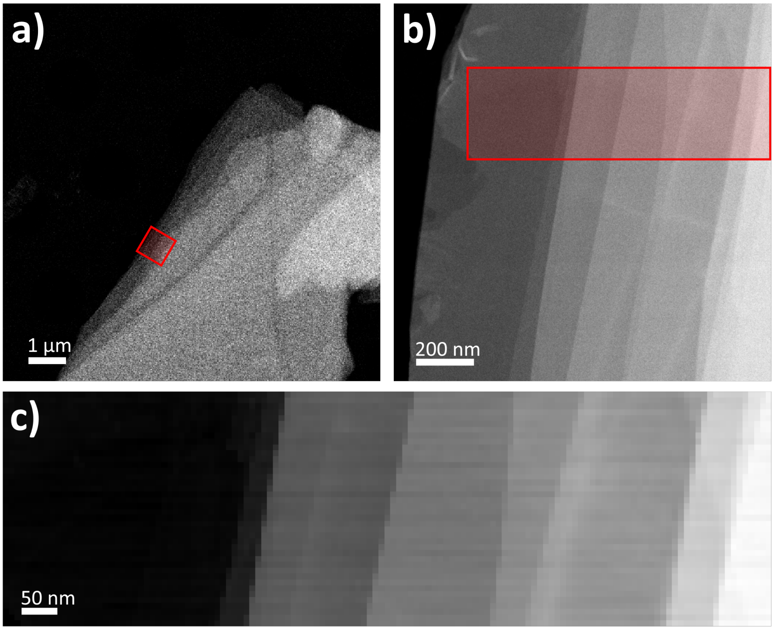

Figure B.1: **(a)** Low-magnification HAADF-STEM image of one of the n-doped InSe specimens analysed in this work. **(b)** Magnification of the region indicated with a red square in (a). **(c)** EELS-SI acquired on the region indicated with a red rectangle in (b). Note that the grey-scale is different in each panel.

Figure B.1a displays a low-magnification High-Angle Annular Dark Field (HAADF) STEM image of one of the specimens obtained from this procedure. The flake is lying on top of the holey carbon grid, and most of its volume is on top of the vacuum. Figure B.1b shows then a magnification of the region indicated with a red square in B.1a, while in turn the red rectangle in B.1b marks the region where the corresponding EELS-SI, provided in Figure B.1c, has been extracted. The spatial resolution in this EELS-SI is around 8 nm. Note that the (artificial) grey-scale convention adopted is different in Figure B.1b and c. It can be observed that most of the flake turns out to be bulk, exhibiting thicknesses of several monolayers at least, with some thinner regions at the edges.

In order to identify the crystalline phase of the specimen under consideration, Figure B.2a displays a low-magnification HAADF-STEM image of a different InSe flake. This flake has been obtained from the same bulk material as that of Figure B.1a and hence shares its crystalline structure. Notice how this InSe flake is standing on top of a hole of the TEM grid. Figure B.2b then shows a high-resolution HAADF-STEM image corresponding to the red square in B.2a, and whose inset highlights the atomic arrangement in the region indicated with a red square. Figure B.2c provides the HAADF intensity line profile taken along the blue rectangle in B.2b, where the three colours correspond to the three-fold periodicity observed in the line profile. HAADF-STEM images are approximately proportional to $Z^{1.7}$, with Z being the atomic number. By comparing with the expectations based on possible atomic models, these images provide useful information to identify the underlying crystalline sequence. The line profile of Figure B.2c is consistent with the atomic model of ε-phase InSe shown in Figure B.2d, both for top-view and for cross-view, and which uses the same choice of colours as in Figure B.2c. The

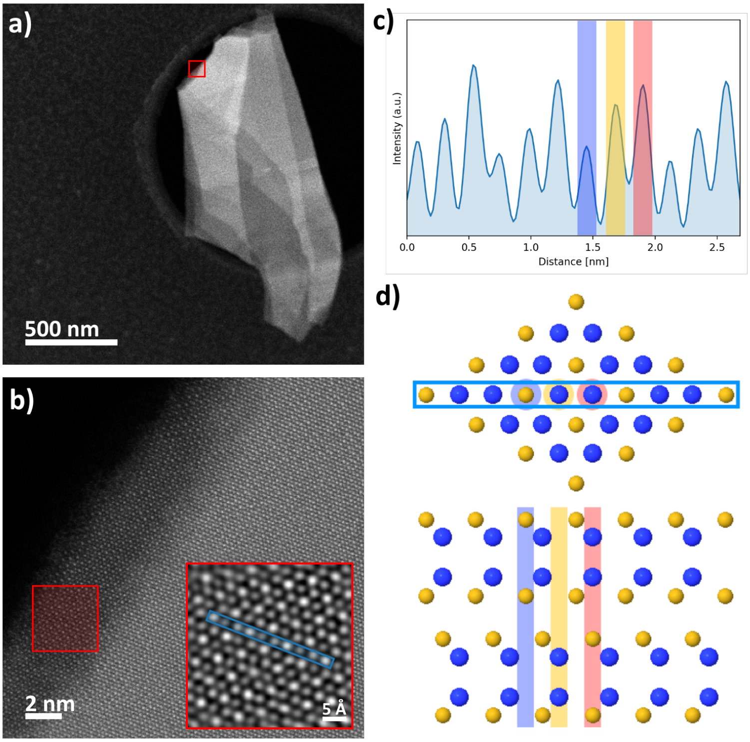

Figure B.2: **(a)** Low-magnification HAADF-STEM image of another n-doped InSe flake standing on top of a hole in the TEM grid. **(b)** High-resolution HAADF-STEM image acquired in the red square in (a), where the inset highlights the atomic crystalline structure. **(c)** HAADF intensity line profile taken along the blue rectangle in (b), where the three colors correspond to the three-fold periodicity observed in the line profile. **(d)** Atomic model of ε-phase InSe, with the same choice of colours labelling the atomic layers as in (c), displaying top-view (upper) and cross-view (lower panel).

structural analysis presented in Figure B.2 indicates that the n-doped InSe specimens considered in this work exhibit a crystalline structure characterised by a pure ε-phase.

In order to further elucidate the type of the band gap exhibited by this material, photoluminescence (PL) measurements are carried out. The results, displayed in Figure B.3, exhibit a well-defined peak located around 1.26 eV. Hence, we conclude that this material is characterised by a direct band gap with energy value $E_{\mathrm{bg}} \approx 1.26$ eV, consistent with the findings of [5]. Note that PL measurements are characterised by a limited spatial resolution as compared to the STEM-EELS results, and therefore this band gap value corresponds to an average across the specimen. Hence, PL results are not sensitive to spatially-resolved features in the band gap map such as those reported in Fig. 3.3b of the main manuscript.

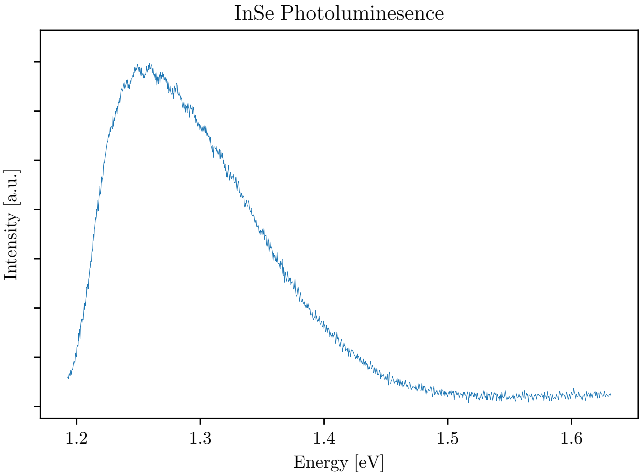

Figure B.3: Photoluminescence spectrum acquired in the n-doped InSe specimen. A well-defined peak, is observed indicating that this material is characterised by a direct bandgap with energy value $E_{\mathrm{bg}} \approx 1.26$ eV.

B.3. BAND GAP ANALYSIS OF 2H/3R WS_2 NANOFLOWERS

Here we apply our new approach to the band gap analysis of same WS_2 specimen considered in the original study [7], [8]. This specimen consisted on a horizontally-standing WS_2 flake belonging to flower-like nanostructures characterised by a mixed 2H/3R polytypism. While [8] restricted its band gap analysis to a small subset of individual EELS spectra, here we extend it to the whole specimen and as a by-product also we provide the local thickness map. The goal is to demonstrate how our updated analysis is consistent with the results presented in [8]. The corresponding results for the dielectric function are presented in Section 3.4.2.

Figure B.4 displays the outcome of the thickness map determination obtained using the EELS-SI from Figure 5.1a of [8] as input. Figure B.4a shows the results of the K-means clustering procedure for $K = 5$. The choice of $K = 5$ clusters is found to be a good compromise between minimising the variance within each cluster while ensuring a sufficiently large number of members, as required by the applicability the Monte Carlo replica method. The WS_2 specimen itself turns out to be classified into three thickness clusters, surrounded by vacuum (dark blue) at the top and by the Si_3N_4 substrate (red) in the bottom-right region of the map. Then Figure B.4b displays the corresponding thickness map evaluated by means of Equation (3.1). Note that the image has been masked by retaining only the pixels associated to the WS_2 specimen, to ease visualisation. The qualitative agreement with the outcome of the K-means clustering confirms the reliability of the total integrated intensity N_{tot} as a suitable proxy for the local specimen thickness when modelling the ZLP parametrisation.

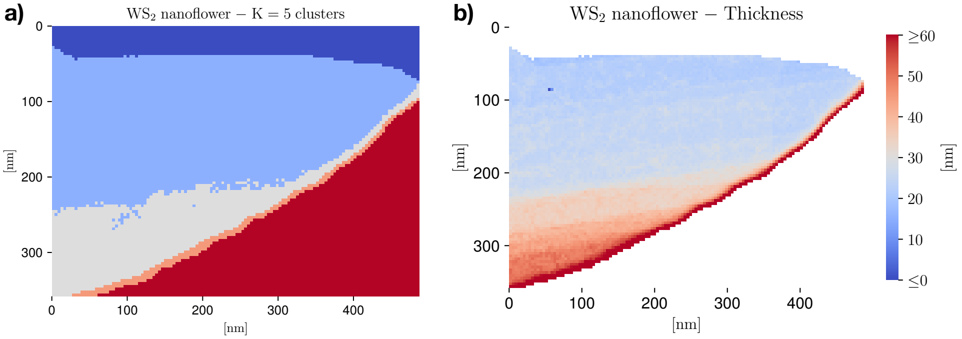

Figure B.4: Thickness analysis obtained from the EELS-SI presented in Fig. 5.1(a) of [8] as input. The specimen under consideration is a horizontally-standing flake belonging to a 2H/3R polytypic WS_2 flower-like nanostructure. **(a)** The outcome of the K-means clustering procedure for $K = 5$. **(b)** The resulting thickness map. Only pixels associated to the WS_2 specimen are displayed.

Figure B.5 then presents the corresponding band gap analysis obtained from the same EELS-SI used to evaluate Figure B.4, where again the maps have been filtered such that only those pixels corresponding to the WS_2 specimen are retained. First of all, Figure B.5(a) displays the spatially-resolved map displaying the median value of the band gap energy E_{bg} evaluated across the WS_2 specimen, where the spatial resolution achieved is around 10 nm. These band gap energies have been obtained from the procedure described in Section 3.3, specifically by fitting Equation (3.7) to the onset of the inelastic spectra. A fixed value of the exponent $b = 1.5$, corresponding to the indirect band gap reported for this material, is used to stabilise the model fit. Then Figure B.5(b) shows the associated relative uncertainty δE_{bg} on the extracted band gap energy. It is estimated as half the magnitude of the 68% CL interval (corresponding to one standard deviation for a Gaussian distribution) from the Monte Carlo replica sample for each pixel of the SI. One finds that the typical uncertainties δE_{bg} range between 15% and 25%. Finally, Figure B.5(c) indicates the lower limit of the 68% CL interval for E_{bg}.

Reference [8] reported a value of the band gap of 2H/3R polytypic WS_2 of $E_{\text{bg}} = (1.6 \pm 0.3)$ eV with a exponent of $b = 1.3^{+0.3}_{-0.7}$ extracted from single EELS spectrum. From the spatially-resolved band gap maps of Figure B.5, one observes how our updated results are in agreement with those from the previous study within uncertainties. Furthermore, this spatially-resolved determination of E_{bg} is in agreement within uncertainties with first-principles calculations based on Density Functional Theory (DFT) of the band structure of 2H/3R polytypic WS_2 [9]. These DFT calculations, which also account for

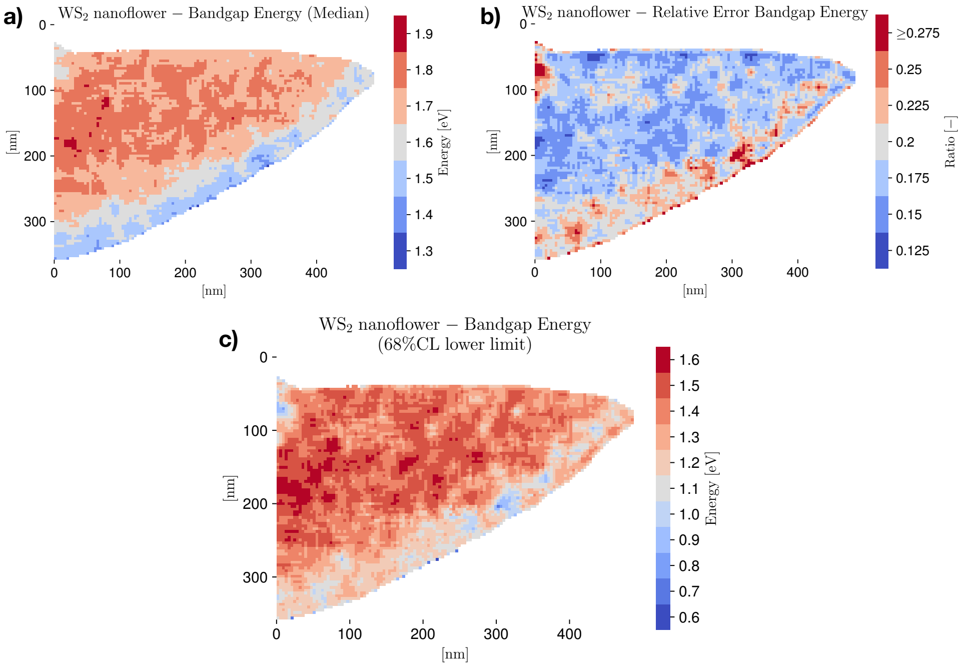

Figure B.5: Band gap analysis of the same EELS-SI used to evaluate Figure B.4. **(a)** Spatially-resolved map displaying the median value of the band gap energy $E_{\rm bg}$ evaluated across the specimen. **(b)** Same as (a) for the corresponding relative uncertainty $\delta E_{\rm bg}$, evaluated as half of the 68% CL interval from the Monte Carlo replica sample. **(c)** Same as (a) indicating the lower limit of the 68% CL interval for $E_{\rm bg}$. In the three panels, the maps have been filtered such that only those pixels corresponding to the WS$_2$ specimen are retained.

spin-orbit coupling effects, find values of $E_{\rm bg}$ in the range between 1.40 eV and 1.48 eV depending on the settings of the calculation. The DFT predictions are hence consistent with the 68% CL interval for the $E_{\rm bg}$ for a wide region of the specimen, as indicated by Figure B.5(c).

Furthermore, inspection of the thickness and band gap maps, Figures B.4b and B.5a respectively, reveals an apparent dependence of the value of $E_{\rm bg}$ on the local specimen thickness. Specifically, the band gap energies tend to increase in the thinner region of the specimen, with $t \approx 25$ nm, and then to decrease as one moves towards the thicker regions with $t \approx 50$ nm. While this dependence with the thickness is suggestive of the known property of WS$_2$ that $E_{\rm bg}$ increases when going from bulk to monolayer form, uncertainties remain too large to be able to assign significance to this effect.

B.4. Validation of Kramer-Krönig analysis against HyperSpy

The calculations of the local specimen thickness, Equation (3.1), and of the complex dielectric function, Equation (3.17) presented in this work have been benchmarked with the corresponding implementation available within the HyperSpy framework [10]. Provided one inputs the same inelastic spectra and ZLP parametrisation, agreement between the two calculations is obtained. This benchmark is illustrated in Figure B.6, which compares the EELSFITTER-based results with those available from HYPERSPY separately for the real and imaginary components of the dielectric function. Both calculations use for the same input ZLP and inelastic spectra, associated to a representative pixel of the WS_2 nanoflower specimen. Residual differences can be attributed to implementation differences e.g. for the discrete Fourier transforms. This validation test further confirms the robustness of the calculations presented in this work.

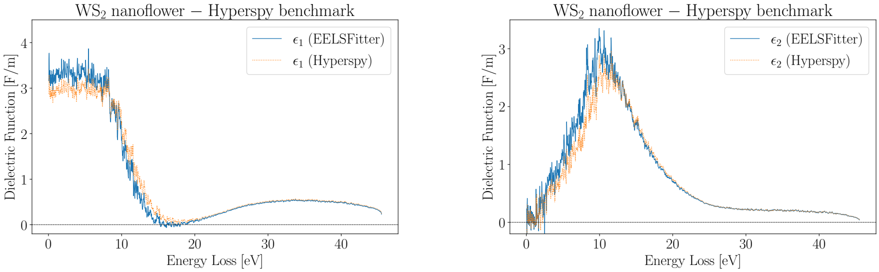

Figure B.6: Comparison of the EELSFITTER-based results for the real (left) and imaginary (right panel) components of the dielectric function with those available from HYPERSPY for the same input ZLP and inelastic spectrum, associated to a representative pixel of the WS_2 nanoflower specimen.

REFERENCES

[1] B. Gürbulak, M. Şata, S. Dogan, S. Duman, A. Ashkhasi, and E. F. Keskenler, "Structural characterizations and optical properties of inse and inse:ag semiconductors grown by bridgman/stockbarger technique", *Physica E: Low-Dimensional Systems and Nanostructures*, vol. 64, pp. 106–111, 2014, ISSN: 13869477. DOI: 10.1016/j.physe.2014.07.002.

[2] C. M. Julien and M. Balkanski, "Lithium reactivity with iii-vi layered compounds", *Materials Science and Engineering: B*, vol. 100, pp. 263–270, 3 Jul. 2003, ISSN: 09215107. DOI: 10.1016/S0921-5107(03)00113-2.

[3] J. Rigoult, A. Rimsky, and A. Kuhn, "Refinement of the 3r γ-indium monoselenide structure type", *Acta Crystallographica Section B Structural Crystallography and Crystal Chemistry*, vol. 36, pp. 916–918, 4 1980, ISSN: 05677408. DOI: 10.1107/s0567740880004840.

[4] S. Lei, L. Ge, S. Najmaei, *et al.*, "Evolution of the electronic band structure and efficient photo-detection in atomic layers of inse", *ACS Nano*, vol. 8, pp. 1263–1272, 2 Feb. 2014, ISSN: 19360851. DOI: 10.1021/nn405036u.

[5] H. Henck, D. Pierucci, J. Zribi, *et al.*, "Evidence of direct electronic band gap in two-dimensional van der waals indium selenide crystals", *Physical Review Materials*, vol. 3, 3 Mar. 2019, ISSN: 24759953. DOI: 10.1103/PhysRevMaterials.3.034004.

[6] E. Petroni, E. Lago, S. Bellani, *et al.*, “Liquid-phase exfoliated indium–selenide flakes and their application in hydrogen evolution reaction”, *Small*, vol. 14, pp. 1–11, 26 2018, PT12- Sonication technique to split layers- IPA used as solvent2 mg of TI per 1 ml IPASonicated for 6hSolutions centrifuged at 1000, 2500 or 5000 rpm for 30 min., ISSN: 16136829. DOI: `10.1002/smll.201800749`.

[7] S. E. van Heijst, M. Mukai, E. Okunishi, *et al.*, “Illuminating the electronic properties of ws2 polytypism with electron microscopy”, *Annalen der Physik*, vol. 533, 3 Mar. 2021, ISSN: 15213889. DOI: `10.1002/andp.202000499`.

[8] L. I. Roest, S. E. van Heijst, L. Maduro, J. Rojo, and S. Conesa-Boj, “Charting the low-loss region in electron energy loss spectroscopy with machine learning”, *Ultramicroscopy*, vol. 222, p. 113 202, 2021, ISSN: 0304-3991. DOI: `https://doi.org/10.1016/j.ultramic.2021.113202`.

[9] L. Maduro, S. E. van Heijst, and S. Conesa-Boj, “First-principles calculation of optoelectronic properties in 2d materials: The polytypic ws2 case”, *ACS Physical Chemistry Au*, vol. 2, pp. 191–198, 3 May 2022, ISSN: 26942445. DOI: `10.1021/acsphyschemau.1c00038`.

[10] F. de la Peña, E. Prestat, V. T. Fauske, *et al.*, *Hyperspy/hyperspy: Release v1.6.3*, version v1.6.3, Jun. 2021. DOI: `10.5281/zenodo.4923970`.

C

SUPPLEMENTARY INFORMATION TO CHAPTER 4

C.1. CASE STUDY: 1D-MoS_2 NANOSTRUCTURES

C.1.1. METHODS

Synthesis of the 1D-MoS_2 nanostructures The 1D-MoS_2 nanostructures were synthesized using chemical vapour deposition (CVD) on a TEM grid. The TEM grid used in this study consisted of nine viewing windows with a Si_3N_4 thin film spanning across the entire grid (EMS Catalog #76042). To initiate the synthesis, a small amount of MoO_2 (99 %, Sigma-Aldrich 234761) was drop-casted onto the TEM grid. This involved using a solution containing 2.6 mg of MoO_2 suspended in 6 ml of isopropanol. The grid, with the MoO_2 precursor, was then positioned in an alumina crucible, approximately 2 cm away from 7.5 mg of MoO_2 powder.

The experimental setup included a gradient tube furnace from Carbolite Gero, with the alumina crucible placed in the middle of the furnace. Upstream from this crucible, another alumina crucible contained 400 mg of sulfur (99.5 %, Alfa Aesar 10785). Throughout the synthesis process, argon was used as a carrier gas at a flow rate of 100 sccm. The middle zone of the furnace was heated to 780 °C, while the sulfur reached a maximum temperature of 270 °C. It is noteworthy that a small fraction of the resulting nanostructures exhibited MoO_3 cores instead of MoS_2. This indicates that the sulfurization process was not fully completed for these particular nanostructures. Additionally, it was observed that the MoO_2 powder used as a seed material during the synthesis underwent a conversion to MoO_3. The confirmation of this conversion from MoO_2 to MoO_3 was achieved trough the mapping of the bulk plasmon characteristic of MoO_3. This analysis is depicted in Figure C.3. This growth procedure results into 1D-MoS_2 nanostructures exhibiting the 2H crystal phase.

C.1.2. CHARACTERIZATION OF 1D-MoS_2 NANOSTRUCTURES

Figure C.1 provides a representative overview of high-angle annular dark-field (HAADF) scanning transmission electron microscope (STEM) images of the 1D-MoS_2 nanostructures synthesised following the procedure described in the Methods section in the main manuscript. Their lengths vary between 90 nm and 2450 nm with an average length of 960 nm, while their diameters range from 40 nm to 95 nm with an average value of 60 nm. A fraction of these 1D-MoS_2 nanostructures end up being connected by their endpoints generating to novel morphologies, as shown in Figure C.1e,f. Figure C.2 displays HAADF-STEM images of two other specimens with 1D-MoS_2 nanostructures connected by one end. The top and bottom nanostructure in Figure C.2a have a length of 540 nm and 336 nm respectively, while their diameters are 57 nm and 62 nm respectively. STEM-EELS analysis of this specimen is presented in Figure 4.5 4 in the main manuscript. The left and right nanostructure in Figure C.2b have a length of 349 nm and 278 nm respectively, while their diameters are 64 nm and 44 nm respectively. The STEM-EELS analysis corresponding to this specimen is presented in Figure C.4.

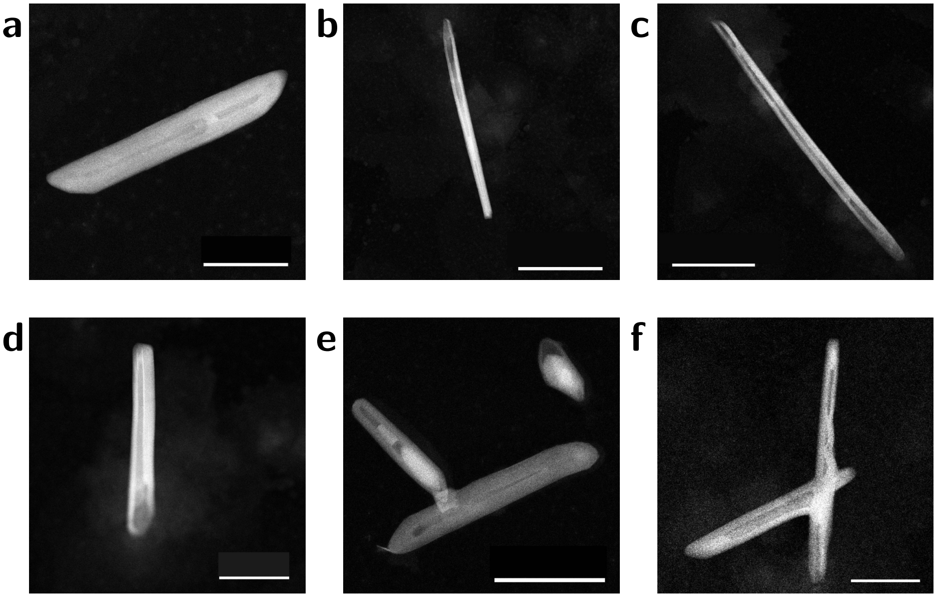

Figure C.1: **HAADF-STEM images of representative 1D-MoS_2 nanostructures.** **(a)-(d)** Images of individual nanostructures. **(e)-(f)** Same as **(a)-(d)** for nanostructures connected by one end. The size of the scale bar is 100 nm in panel **(a)**, 500 nm in panels **(b)-(c)**, and 200 nm in panels **(d)-(f)**.

C.1.3. PARTIAL SULFURIZATION AND INTERMEDIATE MoO_3 FORMATION

Figure C.3a displays the HAADF-STEM image of a nanostructure that, as a result of incomplete sulfurization during the synthesis process, exhibits a MoO_3 core. This MoO_3 core is identified by tracking the location of the bulk plasmon peak across the specimen specimen in Figure C.3b. It is observed that the bulk plasmon peak undergoes a shift as

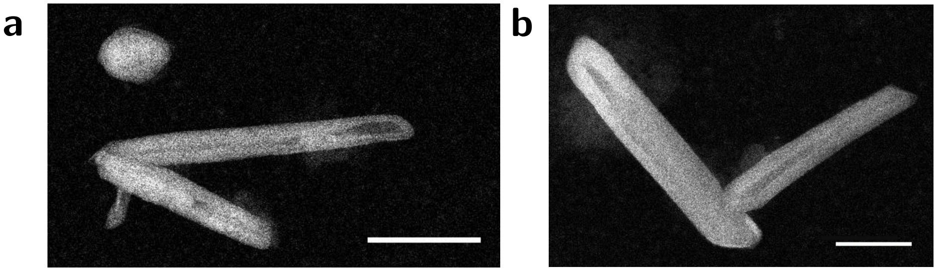

Figure C.2: **HAADF-STEM images of 1D-MoS_2 nanostructures connected by one end. (a)** The top (bottom) nanostructure has a length of 540 nm (336 nm) and a width of 57 nm (62 nm). The MoS_2 region visible in the top-left is a remnant of the synthesis procedure. **(b)** The left (right) nanostructure has a length of 349 nm (278 nm) and a width of 64 nm (44 nm). The size of the scale bar is 200 nm. The STEM-EELS analyses of **a** and **b** are presented in Fig. 4 in the main manuscript and in Fig. C.4 respectively.

we move from the edge to the inner region. Initially, at the edge regions, the peak is at 22.5 eV, which corresponds to MoS_2 [1]–[5]. However, towards the inner region, the peak shifts to approximately 25 eV, matching the expected location of the bulk plasmon of MoO_3 [6]–[8]. This observation suggests that the MoO_2 powder used as a seed material in the CVD synthesis process undergoes an intermediate conversion to MoO_3 before it can fully transform into MoS_2. Ensuring complete sulfurization of the 1D-MoS_2 nanostructures is therefore essential to avoid these MoO_3 remnants.

C.1.4. EELS ANALYSIS OF AN INTERCONNECTED 1D-MoS_2 NANOSTRUCTURE

Here we present the spatially-resolved EELS analysis of another specimen composed by two 1D-MoS_2 nanostructures connected by one end, for which the corresponding HAADF-STEM image is displayed in Figure C.2b. Figure C.4a reveals characteristic peaks at specific energies. We display spectra taken at various locations in the sample in Figure C.4b. Spectrum 1 (sp1) exhibits a peak at approximately 1.9 eV, while sp2 displays a distinct peak centred around 2.7 eV. Furthermore, sp3 showcases peaks at both 1.9 eV and 3.0 eV, and sp4 exhibits peaks at both 3.0 eV and 8.3 eV.

Concerning the spatial distribution of these enhanced-intensity features, displayed in Figure C.4c-f, in the $[1.8, 2.0]$ eV range the intensity is largest at the tips of nanostructures. For the interval $[2.6, 2.8]$ eV, there is an enhancement in intensity visible along the edges in the middle regions of the nanostructures. In the $[2.9, 3.1]$ eV range, the signal is largest along the edge in the middle region of the left nanostructure, as well as at its tip. In the interval $[8.2, 8.4]$ eV, the intensity is strongest in the inner part of the nanostructures. These results are consistent with those obtained from the interconnected 1D-MoS_2 nanostructure analysed in Figure 4.3 of the main manuscript.

C.1.5. BAND GAP ENERGY MAP OF 1D-MoS_2 NANOSTRUCTURES

For the specimen analysed in section C.1.4, we provide here the results of the corresponding spatially-resolved band gap analysis, like is done in the main manuscript. The

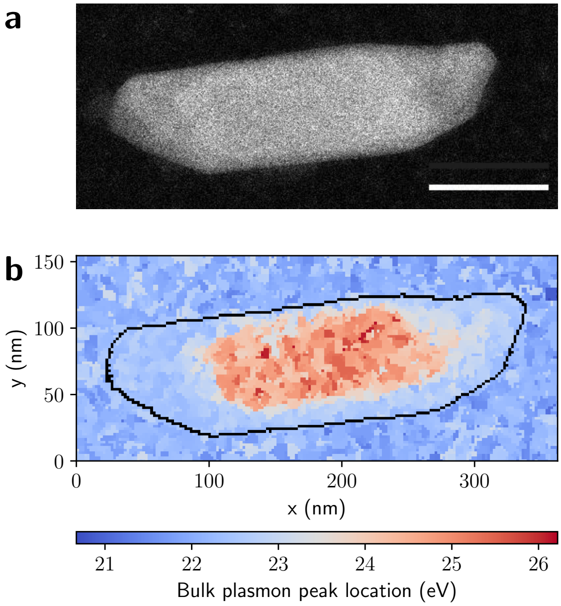

Figure C.3: **Analysis of a 1D-MoS_2 nanostructure with incomplete sulfurisation.** **(a)** HAADF-STEM image of a nanostructure for which the sulfurization process was not fully complete. **(b)** The bulk plasmon peak energy across the specimen, where the black line indicates its boundary.

spatially-resolved band gap map is presented in Fig. C.5. Additionally, the weighted average band gap energies E_{bg} over the different regions in the nanostructure are summarised in Table C.1. As in the case of the 1D-MoS_2 nanostructures analysed in the main manuscript, we obtain that in the central region of the specimen the value of E_{bg} agrees with the MoS_2 bulk band gap, and that this value is reduced in the endpoint regions due to the presence of curvature-induced local strain. This analysis further indicates that our findings of reduced E_{bg} in strain-enhanced regions are robust and reproducible.

Table C.1: The weighted average for E_{bg} (in eV) for the 1D-MoS_2 nanostructure analysed in Fig. C.5, separated into three regions: the left-most endpoint (20% of the total length of the nanostructure), the central region (60%), and right-most endpoint (20%). We also indicate the uncertainty obtained from the 90% CL interval for the weighted average band gap energy.

Specimen	**Left-most endpoint**	**Central region**	**Right-most endpoint**
Fig. C.4 left	1.0 ± 0.2	1.2 ± 0.2	1.0 ± 0.1
Fig. C.4 right	1.1 ± 0.2	1.4 ± 0.2	1.1 ± 0.2

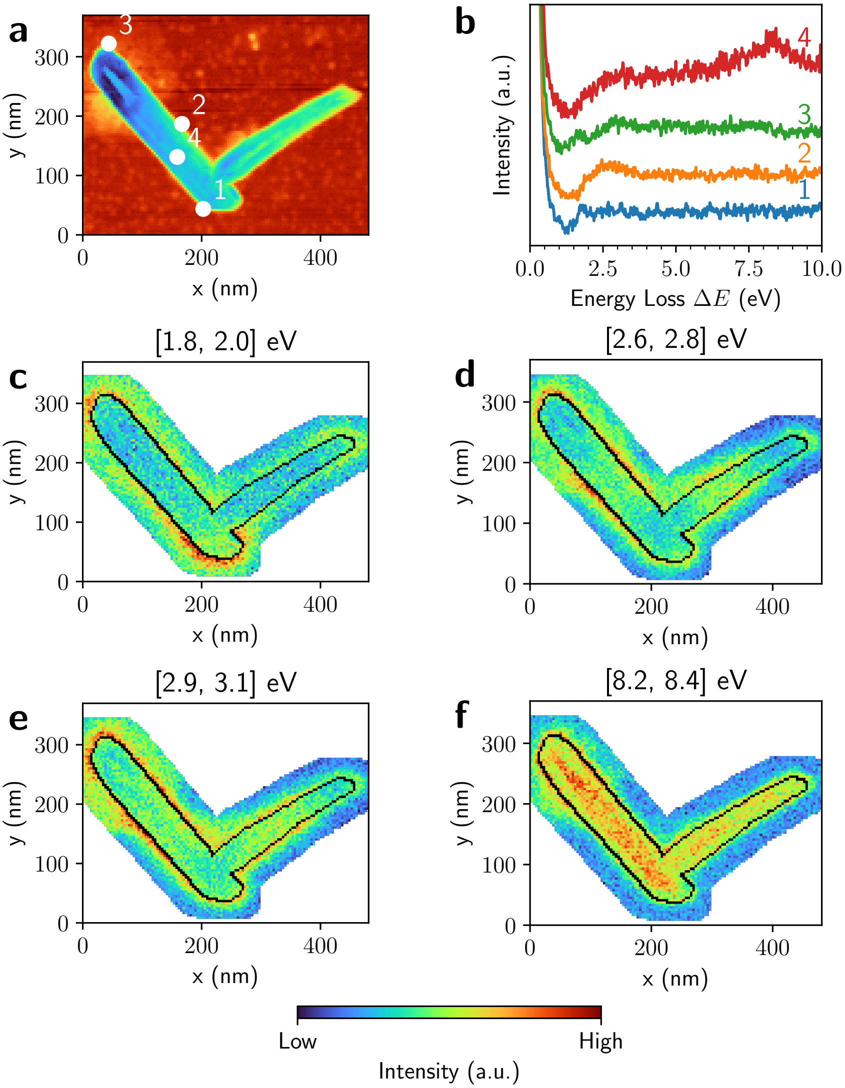

Figure C.4: **EELS analysis of MoS$_2$ nanostructures connected by one end.** Same as Figure 4.3 in the main manuscript, now for two 1D-MoS$_2$ nanostructures, with a length of 349 nm and a diameter of 64 nm (left), and a length of 278 nm and a diameter of 44 nm (right), connected by their ends. The corresponding HAADF-STEM image is provided in Figure C.2b.

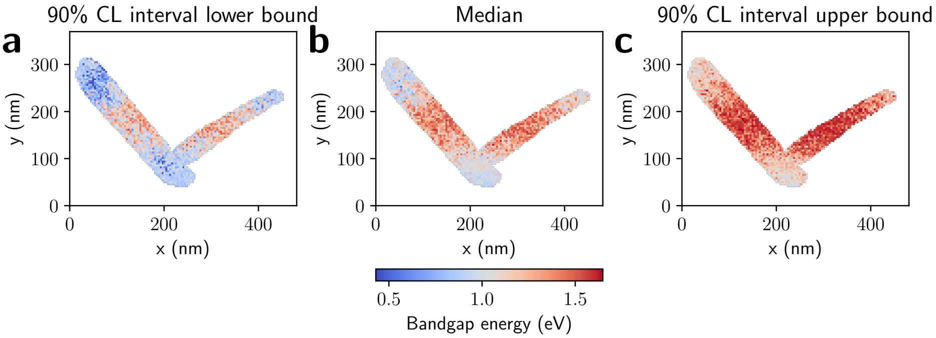

Figure C.5: **Spatially-resolved band gap energy in a 1D-MoS$_2$ nanostructure**. The median value (second column) and 90% CL lower and upper bounds (first and third column, respectively) for the band gap energy E_{bg} determined across the entire 1D-MoS$_2$ nanostructures considered in Figure C.4.

C.2. Case study: Topological Insulator Bi$_2$Te$_3$

C.2.1. Methods

Specimen preparation The specimen used in this study were Bi$_2$Te$_3$flakes that were mechanically exfoliated from bulk crystals through sonication in isopropanol (IPA) at a ratio of 2 mg of Bi$_2$Te$_3$per 1 ml of IPA. The exfoliated flakes were then transferred onto holey carbon grids for EELS investigations.

STEM-EELS settings The scanning transmission electron microscopy (STEM) images and electron energy-loss/gain spectra were obtained using a JEOL200F monochromated equipped with aberration corrector and a Gatan Imaging Filter (GIF) continuum spectrometer. The instrument was operated at 200 kV and the convergence semi-angle was 14 mrad. The collection semi-angle for EELS acquisition was 18.3 mrad obtained by inserting a 5 mm EELS entrance aperture. The EELS dispersion was 50 meV per channel.

C.2.2. Atomic structure characterisation of Bi$_2$Te$_3$

Figure C.6 presents the STEM analysis of the Bi$_2$Te$_3$ specimen considered in the main manuscript. Figure C.6a shows a low-magnification high-angle annular dark-field (HAADF) STEM image taken on the same Bi$_2$Te$_3$ crystal inspected by EELS. The corresponding atomic-resolution HAADF-STEM image of the region indicated with a blue square in Figure C.6a is displayed in Figure C.6b. As well known, Bi$_2$Te$_3$ is characterised by a hexagonal primitive cell. From the corresponding fast Fourier transform (FFT), Figure C.6c, it is found that this Bi$_2$Te$_3$ crystal is oriented along the $[-1\ 1\ 1]$ direction. Figure C.6d shows an atomic model of the Bi$_2$Te$_3$ crystal viewed along the same $[-1\ 1\ 1]$ direction, displaying the characteristic hexagonal crystal structure of Bi$_2$Te$_3$.

C.2.3. Robustness of the models

The robustness of the results presented in this work upon variations of the model assumed for the ZLP is demonstrated by repeating the analysis using other functional forms for the ZLP model. Specifically, in addition to the Gaussian model Equation (4.1) we consider a split Gaussian function, a Pearson VII function, and a Pseudo-Voigt function to parametrise the ZLP, all other aspects of the fitting procedure unchanged. These three models are described below and have been considered in the EELS literature in the context of the ZLP subtraction.

Split Gaussian function. This model is the same as the Gaussian function of Equation (4.1) with the difference that the variance is different at the left side and at the right side of the peak. An asymmetric model such a split Gaussian may be more adequate to describe the ZLP in the presence of an intrinsic asymmetry in the energy loss ΔE.

Pearson VII function. This function is often used to describe peak shapes from X-ray powder diffraction patterns [9] and is defined as

$$I(\Delta E) = I_{\max} \frac{w^{2m}}{\left[w^2 + \left(2^{1/m} - 1\right)(\Delta E - \Delta E_0)^2\right]^m} , \tag{C.1}$$

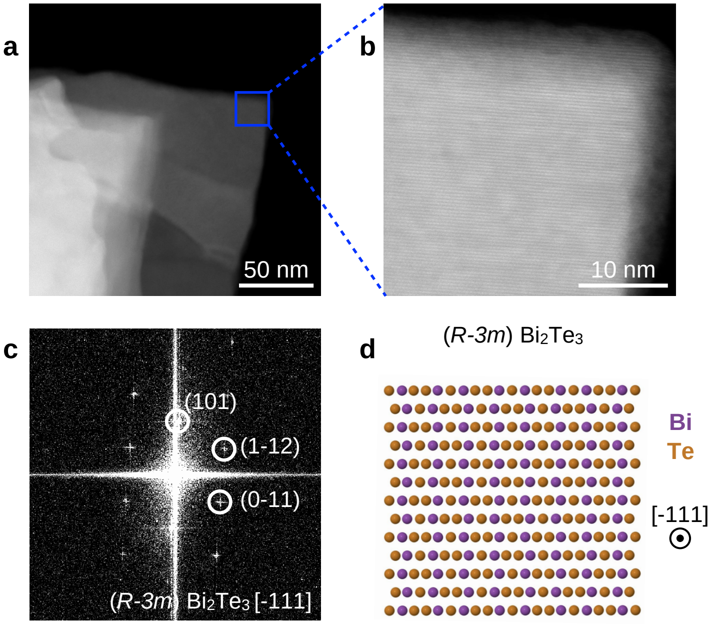

Figure C.6: **STEM analysis of the Bi_2Te_3 crystal analysed.** **(a)** Low-magnification HAADF-STEM image of the Bi_2Te_3 specimen considered in this work. **(b)** Atomic-resolution HAADF-STEM image of the region indicated with a blue squared in (a). The Bi_2Te_3 crystal is oriented along the $[-1\ 1\ 1]$ direction, as shown in the corresponding Fast Fourier transform (FFT) in **(c)**. **(d)** Atomic model of the Bi_2Te_3 crystal viewed along the $[-1\ 1\ 1]$ direction.

with w defining the peak width. The model parameter m can be adjusted and here we find that $m = 4$ provides the best description of the ZLP.

The pseudo-Voigt function. The Voigt function is defined as the convolution of two broadening functions, one a Gaussian and the other a Lorentzian function. The pseudo-Voigt function is also a popular choice in describing peak shapes in diffraction patterns [10] and approximates the exact convolution by a linear combination of a Gaussian and a Lorentzian. Their mixing can be adjusted by a model parameter η as follows,

$$I(\Delta E) = I_{\max}\left[\eta G\left(\Delta E, \sigma^2\right) + (1-\eta)\, L\left(\Delta E, \sigma^2\right)\right], \tag{C.2}$$

where $G\left(\Delta E, \sigma^2\right)$ and $L\left(\Delta E, \sigma^2\right)$ are normalised Gaussian and Lorentzian functions with a common variance σ^2 respectively.

Stability upon choice of ZLP model. Figure C.7 displays, as done in Figure 4.13a, the ZLP-subtracted EELS intensity integrated in the region $[-1.1, -0.6]$ eV around the identified energy-gain peak. We compare the outcome of our baseline choice, a Gaussian model for the ZLP, panel (a), with the corresponding results based on panel (b) split Gaussian, panel (c) Pearson VII, and panel (d) pseudo-Voigt functions for the ZLP parametrisation. Each panel adopts its own intensity range, and similar colours in the different panels in general do not correspond to similar intensity values. Irrespective of the choice of ZLP model function, the highest integrated intensity is found in the edge region of the specimen. We have verified that other relevant properties of the energy-gain peak at $\Delta E \simeq -1$ eV, such as its mean and width, are also stable with respect to this choice. We conclude that our energy-gain peak identification algorithm is robust with respect to the modelling of the ZLP.

Figure 4.12 summarises the adopted strategy for the spatially-resolved identification of energy-gain peaks. First, Figure 4.12a shows the EEL spectrum for the pixel indicated with a star in Figure 4.11c together with the corresponding ZLP fit. Closing up on the energy-gain region, Figure 4.12b displays the resulting subtracted spectrum, to which a Lorentzian function is fitted to extract the position E_g and intensity of the dominant energy-gain peak. The procedure is repeated for the complete EELS spectral image, making it possible to construct the spatially-resolved map of E_g shown in Figure 4.12c across the inspected region of the $\mathrm{Bi_2Te_3}$ specimen. As in Figure 4.11c, the black line indicates the boundary of the $\mathrm{Bi_2Te_3}$ sample. Figure 4.12c reveals the presence of an energy-gain peak in the specimen with E_g values between -1.1 eV and -0.85 eV. We demonstrate in Section 4.3.3 that results for the ZLP removal and energy-gain peak identification are robust with respect to the choice of ZLP model function. Then Figure 4.12d displays the $\mathrm{Bi_2Te_3}$ thickness map as obtained from the deconvolution of the single-scattering EELS distribution [11]. The dark blue region beyond the specimen corresponds to either the vacuum or the $\mathrm{Bi_2O_3}$ regions. In the edge region there is a sharp increase in thickness, while in the bulk region the thickness exhibits an approximately constant value of 70 nm.

C.2.4. PEAK LOCATION IN THE ENERGY-LOSS REGION

Figure 4.12c in the main manuscript displays a spatially-resolved map with the value of E_g, the median of the Lorentzian peak fitted to the ZLP-subtracted energy-gain region.

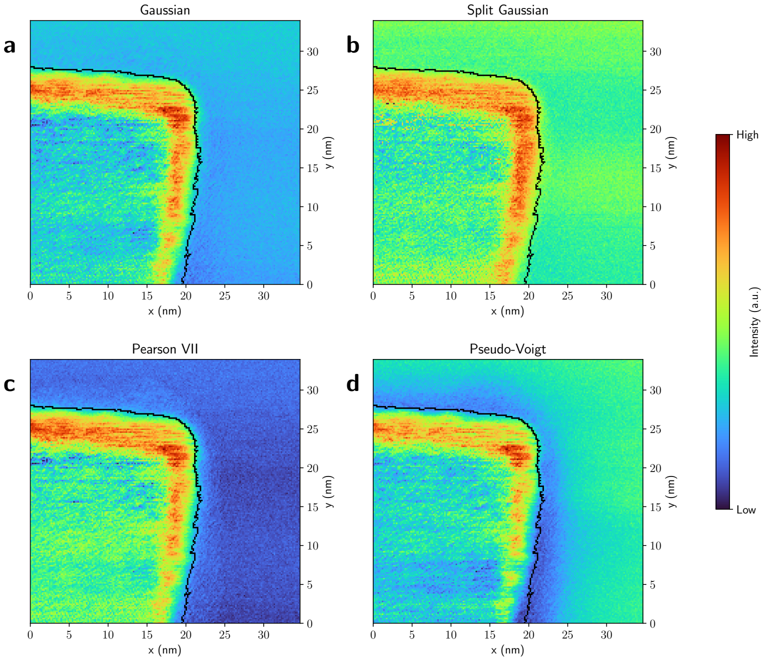

Figure C.7: Same as Figure 4.13a, displaying the ZLP-subtracted EELS intensity integrated in the region $[-1.1,-0.6]$ eV around the identified energy-gain peak. We compare the outcome of our baseline choice, a Gaussian model for the ZLP **(a)**, with the corresponding results based on **(b)** split Gaussian, **(c)** Pearson VII, and **(d)** pseudo-Voigt functions for the ZLP parametrisation. Each panel adopts its own intensity range, and similar colours in the different panels in general do not correspond to similar intensity values. Irrespective of the choice of ZLP model function, the highest integrated intensities are found near the edge region indicated by a black curve.

For completeness, we show in Figure C.8b the same map now for E_ℓ, the median of the Lorentzian peak fitted to the ZLP-subtracted energy-loss region. We emphasise that our model for the energy-loss region is incomplete, given that the data contains additional contributions beyond this dominant peak.

In the region of the specimen where the energy-gain peak exhibits the highest significance, namely close to the edge, the value of the fitted energy-loss peak is $E_\ell \sim 1$ eV, corresponding to approximately the energy-mirrored value of its energy-gain counterpart. However, the significance of this energy-loss feature is weaker, see Figure 4.13d, and only with a complete model of the energy-loss region would it be possible to robustly disentangle the different energy-loss features present in the considered specimen.

C.2.5. ENERGY-GAIN PEAKS IN DIFFERENT Bi_2Te_3 SPECIMENS

While the results presented in the main manuscript consider the EELS analysis of a specific Bi_2Te_3 specimen, we found that consistent results are obtained in other comparable specimens. In the following, the microscope parameters that were used are the same as the ones mentioned in the Methods section of the main manuscript.

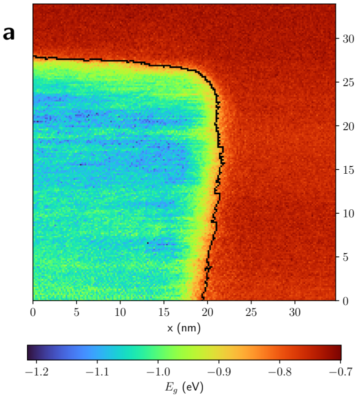

Figure C.8: **(a)** Same as Fig. 4.12**c**. **(b)** Same as Fig. 4.12**c** now displaying the value of E_ℓ, the median of the Lorentzian peak fitted to the ZLP-subtracted energy-loss region.

Figure C.9a shows an HAADF image of another Bi_2Te_3 specimen, different from the one in the main manuscript, and characterised by the presence of a channel, indicated by the darker contrast. Figure C.9b focuses on the region above the channel which is subsequently analysed with electron energy-gain spectroscopy. This region is composed by a flat layer alongside some edges. The channel region is characterised by sharp variations of the specimen thickness, which motivate the inspection of the specimen for edge- and surface-induced excitations.

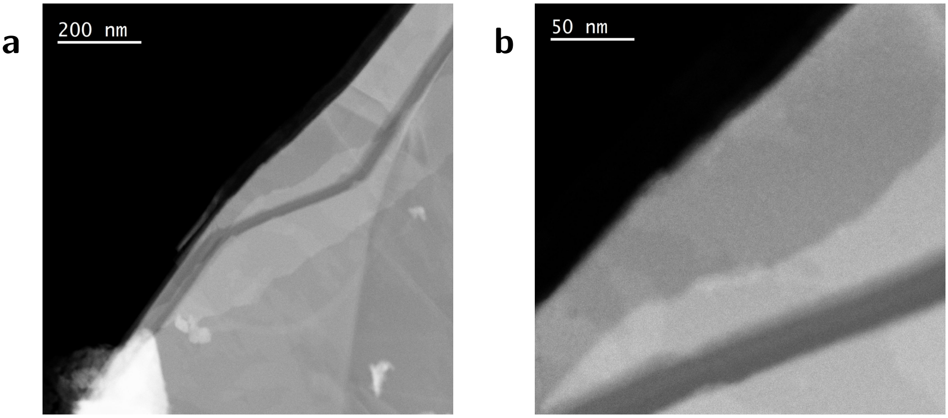

Figure C.9: **(a)** HAADF image of another Bi_2Te_3 specimen, characterised by the presence of a channel (darker contrast). **(b)** A zoomed-in image of the same specimen, focusing on the region above the channel which is analysed by means of EELS.

Figures C.10 and C.11 present the same spatially-resolved electron energy-gain analyses of Figures 4.12 and 4.13 in the main manuscript respectively, now corresponding to the Bi_2Te_3 specimen displayed in Figure C.9. The black line indicates the specimen boundary, and pixels in which the fitting procedure is numerically unstable are masked out. An enhancement of the intensity in the ΔE gain region located around -0.7 eV is observed in specific regions of the sample, as illustrated by the representative spectrum in Figure C.10b corresponding to the location marked with a star in Figure C.10a. This feature is most prominent in the region above the channel identified in Figure C.9 and close to the specimen surface. No equivalent enhancement is observed in the loss region, where it could be confounded by other mechanisms contributing to energy-loss inelastic scatterings.

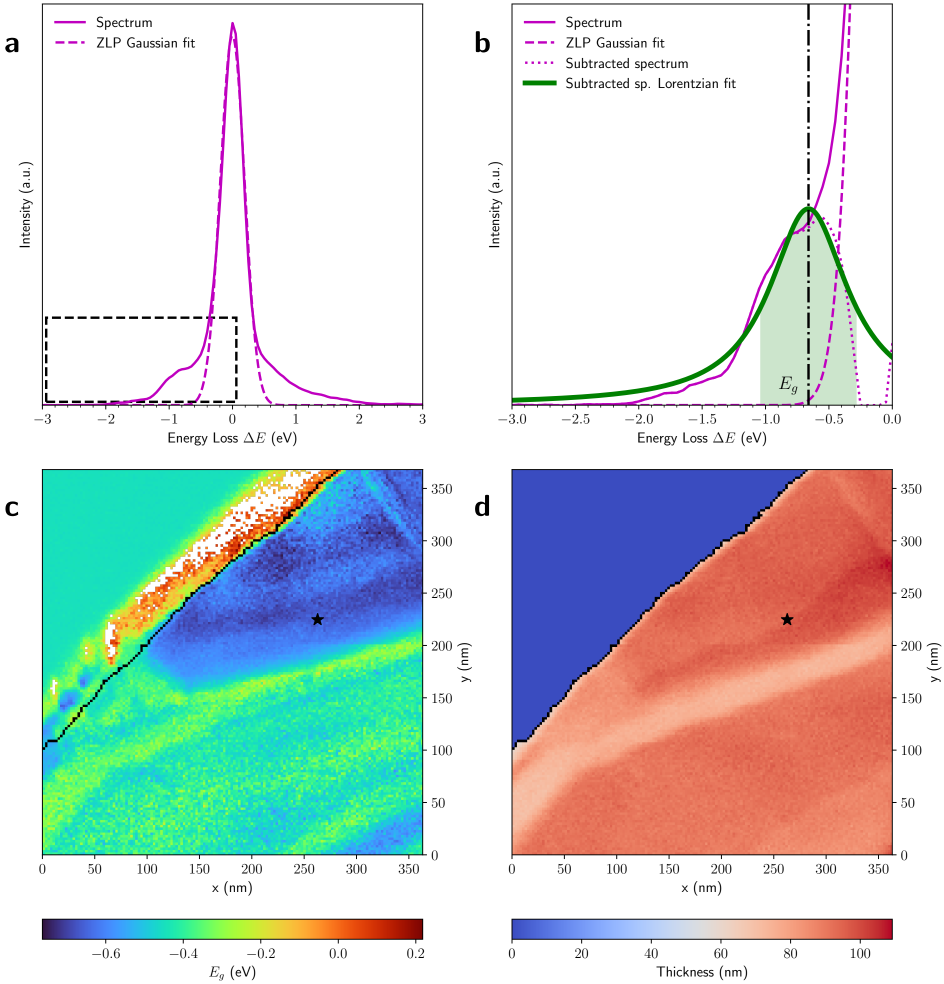

Figure C.10: Same as Fig. 4.12 in the main manuscript for a different Bi_2Te_3 crystal. The star indicates the location in the specimen in which the individual EEL spectrum of **(a)** and **(b)** is extracted.

Applying the same peak identification procedure used for the specimen in the main manuscript and further detailed in Section 4.3.3, we find that in the region where the energy gain peak is more marked the centre of the Lorentzian is located around $\Delta E = -0.7$ eV, see Figure C.10d for the associated spatially-resolved map. Integrating in the energy gain region defined by the window $[-1.1, -0.6]$ eV the intensity is highest in the region just above the channel, Figure C.11a. The ratio of the area under the FWHM of the Lorentzian peak over that under the ZLP, Figure C.11c, is also enhanced in the same region, where it takes values between 2 and 3.5. In the region of the specimen with the highest signal-to-noise significance, the position of the Lorentzian median is approximately constant and takes value $E_g \sim -0.7$ eV. We verify, by means of the same procedure adopted for Figure C.7, that our results are independent of the specific choice of functional form model for the ZLP.

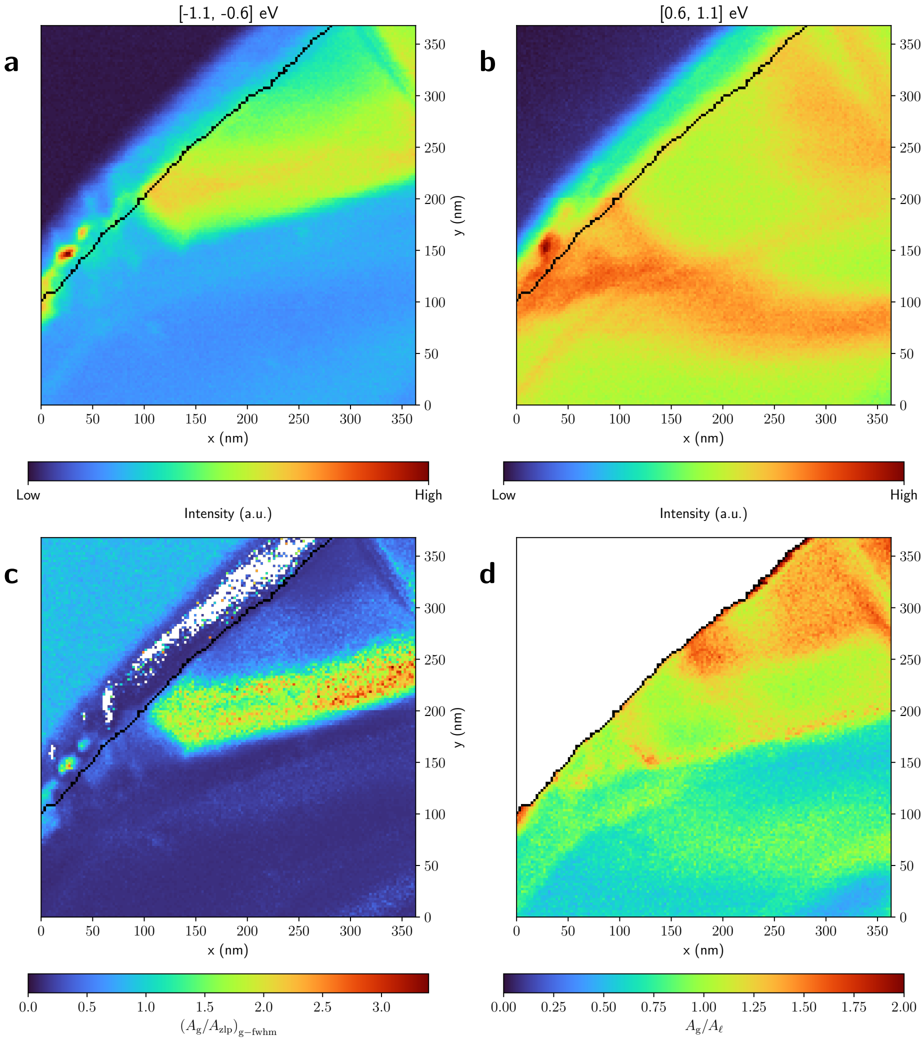

Figure C.11: Same as Fig. 4.13 in the main manuscript for the same Bi_2Te_3 crystal analysed in Fig. C.10.

The analysis presented here, performed on a different Bi_2Te_3 specimen but with the same crystal structure and comparable features as that of the main manuscript, confirms the robustness of our characterisation of the energy gain region of Bi_2Te_3, establishing the presence of a distinctive gain peak located in the region around $\Delta E = -0.7$ eV. This feature can be disentangled from the dominant ZLP emission with high significance and is also found to be enhanced in the regions of the specimen displaying sharp thickness variations with the associated exposed surfaces and edges.

C.2.6. HRTEM ANALYSIS OF THE Bi_2O_3 REGION

Figure C.12 displays a HRTEM analysis of the edge region of the specimen showing the Bi_2Te_3 (lower part, darker contrast), Bi_2O_3 (intermediate part, lighter contrast), and vacuum (top part) areas. The inset contains the diffraction pattern taken in the intermediate part of the image, whose indexation further confirms the presence of Bi_2O_3, consistently with the findings of the spatially-resolved EELS analysis of Figure C.6e in the main manuscript.

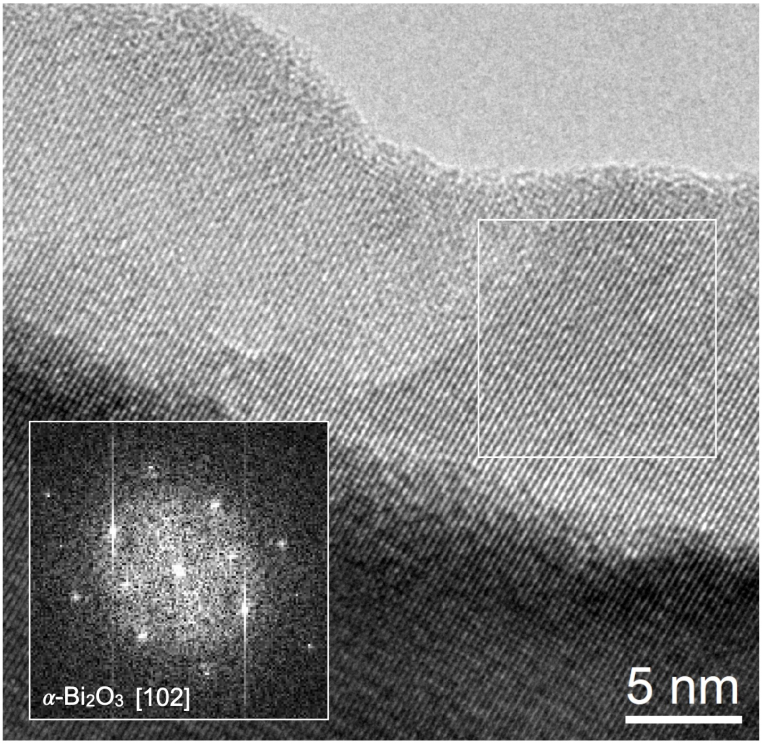

Figure C.12: HRTEM analysis of the edge region of the specimen, displaying the presence of Bi_2O_3 as confirmed by the corresponding indexed diffraction pattern (inset).

REFERENCES

[1] M. Tinoco, L. Maduro, M. Masaki, E. Okunishi, and S. Conesa-Boj, “Strain-dependent edge structures in mos2 layers”, *Nano Letters*, vol. 17, pp. 7021–7026, 11 Nov. 2017, ISSN: 15306992. DOI: 10.1021/acs.nanolett.7b03627.

[2] B. Yue, F. Hong, K.-D. Tsuei, *et al.*, “High-energy electronic excitations in a bulk MoS_2 single crystal”, *Phys. Rev. B*, vol. 96, no. 12, p. 125 118, 2017, ISSN: 2469-9969. DOI: 10.1103/PhysRevB.96.125118.

[3] L. Martin, R. Mamy, A. Couget, and C. Raisin, “Optical Properties and Collective Excitations in MoS2 and NbSe2 in the 1.7 to 30 eV Range”, *Phys. Status Solidi B*, vol. 58, no. 2, pp. 623–627, 1973, ISSN: 0370-1972. DOI: 10.1002/pssb.2220580223.

[4] K. Zeppenfeld, “Electron energy losses and optical anisotropy of MoS2 single crystals”, *Opt. Commun.*, vol. 1, no. 8, pp. 377–378, 1970, ISSN: 0030-4018. DOI: 10.1016/0030-4018(70)90074-X.

[5] W. Y. Liang and S. L. Cundy, “Electron energy loss studies of the transition metal dichalcogenides”, *Philosophical Magazine: A Journal of Theoretical Experimental and Applied Physics*, vol. 19, no. 161, pp. 1031–1043, 1969, ISSN: 0031-8086. DOI: 10.1080/14786436908225867.

[6] L. Lajaunie, F. Boucher, R. Dessapt, and P. Moreau, “Strong anisotropic influence of local-field effects on the dielectric response of α-MoO_3”, *Phys. Rev. B*, vol. 88, no. 11, p. 115 141, 2013, ISSN: 2469-9969. DOI: 10.1103/PhysRevB.88.115141.

[7] M. M. Y. A. Alsaif, M. R. Field, B. J. Murdoch, *et al.*, “Substoichiometric two-dimensional molybdenum oxide flakes: a plasmonic gas sensing platform”, *Nanoscale*, vol. 6, no. 21, pp. 12 780–12 791, 2014, ISSN: 2040-3364. DOI: 10.1039/C4NR03073G.

[8] E. D. Hanson, L. Lajaunie, S. Hao, *et al.*, “Systematic Study of Oxygen Vacancy Tunable Transport Properties of Few-Layer MoO3-x Enabled by Vapor-Based Synthesis”, *Adv. Funct. Mater.*, vol. 27, no. 17, p. 1 605 380, 2017, ISSN: 1616-301X. DOI: 10.1002/adfm.201605380.

[9] *Peak Shape Functions: Pearson VII*, Birkbeck College, University of London, http://pd.chem.ucl.ac.uk/pdnn/peaks/pvii.htm, 2006.

[10] *Peak Shape Functions: Pseudo-Voigt and Other Functions*, Birkbeck College, University of London, http://pd.chem.ucl.ac.uk/pdnn/peaks/others.htm, 2006.

[11] A. Brokkelkamp, J. T. Hoeve, I. Postmes, *et al.*, “Spatially resolved band gap and dielectric function in two-dimensional materials from electron energy loss spectroscopy”, *Journal of Physical Chemistry A*, vol. 126, pp. 1255–1262, 7 Feb. 2022, ISSN: 15205215. DOI: 10.1021/acs.jpca.1c09566.

D

SUPPLEMENTARY INFORMATION TO CHAPTER 5

METHODS

Fabrication of WS_2 nanotriangles. The twisted WS_2 specimens were grown directly on a silicon TEM grid with nine windows, each spanned by a 5 nm thick Si_3N_4 membrane. Tungsten trioxide (WO_3) powder, which acts as a seeding material, was deposited on this substrate by dispersing 50 mg of WO_3 in 1 mL of isopropanol. A few drops of this solutions where then deposited onto the substrate using a pipette. After the sample was left to dry, the WO_3 had been successfully spread over the substrate. Following this preparation, the WO_3 coated substrate was placed in the central heating zone of a gradient tube furnace from Carbolite Gero. A crucible containing sulfur powder was positioned in a separate heating zone upstream. The central heating zone was heated to a temperature of 750 °C, followed by heating the zone containing the sulfur powder to 220 °C. The system was maintained at these temperatures for one hour under a consistent argon flow of 150 sccm. Before this process, the system was flushed using an argon flow of 500 sccm for 30 min. Once the reaction time has passed, the furnace was cooled down naturally.

STEM-EELS analyses. The STEM-EELS measurements were performed on an ARM200F Mono-JEOL microscope. The microscope was operated at 200 kV with the monochromator ON and a slit of 1.3 µm inserted for the stacked nanotriangles and a slit of 2.0 µm for the single nanotriangles. A Gatan GIF Quantum ERS system (model 966) was used for the EELS acquisition. The convergence and collection semi-angles were 19.96 and 14.5 mrad respectively. EEL spectra of the stacked nanotriangles were acquired with an entrance aperture diameter of 5 mm, energy dispersion of 0.015 eV/channel, and pixel time of 0.5 s. resulting in a ZLP FWHM of 0.12 eV. For the single nanotriangles, the EEL spectra were acquired with the same entrance aperture diameter of 5 mm, but with an energy dispersion of 0.05 eV/channel, and a pixel time of 1.0 s, yielding a ZLP FWHM of 0.25 eV

D.1. STRUCTURAL CHARACTERIZATION OF WS_2 NANOSTRUCTURES

Here we present the morphological and structural analysis of WS_2 nanotriangles with different side lengths. This characterization, using scanning transmission electron microscopy-high angle annular dark-field (STEM-HAADF) imaging and thickness mapping, provides essential insights into how size and thickness variations impact the plasmonic properties of the nanotriangles. This analyses also allow comparisons between single and stacked triangular structures, revealing the potential for larger or thicker structures to support higher-order plasmonic modes.

D.1.1. WS_2 NANOSTRUCTURE THICKNESS MAPPING

Fig. 5.1c in the main manuscript shows the thickness map of the specimen, calculated using the log-ratio method and mass density of the material to determine the mean free path of the electrons [1]. After subtracting the thickness of the Si_3N_4 membrane, the large triangle has an average thickness of approximately 30 nm, with side lengths measuring around 980 nm. The small triangle has an average thickness of approximately 35 nm, after accounting for the thickness of the Si_3N_4 membrane and the large triangle. However, it exhibits greater variation in thickness, ranging from about 30 nm to 50 nm, with side lengths measuring around 680 nm. In both triangles, the corners are slightly truncated, and the edges are slightly tapered.

D.1.2. MORPHOLOGY AND THICKNESS MAPPING OF ADDITIONAL WS_2 NANOSTRUCTURES

Figures S1 trough S3 display the morphology of WS_2 nanotriangles with side lengths of 330 nm, 880 nm, and 920 nm, using STEM-HAADF and corresponding thickness maps. These morphological details provide a basis for comparing the influence of size and thickness on plasmonic behaviour, specifically showing how larger or thicker nanotriangles may support higher-order plasmon modes.

The WS_2 nanotriangle presented in Fig. D.1 has side lengths of approximately 920 nm and average thickness of about 70 nm, with the top right side being slightly thinner than the bottom left. This thickness closely resembles that of the stacked WS_2 nanotriangles, making it a suitable morphological comparison in the main text.

The next WS_2 nanotriangle, shown in Fig. D.2, has side lengths of approximately 330 nm and and average thickness of about 85 nm, with the top part being the thinnest and the bottom part showing the greatest thickness. The final WS_2 nanotriangle presented in Fig. D.3, has side lengths of approximately 880 nm. Notable defects include a more truncated tip on the left side and the gap on the right, with spikes near the gap location. This nanotriangle is significantly thicker than the others, averaging around 225 nm, with the top thinner than the bottom. The gap and proximity of the beam to the nanostructure lead to an increase in the overall spectral intensity, slightly distorting the thickness measurement.

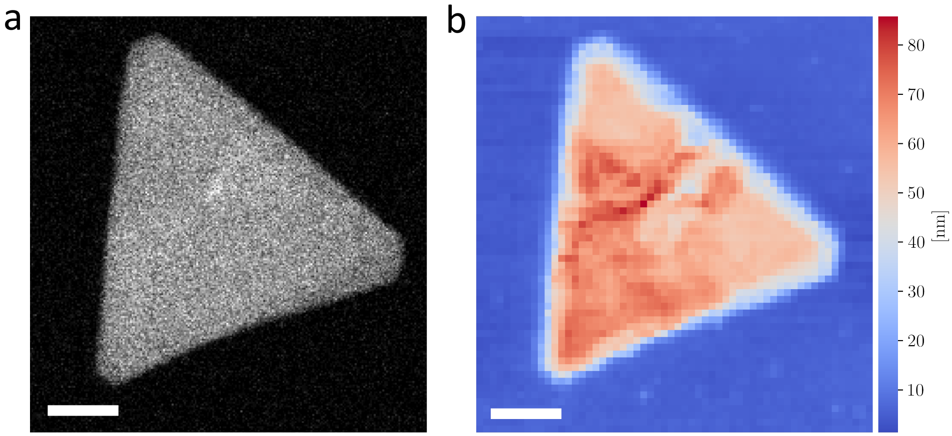

Figure D.1: **Morphology of the WS_2 triangular nanotriangle with a side length of approximately** 920 **nm.** **(a)** STEM-HAADF image illustrating the structural features. **(b)** Thickness map with an average thickness of around 70 nm, showing thickness variations from the top right to the bottom left. Scale bars are 200 nm.

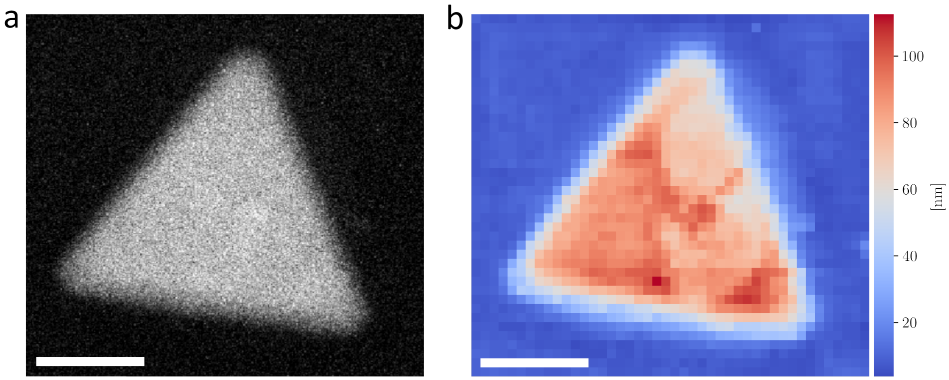

Figure D.2: **Morphology of a WS_2 nanotriangle with a side length of approximately** 330 **nm.** **(a)** STEM-HAADF image showing the overall structure. **(b)** Thickness map with an average thickness of about 85 nm. Scale bars represent 100 nm.

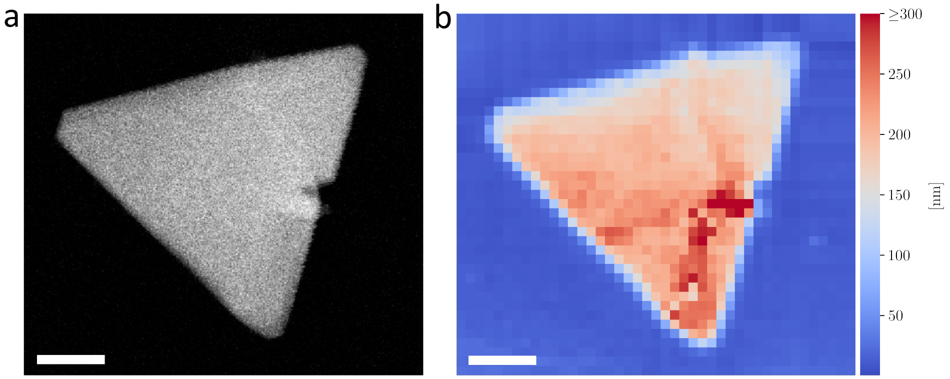

Figure D.3: **Morphology of a WS_2 nanotriangle with a side length of approximately** 880 **nm.** **(a)** STEM-HAADF image showing structural details, including notable defects. **(b)** Thickness map with and average thickness of about 225 nm. Notable defects include a truncated tip on the left and a gap on the right side, causing intensity distortions near the gap. Scale bars represent 200 nm.

D.2. SPATIALLY-RESOLVED EELS DATA PROCESSING

In this section, we outline the processing steps for electron energy loss spectroscopy (EELS) data obtained from WS_2 nanotriangles. The methods include Zero Loss Peak (ZLP) subtraction using a deep-learning approach (as outlined in chapter 2), followed by decomposition of the EELS data using non-negative matrix factorization (NMF). These steps are essential for isolating meaningful spectral features and improving the accuracy of plasmonic and electronic property analysis across different energy windows.

D.2.1. DECOMPOSITION OF EELS DATA USING NMF

Non-negative matrix factorization (NMF) is a multivariate analysis (MVA) algorithm often referred to as blind-source separation (BSS). Another example of such family of techniques is principal component analysis (PCA), which has already seen widespread use in EELS applications.

The spectral image can be expressed as a three-dimensional matrix, $D(x, y, \Delta E)$, where (x, y) denotes the two-dimensional probe position from which spectral data is collected, and ΔE denotes the energy channels of the spectrometer. To facilitate analysis, the spectral image can be reshape into a two-dimensional matrix $\mathbf{X}(n_{xy}, n_{ch})$, where $n_{xy} = n_x \times n_y$ is the total number of probe positions (pixels), and n_{ch} $(= \Delta E)$ is the number of energy channels.

The information within an EEL spectrum is assumed to be a linear combination of basis spectra linked to underlying features and excitations. If there are k basis spectra, with k significantly smaller than the matrix dimensions $n_{xy} \times n_{ch} \gg n_{xy} \times k + n_{ch} \times k$, we can store the basis spectra in matrix $\mathbf{W}$ $n_{ch} \times k$ and the concentration coefficients in matrix $\mathbf{H}$ $n_{xy} \times k$. The original matrix $\mathbf{X}$ can then be approximated as:

$$\mathbf{X} \approx \mathbf{W}\mathbf{H}^T \tag{D.1}$$

where the superscript T denotes the transpose. In MVA terminology, $\mathbf{H}$ is called the load-

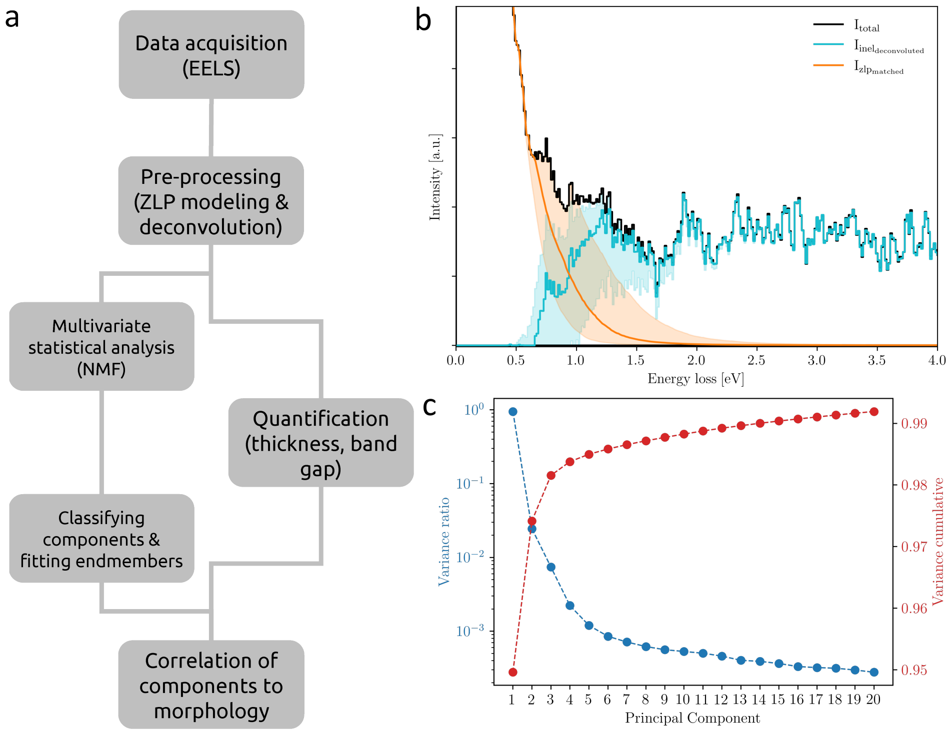

Figure D.4: **Data Processing of EELS Spectral Images.** **(a)** Schematic of the EELS data processing steps. **(b)** Deconvolution of the ZLP from a representative EEL spectrum, with the orange shaded area representing the 90% confidence level (CL) interval obtained from the trained ZLP models. **(c)** Scree plot from principal component analysis (PCA) applied to the ZLP-subtracted EELS data within the 0.5 to 2.5 eV energy window. From the variance ratio and the cumulative variance, we determine the first four components to be most statistically significant (adding up to 98.5% of the total variance). These first four components are discussed in Fig. 5.2 in the main text.

ing matrix, with each column vector (or loading) representing an "endmember" in the main text. Each endmember corresponds to a basis spectrum, ideally capturing a pure signal of the feature it represents. **W**, known as the score matrix, contains scores in each column vector, representing the weight of the endmember at each location, referred to as the "abundance" in the main text.

As previously mentioned, PCA is the most widely known type of multivariate analysis (MVA) algorithm, with a common application being noise reduction. One important property of PCA is that its principal components are orthogonal and uncorrelated. This means that the first component captures the greatest variance in the data, and each subsequent component maximizes the remaining variance while maintaining orthogonality to all previous components. This structure allows for the creation of a scree plot, as seen in Fig. D.4c, which makes it possible to determine the number of statistically relevant components.

EELS data consists of spectroscopic counts that are inherently positive, as negative counts are unphysical. However, when PCA is applied to EELS data, the first component typically represents an averaged base spectrum, but subsequent components, constrained by orthogonality, may contain negative values in their endmembers and abundances. This characteristic often complicates the physical interpretation of the components.

NMF differs from PCA by solving Eq. (D.1) with the constraint that **X**, **W**, and **H** are all non-negative. The absence of negative values in NMF components provides a more interpretable solution for spectroscopic data. However, a consequence of this non-negativity constraint is that the components are no longer orthogonal. Matrix **W** and matrix **H** are thus numerically approximated by minimizing the following loss function:

$$\|\mathbf{X}-\mathbf{W}\mathbf{H}^T\|_F \tag{D.2}$$

Here F denotes as the Frobenius norm. Several approaches have been developed to use this form as the basis for minimizing and obtaining solution for **W** and **H**. Although NMF and PCA differ in their component-determination methods, they share the goal of image decomposition, allowing us to use a PCA-derived scree plot as a rough guide for the number of components needed for NMF..

For EELS data, proper normalisation is essential before performing NMF or PCA. In this case, normalisation involves dividing each pixel's spectrum by its ZLP intensity. This step is crucial because the probability of electron interactions is independent of material thickness, but the counts reaching the detector may vary with thickness. For instance, a plasmonic feature may yield higher counts along or near an edge compared to the bulk, due to thickness effects.

D.2.2. NMF DECOMPOSITION OF ALL NANOTRIANGLES

In Fig. 5.2 of the main text, we examine energy windows between 0.5 to 2.5 eV to decompose the spectral image. Narrowing the energy window can benefit the decomposition process by enhancing feature separation. The exception to this rule is the energy window of the smallest triangle (0.5 to 4.0 eV, as there are a lower amount of resonance modes to be separated (see Fig. D.12(c,d).

In Fig. D.5 we present the same as main text Fig. 5.2, but with an additional fifth component. From the scree plot in Fig. D.4(c) this component is arguably on the side of statistical insignificance, but as the endmember and abundance map do show a distinct feature (that being the second-order mode of the smaller nanotriangle on top), we present it here. The EELS simulation in Fig. D.15 of the small triangle do indicate this being a genuine feature otherwise not observed in the experimental data.

In Fig. D.6, data in the energy window between 2 and 4 eV is decomposed, with three components best describing this range. Components 2 and 3 represent higher-order plasmon modes in both the larger and smaller triangle. Component 2 displays the fourth-order mode in the large triangle and the third-order mode in the small triangle, as shown in the abundance map, the latter being less well defined here. Due to the overlapping energy values of the plasmon modes of the small and large triangle, we do not observe a difference in the endmember, but do see both modes in the abundance map. The higher order resonances modes are less well defined and spectrally more spread out. The dominating 2.1 eV peak is associated with the fourth-order plasmon resonances of the large triangle and a bump at 2.3 eV to the third-order plasmon mode in the small triangle, consistent with the EELS-GDM simulations in Figures D.11 and D.12. Similarly, Component 3 represents the fifth-order plasmon mode in the large triangle and the fourth-order mode in the small triangle, both near 2.75 eV as indicated by the EELS-GDM simulations. Component 4 is most likely related to the bulk WS_2 crystal, specifically the surface of the large triangle. The rest of this section presents NMF decomposition of additional WS_2 nanotriangles.

We used the NMF implementation in SCIKIT-LEARN version 1.5.2 for the results presented in this work. Most parameters in the NMF algorithm were kept at their default values, with two exceptions. First, the `solver` parameter was set to 'multiplicative update,' as it provided significantly better and faster results compared to the 'coordinate descent' option. Second, the `maximum_iterations` parameter was set to 10^5, which we confirmed is sufficiently large to ensure convergence for all cases relevant to our analysis.

D.2.3. VALIDATION OF THE NMF ABUNDANCE MAPS FROM EELS POINT SPECTRA

To further confirm the presence of the features identified by the endmembers of the NMF decomposition and their abundance, we compare the NMF abundance maps to EELS point spectra selected in areas of the specimen corresponding to high and low abundance in the NMF maps. In Fig. D.10 we compare the abundance maps of components 2 to 4 as provided in the main text in Fig. 5.2, where the locations of the plasmon modes associated to the relevant endmembers are indicated by the grey dotted vertical lines. In all three cases considered, we clearly observe the presence of the expected features in the EELS point spectra taken from areas of high abundance, as well as the absence or significant reduction of the same features in the point spectra taken from areas of low abundance.

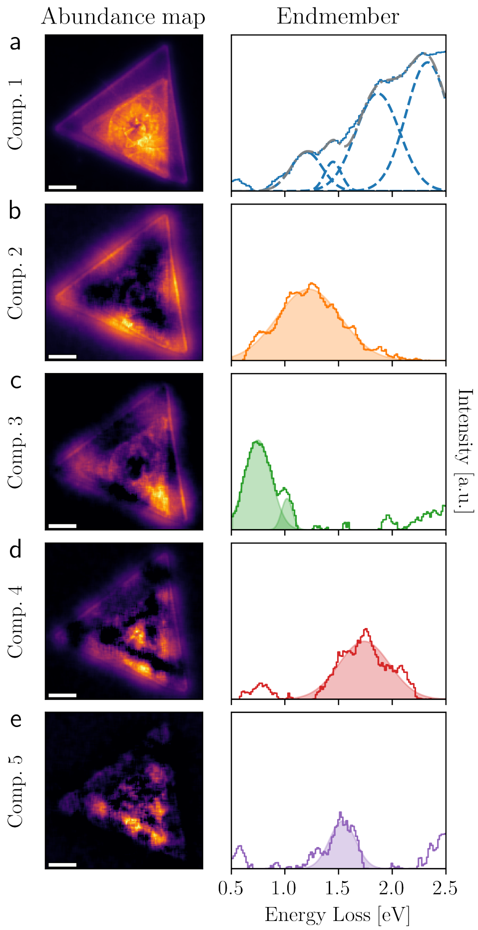

Figure D.5: **NMF decomposition of the stacked WS_2 nanotriangles.** **(a-d)** The abundance maps (left) and endmembers (right panel) of the first four components of the NMF decomposition from the stacked WS_2 nanotriangles, same as Fig. 5.2 now with the results of Gaussian fits to the endmembers (right panel). The dashed Gaussians in component 1 represent crystal-structure specific features such as excitons. The shaded Gaussians in components 2-4 indicate the characteristics energies of the plasmonic resonance modes of different order. **(e)** Same as (a-d) now for the fifth component of the NMF decomposition, which can be associated to the 2nd-order resonance mode of the smaller triangle as shown in Fig. D.15. All vertical axes are uniformly scaled. Scale bars represent 200 nm.

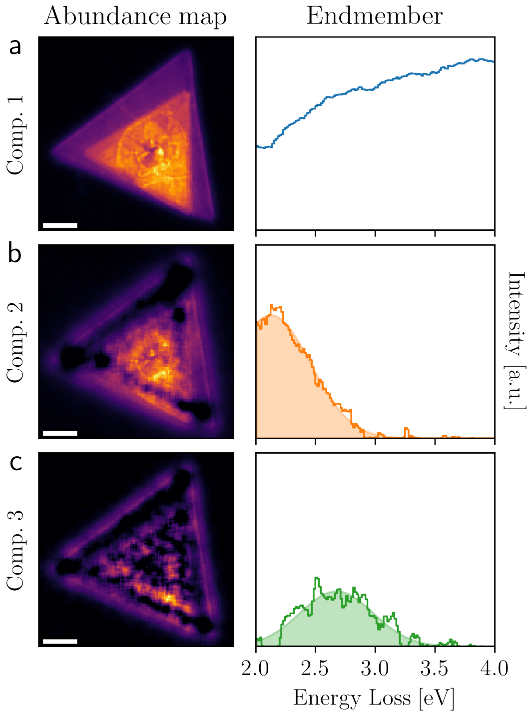

Figure D.6: **NMF components from energy window** 2.0 **to** 4.0 **eV. (a)** Component 1 represents the bulk WS_2 spectrum. **(b)** Component 2 represents the 4th-order resonance mode of the large triangle and possibly the 3rd-order resonance mode of the small triangle. **(c)** Component 3 represents the 5th-order resonance mode of the large triangle and possibly the the 4th-order resonance mode of the small triangle. Scale bars represent 200 nm

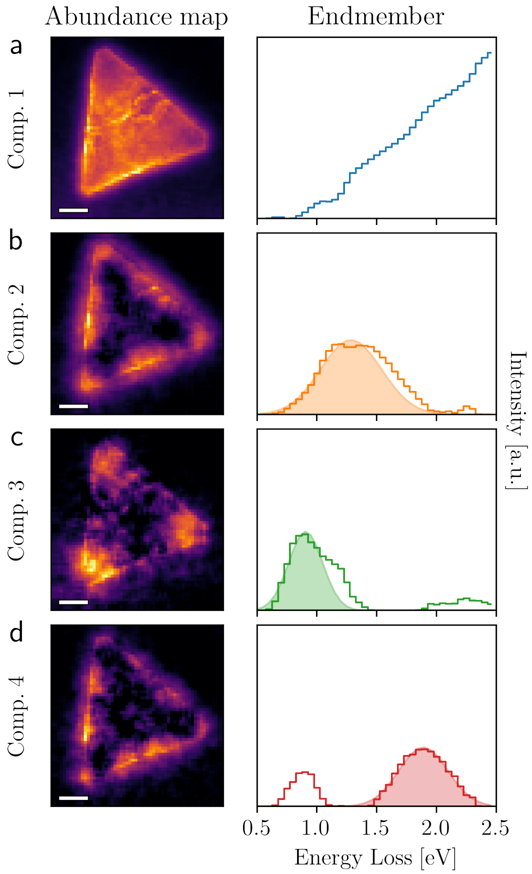

Figure D.7: **NMF components of WS_2 nanotriangle with** 920 **nm side lengths, energy window** 0.5 **to** 2.5 **eV. (a)** Component 1 predominantly represents the bulk WS_2 spectrum. **(b)** Component 2 represents the 2nd-order resonance mode. **(c)** Component 3 represents the 1st-order resonance mode. **(d)** Component 4 represents the 3rd-order resonance mode. Scale bars represent 200 nm

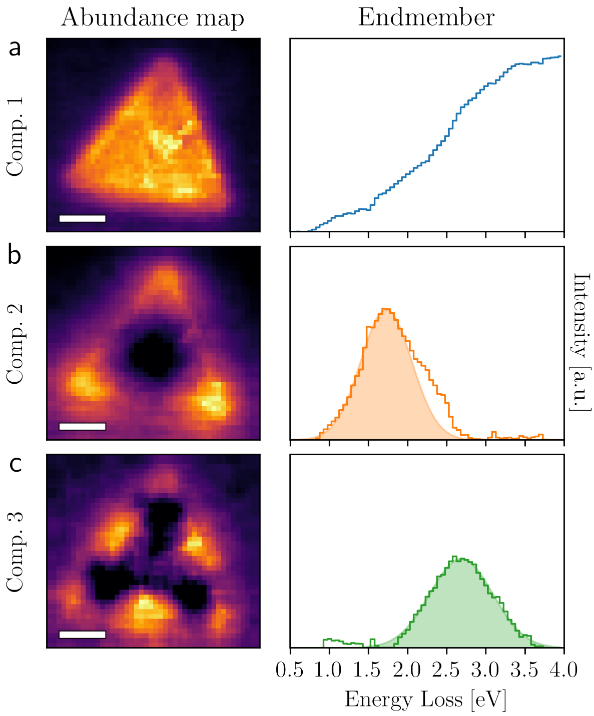

Figure D.8: **NMF components of WS_2 nanotriangle with** 330 **nm side lengths, energy window** 0.5 **to** 4.0 **eV. (a)** Component 1 predominantly represents the bulk WS_2 spectrum. **(b)** Component 2 represents the 1st-order resonance mode. **(c)** Component 3 represents the 2nd-order resonance mode. Scale bars represent 100 nm

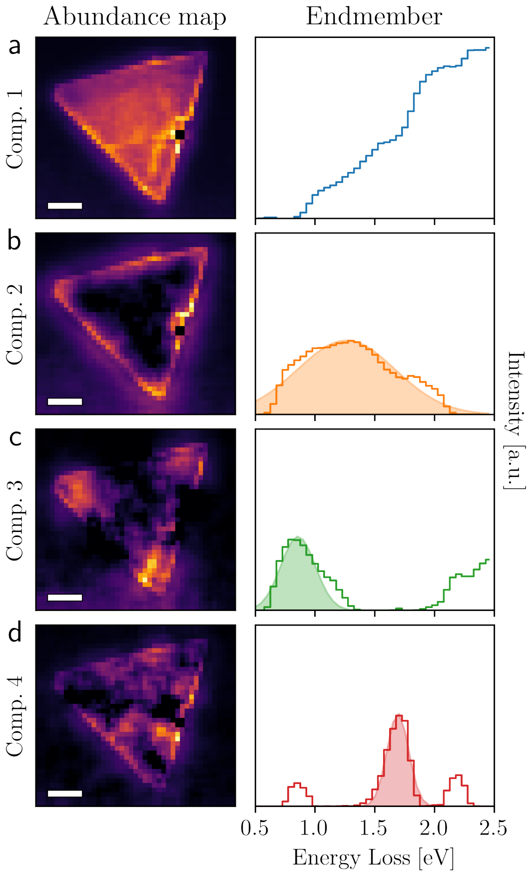

Figure D.9: **NMF components of WS_2 nanotriangle with** 880 **nm side lengths, energy window** 0.5 **to** 2.5 **eV. (a)** Component 1 predominantly represents the bulk WS_2 spectrum. **(b)** Component 2 represents the 2nd-order resonance mode. **(c)** Component 3 represents the 1st-order resonance mode. **(d)** Component 4 represents the 3rd-order resonance mode. Scale bars represent 200 nm

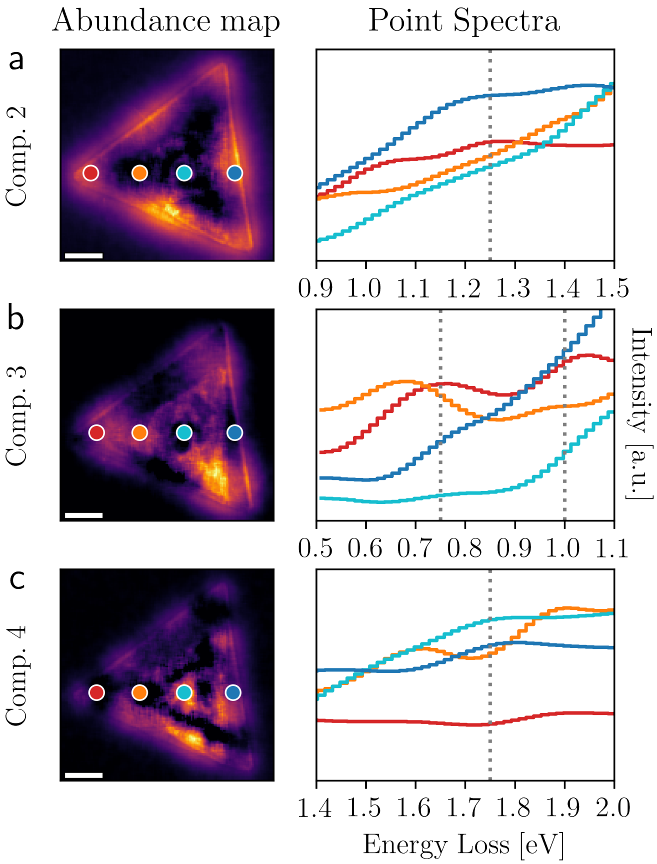

Figure D.10: **Additional validation of the NMF abundances maps with EELS point spectra.** The NMF abundance maps of components #2, #3, and #4 extracted from Fig. 5.2 are compared to EELS point spectra taken at the indicated locations in the specimen (with the same colour labelling the location and the spectrum), which validate the presence of the specific feature associated to the endmember of the corresponding NMF component. **(a)** The plasmon mode around 1.25 eV in component 2 is present in locations of high abundance (red and blue markers) and absent in locations of low abundance (orange and cyan markers). **(b)** The plasmon modes around around 0.75 eV and 1.0 eV in component 3 are present in locations of high abundance (red and orange markers) and absent in locations of low abundance (cyan and blue markers). **(c)** The plasmon mode around 1.75 eV in component 4 is present in locations of high abundance (cyan and blue markers) and absent in locations of low abundance (red and orange markers). Scale bars represent 200 nm

D.3. EELS-GDM ELECTRODYNAMICAL SIMULATIONS

Electrodynamical simulations of the EELS response of WS_2 nanotriangles for different morphologies were performed using the PYGDM Python package [2], [3] based on the Green Dyadic Method (GDM) to calculate the total electromagnetic field within a nanostructure. The simulations used thickness and side lengths obtained from the structural analysis summarised in Sect. D.1 to define the nanostructure volumes. A hexagonal compact mesh was employed for optimal density, with the simulation environment consisting of the nanostructure placed on a Si_3N_4 substrate in vacuum.

D.3.1. EDGE DISPERSIONS OF NANOTRIANGLES

The first simulation series involved an energy window of $[0.5, 2.5]$ eV focusing on plasmonic edge dispersion along the edges of the nanotriangles, as shown in Fig. 5.3 of the main text. Figs. D.11 and D.12 present a complete comparison of edges dispersions, showing both experimental data and simulation for corresponding edges.

In Fig. D.11, the three edges of the stacked WS_2 nanotriangles are analysed. Due to the small triangle's proximity to the large triangle's edges, thickness influences on plasmonic resonances are observed. Figs. D.11a,b show the experimental edge dispersion and simulation of the upper edge, with the latter mirroring Fig. 5.3b in the main text. Overall, there is good agreement between the experimental dispersion and simulation, with the exception of a 1 eV feature in the experimental data, which is not captured by the simulation. As noted in the main text, this feature originates from the first-order resonance of the small triangle, which "leaks" to the large triangle's edge.

The bottom edge, shown in Figures D.11c,d exhibits the significant distortion due to complete overlap between parts of the small triangle and the large triangle's edge. The edge on the right side of the stacked WS_2 nanotriangles, shown in Figures D.11e,f, has the small triangle in close proximity to the edge of the large triangle, but without the overlap as seen on the bottom edge.

Although the simulation captures some interesting distortions, many finer details are obscured in the experimental data by the scattering continuum. The 1.25 eV resonance in the edge of the right side of the stacked WS_2 nanotriangles appears diagonally distorted due to thickness differences on each side of the edge. Comparing this with the experimental data, we observe a similar distortion, although leaking of the first-order plasmon mode from the small triangle to the edge of the large triangle may also contribute to the appearance of the distortion, as observed on the other edges.

The edge dispersions of the other nanotriangles are presented in Fig. D.12. As the morphologies of these triangles are symmetric, only a single edge was simulated and compared with the experimental data. The experimental edge dispersions show good agreement with the simulated results across all three samples.

D.3.2. EELS PROBABILITY MAPS

Similar to Fig. 5.4 in the main text, we compare the abundance maps of the additional nanotriangles and their resonances modes with the simulated EELS probability maps.

In Fig. D.13d, the second-order resonance shows a high probability at the centre of the triangle, though this feature is not captured in the decomposition-based abundance map shown in Fig. D.13b.

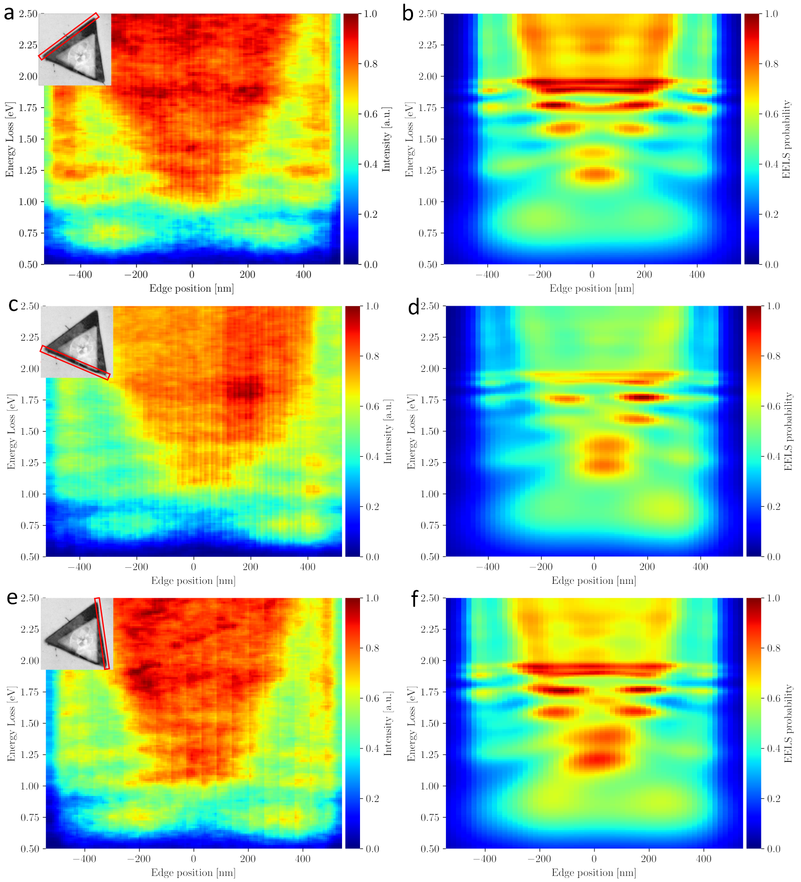

Figure D.11: **EELS edge profiles of stacked WS_2 nanotriangles. (a,b)** Experimental and prediction of the upper edge profile. The experimental data shows a 1 eV feature along the edge originating from the smaller triangle on top, which is not captured in the simulation. The A-exciton at 1.9 eV is clearly visible in both experimental and simulated data, though the detailed split present in the simulation in not observed in the experimental data. **(c,d)** Bottom edge, illustrating thickness effects. The 1.75 eV feature becomes noticeably more intense, as represented in both experimental and simulation data. **(e,f)** Rightmost edge, with parts of the small triangle in close proximity to, but not overlapping with, the egde of the large triangle. This results in a distorted edge profile similar to the upper edge in (a) and (b), with notable differences. The 1 eV resonances from the small triangle appears with greater clarity here. All plots are normalised with their respective maximum values.

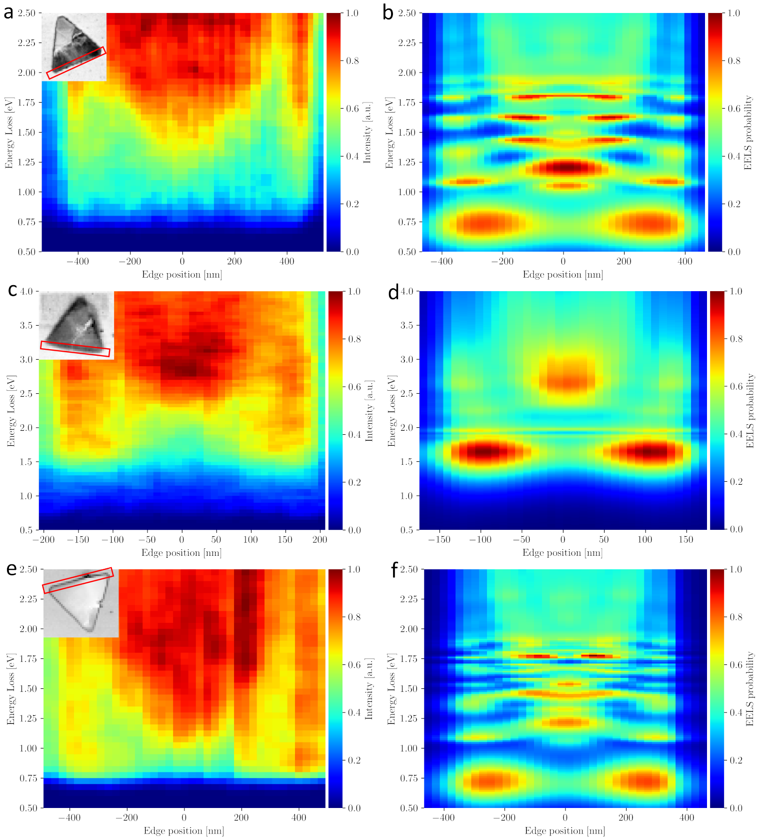

Figure D.12: **Edge dispersions of the other three triangles.** **(a,b)** Experimental and prediction for the edge profile of the 920 nm triangle. Due to the lower spectral resolution, the experimental data is less detailed than in Fig. D.11. **(c,d)** Experimental and prediction for the edge profile of the 330 nm triangle. The two plasmonic resonances observed near 1.75 eV and 2.7 eV in the experimental data correspond well with the simulation. **(e,f)** Experimental and prediction for the edge profile of the 880 nm triangle. All colour bars are normalized to their respective maximum values.

In Fig. D.14f, the third-order resonance appears notably different from other third-order resonances. Likely due to the increased thickness of the nanotriangle, the central region exhibit a much higher probability. This higher probability is partially reflected in the abundance map in Fig. D.14c, albeit at a lower intensity than seen in the simulation.

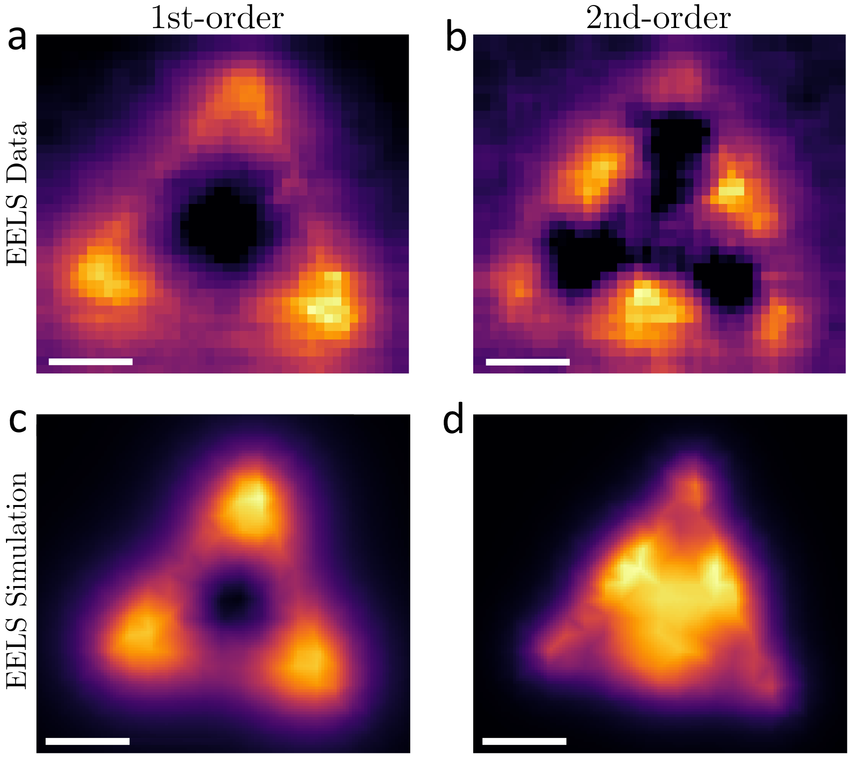

Figure D.13: **EELS probability maps of localised plasmon resonances in a** 330 **nm nanotriangle.** **(a,b)** Abundance maps of the 330 nm nanotriangle. The energy loss values for the modes derived from the endmembers are: **a** 1.78 eV and **b** 2.68 eV. **(c,d)** Corresponding simulated maps. The simulation intervals are: **c** [1.65, 1.85] eV and **d** [2.6, 2.8] eV. All scale bars are 100 nm.

D.3.3. POTENTIAL LIMITATIONS OF THE SIMULATION MODEL

Given that the WS_2 nanostructures considered in this work are CVD-grown, small imperfections such as asymmetries or structural defects are naturally present. In the PYGDM simulation model used here, these natural imperfections are not accounted for. This choice is based on the rationale that residual crystal imperfections are not expected to have a qualitative impact on the features being simulated.

While the rasterization and spectral bin sizes in the simulation were matched to the EELS experiments for an accurate one-to-one comparison, microscope conditions such as lens aberrations are not included in the numerical simulation. Specifically, the incoming fast electron is assumed to be perpendicular to the specimen, with an energy of

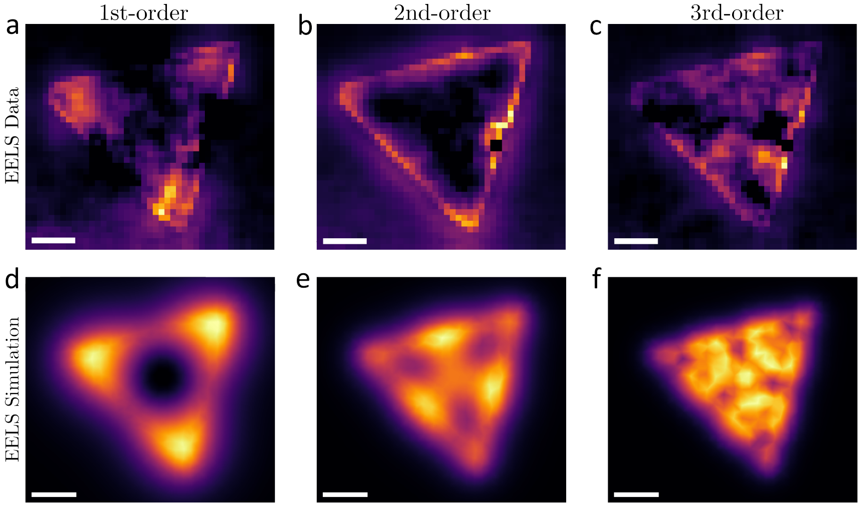

Figure D.14: **EELS probability maps of localised plasmon resonances in an** 880 **nm nanotriangle.** **(a-c)** Abundance maps of the 880 nm nanotriangle. The energy loss values for the modes obtained from the endmembers are: **a** 0.87 eV, **b** 1.26 eV and **c** 1.69 eV. **(c-e)** Corresponding simulated maps. The simulation intervals are: **d** $[0.7, 0.9]$ eV, **e** $[1.1, 1.3]$ eV and **f** $[1.65, 1.85]$ eV. All scale bars are 200 nm.

200 keV and no broadening function applied. Nevertheless, due to our data-driven machine learning approach to remove the zero-loss peak, these simplifications do not introduce any practical issues for interpreting the numerical simulation outcomes in terms of the underlying plasmonic dynamics.

Regarding the mathematical framework underlying the PYGDM simulations, as stated in Wiecha et al. (2022) [3], additional losses described by the so-called *bulk loss probability*, proportional to the thickness of the traversed material and the imaginary part of $1/\varepsilon(\omega)$, are not included. Given that our specimens are relatively thin and these effects do not significantly influence the edge-localised plasmonic resonances, no qualitative impact on the interpretation of the results is expected.

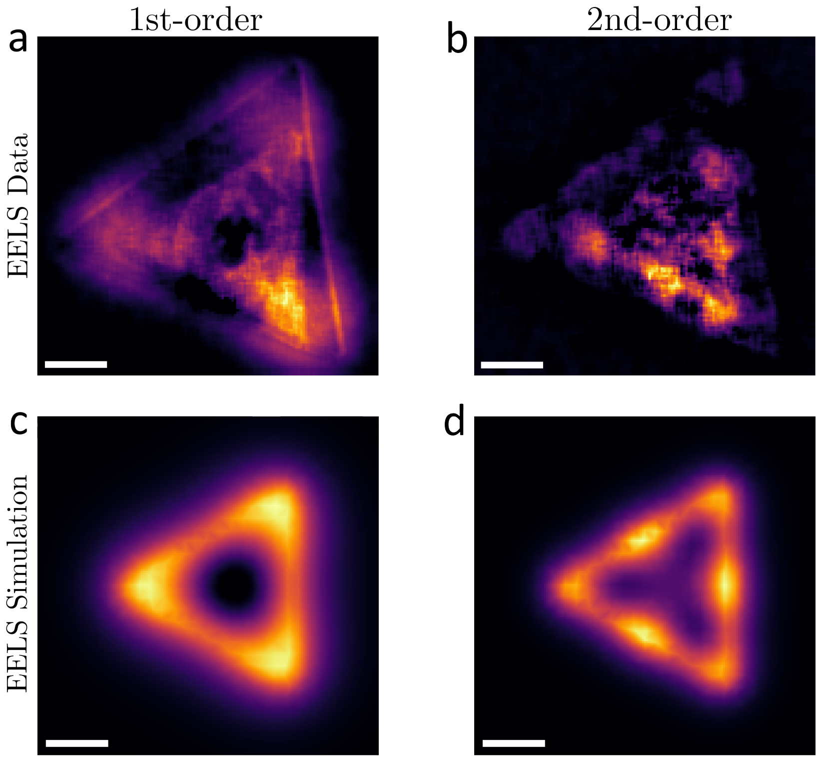

Figure D.15: **EELS probability maps of localised plasmon resonances in a** 680 **nm nanotriangle. (a,b)** Abundance maps of the 680 nm nanotriangle. The energy loss values for the modes obtained from the endmembers are: **a** 1.02 eV and **b** 1.54 eV. **(c,d)** Corresponding simulated maps. The simulation intervals are: **c** $[0.9, 1.1]$ eV and **d** $[1.4, 1.6]$ eV. All scale bars are 200 nm.

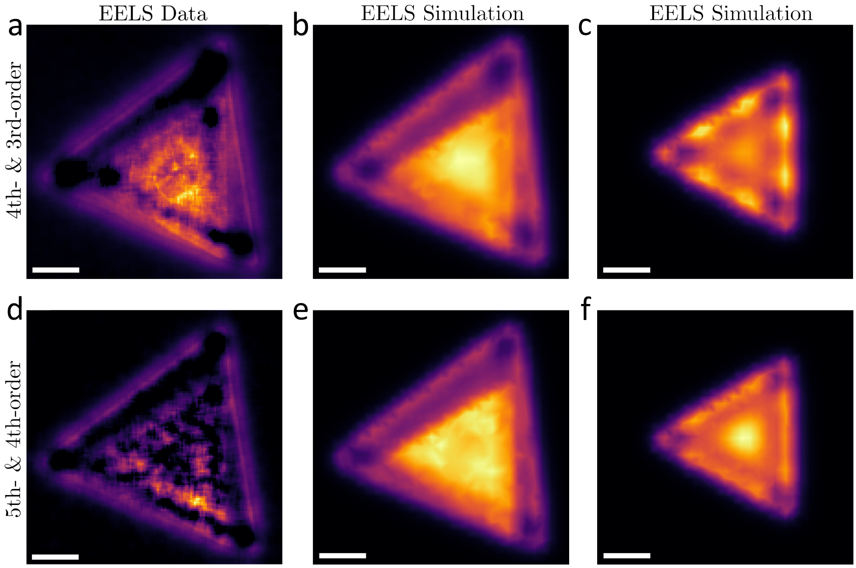

Figure D.16: **EELS probability maps of higher order localised plasmon resonances in the** 680 **nm and** 980 **nm nanotriangle.** **(a,d)** Abundance maps of the stacked WS_2 nanotriangles, displaying high-order plasmon resonances. The energy loss values for the modes obtained from the endmembers are: **a** 2.09 eV and 2.65 eV. **(b,c,e,f)** Corresponding simulated maps for the modes shown in (a) and (d). The simulation intervals are: **b** $[2.05, 2.25]$ eV, **c** $[2.1, 2.3]$ eV, **e** $[2.5, 2.7]$ eV and **f** $[2.6, 2.8]$ eV. The higher order resonance modes of the small triangle, although present in the same energy range, are most likely mixed with the saturation seen in the simulation maps of the large triangle. As a result, although the abundance maps do show hints along the edges of the resonance modes of the small triangle, the nodes are not distinct enough to extract the edge profiles. All scale bars are 200 nm.

D.4. EXTRACTING EDGE MODES IN WS$_2$ NANOTRIANGLES FROM NMF

The values of the energy loss associated to each of the identified edge-localised plasmonic modes are obtained by fitting the endmembers of the NMF components with Gaussians functions, as shown for illustration in Fig. D.5.

In order to extract the phase shift and wavenumbers of the edge modes in the WS$_2$ nanotriangles, we model the system as a linear Fabry-Perot cavity of length L [4], where the incident plasmon wave reflects at the cavity boundary with a phase shift φ. In this model, the incident and reflected localised plasmonic resonances waves can be expressed as plane waves:

$$E_i = e^{ik(x-x_0)}\,, \tag{D.3}$$

$$E_r = |r|e^{ik(2L-x)}e^{i\varphi}\,. \tag{D.4}$$

Assuming a reflection coefficient $|r| = 1$, the total electric field E_{total} is the sum of the incident and the reflected waves:

$$E_{\text{total}} = e^{ik(x-x_0)} + e^{ik(2L-(x-x_0))}e^{i\varphi}\,. \tag{D.5}$$

Rewriting E_{total} in the terms of sine and cosine components, we get:

$$E^2_{\text{total}} = [\cos(k(x-x_0))+\cos(2kL-k(x-x_0)+\varphi)]^2+[\sin(k(x-x_0))+\sin(2kL-k(x-x_0)+\varphi)]^2$$

The wavenumber k_n is related to the phase shift φ by the following relation:

$$k_n L = n\pi - \varphi\,. \tag{D.6}$$

By fitting Eq. (D.6) to the edge profiles obtained from the NMF abundance map, we can obtain the phase shift φ and thereby calculate the wavenumbers k_n of the associated edge modes.

Fig. 5 in the main manuscript, it was shown how the experimental measurements of the dispersion relations of the plasmonic modes are well described by a quadratic model, as expected from surface plasmon characteristics. In Fig. D.17 we add to Fig. 5.5 also the results of a linear fit. It is clear from the data versus model comparison that the linear fit is insufficient to describe the observed values of the dispersion relations for the resonance modes, further validating its plasmonic interpretation.

The Fabry-Perot interpretation assumed here is thus consistent with the quadratic dispersion that is expected for edge-localised plasmonic resonances [5], [6]. Together with the excellent quantitative agreement between the observed abundance maps and the associated PyGDM electrodynamical simulations, this dispersion relation analysis provides corroborating evidence for the plasmonic nature of the observed modes. We note that WS$_2$ in particular, and TMDs in general, are known to display metallic-like behaviour along the edges due to exposed transition metal atoms [7]–[10]. The resulting metallic-dielectric interface provides favourable conditions for the formation plasmonic resonances, similar to noble metal structures.

Other standing wave phenomena such as Whispering Gallery Modes (WGM) have been observed in both dielectric and metallic nanoparticles [11], [12]. However, WGM require high-rotational symmetry (e.g. circular or spheric) to appear, which is not present in the nanotriangle geometry under consideration. Furthermore, WGM are not expected to follow a quadratic dispersion relation. Likewise, while Mie resonances often associated to dielectric particles can support multipolar modes, their dispersion relation is not inherently quadratic and also they are typically volumetric and lack strong edge localisation.

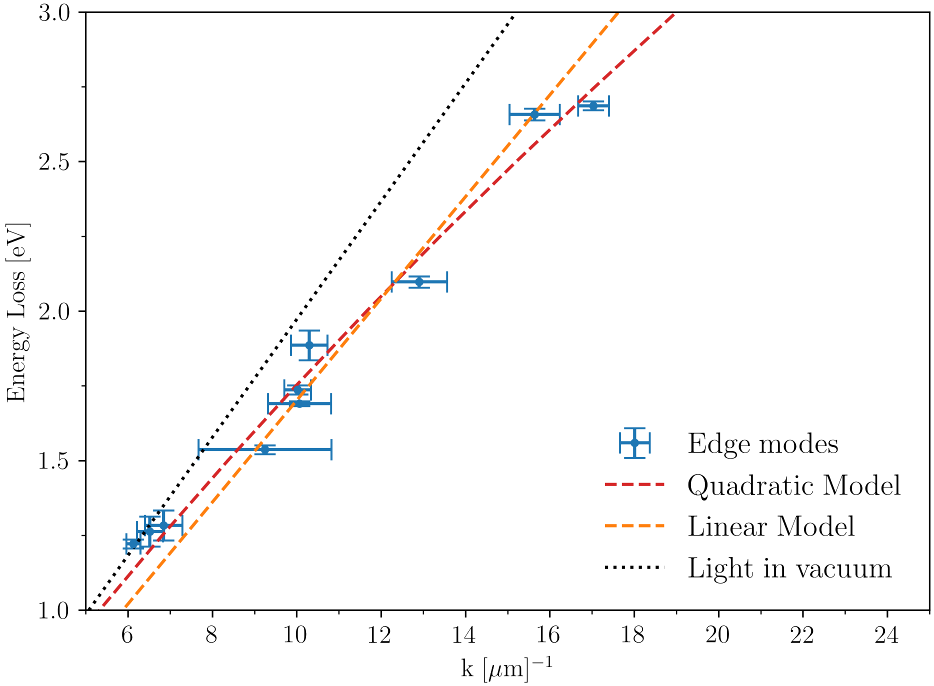

Figure D.17: **Linear fit to the dispersion relation.** Same as Fig. 5 in the main manuscript, now with the addition of a linear model fit. The linear model ($R^2 = 0.95$) describes the experimental measurements of the dispersion relations of the plasmonic modes markedly worse than the default quadratic model ($R^2 = 0.98$) .

D.4.1. ADVANTAGES OF NMF OVER CONVENTIONAL INTENSITY MAPPING METHODS

In Fig. D.18 we compare the edge mode profile obtained from NMF-derived abundance mapping to that from conventional integrated intensity mapping, using the fifth-order resonance mode of the large triangle as an example. The abundance map from NMF decomposition reveals the modes of the resonance mode much more clearly than the integrated intensity method, which does not resolve the nodes as well and make it difficult to fit the profile accurately with Eq. (D.6). Using NMF decomposition provides unambiguous energy loss values and a well-defined map profile, offering a clearer interpretation of resonance modes and their spatial distribution compared to traditional intensity mapping methods.

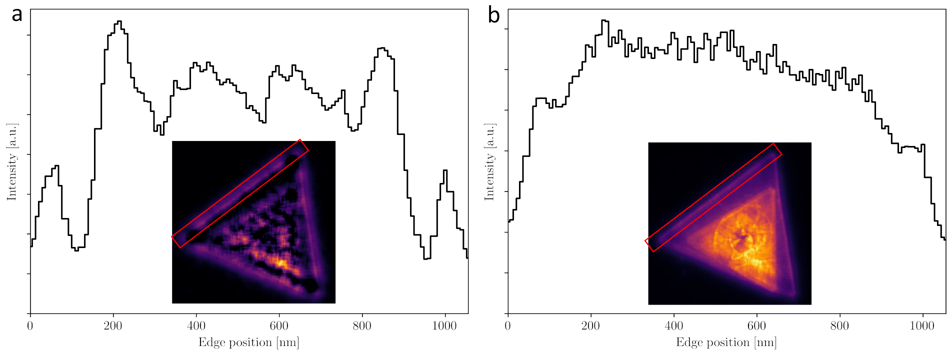

Figure D.18: **Comparison of NMF-based abundance mapping with integrated intensity mapping. a)** Edge profile of the fifth-order resonance mode of the large triangle as shown by the abundance map (inset) derived from NMF decomposition. **b)** Edge profile of the same resonance mode obtained by integrating the EELS intensity over the energy window from 2.3 to 2.6 eV where the fifth-order mode is present.

REFERENCES

[1] K. Iakoubovskii, K. Mitsuishi, Y. Nakayama, and K. Furuya, “Thickness measurements with electron energy loss spectroscopy”, *Microscopy Research and Technique*, vol. 71, pp. 626–631, 8 2008, ISSN: 10970029. DOI: 10.1002/jemt.20597.

[2] P. R. Wiecha, “Pygdm—a python toolkit for full-field electro-dynamical simulations and evolutionary optimization of nanostructures”, *Computer Physics Communications*, vol. 233, pp. 167–192, Jun. 2018, ISSN: 00104655. DOI: https://doi.org/10.1016/j.cpc.2018.06.017.

[3] P. R. Wiecha, C. Majorel, A. Arbouet, *et al.*, ““pygdm” - new functionalities and major improvements to the python toolkit for nano-optics full-field simulations”, *Computer Physics Communications*, vol. 270, Jan. 2022, ISSN: 00104655. DOI: 10.1016/j.cpc.2021.108142.

[4] A. Campos, A. Arbouet, J. Martin, *et al.*, “Plasmonic breathing and edge modes in aluminum nanotriangles”, *ACS Photonics*, vol. 4, pp. 1257–1263, 5 May 2017, ISSN: 23304022. DOI: 10.1021/acsphotonics.7b00204.

[5] H. Saito and H. Kurata, “Direct measurement of dispersion relation for surface plasmon-polaritons on silver nanoantennas”, *Microscopy*, vol. 63, pp. 155–159, 2 Apr. 2014, ISSN: 20505701. DOI: 10.1093/jmicro/dft048.

[6] Y. Wu, Z. Hu, X. T. Kong, *et al.*, “Infrared plasmonics: Stem-eels characterization of fabry-pérot resonance damping in gold nanowires”, *Physical Review B*, vol. 101, 8 Feb. 2020, ISSN: 24699969. DOI: 10.1103/PhysRevB.101.085409.

[7] F. López-Urías, A. L. Elías, N. Perea-López, H. R. Gutiérrez, M. Terrones, and H. Terrones, “Electronic, magnetic, optical, and edge-reactivity properties of semiconducting and metallic ws2 nanoribbons”, *2D Materials*, vol. 2, 1 Dec. 2015, ISSN: 20531583. DOI: 10.1088/2053-1583/2/1/015002.

[8] E. Skúlason, G. S. Karlberg, J. Rossmeisl, *et al.*, “Density functional theory calculations for the hydrogen evolution reaction in an electrochemical double layer on the pt(111) electrode”, *Physical Chemistry Chemical Physics*, vol. 9, pp. 3241–3250, 25 2007, ISSN: 14639076. DOI: 10.1039/b700099e.

[9] M. Tinoco, L. Maduro, and S. Conesa-Boj, “Metallic edge states in zig-zag vertically-oriented mos2 nanowalls”, *Scientific Reports*, vol. 9, 1 Dec. 2019, ISSN: 20452322. DOI: 10.1038/s41598-019-52119-3.

[10] W. Lei, J. L. Xiao, H. P. Liu, Q. L. Jia, and H. J. Zhang, “Tungsten disulfide: Synthesis and applications in electrochemical energy storage and conversion”, *Tungsten*, vol. 2, pp. 217–239, 3 Sep. 2020, ISSN: 26618036. DOI: 10.1007/s42864-020-00054-6.

[11] J. K. Hyun, M. Couillard, P. Rajendran, C. M. Liddell, and D. A. Muller, “Measuring far-ultraviolet whispering gallery modes with high energy electrons”, *Applied Physics Letters*, vol. 93, 24 2008, ISSN: 00036951. DOI: 10.1063/1.3046731.

[12] Y. Auad, C. Hamon, M. Tencé, *et al.*, “Unveiling the coupling of single metallic nanoparticles to whispering-gallery microcavities”, *Nano Letters*, vol. 22, pp. 319–327, 1 Jan. 2022, ISSN: 15306992. DOI: 10.1021/acs.nanolett.1c03826.

CURRICULUM VITÆ

Abel Rutger BROKKELKAMP

24-04-1996	Born in Diemen, The Netherlands.

EDUCATION

2008–2014	**Voortgezet Wetenschappelijk Onderwijs** Jan van Egmond Lyceum, Purmerend, The Netherlands
2014–2017	**Bachelor of Science in Physics & Astronomy** Universiteit van Amsterdam, Amsterdam, The Netherlands *Thesis:* Rotational symmetry breaking in topological superconductor $Sr_xBi_2Se_3$ *Supervisor:* Dr. A. de Visser
2017–2020	**Master of Science in Applied Physics** Delft University of Technology, Delft, The Netherlands *Thesis:* Selective area growth of transition metal dichalcogenides *Supervisor:* Dr. S. Conesa-Boj
2020–2024	**PhD in Physics** Delft University of Technology, Delft, The Netherlands *Thesis:* Enhanced Nanoscale Characterization of Two-Dimensional van der Waals Materials: Combining Electron Energy Loss Spectroscopy with Machine Learning *Promotor:* Dr. S. Conesa-Boj

LIST OF PUBLICATIONS

6. M. Bolhuis **A. Brokkelkamp**, S. Conesa-Boj, *Edge Effects and Grain Boundaries in van der Waals Materials from Pixelated Detectors*, Under review.

5. **A. Brokkelkamp**, S. E. van Heijst, S. Conesa-Boj, *Edge-Localised Plasmonic Resonances in* WS_2 *Nanostructures from Electron Energy-Loss Spectroscopy*, Small Science, 2400558 (2025).

4. S. E. van Heijst, M. Bolhuis, **A. Brokkelkamp**, J. J. M. Sangers, S. Conesa-Boj, *Heterostrain-Driven Bandgap Increase in Twisted* WS_2*: A Nanoscale Study*, Advanced Functional Materials **34**, 2307893 (2024).

3. S. van der Lippe, **A. Brokkelkamp**, J. Rojo, S. Conesa-Boj, *Localized Exciton Anatomy and Band Gap Energy Modulation in One-Dimensional* MoS_2 *Nanostructures*, Advanced Functional Materials **33**, 2307610 (2023).

2. **A. Brokkelkamp**†, H. La†, S. van der Lippe†, J. ter Hoeve, J. Rojo, S. Conesa-Boj *Edge-Induced Excitations in* Bi_2Te_3 *from Spatially-Resolved Electron Energy-Gain Spectroscopy*, Ultramicroscopy **254**, 113841 (2023).

1. **A. Brokkelkamp**†, J. ter Hoeve†, I. Postmes†, S. E. van Heijst, L. Maduro, A. V. Davydov, S. Krylyuk, J. Rojo, S. Conesa-Boj *Spatially Resolved Band Gap and Dielectric Function in Two-Dimensional Materials from Electron Energy Loss Spectroscopy*, The Journal of Physical Chemistry A **126**, 1255-1262 (2022).

---

† Equal Contribution

ACKNOWLEDGEMENTS

Who would have thought, but here we are after a little bit over four years. I got to the end of education, there is nothing left. All jokes of course, but I have been with the University long enough now (almost ten years!) and what a journey it has been. I started the PhD in peak Covid times, but I have been with the Conesa Boj Lab (CBL) since my MSc project starting back in 2019. During this time I have met plenty of people that directly or indirectly provided support that have helped me finish this trajectory successfully.

Starting with the whole reason we are here right now: **Sonia**, I think I will still need some time to really understand why you offered me the PhD position, but it all worked out in the end. We first met before when I was looking for a MSc project, and I had this vague idea of doing something with layered materials since my BSc project. However, with the PhD I got to the best part of your lab: transmission electron microscopy (TEM) and electron energy loss spectroscopy (EELS). I do have to admit, while layered materials are cool and all, the magic around them has wavered a bit for me, but TEM and all its aspects will forever remain fascinating to me. When I wasn't sure how to continue with a problem or needed some motivation, I could always walk into your office and have a chat, and if you weren't there the microscope was the next best place. The latter gave me some great memories of walking into the lab with you doing measurements in the dark with stacks of coffee cups to the side, although you went the healthier route of drinking less coffee now. Gràcies per la vostra cura i orientació, i gràcies pels dolços records!

I also want to thank my other promoter **Kobus**, although we did not have that many meetings specific to my research, from the conversations and meetings that we have had they were incredibly useful and helped me along in my PhD trajectory. I also wish you the best of luck with your new endeavour as member of the board of directors of Jülich Forschungszentrum!

Next I want to thank my two paranymphs: **Chris**, you started exactly 2 years after me and I'm happy to call you a good friend. It helped a lot that we shared our office space together, which made the spontaneous chat or venting much easier as we had this private space. With your kindness and sensitivity to social aspects you brought a new perspective that helped me see things in a different light and be a bit more aware, for that I am very grateful to you. I have no doubt that you'll finish the PhD in time and that you'll manage to fulfil your dream of emigrating to Australia!

Jeroen, you started exactly 3 years after me! Very coincidental indeed, but you've also been around at CBL for longer than that, as you also did the bachelor and master thesis here. Very convenient as well, you were particularly adept at stamping, since I struggled to produce anything significant from that. I really enjoyed our time together as well, particularly the laughs we could have about the state of affairs of the balpol where we both lived. For you I also have no doubt that you'll finish the PhD successfully, best of luck!

Now there are a few CBL people to highlight in particular. **Luigiii**, the cleanroom maestro, you taught me so much about working in the cleanroom, even though I used it less and less as my time at PhD progressed, those skills will be valuable indeed in the future. I will never forget passing out at your house (you remember why), in hindsight the funniest thing ever, but I did feel a bit of shame in that moment. It also never felt like you ever left after you left, since you kept popping up quite a bit afterwards, but it is always good to see you again. There was always a good story or conversation to be had with you, so looking forward what your next endeavours will bring after being stuck in Manchester.

Sabrya, we started the Master Applied Physics together, I do remember the MSc kick off in the Hague where we had to do the crazy 88 like game and we were in the same group. You finished the MSc a bit sooner then I did, but that fact actually did help me to finish my thesis, since the last chapter is thanks to your CVD skills from back during your MSc project/beginning of your PhD. And of course, I was very happy you asked me to be your paranymph for your defence, sorry for not returning the favour, but we were together already busy preparing for Maarten's defence.

Speaking of which: **Maarten**, the wisest man of the lab, you always knew what you were doing whatever the situation. You were the Titan and FIB maestro of the lab, if I had an issue with either of these two, you always had and answered. I also really liked hearing about your hobbies, such as tinkering with the digital photo frame or creating the ever going D&D campaign. I will always be forever grateful that you helped me in Madrid when my luggage was stolen from the hotel we were staying in, even though you were also busy finishing your thesis. It really was your calming and confident presence that made the whole situation bearable for me, so again thank you! I didn't expect it at first, but I was very happy when you asked me to be your paranymph. Also sorry for not returning the favour, but with your own defence being a bit sooner then mine and you moving place sooner after, you'd already have enough on your plate.

Then there are all the people of the EELSFitter project: collectively I want to thank you all, since without you guys this thesis wouldn't have come out the way it is now and it is really thanks to the work of you guys that I managed to finish this thesis. Individually, I want to thank you guys as well! **Laurien** even though we were doing our MSc thesis projects around the same time, we didn't have a lot of contact in person, but the groundwork you did on EELSFitter has helped so much. **Isabel** you improved the work of Laurien even further and gave us a strong foundation to build upon. I also really enjoyed that we got to work together as I just started my PhD at the time, going full speed towards our first paper for the both of us. **Helena** although the whole PhD thing didn't work out for you, you got your footing at the big Dutch tech company. Nonetheless, I found the time we shared the office very enjoyable, finding a bit of common ground in the competitive swimming. **Stijn** pumping out two papers during the masters is no small feat, working together with you was a blast, improving EELSFitter even further. When Sonia asked me to speak at your graduation I gladly accepted, even if the speech provided by Sonia was maybe a bit technical regarding the occasion, I was very proud nonetheless.

Jacooo, we started our PhD's around the same time and for our first in person meeting we played on the ice and snow! We both got our first paper from this collaboration and afterwards we kept it going. It was great to work together and I learned a lot from you as well regarding machine learning and computational physics. Now that you live and work in Edinburgh at the time of writing this, I have good excuse to definitely visit Scotland as soon as possible!

Juan, thank you so much for your wisdom and insights, in a certain way you were a third promoter of mine and we shared many publications together. I learned a lot from your approach to tackling computational problems, as long as the methodology is good, the physics will follow. I certainly enjoyed all the barbecues we had in you and Sonia's garden, talking about the skydiving, I'm not entirely convinced you really don't want to try it at least once at some point. En een belangrijke vraag natuurlijk: gaan we weer een keer meedoen met de Golden Ten Loop?

During my time as PhD at CBL I've also seen many alumni come and go that I haven't mentioned yet, all the Master students: **Ruben**, **Boran**, **Philip**, **Steven**, **Christina**, **Nicole**, **Zahra**, **Floris** and **Alexandra**. And all the Bachelor students: **Jorien**, **James**, **Ties**, **Batuhan** and **Patricia**. A funny thing is that during the PhD you get a different perspective on the MSc and BSc projects as the time goes on, as in many cases you can already quickly tell it will all be fine. Big thank you all for all the enthusiasm you brought to the lab, I certainly enjoyed all the conversations we had, all the lunches we shared together and all the activities we did as a group. Hopefully there was enough to remember each other by both ways!

The many people at Quantum Nanoscience throughout the years have also been great to be around with. My first long time office buddy **Niccooo**, you were such a unique character and it always felt like the PhD was just a minor speedbump for you. I couldn't help but feel a bit sad to see you go, I enjoyed the occasional chats we had and that you weren't afraid to be yourself. Also, the insta-stories of outside bouldering and touring in California look amazing. There was also the wonderful people of the sadly now defunct Kobus Fotonics Crew (or officially the NanoOptics group), **Sonakshi**, **Mark**, **Thijs**, **Irina**, you guys were like a second family, joining us on the Fun Forest adventure and always sharing lunch together. Of course, not forgetting **Daniël** and **Onima**, now adopted in CBL, you can keep the spirit alive for a little bit longer. And all the other QN people I've interacted with throughout the PhD: **Parsa**, **Lorenzo**, **Jana**, **Serena (Liu)**, **Jan**, **Alexander**, **Emanuele**, **Evert**, **Nina**, **Hester**, **Allard**, **Rasa**, **Mattias** thank you for all the good times and fun at QN.

Finally a big thanks to the technical staff at QN and at the **Kavli Nanolab** that work tirelessly to keep all the machines up and running. In particular **Frans**, it's sometimes easy to forget how convenient it was to have someone take care of the Titan, for that I'm grateful.

Buiten de TU Delft heb ik ook veel vrienden en family die ik wil bedanken. Beginnend met de Hennies! **Rick**, speciaal woordje voor jou, want wij kennen elkaar al sinds de wieg. Ik blijf het mooi vinden dat deze vriendschap zo sterk staat. **Stan**, **Björn**, **Eugene**, **Thomas**, **Vincent** en **Brian**, Jullie heb ik allemaal via Rick leren kennen toen ik eigenlijk net in Delft ging studeren, maar het voelt ondertussen dat ik jullie ook al allemaal langer ken dan dat, mede dankzij alle goeie tijden op alle festivals, vrienden weekenden, feestjes en chill avonden, niet alle verhalen zijn safe for work, maar maken wel hele mooie herinneren.

Dion, **Mitchell** en **Tjibbe**, heel veel dank voor alle gezellige avondjes. **Richard**, nog altijd ook super bedankt dat je mij en Dennis had geholpen verhuizen, dankzij jou hebben we het toch binnen een dag kunnen fixen.

Robbert, **Sam** en **Ivo**, ik vind het super leuk dat we na de bachelor contact zijn blijven houden. Heel veel dank voor de leuke uitstapjes die we zo af en toe doen, laten we dit vooral doorzetten!

Mijn studenten en PhD tijd in Delft is ook gekenmerkt door DSZ WAVE en de toffe mensen die ik daar heb leren kennen. **Dennis**, bestuursgenootje, huisgenootje en ook tripgenootje, het bospad tussen X en de kruithuisweg zal altijd een gigantisch bos blijven. Huize DennenAbpol was prachtig. **Nina**, de beste polocom, de gezellige avondjes beeriokart en dat ik eindigde op een luchtbedje zal ik ook nooit vergeten. Of af en toe terug blikken op ons onvergetelijke bestuursjaar, daar zijn veel goede leer momentjes geweest. **Hielke** en **Gerda**, uiteraard is bestuur 29 niet compleet zonder jullie, ook heel veel dank voor het tumultueuze bestuursjaar. **Constance**, **Kevin** en **Nils**, goeie tijden met de meest minimum effort commissie, we moeten zeker blijven af en toe eens samenkomen, dus belangrijk: wanneer gaan we bij Nils eten (en nu ook een tripje naar Kopenhagen inplannen)?

En uiteraard wil ik mijn lieve lieve familie bedanken, **Papa**, **Mama**, **Ruben**, **Rona**, **Joram** en ook **Isabella**, **Danilla** en **Casper**, ik ben zo blij dat jullie mijn familie zijn en dat we op elkaar kunnen steunen. Het is en blijft altijd super leuk als we allemaal bij elkaar kunnen komen, ik hou van jullie allemaal.

Volgens mij is dat iedereen wel?
Niemand vergeten toch... Oh wie is dit hier naast mij?
Oepsieee, zomaar over je heen gekeken (grapjuh). Lieve lieve lieve **Yashoda**, de PhD ging niet altijd even soepel voor mij en soms vroeg ik mij af waarom ik dit had gekozen, maar dat ik jou erdoor heb leren kennen maakt dat ik het zo weer zou doen (nee, ik was niet haar begeleider, dat was Luigi). Blijkbaar hielden ze bij CBL hun hart vast of het wel goed zou gaan, maar nu na ruim drie jaar samen kunnen we ze een hand op het hart kunnen doen. Die drie jaar is ook zo voorbij gevlogen en voelt het alsof we al veel langer bij elkaar zijn. Ik heb met al zoveel leuke reisjes gemaakt en dingen meegemaakt: kruipend door de kamertjes van Doloris, spelen in de Sahara, een prachtige sterrenhemel op Ameland, of gewoon lekker knus thuis op de bank. Tijdens dat ik dit schrijf hebben we Japan op planning staan waar ik echt enorm veel zin in heb en, dit is natuurlijk nog maar het begin. Ik heb zoveel op jou kunnen steunen en kan ik mijzelf zijn. Ik hou van jou, op naar de volgende avonturen! Daarbij wil ik ook jou familie bedanken, **Pa**, **Ma** en **Anisha**, maar ook de rest van de hele familie voor de enorme warmte en openheid die ze voor mij hebben.